Ion implantation in nanostructured ZnO: A study on defect evolution

Thesis submitted for the award of degree of

Doctor of Philosophy (Science)

JADAVPUR UNIVERSITY

August 2022

By

Amaresh Das

School of Physical Sciences

Indian Association for the Cultivation of Science

Jadavpur, Kolkata - 700032, India

Dedicated to my beloved Family

.......especially the Parents ....

Along with all my respected Teachers

INDIAN ASSOCIATION FOR THE CULTIVATION OF SCIENCE
JADAVPUR, KOLKATA - 700032, INDIA

Prof. Durga Basak
Senior Professor
School of Physical Sciences

CERTIFICATE FROM THE SUPERVISOR

This is to certify that the thesis entitled **"Ion implantation in nanostructured ZnO: A study on defect evolution"** submitted by **Mr. Amaresh Das** who got his name registered on 24.09.2018 for the award of Ph.D. (Science) degree of Jadavpur University, is absolutely based upon his own work under the supervision of **Prof. Durga Basak** and that neither this thesis nor any part of it has been submitted for either any degree/diploma or any other academic award anywhere before.

29/3/23

(Signature of the supervisor
and date with official seal)

Dr. D. Basak, **Ph.D.**
Professor
Department of Solid State Physics
Indian Association for the
Cultivation of Science
Jadavpur, Kolkata - 700 032

Phone: 033-24734971 Ext: 1316   Fax: +91-33-24732805   Email: sspdb@iacs.res.in

Acknowledgement

Investigation embodied in this thesis entitled "Ion implantation in nanostructured ZnO: A study on defect evolution" was initiated in March, 2017 at Indian Association for the Cultivation of Science (IACS) under the supervision of Prof. Durga Basak, School of Physical Sciences. My experience at IACS has been wonderful. Since my first day, I have always found a homely atmosphere at IACS.

I feel deeply moved while writing this section to acknowledge and thank the countless number of people I came across in last five years. My mind is full of images of those who have helped directly and indirectly me in this endeavor. Words are not enough to thank them in writing.

First and foremost, I would like to express my sincere gratitude to my supervisor Prof. Durga Basak, School of Physical Sciences, IACS for her esteemed supervision and incessant support throughout my thesis work. I sincerely appreciate her patience and encouragement for accomplishing the present work in time. Her regular constructive discussions and never giving up approaches have guided me in many ways to improve my research. I am really thankful to her for her constant guidance for which the thesis has taken this shape.

I would like to acknowledge Council of Scientific and Industrial Research (CSIR) and IACS for the financial assistance throughout my research tenure. I also record my acknowledge to IUAC, New Delhi and my institute IACS for providing me all the scientific facilities to carry on my research work.

I would like to thank my seniors Dr. Sanjit Sarkar, Dr. Arindam Mallick, Dr. Shuvaraj Ghosh, Dr. Ayon Das Mahapatra, Dr. Dipanwita Sett, Ms. Sulakshana Mondal for sharing their understanding and giving correctional inputs regarding my task. I also like to thank my juniors Santanu, Sourav, Barnali, Santanu (junior) for their companionship and cooperations. It was so much full of joy and fun that I will never forget the time which I spent especially with Arindam da, Shuvaraj da, Ayon da, Santanu, and Sourav in my lab and outside the lab.

I also extend my gratitude to the employees of School of Physical Sciences and academic section especially Sujit da, Pandit da, Niranjan da for their administrative support.

I sincerely thank all the faculties and scholars of School of Physical Sciences. It is my pleasure to name some seniors, friends, and juniors especially Soumya da, Biswajit da, Arnab da, Jayjit da, Hrishikesh da, Pulak da, Ankita Di, Sumana Di, Goutam, Salma, Abhishek, Raja, Shubham, Atanu, Pradeepta, Tamal, and Shameek.

The thesis would not have come to a successful completion without the help I received from the staffs of the Central Scientific Service and IACS workshop especially Mr. Tapas Dutta, Mr. Sutapesh Dutta, Mr. Indranath Bhaumik, Mr. Supriya

Chakraborty, Mr. Manash Kumar Ghosh, Mr. Ranajit Sardar, Mr. Rabindranath Banik, Mr. Gopal Krishna Manna, Mr. Somnath Banerjee, Mr. Manoj Kumar Saha, Mr. Jhankar Nath Ghosh, Mr. Biswajit Saha, cleantech workers, security guards, canteen staffs and so many others.

I wouldn't able to express my feelings to my family: Mamoni, Bapi, Bon, Dida, and others by words only. For the last ten years or so I am a hundred kilometers away from them, so could take care nothing of them, but they never complained. What I am today is just because of their sacrifices. I feel proud and will be indebted to them always.

A very special thanks to my forever companion Sanjukta for being my side in every good and bad moment of my life and always wishing me well.

Last but not the least, I would like to acknowledge my all-respected teachers I came across throughout my academic career till date. I can't stop myself from remembering the names of some of them especially Bankim master, Poltu master, Bikash Sir, Haren Sir, Pranab Sir, Ardhendu Sir, Biswajit Sir, Anukul Sir, Shuvendu Sir, Dr. Debabrata Das. I am really grateful to all of them for the education they gave me to reach at this stage.

Thank you all again for the encouragement.

Amaresh Das
29/03/2023

IACS, Kolkata
August, 2022

Abstract

The thesis entitled "Ion implantation in nanostructured ZnO: A study on defect evolution" deals with the defect evolution and interactions with the implanted ions in the ZnO nanorods (NRs) and nanoparticle thin films with the detail characterizations of structural, electrical and optical properties. ZnO is a multifunctional wide bandgap (~3.37 eV) II−VI semiconductor that has distinctive properties, such as large excitonic binding energy of ~60 meV, high optical emission efficiency, visible light transparency, ultraviolet (UV) sensitivity, nontoxicity, and good compatibility, which make ZnO to be used in various low-cost technological applications such as transparent conducting electrode, photoelectrochemical water splitting, UV light-emitting diodes, photodetectors, solar cells, gas sensors, and so on. Moreover, as compared to conventional devices, nanodevices based on one dimensional (1D) NRs of ZnO have advantageous properties like ultrahigh speed as well as frequency, large integration density, and low power consumption other than the size factor. However, the fact is that the electrical and optical properties and therefore the applications of ZnO are vastly driven by its inherent vacancies, interstitials, and anti-sites of Zn and O related defects. From this point of view, study on ZnO nanostructured thin films is of great interest to the researchers because these usually exhibit diverse material properties as compared to the corresponding bulk crystal owing to the modified defect states, lattice imperfection, structural disorder, high surface area, exotic polar topology, and so on. To produce highly performing devices, the key factor is the processing of better-quality materials. Doping is one of the well-known processing steps in the semiconductor industry for the fabrication of various optoelectronic devices. Though the impurity incorporation into ZnO nanostructured thin films has been already achieved successfully using doping during growth and doping by diffusion, a controllable and reproducible doping is still difficult for 1D NRs. In such cases, the post-growth doping via ion implantation method can be a solution for successful doping in ZnO NRs. However, in the process of ion implantation, the interaction between the host lattice and the energetic ions produces point defects inside the target material due to the collisions by the energetic ions. Minute concentrations of defects and impurities can hugely alter the mechanical, electrical, and optical properties of ZnO. The implantation induced defect states in ZnO crystal act as recombination or trapping centres and thus affect the relaxation process of the photoexcited carriers. In addition to it, the implanted induced complex defects control the charge carrier profiles and modifies the conductivity of ZnO. ZnO always exhibits n-type conductivity which can further be enhanced by doping with n-type dopants. But the formation of reproducible and

stable p-type ZnO still remains a major challenge due to low or limited solubility and high activation energies of the acceptor dopants and the presence of huge compensating defects. Therefore, the effort to overcome the difficulty of achieving controllable and reproducible p-type ZnO is still one of the needs for the successful fabrication of p-n homojunction based nanodevices.

With the above-said motivation, the work embodied in this thesis has focused mainly on two aspects:

(i) Studies on the role of defects on the room temperature (RT) photoluminescence (PL) and electrical properties and the defects identification mechanism in ZnO nanoparticle thin films as well as in ZnO NRs implanted with donor dopant (Al ion).

(ii) Studies on the evolution of the acceptor defects and their compensation with the donor defects in ZnO NRs implanted with various acceptor dopants (N, Li ions) under various ion fluences and post-implantation annealing ambiences.

The entire thesis consists of total nine chapters. The chapter wise contents are given below:

The chapter 1 provides a brief general introduction on ZnO and ion implantation followed by the objectives and organization of the thesis work. In the chapter 2, a critical assessment of the recent ion implantation efforts in ZnO mainly focusing on the status, opportunities, and challenges in the modification of the optical and electrical properties followed by their applications in optoelectronic devices have been presented. The chapter 3 consists two sections: (i) Details of the growth techniques for ZnO nanoparticle thin films by sol-gel and 1D ZnO NRs by aqueous chemical growth techniques have mainly been elaborated firstly. (ii) Secondly, the characterization techniques used for this thesis work have been illustrated in details. The formation of various structural defects and the modifications of the optical and electrical properties in sol-gel grown ZnO thin films implanted with various fluences (1×10^{13} to 6×10^{15} ions/cm^2) of 100 keV Al ions have been assessed extensively in the chapter 4. For the highest fluence (6×10^{15} ions/cm^2), the sheet resistance is found to be 156 Ω/sq with an average visible transmission of 82%. The high figure of merit value of the Al implanted ZnO films are of prospective as a transparent conducting electrode. Detailed investigation of the implantation mechanism reveals that zinc vacancy (V_{Zn}) defects are formed in large number due to implantation, which on healing produces further higher conductivity in the films. A comprehensive study on the effect of Al ion implantation on RT PL properties of vertically-aligned ZnO NRs implanted with 100 keV Al ions by varying the fluences from 1×10^{13} to 1×10^{16} ions/cm^2 followed by an annealing

process at 450 °C in an inert ambient has been presented in the chapter 5. As compared to pristine, an unprecedented enhancement (1.4 times) in the ratio of the intensities of the near band edge, I_{NBE} (UV) to the defect level, I_{DL} (visible) emissions has been observed for the ZnO NRs implanted with of Al ions of 5×10^{13} ions/cm^2. The ratio I_{NBE}/I_{DL} decreases beyond 5×10^{13} ions/cm^2 with an increase in Al ion fluence. Detailed analyses of the recombination mechanism show that the excitons bound to neutral Al donors are responsible for highly enhanced PL emissions in lower fluence Al implanted ZnO NRs. On the other hand, the implantation induced defects acting as non-radiative recombination centres are responsible for the reduced PL emissions in higher fluence Al implanted ZnO NRs. In the chapter 6, the interplay of point defects in ZnO NRs implanted with 50 keV N ions having fluences from 1×10^{14} to 1×10^{16} ions/cm^2 followed by a thermal annealing at 450 °C separately in Ar, O$_2$, and excess Zn ambiences has been discussed. The detailed analyses validate the incorporation of N at O sublattice forming isolated N_O acceptor and N_O-V_{Zn} acceptor complex in the implanted NRs and N implantation-induced structural disorders increase with an increase in the N ion fluence. The study on the influence of post-implantation annealing reveals that annealing in Ar and O$_2$ ambiences causes only N_O state, while annealing in excess Zn ambient induces an additional shallow donor $(N_2)_O$ by substituting N$_2$ at O site. Thus, the post-implantation annealing in O$_2$ and Ar ambiences play a key role to stabilize the N dopants in ZnO. The evolution of various point defects in 100 keV Li ion implanted ZnO NRs with varying the fluences from 1×10^{14} to 7×10^{15} ions/cm^2 has been discussed with the experimental and theoretical simulation results in the chapter 7. The experimental results indicate that the Li^{1+} ions are incorporated at Zn^{2+} sites forming Li_{Zn} acceptor in the implanted NRs and the structural disorders increase drastically with an increase in the Li fluence. Both the formation of acceptors and implantation-induced defects make the Li implanted NRs electrically highly resistive. The yellow-orange PL emission of the as-grown ZnO NRs has been evolved into a green emission in the implanted NRs. The simulation results explain the quantitative energy loss, the distributions of the implanted Li ions and the point defects along the target ZnO NRs. The consistency between the experimental and theoretical simulations validates our analyses on the formation and evolution of various point defects in highly resistive Li implanted ZnO NRs. The formation and evolution of various point defects in 1D ZnO NRs co-implanted with 100 keV N and Li ions as a function of various co-implantation fluences resulting in the changes in structural, and optical properties have been presented in the chapter 8. Detailed analyses show that the implantation-induced structural disorder increases with an increase in the implantation fluence and both the N_O and Li_{Zn} acceptors are produced in co-implanted NRs. The N_O may form Li_i −

N_O complex with the Li interstitials (Li_i) and thus the concentration of Li_i and the possibility of the generation of $(N_2)_O$ donors are reduced. As a matter of fact, there still exits Li_{Zn} acceptors which may contribute to creating p-type ZnO NRs in case of N-Li co-implanted ZnO NRs. Due to co-implantation implantation, the formation of V_{Zn} is indicated by the appearance of a green PL emission.

A list of up-to-date references relevant to the topic has been included at the end of each chapter.

Finally, in the chapter 9, a summary of the important results emerging from this thesis work has been presented followed by a future outlook of the work.

List of Publications

1. "Highly enhanced ultraviolet to visible room temperature photoluminescence emission ratio in Al implanted ZnO nanorods", **Amaresh Das**, Shuvaraj Ghosh, Ayon Das Mahapatra, Debdulal Kabiraj, Durga Basak, Applied Surface Science 495 (2019) 143615.

2. "High conductivity along with high visible light transparency in Al implanted sol-gel ZnO thin film with an elevated figure of merit value as a transparent conducting layer", **Amaresh Das**, Gangadhar Das, Debdulal Kabiraj, Durga Basak, Journal of Alloys and Compounds 835 (2020) 155221.

3. "Interplay of defects in low energy nitrogen implanted ZnO nanorods", **Amaresh Das**, Durga Basak, Applied Surface Science 564 (2021) 150424.

4. "Efficacy of Ion Implantation in Zinc Oxide for Optoelectronic Applications: A Review, **Amaresh Das**, Durga Basak, ACS Applied Electronic Materials 3 (2021) 3693.

5. "Drastic evolution of point defects in vertically grown ZnO nanorods induced by lithium ion implantation", **Amaresh Das**, Durga Basak, Physical Chemistry Chemical Physics, 24 (2022) 23858.

6. "Defect-Assisted Broad-Band Photosensivity with High Responsivity in Au/Self-Seeded TiO_2 NR/Au-Based Back-to-Back Schottky Junctions", Ayon Das Mahapatra, **Amaresh Das**, Shuvaraj Ghosh, Durga Basak, ACS Omega 4 (2019) 1364.

7. "Defect interaction in nitrogen and lithium co-implanted ZnO nanorods", **Amaresh Das**, Durga Basak (communicated, 2022)

Contents

[viii]

List of Abbreviations

Acronyms

1D	One dimensional
at. %	Atomic percentage
AFM	Atomic force microscopy
ACG	Aqueous chemical growth
AZO	Al doped ZnO
BM	Burstein-Moss
BF	Bright field
CL	Cathodoluminescence
CB	Conduction band
CBM	Conduction band minima
DF	Dark field
DL	Defect level
DEA	Diethanolamine
EL	Electroluminescence
EDS	Energy dispersive X-ray analysis
Fig.	Figure
(FE)SEM	(Field emission) scanning electron microscopy
FWHM	Full width at half maxima
FOM	Figure of merit
FX	Free exciton
(HR)TEM	(High resolution) transmission electron microscopy
ITO	Indium Tin Oxide
I-V	Current-voltage
LED(s)	Light Emitting Diode(s)
LEIBF	Low energy ion beam facility
MEA	Monoethanolamine
NBE	Near band edge emission
NRs	Nanorods
NPs	Nanoparticles
NWs	Nanowires
PAS	Positron annihilation spectroscopy
PEC	Photoelectrochemical
PC	Photoconductivity
PL	Photoluminescence
PVD	Physical vapor deposition
PPC	Persistent Photocurrent
RT	Room temperature
RPM	Rotation per minute
RL	Radioluminescence
SRIM	Stopping and Range of Ions and Matter
SPR	Surface plasmon resonance
SO	Surface optical
TCO	Transparent conducting oxide
TRIM	Transport in Matter
UV	Ultraviolet

VB	Valence band
VBM	valence band maxima
VIS	Visible
XPS	X-ray Photoelectron Spectroscopy
XRD	X-ray diffractometry
ZnO	Zinc Oxide

Symbols and notations

$\alpha(\lambda)$	The absorption coefficient.
β	Kurtosis/FWHM
γ	Skewness
ρ	Resistivity
δ	Dislocation density
λ	Wavelength
φ	Work-function
σ	Stress
$\sigma\perp$	Lateral Gaussian distribution
σ_p	Projected straggle
μ_h	Hall mobility
ε	strain
η	Ideality factor
$\Delta\omega_{1/2}$	half-width
As_{Zn}	As at Zn site
$Al\ D^0X$	Excitons bound to neutral Al donor
a	a-axis lattice parameter
B	Magnetic field
c	c-axis lattice parameter
D	Crystallite size
D^0X	Donor bound excitons
DBX	Excitons bound to defect state
E_b	Binding energy
E_d	Displacement energy
E_g	Band gap energy
E_F	Fermi Energy / Fermi Level
E_k	Kinetic energy of photoelectron
E_u	Urbach energy
FX	Free excitons
$h\nu$	Photon energy
I_{NBE}	Intensity of NBE emission
I_{DL}	Intensity of defect level emission
k	Shape factor
Li_{Zn}	Lithium at Zn site
Li_i	Lithium interstitial
n	Carrier concentration
N_O	N at O site
$(N_2)_O$	N_2 at O site
O_i	Oxygen interstitial
O_{Zn}	Oxygen antisite

P_O	P at O site
P_{Zn}	P at Zn site
R_p	Projected range
R_s	Sheet resistance
R_H	Hall resistance
S_e	Electronic energy loss
R_{rms}	RMS roughness
S_n	Nuclear energy loss
T_{av}	Average Trasparency
V_{Zn}	Zinc vacancy
V_H	Hall voltage
V_O	Oxygen vacancy
Zn_i	Zn interstitial
Zn_O	Zinc antisite

List of tables

List of figures

[xviii]

[xix]

[xxi]

CHAPTER-1

Introduction and motivation

1.1 Background of the work

The advancements in the field of electronics have revolutionised the way we live. Using electronics today is so much part of our live that we hardly think of the way the world would be without electronics. Semiconductors are the foundations of modern electronics. During the beginning of semiconductor industry, Si became popular in the commercial market for its usages in computing, data storage and communications as integrated circuits. But Si failed to meet the necessity of the optoelectronic devices such as light emitting diodes (LEDs), laser diodes due to its indirect band gap. In the meantime, GaAs was emerged as an important class of compounds in semiconductor industry due to its direct band gap. However, GaAs-based devices also failed to meet the necessity of the ultraviolet (UV)/blue light emitter for display applications. As a result, the wide band gap semiconductors like ZnSe, SiC, GaN, ZnO came forth and became the research focus in the field of semiconductor. The past decade has seen varying degrees of research effort and pronounced advancements of wide band gap semiconductors-based devices ranging from the solar cells to the blue lasers [1-4]. Among wide band gap semiconductors, ZnO has attracted invigorated interest as an optoelectronic material for numerous applications over more than the last two decades. Lately, this effort has been strengthened in order to have an in-depth understanding of its unique physical properties and to grow high quality ZnO nanostructured films and nanocrystals for device applications [5-8]. As compared to other wide band gap materials, ZnO has some unique properties and some advantages such as high emission efficiency, visible light transparency, UV absorbance sensitivity, nontoxicity which make them to be used in various technological applications such as photoelectrochemical (PEC) water splitting, UV LEDs, photodetectors, solar cells, catalysis, varistors, supercapacitors, gas sensors, and so on [9-24]. ZnO is a competitor of GaN, a well-known III−V wide band gap material which is now widely used for commercial production of short wavelength (λ) as well as white light emitting devices [25-27]. ZnO has many advantages over GaN such availability of large size bulk crystals, easy growth of controllable nanostructures, and earth abundant constituents which create a situation that allows excitation-based lasing action with a very low threshold current [28-30]. In addition to optoelectronic and electronic devices, ZnO has also become a key material for spintronic applications such as spin LEDs, spin polarized solar cells, and magneto-optical switches [31, 32]. Moreover, compared to conventional devices, nanodevices based on nanostructures of ZnO have advantageous properties like ease in fabrication, ultrahigh speed as well as frequency, large integration density, and low power consumption [6, 8, 33]. It has been seen that ZnO shows a diverse

group of growth morphologies in the form of powders, single crystals, and nanostructured thin films such as nanoparticles, nanorods (NRs) array, nanowires (NWs), nanobelts, nanocombs, nanorings, and so on [34-39]. With a reduction in size to nanometre regime, ZnO shows novel physical properties as a result of surface and quantum confinement effects. In addition to that, a large surface to volume ratio results in forming large number intrinsic or extrinsic surface defects leading to various trap level related emission in the visible range which contribute to the optical transitions more significantly in addition to UV emission under proper excitation.

To realize highly performing devices, the key problem lies with the grasp of better-quality materials. Doping is one of the well-known processing steps in the semiconductor industry for the fabrication of various optoelectronic devices. Conventional methods of doping can generally be divided into three types: doping during crystal growth, doping by diffusion, and doping by ion implantation. Impurity doping into ZnO nanoparticle thin films using the first two type of methods has been achieved already [40-43]; nonetheless, a controllable and reproducible doping technique during crystal growth is still difficult to be achieved, especially for one dimensional (1D) nanostructure such as NRs [44, 45]. In this situation, post-growth doping via ion implantation is believed to be a controllable and rather exact manner for any solid target as compared with the other two methods [43, 46-48]. This method is regarded as an advanced technology for doping which being applied nearly for the past 40 years for modifying the surface of bulk materials as well as improving the semiconductor properties due to its following tremendous advantages:

- An accurate fluence (number of ions implanted per unit area of the target) can be controlled by the measurement of ion current.
- The depth distribution of the implanted dopant ions and the induced lattice disorder are directly related to the ion energy and the masses of the target material and ion.
- By varying the ion energy and fluence, the concentration profile of the impurities and also the structural changes can be tailored.
- In contrast to high temperature processing, the ion implantation is apparently low temperature process, although subsequent annealing is generally required to recover implantation induced damages. In this respect, it differs greatly from the diffusion approach, where high temperatures during doping may lead to decomposition of the near surface region.
- The implantation process is not constrained by thermodynamic considerations. This means that any species of ion may be implanted into any host. A wide concentration

range can be achieved with the upper limit generally set by the sputtering yield rather than by equilibrium solubility.

- Ion implantation can be included in the semiconductor process technology and implantation machines can be designed for specific applications.

Thus, the ion implantation has become an important means for fundamental research as well as applications for functional materials. In addition, material properties can be altered flexibly if proper selection of ion species, energy, and fluencies is made.

1.2 Motivation and Objective of the thesis

From the above discussion, it is evident that ZnO nanostructured thin films are of great interest to the researchers because these usually exhibit diverse material properties as compared to the corresponding bulk single crystal owing to the modified defect states, lattice imperfection, structural disorder, high surface area, exotic polar topology, and so on [49-52]. It offers immense possibility for fundamental studies as well as applications in optoelectronic devices. But the fact is that the electrical and optical properties and therefore the applications of ZnO nanostructured thin films are vastly driven by its inherent vacancies, interstitials, and antisites of Zn and O related defects. A control over its inherent defects and dopants is still lacking, which generates an obstacle in realization of practical devices [53-55]. Therefore, before such devices can be manufactured, a vast knowledge of the evolution of the defects of this material during various processing is needed.

Besides the incorporation of impurities, the interaction between the host lattice and the energetic ions in the process of ion implantation produces point defects inside the target material due to collisions by the energetic ions. Minute concentrations of defects and impurities can hugely alter the mechanical, electrical, and optical properties of ZnO [56-60]. The ion-induced defect states in ZnO crystal act as recombination or trapping centres and thus affect the relaxation process of the photoexcited carriers [61, 62]. In addition to it, the implanted ion-induced complex defects control the charge carrier profiles and modifies the conductivity of ZnO [63, 64]. Therefore, for an application of ion implantation as a doping technique, a knowledge of the fundamental physics and chemistry behind the interaction of the ion beam and the target is required. Characterization of both the implanted species and the damage introduced to the target open up a new horizon in this area of research.

ZnO is a n-type semiconducting material irrespective of its growth technique and its n-type conductivity can easily be enhanced by doping with elements having valency higher than +2 [65, 66]. However, a stable and reproducible p-type ZnO with good conductivity is still difficult to achieve, which is a bottleneck for practical ZnO-based applications [67]. The low or limited solubility and high activation energies of the acceptor dopants and presence of huge compensating defects are main hindrances in obtaining p-type ZnO [68]. Not only the electrical conductivity, other characteristics such as optical and optoelectronic properties show a huge change upon doping with p-type dopants. Therefore, the effort to know the evolution in the properties and to achieve controllable and reproducible p-type ZnO is still one of the needs for successful fabrication of p-n homojunction based nanodevices.

Being inspired with the growing interest and gathering knowledge in the above-mentioned issues, the objectives of the present thesis work have been defined as follows:

(i) Understanding the role of compensating defects and implantation mechanism in the Al implanted ZnO thin films to correlate the resultant electrical properties to develop transparent conducting ZnO films.

(ii) To study the role of defects in the modified room temperature (RT) photoluminescence (PL) and photoconductivity properties of ZnO NRs implanted with n-type dopants.

(iii) To study the evolution of the acceptor defects and their compensation with the donor defects in ZnO NRs implanted with various acceptor dopants under various ion fluences and post-implantation annealing ambiences.

1.3 Organization of the thesis

In this thesis work, both the ZnO nanoparticle thin films and NRs arrays have been implanted with various ions such as Al, Ar, N, Li. Comprehensive studies on the defect evolution and their interactions with the implanted ions via structural, optical, and electrical characterizations have been carried out. The entire thesis consists of total nine chapters. After presenting a brief general introduction on ZnO as well as ion implantation followed by the objectives, organization of the thesis has been presented at the end of the chapter 1. A critical assessment of the recent implantation efforts focusing on the status, opportunities, challenges of ion implantation in ZnO, the modified optical and electrical properties and applications of ion implanted ZnO have been presented in the chapter 2. In the chapter 3, the depositions methods for ZnO nanoparticle thin films by sol-gel and ZnO NRs arrays by aqueous chemical

growth techniques have been mainly elaborated followed by the description of various types of characterization techniques which have been particularly used in the present thesis work. In the chapter 4, the formation of various structural defects and the modifications of the optical and electrical properties in sol-gel grown ZnO thin films implanted with various fluences of Al ions have been discussed extensively. In the chapter 5, a comprehensive study on the effect of Al ion implantation fluence on the RT PL emission properties of ZnO NRs has been presented. The role of defects and the recombination mechanism have been discussed exclusively by comparing the results with the Ar implanted ZnO NRs. In the chapter 6, an in-depth comprehensive study on the interplay of defects in N implanted ZnO NRs manifesting the changes in structural, optical, and electrical properties with the increase in N ion fluence has been presented. The properties of the implanted ZnO NRs have also been studied for various annealing ambiences. The evolution of various point defects in Li ion implanted ZnO NRs with the variation in fluences has been discussed with the experimental and theoretical simulation results in the chapter 7. In the chapter 8, a study on the formation of acceptor defect complex (instead of isolated single p-type point defect) using a technique of co-implantation with Li and N has been explored. A list of up-to-date references relevant to the topics of the chapter has been included at the end of each chapter. Finally in the chapter 9, a summary of the important results emerging from this thesis work has been presented followed by a future outlook of the work.

1.4 References

[1] P.V. Kamat, Quantum Dot Solar Cells. Semiconductor Nanocrystals as Light Harvesters, J. Phys. Chem. C, 112 (2008) 18737-18753.
[2] F.A. Ponce, D.P. Bour, NItride-based semiconductors for blue and green light-emitting devices, Nature, 386 (1997) 351-359.
[3] S.N. Mohammad, A.A. Salvador, H. Morkoc, EMERGING GALLIUM NITRIDE BASED DEVICES, Proc. IEEE, 83 (1995) 1306-1355.
[4] R. Ghosh, S. Fujihara, D. Basak, Studies of the optoelectronic properties of ZnO thin films, J. Electron. Mater., 35 (2006) 1728-1733.
[5] Ü. Özgür, D. Hofstetter, H. Morkoc, ZnO devices and applications: a review of current status and future prospects, Proceedings of the IEEE, 98 (2010) 1255-1268.
[6] D. Panda, T.-Y. Tseng, One-dimensional ZnO nanostructures: fabrication, optoelectronic properties, and device applications, Journal of Materials Science, 48 (2013) 6849-6877.
[7] D.C. Look, Recent advances in ZnO materials and devices, Materials Science Engineering: B, 80 (2001) 383-387.
[8] A. Mallick, S. Ghosh, D. Basak, Highly conducting and transparent low-E window films with high figure of merit values based on RF sputtered Al and In co-doped ZnO, Materials Science in Semiconductor Processing, 119 (2020) 105240.
[9] Y. Zhu, H. Zhang, X. Sun, S. Feng, J. Xu, Q. Zhao, B. Xiang, R. Wang, D. Yu, Efficient field emission from ZnO nanoneedle arrays, Appl. Phys. Lett., 83 (2003) 144-146.

[10] S. Masuda, K. Kitamura, Y. Okumura, S. Miyatake, H. Tabata, T. Kawai, Transparent thin film transistors using ZnO as an active channel layer and their electrical properties, J. Appl. Phys., 93 (2003) 1624-1630.

[11] Z. Tang, G.K. Wong, P. Yu, M. Kawasaki, A. Ohtomo, H. Koinuma, Y. Segawa, Room-temperature ultraviolet laser emission from self-assembled ZnO microcrystallite thin films, Appl. Phys. Lett., 72 (1998) 3270-3272.

[12] Y.-K. Su, S. Peng, L. Ji, C. Wu, W. Cheng, C. Liu, Ultraviolet ZnO nanorod photosensors, Langmuir, 26 (2010) 603-606.

[13] X. Yang, A. Wolcott, G. Wang, A. Sobo, R.C. Fitzmorris, F. Qian, J.Z. Zhang, Y. Li, Nitrogen-doped ZnO nanowire arrays for photoelectrochemical water splitting, Nano letters, 9 (2009) 2331-2336.

[14] Y.-S. Choi, J.-W. Kang, D.-K. Hwang, S.-J. Park, Recent advances in ZnO-based light-emitting diodes, IEEE Transactions on electron devices, 57 (2009) 26-41.

[15] K. Matsubara, P. Fons, K. Iwata, A. Yamada, K. Sakurai, H. Tampo, S. Niki, ZnO transparent conducting films deposited by pulsed laser deposition for solar cell applications, Thin Solid Films, 431 (2003) 369-372.

[16] S. Sakthivel, B. Neppolian, M. Shankar, B. Arabindoo, M. Palanichamy, V. Murugesan, Solar photocatalytic degradation of azo dye: comparison of photocatalytic efficiency of ZnO and TiO2, Solar energy materials solar cells, 77 (2003) 65-82.

[17] T.K. Gupta, Application of zinc oxide varistors, Journal of the American Ceramic Society, 73 (1990) 1817-1840.

[18] P. Yang, X. Xiao, Y. Li, Y. Ding, P. Qiang, X. Tan, W. Mai, Z. Lin, W. Wu, T. Li, Hydrogenated ZnO core–shell nanocables for flexible supercapacitors and self-powered systems, ACS nano, 7 (2013) 2617-2626.

[19] Q. Wan, Q. Li, Y. Chen, T.-H. Wang, X. He, J. Li, C. Lin, Fabrication and ethanol sensing characteristics of ZnO nanowire gas sensors, Appl. Phys. Lett., 84 (2004) 3654-3656.

[20] A. Thote, I. Jeon, H.-S. Lin, S. Manzhos, T. Nakagawa, D. Suh, J. Hwang, M. Kashiwagi, J. Shiomi, S. Maruyama, H. Daiguji, Y. Matsuo, High-Working-Pressure Sputtering of ZnO for Stable and Efficient Perovskite Solar Cells, ACS Applied Electronic Materials, 1 (2019) 389-396.

[21] A. Pickett, A.A. Mohapatra, S. Ray, Q. Lu, G. Bian, K. Ghosh, S. Patil, S. Guha, UV–Ozone Modified Sol–Gel Processed ZnO for Improved Diketopyrrolopyrrole-Based Hybrid Photodetectors, ACS Applied Electronic Materials, 1 (2019) 2455-2462.

[22] B. Sanches de Lima, P.R. Martínez-Alanis, F. Güell, W.A. dos Santos Silva, M.I.B. Bernardi, N.L. Marana, E. Longo, J.R. Sambrano, V.R. Mastelaro, Experimental and Theoretical Insights into the Structural Disorder and Gas Sensing Properties of ZnO, ACS Applied Electronic Materials, 3 (2021) 1447-1457.

[23] S. Ghosh, A. Mallick, B. Dou, M.F. Van Hest, S.M. Garner, D. Basak, A novel blanket annealing process to achieve highly transparent and conducting Al doped ZnO thin films: Its mechanism and application in perovskite solar cells, Solar Energy, 174 (2018) 815-825.

[24] S. Pal, S. Ghosh, D. Basak, Room temperature deposition of pulsed laser-assisted (Al, In) co-doped ZnO transparent conducting films appropriate for flexible substrates, Journal of Materials Science: Materials in Electronics, (2021) 1-12.

[25] A. Tsukazaki, A. Ohtomo, T. Onuma, M. Ohtani, T. Makino, M. Sumiya, K. Ohtani, S.F. Chichibu, S. Fuke, Y. Segawa, Repeated temperature modulation epitaxy for p-type doping and light-emitting diode based on ZnO, Nature materials, 4 (2005) 42-46.

[26] D.I. Son, B.W. Kwon, D.H. Park, W.-S. Seo, Y. Yi, B. Angadi, C.-L. Lee, W.K. Choi, Emissive ZnO–graphene quantum dots for white-light-emitting diodes, Nature nanotechnology, 7 (2012) 465-471.

[27] S.H. Ferreira, J. Deuermeier, S. Sequeira, D. Nunes, A. Gonçalves, R. Martins, R. Monteiro, E. Fortunato, Industrial Waste Residue Converted into Value-Added ZnO for Optoelectronic Applications, ACS Applied Electronic Materials, 2 (2020) 1960-1969.

[28] A.B. Djurišić, Y.H.J.s. Leung, Optical properties of ZnO nanostructures, Small, 2 (2006) 944-961.

[29] E. Ohshima, H. Ogino, I. Niikura, K. Maeda, M. Sato, M. Ito, T. Fukuda, Growth of the 2-in-size bulk ZnO single crystals by the hydrothermal method, J. Cryst. Growth, 260 (2004) 166-170.

[30] B. Wen, Y. Huang, J.J. Boland, Controllable growth of ZnO nanostructures by a simple solvothermal process, The Journal of Physical Chemistry C, 112 (2008) 106-111.

[31] F. Pan, C. Song, X. Liu, Y. Yang, F. Zeng, Ferromagnetism and possible application in spintronics of transition-metal-doped ZnO films, Materials Science Engineering: R: Reports, 62 (2008) 1-35.

[32] S. Pearton, D. Norton, Y. Heo, L. Tien, M. Ivill, Y. Li, B. Kang, F. Ren, J. Kelly, A. Hebard, ZnO spintronics and nanowire devices, Journal of electronic materials, 35 (2006) 862-868.

[33] S.K. Arya, S. Saha, J.E. Ramirez-Vick, V. Gupta, S. Bhansali, S.P. Singh, Recent advances in ZnO nanostructures and thin films for biosensor applications, Analytica chimica acta, 737 (2012) 1-21.

[34] A. Ghosh, R. Sharma, A. Ghule, V.S. Taur, R.A. Joshi, D.J. Desale, Y.G. Gudage, K. Jadhav, S.-H.J.S. Han, A.B. Chemical, Low temperature LPG sensing properties of wet chemically grown zinc oxide nanoparticle thin film, 146 (2010) 69-74.

[35] F. Solís-Pomar, E. Martínez, M.F. Meléndrez, E.J.N.R.L. Pérez-Tijerina, Growth of vertically aligned ZnO nanorods using textured ZnO films, 6 (2011) 1-11.

[36] S. Jo, J. Lao, Z. Ren, R. Farrer, T. Baldacchini, J.J.A.p.l. Fourkas, Field-emission studies on thin films of zinc oxide nanowires, 83 (2003) 4821-4823.

[37] M. Kaur, S. Kailasaganapathi, N. Ramgir, N. Datta, S. Kumar, A. Debnath, D. Aswal, S.J.A.S.S. Gupta, Gas dependent sensing mechanism in ZnO nanobelt sensor, 394 (2017) 258-266.

[38] J. Wang, X.W. Sun, A. Wei, Y. Lei, X. Cai, C.M. Li, Z.L.J.A.p.l. Dong, Zinc oxide nanocomb biosensor for glucose detection, 88 (2006) 233106.

[39] Z.L.J.J.o.p.c.m. Wang, Zinc oxide nanostructures: growth, properties and applications, 16 (2004) R829.

[40] T. Minami, H. Sato, H. Nanto, S. Takata, Group III impurity doped zinc oxide thin films prepared by RF magnetron sputtering, Jpn. J. Appl. Phys., 24 (1985) L781.

[41] W. Yu, J. Zhang, T. Peng, New insight into the enhanced photocatalytic activity of N-, C-and S-doped ZnO photocatalysts, Applied Catalysis B: Environmental, 181 (2016) 220-227.

[42] S.J. Pearton, D.P. Norton, M.P. Ivill, A.F. Hebard, J.M. Zavada, W.M. Chen, I.A. Buyanova, ZnO doped with transition metal ions, IEEE Transactions on electron devices, 54 (2007) 1040-1048.

[43] W.Q. Li, X.H. Xiao, A.L. Stepanov, Z.G. Dai, W. Wu, G.X. Cai, F. Ren, C.Z. Jiang, The ion implantation-induced properties of one-dimensional nanomaterials, Nanoscale research letters, 8 (2013) 1-13.

[44] M.M. Ba-Abbad, A.A.H. Kadhum, A. Mohamad, M.S. Takriff, K. Sopian, Visible light photocatalytic activity of Fe3+-doped ZnO nanoparticle prepared via sol-gel technique, Chemosphere, 91 (2013) 1604-1611.

[45] O. Lupan, L. Chow, L.K. Ono, B. Roldan Cuenya, G.Y. Chai, H. Khallaf, S. Park, A. Schulte, Synthesis and Characterization of Ag- or Sb-Doped ZnO Nanorods by a Facile Hydrothermal Route, J. Phys. Chem. C, 114 (2010) 12401-12408.

[46] H. Ryssel, I. Ruge, Ion implantation, (1986).

[47] J. Williams, Ion implantation of semiconductors, Materials Science Engineering: A, 253 (1998) 8-15.

[48] L.A. Larson, J.M. Williams, M.I. Current, t. Environment, Ion implantation for semiconductor doping and materials modification, Reviews Of Accelerator Science and Technology, 4 (2011) 11-40.

[49] D. Pradhan, K.T. Leung, Controlled growth of two-dimensional and one-dimensional ZnO nanostructures on indium tin oxide coated glass by direct electrodeposition, Langmuir, 24 (2008) 9707-9716.

[50] M. Tonezzer, T.T. Le Dang, N. Bazzanella, V.H. Nguyen, S. Iannotta, Comparative gas-sensing performance of 1D and 2D ZnO nanostructures, Sensors Actuators B: Chemical, 220 (2015) 1152-1160.

[51] S. Xu, Z.L. Wang, One-dimensional ZnO nanostructures: solution growth and functional properties, Nano Res., 4 (2011) 1013-1098.

[52] A. Mallick, D. Basak, Comparative investigation on cation-cation (Al-Sn) and cation-anion (Al-F) co-doping in RF sputtered ZnO thin films: Mechanistic insight, Appl. Surf. Sci., 410 (2017) 540-546.

[53] M.D. McCluskey, S. Jokela, Defects in zno, J. Appl. Phys., 106 (2009) 10.

[54] A. Janotti, C.G. Van de Walle, Fundamentals of zinc oxide as a semiconductor, Reports on progress in physics, 72 (2009) 126501.

[55] A. Mallick, S. Sarkar, T. Ghosh, D. Basak, An insight into doping mechanism in Sn–F co-doped transparent conducting ZnO films by correlating structural, electrical and optical properties, Journal of Alloys Compounds, 646 (2015) 56-62.

[56] S. Venkataraj, N. Ohashi, I. Sakaguchi, Y. Adachi, T. Ohgaki, H. Ryoken, H. Haneda, Structural and magnetic properties of Mn-ion implanted ZnO films, J. Appl. Phys., 102 (2007) 014905.

[57] Y.-Y. Chang, Y.-N. Shieh, H.-Y. Kao, Optical properties of TiO2 thin films after Ag ion implantation, Thin Solid Films, 519 (2011) 6935-6939.

[58] J. Chen, S.P. Lau, Z. Sun, B. Tay, G. Yu, F. Zhu, D. Zhu, H. Xu, Structural and mechanical properties of nitrogen ion implanted ultra high molecular weight polyethylene, Surface Coatings Technology, 138 (2001) 33-38.

[59] J. Kennedy, P. Murmu, E. Manikandan, S. Lee, Investigation of structural and photoluminescence properties of gas and metal ions doped zinc oxide single crystals, Journal of alloys compounds, 616 (2014) 614-617.

[60] J. Kennedy, G.V. Williams, P.P. Murmu, B.J. Ruck, Intrinsic magnetic order and inhomogeneous transport in Gd-implanted zinc oxide, Physical review B, 88 (2013) 214423.

[61] Y.G. Fedorenko, Ion-beam-induced defects in CMOS technology: methods of study, Ion Implantation: Research Application, (2017) 67.

[62] T. Wu, A. Wang, L. Zheng, G. Wang, Q. Tu, B. Lv, Z. Liu, Z. Wu, Y. Wang, Evolution of native defects in ZnO nanorods irradiated with hydrogen ion, Scientific Reports, 9 (2019) 17393.

[63] J. Kennedy, A. Markwitz, Z. Li, W. Gao, C. Kendrick, S. Durbin, R. Reeves, Modification of electrical conductivity in RF magnetron sputtered ZnO films by low-energy hydrogen ion implantation, Curr. Appl. Phys., 6 (2006) 495-498.

[64] Z. Zhou, K. Kato, T. Komaki, M. Yoshino, H. Yukawa, M. Morinaga, K. Morita, Effects of dopants and hydrogen on the electrical conductivity of ZnO, Journal of the European Ceramic Society, 24 (2004) 139-146.

[65] D.C. Look, J.W. Hemsky, J.R. Sizelove, Residual native shallow donor in ZnO, Phys. Rev. Lett., 82 (1999) 2552-2555.

[66] A. Janotti, C.G.V.d. Walle, Oxygen vacancies in ZnO, Appl. Phys. Lett., 87 (2005) 122102.

[67] J. Li, S.-H. Wei, S.-S. Li, J.-B. Xia, Design of shallow acceptors in ZnO: First-principles band-structure calculations, Physical Review B (Condensed Matter and Materials Physics), 74 (2006) 081201.

[68] C.H. Park, S. Zhang, S.-H. Wei, Origin of p-Type Doping Difficulty in ZnO: The Impurity Perspective, Phys. Rev. B, 66 (2002) 073202.

CHAPTER-2

A status review on ion implantation in ZnO

2.1 Introduction

Ion implantation has been identified as a process used for modifying the surface of bulk materials as well as improving the semiconductor properties such as to make p-type or n-type materials [1-5]. Ion implanters operate in the energy range from tens eV to several MeV according to their applications. Usually, ion implanters having low energy in 1 to 300 keV ranges are utilized for treating the surface of solids or doping in semiconductors [6-8]. Also, low energy ion implanter can be used for welding nanostructures like NWs, nanotubes, or integrating NWs in nanodevices, which are now especial applications of ion implanter in the area of nanotechnology [9-11]. Whereas medium-energy ions in the range ~300 keV to 50 MeV are used for writing proton beam apart from synthesis, and modification of thin films [12-14]. High-energy protons and swift's heavy ions with energies ~50 MeV to hundreds MeV are utilized for modifications of surface and physical properties of thin films [15-17]. Engineered defects in ZnO have received unprecedented attention because intrinsic as well extrinsic defects play a very crucial and fundamental role in controlling the material and/or device performance. Implantation into ZnO to modify its electrical properties not only has important technological applications but also offers stimulating research areas involving physical interactions in these systems [4, 18, 19]. Besides electrical, magnetic doping, optical modifications in ZnO have also been carried out by suitable ion implantation. Furthermore, few groups have investigated damage formation in ZnO upon ion implantation and its effect on material properties [20-22]. All these reports show directly or indirectly that ZnO exhibits relatively high radiation tolerance owing to its inherent property of dynamic annealing during implantation for a large variety of ion species, energies, and implantation temperatures, which further makes ZnO, a promising functional material to be used in radiative environments [23-25]. For example, at and above 77 K, single-crystal ZnO exhibits very strong dynamic annealing that is manifested in the retaining of its crystallinity though heavily damaged, even after a heavy Au ion bombardment with a very high fluence (~10^{16} ions/cm^2) and energy (300 keV) [26]. Lorenz et al. [27] have shown that N, Ar, and Er ion implantation with energies of 80, 200, and 380 keV respectively build several stages of damage in single crystal ZnO for the fluence ranges 1×10^{11} - 7×10^{16} ions/cm^2, but no amorphization takes place. Surprisingly, irradiation with 60 keV Si ions at 77 K to a fluence of 8×10^{16} ions/cm^2 has been found satisfactory for amorphizing the near-surface layer of single crystal ZnO, which has been attributed to the strong chemical effects of implanted Si ions [26]. Ion-induced point defects play a crucial role in this radiation tolerance of ZnO. Lv et al. [28] have

reported that O deficient defects in ZnO are the main causes for the radiation hardness of ZnO. However, further extensive research and in-depth understanding are necessary for the advances of ZnO-based devices.

The field of ion implantation is continuously developing. Advancements in equipment, understanding of beam-solid interactions, applications of new materials, and especially the recent progresses to use implantation for nanostructures always incline towards new directions for ion implantation. Therefore, in this chapter, a critical assessment of the recent implantation efforts focusing on the status, opportunities, and challenges of ion implantation in ZnO has been presented. From a "state-of-the-art" of the domain, some obvious, as well as non-obvious connections, have been drawn and thus hopefully would be able to offer significant new insights for both theoretical and experimental research community working with oxide semiconductors.

2.2 ZnO

ZnO is an II-VI binary semiconductor that crystallizes either in cubic zinc-blende, rock salt or wurtzite structure. Among them, the wurtzite structure is a thermodynamically most stable phase in ambient condition. The unit cell of wurtzite structure is hexagonal with two lattice parameters a and c in the ratio (c/a) ideally can be 1.63 [29]. It belongs to the space group of C_{6v}^4 or P6$_3$mc [30]. In hexagonal wurtzite ZnO, each O is surrounded by four Zn atoms which are located at the corner of a tetrahedron and vice versa. This kind of tetrahedral structure exhibit a typical sp^3 hybridized covalent bonding, although ZnO enjoy both covalent and ionic nature simultaneously [30]. A schematic diagram of the wurtzite ZnO structure is shown in Fig. 2.1. The understanding of the band structure of any semiconductor is essential in defining its efficacy in device applications. Both the theoretical and experimental band structure calculations confirm that ZnO is a direct band gap semiconductor with the fundamental band gap at the center of the Brillouin zone (Γ point at k = 0) [31]. The optical band gap of ZnO has been found to be around 3.37 eV at RT along with a large excitonic binding energy of 60 meV. After the theoretical work on band-structure calculation of ZnO proposed by Rössler [32] using Green's function in 1969, there have been several experimental works [33-35] performed on the wurtzite ZnO which proved Rössler's predicted bulk electronic structure to be far from satisfactory. However, later ab initio density of states calculations shows, that valence band maximum (VBM) and conduction band minimum (CBM), at the Γ point and the surrounding parts, originate 2p states of O and 4s states of Zn

atoms, respectively, whereas Zn 3d states are also part valence band (VB), but its location is at about 7.5 eV below the VBM [36-39]. When the d electrons are explicitly taken as valence electrons, the calculated lattice constants for ZnO have been found to be in excellent agreement with the experimental value. A strong interaction between O 2p and the Zn 3d electrons have also been observed [40].
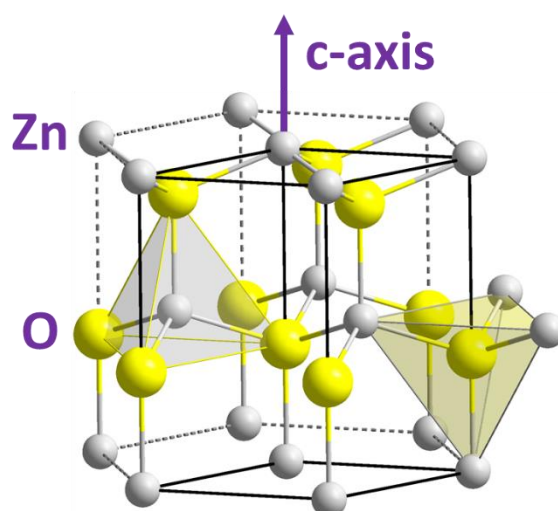
Fig. 2.1 Schematic of hexagonal wurtzite ZnO crystal structure [41].

2.3 Native defects in ZnO

The native point defects are of particular importance in ZnO since many of the primary intrinsic defects are electrically active and are the main source of "native" n-type conduction in ZnO, although there is a great controversy regarding the origin of this n-type conductivity. All the possible native point defects in ZnO are oxygen and zinc vacancies (V_O and V_{Zn}), interstitials (O_i and Zn_i), and antisites (O_{Zn} and Zn_O). V_O and Zn_i defects have long been considered as the source of the unintentional n-type conductivity in ZnO [42-45]. Although V_O has the lowest formation energy among the defects that behave as donors, the density-functional calculations indicate that V_O is a very deep rather than a shallow donor and, consequently, cannot contribute to n-type conductivity [46]. On the other hand, first-principles calculations show that Zn_i defects are shallow donors. But they anneal out at a temperature of 170 K. They have high formation energies in n-type ZnO and are fast diffusers with migration barriers as low as 0.57 eV [47]. Therefore, Zn_i defects are not stable at RT in agreement with the experimental work of Vlasenko and Watkins [48]. Zn_O defects are also reported to be shallow donors, but their high formation energies make their existence

[15]

improbable in ZnO under equilibrium conditions for any position of the Fermi level in the band gap [47, 49]. V_{Zn} acts as an acceptor [50-53]. V_{Zn} have exceedingly high formation energy in p-type ZnO, and therefore exist only in very low concentrations [49]. On the other hand, in n-type ZnO, V_{Zn} has the lowest formation energy among the native point defects, and therefore can more easily be formed in n-type samples and acts as a compensating center [49]. Erhart and Albe [54] reported that O_i defects are electrically active with acceptor transition levels close to the CBM. But the results stated by Janotti et al. [49] do not support this assignment. They suggest that the acceptor charge states found by Erhart and Albe [54] are a result of occupying extended bulk states near the CBM, and not defect-induced states. However, the formation energy of O_i is very high (except under extreme O-rich conditions), and therefore, it cannot be expected that O_i defects to be present in significant concentrations under equilibrium condition [49]. O_{Zn} is an acceptor-type point defect with very high formation energy, even under the most favorable O-rich conditions. This makes it very unlikely that O_{Zn} would be present in significant concentrations under equilibrium [53, 55].

From the above discussion on the native point defects, one can conclude that intrinsic point defects are very unlikely to be the source of unintentional n-type conductivity in ZnO [56]. However, Van de Walle using the first-principles density functional calculations at last showed that unintentionally incorporated H impurities are the origin of native n-type conductivity in ZnO [57]. The positions of these shallow donor states are ~ 30–60 meV below the conduction band (CB). The contribution of H in ZnO in n-type conductivity supporting Van de Walle et al. [57] has also been established exclusively by several experiments [58-61].

2.4 Ion implantation

The basic principle of ion implantation is that ionized dopants are accelerated to energies high enough (eV to MeV) to impact the surface of the target and penetrated into a solid target depending on the energy and slowed down after traversing a certain distance due to collisions with host atoms [62]. The interaction between the host lattice and the energetic ions produces states and structures with metastability through a non-equilibrium process which cannot be achieved by considering other thermodynamic equilibrium means [63-65]. Ion trajectories which are composed of both lateral and vertical motions can be predicted employing statistical means where fluences are higher than 10^{12} ions/cm^2. The average distance of the implanted ions in the vertical direction is called the projected range (R_p), and the distribution of the implanted ions along the R_p can be estimated as Gaussian with a projected straggle or

standard deviation (σ_p). While the lateral motion of the ions leads to a lateral Gaussian distribution ($\sigma_\perp$) [62, 66]. The asymmetry of the distribution is defined by the term skewness (γ). The flatness of the top of the distribution is designated by kurtosis (β) [62, 66].

In general, when an energetic ion enters into a solid target, it traverses a random path and transfers (loses) its energy due to the collisions with target atoms [66]. A particular collision may consist of three independent events: electronic collision, nuclear collision, and charge exchange [67]. Among these, electronic collision is an inelastic type of collision, leading to an excitation and ionization of target atoms. Electronic collisions involve much smaller energy-losses per collision, negligible deflection of the ion trajectory, and negligible lattice disorder. The energy loss involved in this process is known as electronic energy loss (S_e) [68, 69]. When the ions move deeper inside, the energy is transported to the target nuclei via elastic collisions that is recognized as nuclear energy loss (S_n) [68, 69]. Nuclear collisions can involve large discrete energy-losses and significant angular deflection of the trajectory of the ion. As a result of nuclear collision, the target atoms are knocked out from their lattice positions and a large concentration of point defects are produced inside the target material [68]. The sum of S_e and S_n is the total energy lost by an incident ion due to collisions with target atoms. The relative value of S_e and S_n depends on the charge state, mass, and velocity of the incident ions as well as on the target. A proper understanding of the mechanisms of energy-loss is important to control the depth profile of implanted dopant atoms and to determine the nature of the implantation induced lattice disorders. A lattice atom can be displaced from its lattice site after receiving a minimum energy (which is called displacement energy, E_d) due to the collisions with the energetic ion or with a recoiling target atoms [70]. If the transferred energy is less than E_d, the target atom starts to vibrate in its lattice position with large amplitude. The vibrational energy of target atom is rapidly transported to the nearest neighbors, which results the production of heat. However, If the transferred energy is greater than E_d, the target atom comes out of its stable lattice position and starts to recoil. In such cases, the displaced atom creates a vacancy and occupies an interstitial position and thus a vacancy-interstitial defect known as Frenkel pair is generated [71]. A single implanted ion can generate tens of thousands of vacancies and interstitial defects in the target materials. With an increase in the number of incident ions, various type of individual disordered regions are produced and they start to overlap with each other and thus a heavily damaged layer is formed [72]. In addition, the diffusion of defects owing to dynamic annealing processes is also active during implantation [67]. The excitation of target atoms can change the charge state of defects and impact on their diffusivities. Besides defect recombination, the diffusion of point defects also generates extended defects such as dislocation loops, stacking faults

[71]. However, a post-implantation annealing is mostly applied both to eliminate lattice disorders induced by implantation and to electrically/optically activate implanted ions by stimulating their migration into energetically favourable lattice sites.

The orientation of the crystal plane and temperature of the lattice atoms are also important parameters in case of single crystals. The crystal orientation affects the ion dispersion during the implantation via the channeling effect [73-75]. When the motion of an ion is along the atomic rows, the ion moves through the open space of the atomic rows. Initially, the ions bounce from row to row forming an oscillatory motion with a wavelength of some hundreds of Å. These channeled ions do not undergo close encounters with the lattice atoms such as large angle scattering and thus have a much lower rate of energy loss. As a result, the yield of backscattered particles decreases. The reduced scattering yield related to channeling can be used to determine the lattice site position of impurity atoms and defects in the crystal. The channeling distribution is dependent on beam alignment, substrate temperature, surface condition, and the disorder produced during the implantation process itself.

2.5 Simulation of ion implantation

In the field of ion implantation, Monte Carlo and Molecular Dynamics methods are generally involved in the simulation process. Monte Carlo in particular accurately captures the stochastic nature of the implantation process. The simulation software employed in our work is based on this method which is called the Stopping and Range of Ions in Matter (SRIM) [76]. SRIM offers a calculation method involving a quantum mechanical treatment of ion atom collisions based on Monte Carlo simulation method (in the range 10 eV–2 GeV), namely the binary collision approximation with a random selection of the impact parameter of the colliding ions. SRIM is extremely popular in the field of ion implantation. Additionally, it is user-friendly and free. At the core of SRIM is the program called the Transport of Ions in Matter (TRIM) which accepts input parameters such as the ion type and energy, and target material. In addition to information about the ion distribution in the target material in three dimensions, TRIM also outputs the vacancy concentration, straggle of the ions, and other parameters. However, SRIM only predicts the generated displacements of the target atoms. The majority of such defects immediately are annihilated which is the origin of radiation hardness of ZnO [24, 25]. The actual number of stable defects after dynamic recovery is two orders of magnitude less than the generated defects at the Zn sites [68]. Though the dynamic annealing process takes place for ZnO during implantation, enough concentration of defects remains within lattice after implantation. To recover these residual

lattice defects and to activate the dopants, as stated earlier, the implanted samples have to be taken through post-implantation annealing treatment. Nonetheless, it is sufficient as a tool to estimate the ion concentration against depth. In a typical example of SRIM calculation [77], the Gaussian depth distribution of 30 keV N ions in ZnO thin films and the corresponding distributions of V_{Zn} and V_O are shown in Fig. 2.2(a). As the value of E_d for Zn is less than that of the O atom, the concentration of implantation-induced V_{Zn} is always larger as compared to V_O at any fluence of any ion [56, 68, 78]. Fig. 2.2(b) shows the variation of SRIM simulated S_e and S_n with the implantation depth of 1.2 MeV Ar ions in polycrystalline ZnO [68]. As shown in Fig. 2.2(b), S_e dominates over S_n in first ~700 nm depth of the ion trajectory and then S_n starts to predominate. In the case of 180 keV H irradiated ZnO NRs [69], it has been seen that the S_e of H ions distributes almost uniformly along 1.3 μm and S_n is mainly distributed along a narrow region at a depth of 1.5 μm. Thus, the S_e leads over the S_n for most of the penetration path. The values of S_e and S_n for 120 MeV Ag implanted ZnO are 21.67 keV/nm and 0.1054 keV/nm, respectively. The value of S_e has been seen to be almost 200 times higher than that of S_n. Thus, the majority of the modifications in the properties of the ZnO thin films are occurred due to the collisions of the implanted ion with the electrons of the target atoms [79].

(a)   **(b)**
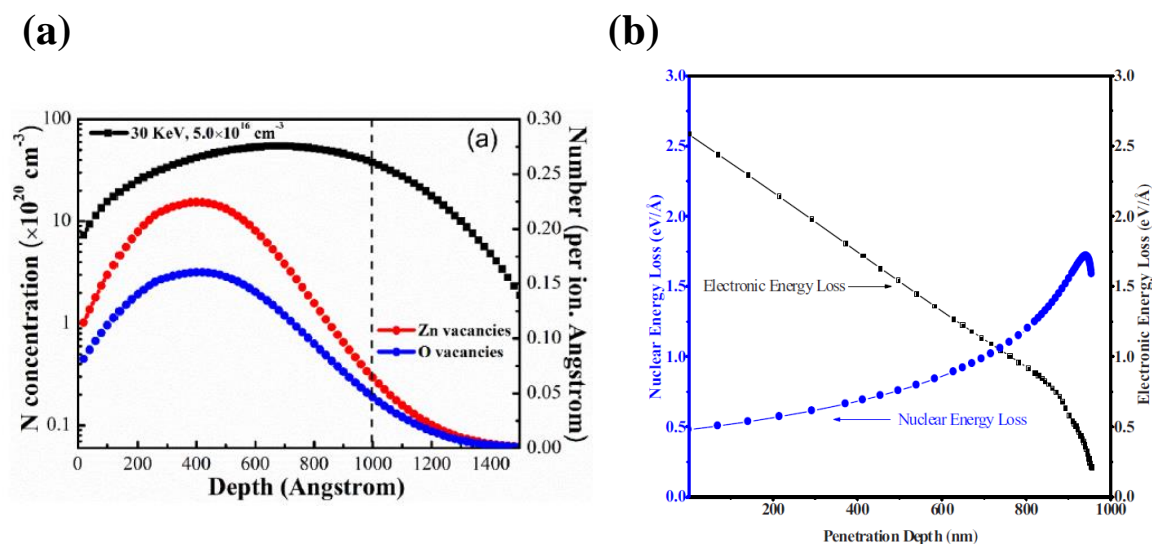
Fig. 2.2 (a) SRIM predicted distribution of the implanted N atoms, and the corresponding Zn and O vacancies [77]. (b) The variation of the electronic and nuclear energy losses along the implantation depth of 1.2 MeV Ar ion implanted polycrystalline ZnO [68].

2.6 Defect interactions in ion implanted ZnO

In the section, the existence of various primary point defects in ZnO has been discussed. The situation becomes even more challenging in case of ion implantation, where the various type defects are accumulated and compensated, by forming defect complexes including clusters and extended defects. The defect formation in ZnO depends strongly on the implanted species. For instance, it has been observed that the interaction between dopant and defect dominates the damage in B implanted ZnO samples and an enhanced concentration of defect clusters is formed as compared to other implanted ion species [23]. Azarov et al. [24] have reported that Ag implantation in ZnO causes an enhanced emergence of extended defects which act as efficient traps for highly mobile Zn_i. Generally, three deep-level defects with thermal activation energies of 300, 730, and 980 meV, respectively, appear in ZnO thin films due to Ar ion implantation and these defects are annealed out at temperatures above 660 °C [80]. Depending on various types of the crystal orientations, the subsequent creation of extended defects can vary. For instance, non-polar a-plane (11-20) ZnO exhibit a lowest level of Zn sublattice disorder evidenced by Rutherford backscattering spectroscopy after implantation with only 5 meV Au ions; in contrast, non-polar m-plane (10-10) ZnO shows the highest disorder [81]. The disorder in the Zn sublattice is produced progressively in the subsurface as well as in the implanted layer in polar c-plane (0001) and m-plane ZnO, while a-plane has shown a slight increase in disorder just in the implanted layer [81]. Therefore, it is very important to investigate the recovery process of implantation-induced damages and the probable interactions between dopant and various defects. In contrast to more common semiconductors Si and GaAs, the defect accumulation and their recovery in implanted ZnO exhibit rather a complex behavior. Chen et al. [82] have adequately addressed the evolution and recovery of defects in P implanted ZnO single crystals. Using Positron annihilation spectroscopy (PAS) measurements (Fig. 2.3(a)), they have shown that the S-parameter increases continuously for annealing temperature up to 600 °C and beyond which the S-parameters begin to drop, followed by a gradual decrease to the bulk value at 1100 °C. The S-parameter generally represents the positron annihilation with the low momentum electrons i.e., in vacancy sites or voids within the sample. The relative values of the S-parameter are characteristics of the defects and their change can throw some light on the major defect evolution process. A gradual increase in S-parameter as shown in Fig. 2.3(a) indicates that the size of V_{Zn} or vacancy clusters increases through the agglomeration of small vacancies up to the annealing temperature 600 °C and after annealing up to a temperature of 1100 °C, the vacancy clusters gradually disappear. This annealing behaviour of the V_{Zn} related defects

probed by positrons differs from the results obtained by the Raman-scattering experiment, where the V_O related defects prevail up to 700 °C. Actually, the broad phonon mode at approximately 575 cm^{-1} in ZnO is said to be due to the presence of V_O. Fig. 2.3(b) shows the ratio of the intensity of 575 cm^{-1} peak to the sum of the 575 and 437 cm^{-1} peaks. At initial stage, the ratio decreases slowly with an increase in the annealing temperature. Beyond the temperature of 400 °C, the ratio starts to decrease sharply reaching the same value as that of the as-grown sample at 700 °C. From this result, it has been inferred that V_O migrates above RT, and thus the amount of the agglomeration of vacancy clusters upto annealing temperature of 600 °C increases and simultaneously the S-parameter as observed in PAS measurements increases. However, the annealing behaviour of vacancy defects is significantly different in case of N implanted sample. Chen et al. [83] have shown that the stabilized vacancy complexes are formed in N implanted ZnO due to the strong interaction between N and vacancy clusters. A sufficient high temperature as high as 1200–1250 °C is needed to remove all these N-related defect complexes. Interestingly, it is seen that if N is co-implanted with O atom, the interaction between N and vacancy clusters is weakened and the concentration of N-related vacancy complexes are effectively removed [83]. The S-parameter of O and N co-implanted sample reaches to a value almost similar to that of the bulk sample after annealing at 800 °C, suggesting that the vacancy clusters are mostly removed. However, these N impurities again combine with vacancies thereby increasing the S-parameter after further annealing above 800 °C [83].
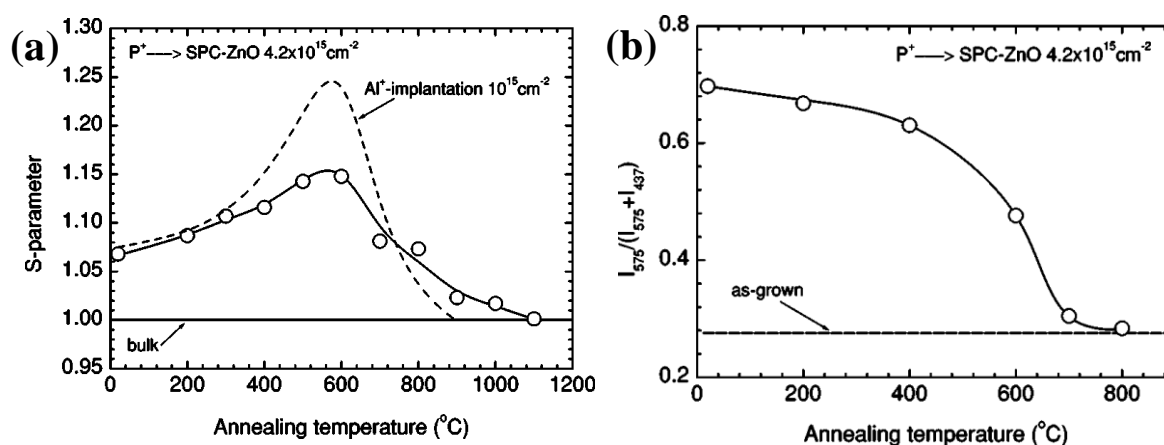
Fig. 2.3 (a) The variation of average S-parameter with the annealing temperature and (b) The variation of the ratio of the intensity of 575 cm^{-1} peak to the sum of the 437 cm^{-1} and 575 cm^{-1} peaks with the annealing temperature for P implanted ZnO with a fluence of 4.23×10^{15} ions/cm^2. The annealing behavior of the Al implanted sample is included for comparison [82].

The effect of both the ion implantation and subsequent annealing treatment on the ZnO matrix can be illustrated with a schematic diagram presented in Fig. 2.4. First, the distorted lattice positions and the formation of intrinsic defects due to energetic ion implantation in ZnO film has been presented. Thereafter, depending on the type of ion species, the implanted ion may substitute Zn site or O site after post-implantation annealing. The vacancy defects (V_{Zn}, V_O) are also recovered under annealing.
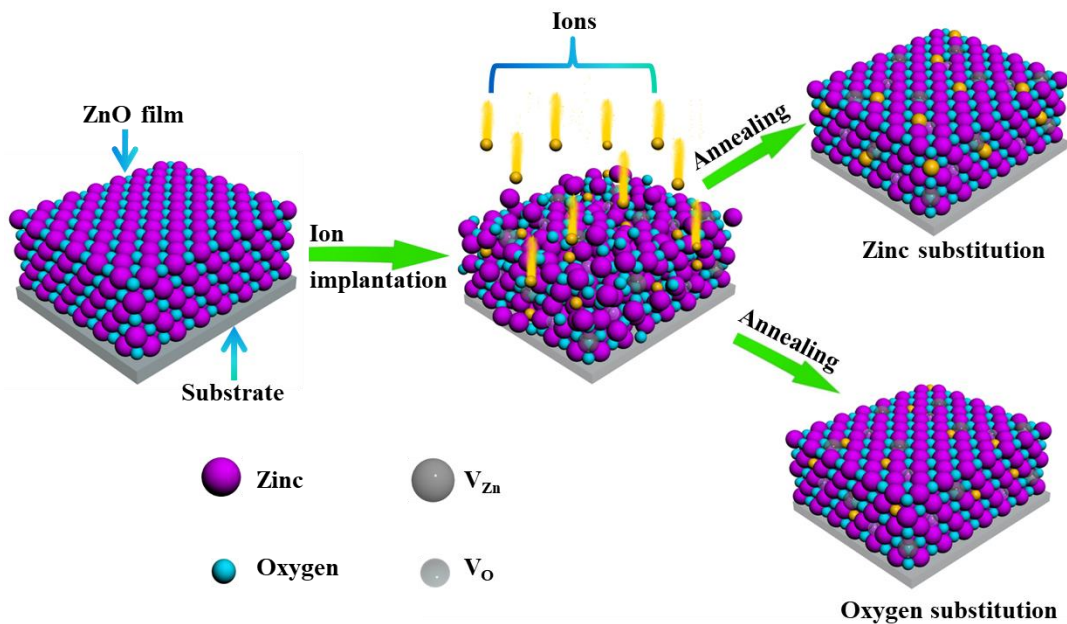
Fig. 2.4 The effect of ion implantation and subsequent post-implantation annealing in ZnO thin films.

2.7 Properties of ion implanted ZnO

2.7.1   Optical properties

2.7.1.1 Surface plasmon resonance property

In the past recent years, considerable fundamental and applied interest has been aroused on the dispersion of metal nanoparticles (NPs) in optical transparent semiconductors for surface plasmon resonance (SPR) in the visible and near-infrared region. For introducing metal NPs controllably in the surface region of ZnO thin films, ion implantation is one of the most capable and facile techniques. The successful embedment of NPs of a noble metal such as Ag [84-86], Cu [87-89], Au [90, 91] in nanocrystalline ZnO thin films as well as in ZnO single crystal by ion implantation technique has already been carried out. In the case of Ag

implantation, a high fluence in the range of $0.25 \times 10^{17} - 1.00 \times 10^{17}$ ions/cm^2 confine Ag NPs in the surface region of ZnO film. As a result of which, SPR occurs as confirmed by the appearance of a selective absorbance peak at around 2.58 eV (~480 nm) (Fig. 2.5(a)) [84]. The intensity, position (λ_p), and half-width ($\Delta\omega_{1/2}$) of the SPR peak strongly depend on the implantation fluence (Fig. 2.5(b)) [84, 85]. The analyses of the optical characteristics of ZnO thin films implanted with Ag ions with respect to the ion current density and implantation fluence show that the fastest and most efficient formation of Ag NPs takes place at an ion current density of 8 A/cm^2 even at the minimum implantation fluence (0.25×10^{17} ions/cm^2) [86]. In contrast to Ag implantation, for Cu implanted ZnO single crystal, the distinctive SPR peak is observed at 2.0 eV (~620 nm) after implanting the sample with a fluence of as high as 1×10^{17} ions/cm^2 [87]. It is not difficult to realize that Cu being lighter than Ag, the damage at higher fluence in the former case is less and thus a well-defined SPR peak sustains. However, Karali et al. [88] have claimed that lower implantation fluence ($<10^{17}$ ions/cm^2) cannot produce Cu NPs in ZnO of size >2 nm and therefore the distinct SPR absorption is not observed for the samples implanted with Cu ions of fluence ~1×10^{16} ions/cm^2. As soon as the implanted sample is annealed at 600 °C, the intensity of plasmon peak is enhanced significantly, which indicates the fact that the annealing enhances precipitation of Cu NPs and decreases point defects in ZnO [87]. Au has been successfully implanted into ZnO thin films and single crystals [22, 81, 90, 91]. But any SPR characteristic in Au implanted ZnO has not been reported.
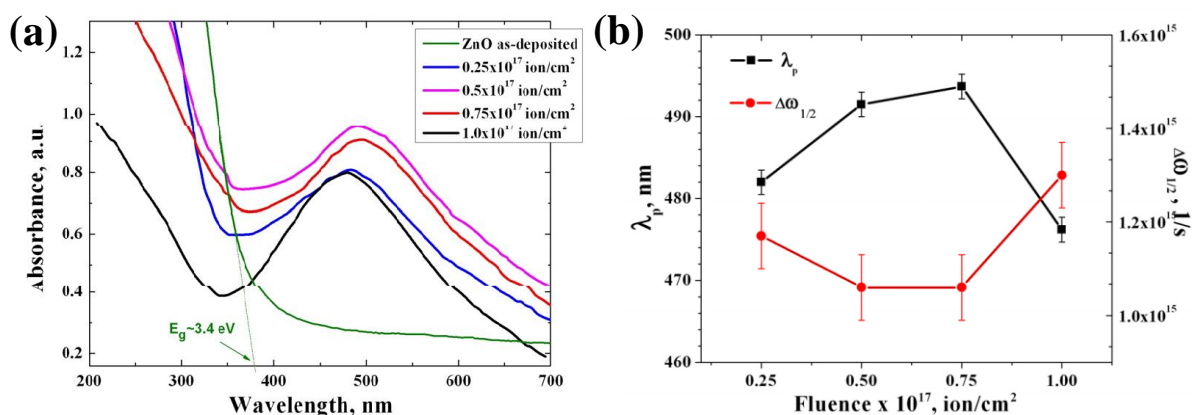
Fig. 2.5 (a) Optical absorption spectra of as-deposited ZnO film and ZnO films implanted with Ag ions to different fluences, identifying the SPR absorption band in the visible region. (b) Fluence dependencies of peak position and half-width of plasmon resonance in Ag-implanted ZnO films [84].

Critical analyses of the reported SPR data

The SPR is strongly dependent on the size of NPs. In the case of ion implantation, different dimensions of NPs are formed along the depth of ZnO thin films due to the Gaussian distribution of implanted ions and the strong sputtering effect during implantation. Fig. 2.6 shows the Gaussian distribution of Cu, Ag, and Au in ZnO, where the energy of each ion has been taken as 50 keV. The Gaussian-like curves in Fig. 2.6 allow one to make an assumption that size distribution of the forming particle is wide along the depth of the implanted region. This means that the higher density of the impurity at the peak of the distribution stimulates the growth of NPs with larger sizes in the near-surface region, whereas lower density of implanted ions near the tail of the concentration curve triggers nucleation of smaller size clusters that dominate at the depth of the ZnO films. According to Fig. 2.6, the Cu NPs are widely distributed inside ZnO films as compared to Ag and Au. The peak of Cu concentration also arises at a higher depth of ZnO films than that of Ag and Au. Another fact is that the maximum concentration at R_p for Au and Ag NPs is higher as compared to Cu. Therefore, most of Au and Ag ions would produce larger-sized NPs near the surface of implanted ZnO thin films. For Cu implanted thin films, in addition to larger-sized NPs, smaller size clusters are also produced (because of the long-tail in concentration curve). If the surface sputtering at the time of ion implantation is considered, the shape of the implantation profile may be changed and the peak concentration shifts to the surface, which is observed for Au and Ag. The lower sputtering yield is observed for Cu ions, which is 6.17 atoms/ion and 3.62 atoms/ion, respectively, for Zn and O atoms. While the sputtering yield is intermediate for Ag ions (7.34 atoms/ion and 4.25 atoms/ion, respectively, for Zn and O atoms) and is higher for Au ions (8.70 atoms/ion and 4.99 atoms/ion, respectively, for Zn and O atoms). Thus, the sputtering effect can be considered as strong for Au ions, intermediate for Ag, and lower for Cu ions. At the time of surface sputtering during implantation, the NPs with large sizes move steadily toward the surface and disappear due to the apparent loss from the sample surface. Therefore, the mean size of NPs at the sample surface reduces. To observe the SPR effect, a critical size of NPs at surfaces is necessary. Because of strong sputtering during implantation, the desired size of Au NPs is not formed in case of Au implantation into ZnO and therefore any reports on SPR by Au implantation have not been reported. On the other hand, the intermediate and lower sputtering effect do not disturb the formation of critical-sized NPs in the case of Ag and Cu implantation in ZnO, which results in distinctive plasmon resonance.
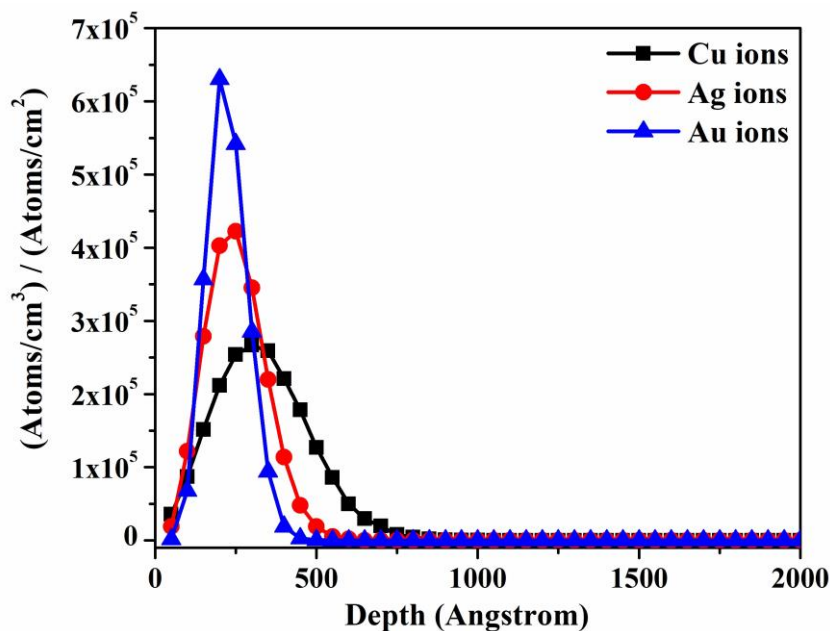
Fig. 2.6 SRIM predicted distributions of 50 keV Cu, Ag and Au ions in ZnO.

2.7.1.2 Luminescence properties

Generally, ZnO shows a sharp near band edge (NBE) emission in the UV region at around 3.34 eV, and a broad defect level (DL) emission in the visible region [92-94]. One or more emission peaks in the visible region is attributed to recombination at different defect levels, the exact origin of which is highly controversial till date. Several hypotheses for different samples have been proposed to explain the defect-related emissions. The yellow-orange emission band centered at ~2.2 eV, which is generally observed for ZnO NRs, is mainly attributed to excess O_2/OH adsorbed on the surface of ZnO [95, 96]. The red luminescence in ZnO appears between 1.6 eV- 2 eV and can be attributed to O_i and V_O [47, 97, 98]. As far as the green luminescence at ~2.4 eV is concerned, its origin is mostly debated. The following luminescence centres are assumed to be responsible for the green luminescence: impurity Cu^{2+} ions[99, 100], V_{Zn} [51, 101, 102], V_O [103, 104], Zn_i [105, 106], O_{Zn} [107], and transitions $Zn_i \rightarrow V_{Zn}$ [108]. One can consider that various centres may be involved in the green luminescence simultaneously. Therefore, the implantation effect on the luminescence properties of ZnO is even more complicated with the given ion-defect interactions. All PL, cathodoluminescence (CL), radioluminescence (RL) data from ion implanted ZnO show that implantation-produced lattice defects act as effective non-radiative recombination centers in ZnO, resulting in a severe quenching of its characteristic

[25]

luminescence peaks [81, 89, 109]. However, post-implantation annealing activates the luminescent centres and enhances the emission intensity by annihilating the implantation-induced damages. For an annealing above 650 °C, the Ag implanted ZnO NWs exhibit a stable UV emission which is stronger than that of the as-prepared samples owing to enhanced visible emission [109]. The V implanted ZnO nano crystalline films show an enhanced NBE PL intensity with an increase in the fluence after annealing at 900 °C in O_2 atmosphere. The intensity reaches a maximum value at 2.5×10^{15} ions/cm^2, which is ~37 times larger than that of the unimplanted ZnO film (Fig. 2.7) [110]. In another report by the same research group [111], it is shown that after annealing at 1000 °C, the NBE PL intensity of Nb implanted ZnO nanocrystalline films is increased with an increase in the fluence as well as annealing temperature, and become maximally ~7.5 times stronger than that of the unimplanted ZnO films at a fluence of 8×10^{15} ions/cm^2. Müller et al. [112] have investigated the CL properties of transition metal (Ni, Fe, Co) implanted ZnO NWs, where they have shown that the intensity of green luminescence band increases drastically and dominates the whole spectrum just after annealing at 700 °C.
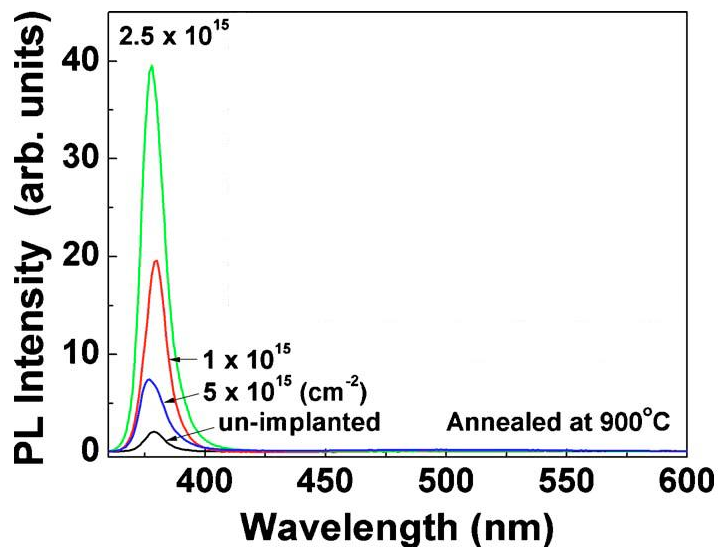
Fig. 2.7 RT PL spectra of unimplanted and V implanted ZnO films. The intensities of all spectra except the fluence 2.5×10^{15} ion/cm^2 are multiplied by 2 for better comparison [110].

Apart from the effect on the luminescence intensity, ion implantation-produced lattice defects (both before and after post-implantation annealing) also gives rise to new luminescence peaks in the UV as well as in the visible part of the spectrum. For example, in

addition to the NBE emission, a new transition related to donor-acceptor pair have been observed at about 3.16 eV for V implanted ZnO thin films [113]. Na related acceptor-bound excitation emission line centered at 3.35 eV has been reported for Na implanted and subsequently annealed (800 °C) ZnO NRs [114]. However, when the PL measurement is carried out at 13 K, a new violet band in the visible region is appeared in Na implanted and subsequently annealed (600 °C) ZnO single crystal [115]. In addition to the NBE peak and broad orange emission at ~590 nm, a weak emission at ~470 nm emerges in W implanted ZnO NRs, which is commonly ascribed to W^{6+} related donor level transition [116]. In addition to green emission, Fe and Co implanted NWs exhibit a new sharp and strong transitions in the red spectral region which is not observed in as-grown, Ni or Ar implanted ZnO NWs. This red emission in the corresponding Fe and Co implanted ZnO samples has been claimed to be associated with the intra-shell 3d transitions of Co^{2+} and Fe^{3+} ions [112].

In addition to defect-mediated luminescence, highly luminescent rare-earth elements such as Sm, Tb, Gd can successfully be implanted in ZnO nanostructured films to make them excellent and efficient luminescent material [117-119]. Fig. 2.8(a) shows the digital photographs showing excellent visible luminescence from unimplanted and Gd implanted ZnO thin films followed by annealing in vacuum at 750 °C, while Fig. 2.8(b) represents the corresponding PL spectrum [117].

(a)   **(b)**
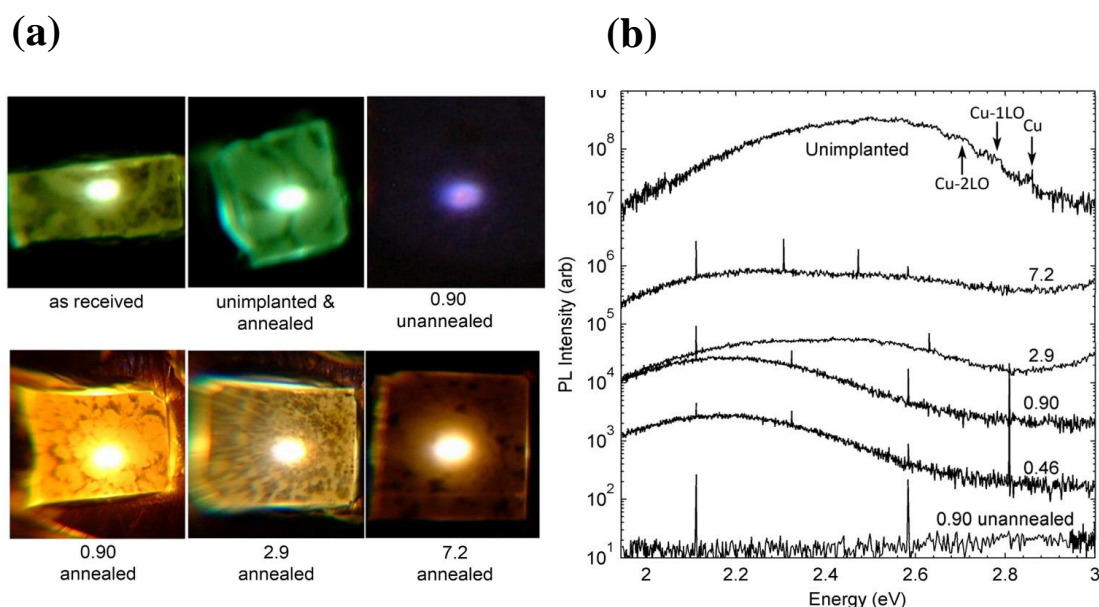
Fig. 2.8 (a) Photographs and (b) spectra of visible PL emission at 4 K for unimplanted and Gd implanted ZnO films without and with annealing. Implanted fluence is shown with unit of 10^{15} ions/cm^2 [117].

Critical analyses of the reported luminescence data

The results discussed in the earlier section indicate that luminescence of ZnO is surely governed by the implantation-induced lattice imperfection, defect complexes. Depending on the mass, fluence, and energy of implanted ions, the evolution of the defect complexes is different, though the primary defects are vacancies and interstitials. To show the dependence of defects on implanted ions, the defect distributions in ZnO for two selective ions Nb and Co in comparison to Ar have been simulated, as shown in Fig. 2.9. Ar is chemically inert element. Therefore, it is expected that Ar creates only the structural damages by not occupying any lattice site. Thus, Ar implantation into ZnO is usually carried out as a reference to eliminate the influence of implantation-induced damages. Thus, the involvement of any bound excitons on the improvement of PL emission can be distinguished. Fig. 2.9 clearly reveals that the defect concentration for various ions is not the same and varies widely even though the implantation energy is fixed. It is expected that some defects might have been migrated depending on their formation energy and annealed out upon thermal annealing. Therefore, the crystallinity of the implanted samples is regained and improved NBE emission is observed. However, the reported data show that the residual defects are retained in samples for higher fluences even after annealing. In these cases, non-radiative defect centres are produced, which leads to a decrease in the NBE. Depending on the ion-induced defect concentration and post-implantation annealing treatment, the observed DL emission would also be different. In addition, the implanted impurity and defects may induce new energy levels, which produce new luminescent centres.
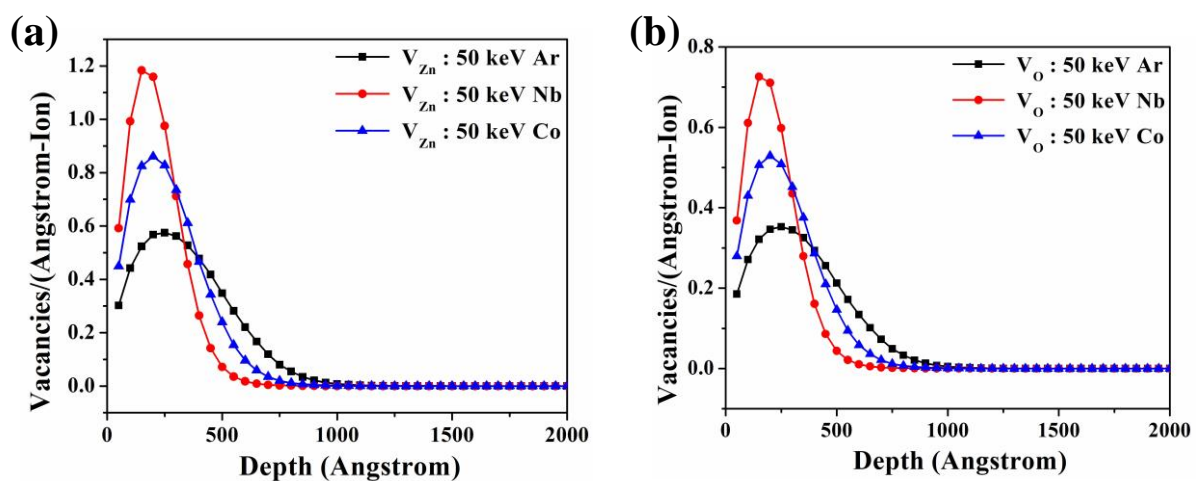
Fig. 2.9 (a) SRIM predicted distribution of (a) V_{Zn} and (b) V_O defects for Ar, Nb and Co ions of energy 50 keV.

2.7.1.3 Absorption and band gap

The transmittance and absorbance and thereafter the band gap of ZnO film is significantly affected by ion implantation due to defects creation and charge carrier density. ZnO should absorb only light of wavelength < 390 nm. The absorption edges for V [120], W [116], Cu [121], and N [122] implanted ZnO NRs array films have been seen to be shifted gradually toward longer wavelengths in the visible region with an increasing implantation fluencies (Fig. 2.10). The new impurity levels in the forbidden band of ZnO NRs leads to the redshift in the absorption edge which induces the narrowing of the band gap of ZnO. The blue shift in absorption edge and subsequently broadening in the band gap are generally observed due to the well-known Burstein-Moss (BM) effect, when ZnO is implanted with donor impurity such as Al [19], Ga [123], In [124]. A high fluence of donor impurity induces higher carrier concentration. Then the Fermi level goes into the CB filled with electrons. Then the electron transition only happens between the VB and about or above the Fermi level, which leads to a blue shift of the absorption edge.
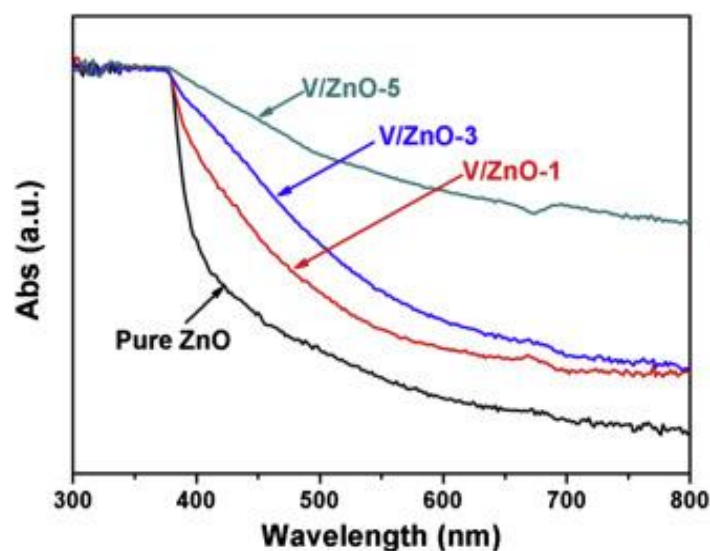
Fig. 2.10 UV-VIS absorption spectra of (a) pure ZnO and V ions implanted ZnO NRs [120].

2.7.2 Electrical properties

2.7.2.1 n-type conductivity

Kohiki et al. [125] have reported that ion implantation with a high concentration of H ($>1\times10^{16}$ ions/cm^2) must result in the overlap of donor sate and the CB in ZnO and therefore,

fluences of H more than 1×10^{16} ions/cm^2 is necessary to reproducibly obtain highly conductive ZnO thin films. With the implantation of H with a fluence of 1×10^{17} ions/cm^2, the electrical conductivity of ZnO thin films after annealing at 200 °C in an N$_2$ atmosphere has been seen to be enhanced from 1×10^{-7} Ω^{-1}cm^{-1} to 5.5×10^2 Ω^{-1}cm^{-1} [125]. With an almost similar fluence of H ion, Arita et al. [126] have obtained comparatively less enhancement in the electrical conductivity from 1×10^{-4} Ω^{-1} cm^{-1} to 9.1×10^1 Ω^{-1} cm^{-1}, which indicates that a thermal activation energy is involved for making the H donors effective. As discussed earlier, the purpose of implantation is mostly to introduce impurity atoms in a target. A lot of implantation work has been reported to improve the n-type electrical conductivity of ZnO using group III elements, such as B, Al, Ga, and In. But the reported data shows that enhancement in n-type conductivity in case of implantation is quite abrupt. It has been seen that the sheet resistance of B implanted ZnO films remains almost unchanged with an increase in ion fluence [127]. After employing annealing treatment, the sheet resistance increases with an increase in the annealing time at lower fluences (2×10^{12} and 1×10^{14} ions/cm^2), and it remains almost constant at higher fluences, which indicates the non-activation of B in the implanted ZnO thin films. The most commonly used n-type dopant for ZnO is Al. Successful doping of Al into ZnO and achieving enhanced n-type conductivity via implantation has been reported by various research groups, which are summarized in Table 2.1.

Table 2.1 Ion energy, fluence, annealing temperature and ambient, resistivity and sheet resistance of various reported n-type Al implanted ZnO thin films.

Ion energy (keV)	Fluence (ions/cm^2)	Annealing (°C) and ambient	Resistivity (Ω.cm)	Sheet resistance (Ω/sq)	Ref.
25	6×10^{15}	-	1.67×10^{-3}	-	[128]
15	1.4×10^{16}	-	7.91×10^{-1}*	3.03×10^4	[129]
100	5×10^{15}	500, Vacuum	9.7×10^{-2}	2.87×10^3*	[130]
35	1×10^{15}	300, Vacuum	8.45×10^3*	1.3×10^9	[123]
40	1×10^{16}	300, Vacuum	6.5×10^{-3}	-	[131]
40	1×10^{16}	-	1.2×10^{-2}	-	[131]
1000	1×10^{17}	500, O$_2$	4.20×10^{-4}	-	[132]

*Calculated from the given data

According to Table 2.1, the lowest resistivity has been achieved after implanting with as high as 1×10^{17} ions/cm^2 Al ions and subsequently annealing at 500 °C in the O$_2$ atmosphere [132]. In other reports, however, the resistivity is quite high as the implantation fluence is low (in the range of 5×10^{15} - 1×10^{16} ions/cm^2), which is actually desirable for producing moderate defects in the materials. Among group III elements, Ga doped ZnO thin films show better n-type conductivity. Resistance measurement on single Ga implanted ZnO nanorod (NR) as performed by Weissenberger et al. [133] shows that an increase in resistivity is observed up to a fluence of $1\times10^{14} - 2\times10^{14}$ ions/cm^2 and beyond which the resistivity is reduced attaining a minimum value of 3×10^{-3} Ω.cm for ion fluences between 3×10^{16} and 6×10^{16} ions/cm^2. The variation of sheet resistance with the annealing temperature for Ga implanted ZnO films as reported by Matsuda et al. [123] indicates that Ga implanted ZnO thin films show relatively high sheet resistance of 2.6×10^6 Ω/sq upon annealing at 300 °C, which is less that of Al implanted samples (1.3×10^{12} Ω/sq). Similar to Ga implantation, In implantation into ZnO thin films is also rarely done. The fluence dependence of resistivity of In implanted ZnO films at different annealing temperatures as demonstrated by Matsuda et al. [124] is shown in Fig. 2.11. The resistivity of In implanted ZnO films decreases as the implantation fluence increases for all annealing temperatures. Beyond the implantation fluence of 5×10^{15} ions/cm^2, the resistivity saturates and becomes as low as ~10^{-2} Ω.cm.
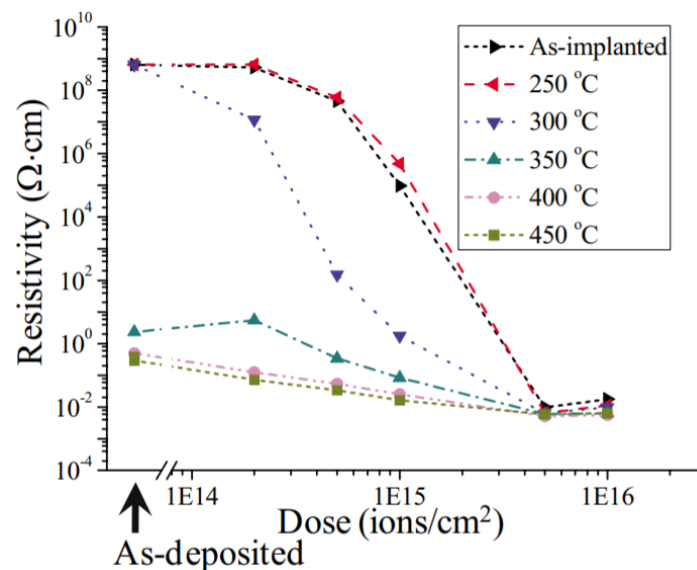
Fig. 2.11 The resistivity of as-deposited and In doped ZnO films at the different annealing temperatures [124].

2.7.2.2 p-type conductivity

A p-n homojunction being an essential component in most electronic and optoelectronic devices, it is essential to produce high-quality, stable, and reproducible p-type ZnO. Quite a few attempts for achieving p-type ZnO by incorporating group I elements (Na, Li) and group V elements (N, P, As, Sb) via various growth methods, such as radio frequency sputtering, pulsed laser deposition, metal-organic chemical vapor deposition, and molecular beam epitaxy have been carried out [134-137]. From the first-principles calculations, it has been established that substitutional group-I elements act as shallow acceptors, while substitutional group-V elements are deep acceptors [138]. However, issues such as low solubility of the acceptor defects, compensation by intrinsic defects, formation of antisites for group-V elements and interstitials for group-I elements result in low hole concentration and thus unstable p-type ZnO is formed [139]. Ion implantation has been claimed to be a successful tool by various research groups to produce high-quality p-type ZnO films by overcoming the low solubility of p-type dopants. Among group V elements, N is a very popular acceptor dopant for ZnO. Successful production of p-type ZnO via N implantation followed by various annealing conditions has been reported [77, 140-143], which has been summarized in Table 2.2

Table 2.2 Ion energy, fluence, annealing temperature and ambient, resistivity, sheet resistance, carrier concentration of various reported p-type N implanted ZnO thin films.

Ion energy (keV)	Fluence (ions/cm^2)	Annealing temperature (°C) and ambient	Resistivity (Ω.cm)	Sheet resistance (Ω/sq)	Carrier concentration (cm^{-3})	Ref.
350	6×10^{15}	600, O_2	4×10^5	-	-	[140]
70	1.2×10^{15}	In-situ annealing, 460	18	-	2.4×10^{17}	[141]
45	1×10^{17}	-	-	-	8.36×10^{20}	[143]
30	5×10^{16}	900, N_2	0.37	-	9.6×10^{17}	[77]
70	1×10^{16}	650, N_2	6.33	-	7.81×10^{16}	[142]
80	1×10^{14}	850, N_2	10.11	-	7.33×10^{17}	[144]

Though Kumar et al. [143] have achieved a high hole concertation of 8.36×10^{20} cm^{-3} without employing annealing, the Table 2.2 shows that heat treatment is indispensable after

implantation to achieve p-type conductivity. It is seen that relatively low resistive p-type ZnO is possible only if it is annealed in the range of 650-900 °C in an N_2 atmosphere. The stability of the p-type N implanted ZnO thin films has been checked by Huang et al. [77], where no reduction of hole conduction has been reported even after three months. The implanted N ions in ZnO can occupy V_O sites or substitute in O atom sites through a kick-out mechanism. The incorporation of N atom into O sublattice (N_O) is generally believed to be an acceptor and origin of p-type conductivity in ZnO [145, 146]. According to the first-principles calculations, it has been seen that the isolated N_O is a deep acceptor whose energy level lies at 1.3 eV above the VBM [147]. Using electron paramagnetic resonance spectra analyses, Stehr et al. [148] have shown that N-induced acceptor level is located at 1.1 eV above the VBM. The acceptor N_O in ZnO has a natural tendency of creating defect-impurity centres by pairing up with intrinsic defects, which may act as donors or acceptors accordingly. Liu et al. [149] have theoretically shown that the N_O-V_{Zn} complex defect acts as shallow acceptors and is responsible for stable p-type conductivity in N doped ZnO. Recent experimental results [77, 150-152] results also confirm the prediction made by Liu et al. In addition to the acceptor-like defect complexes, the complex defect N_O-Zn_i behaves as the shallow donors in N doped ZnO samples [153]. Furthermore, the presence of N_2 at O site $(N_2)_O$, N_O complexes consisting of N_O-O_i and N_O-V_O, Zn_i clusters, and V_O also act as donor in N doped ZnO [154]. In fact, these donors compensate N-related acceptors (e.g., N_O, N_O-V_{Zn}) and overall make it difficult to achieve significant p-type conductivity. In fact, these are believed to be the cause of n-type conductivity as observed in other studies [155, 156]. In the process of As implantation into ZnO, As prefers to substitute on the Zn rather than the O site forming an isolated state As_{Zn} due to a large difference in radius and electronegativity between O and As ions [157]. The isolated point defects As_{Zn} and V_{Zn} coexist in As implanted ZnO and form As_{Zn}–$2V_{Zn}$ defect complexes [157]. These As_{Zn}–$2V_{Zn}$ defect complexes with ionization energy around 136 meV are suggested to be the source of holes and are the main origin of p-type conductivity in As implanted ZnO single crystal [157, 158]. According to a study [159], the p-type conductivity in As implanted ZnO polycrystalline thin films is only possible if the so-called cold implantation rapid annealing approach followed by subsequent thermal annealing is used. In contrast, the similar method adopted for N and P implantation into ZnO polycrystalline films has not been seen to induce p-type conductivity which may be due to the high compensation of acceptors by the donors produced by the high temperature ex-situ annealing of the samples [159]. The first-principles calculations [160] have revealed that the electrical activity of P largely depends on its local configuration as well as surroundings in

the crystal lattice. When P simply substitutes an O atom, the sate P_O behaves as a deep acceptor. Simultaneously, when P substitutes a Zn site and forms a complex with two nearby V_{Zn} (P_{Zn}-$2V_{Zn}$), it introduces a shallow acceptor state at 150 meV above the VB [161]. Using conventional doping technique, several groups have indeed reported p-type conductivity in P-doped ZnO [162, 163]. However, in many studies on P implantation [82, 164, 165], only a significant reduction in the donor concentrations has been attained rather than achieving a stable p-type conductivity. The success of getting p-type ZnO via Sb implantation is very trivial. After Sb implantation and subsequent annealing at 900 °C in N_2, ZnO possesses n-type conductivity with carrier concentration 2×10^{20} cm^{-3} instead of having p-type conductivity [166]. Interestingly, it has been seen that if the Sb implanted ZnO thin film is annealed at 900 °C in air, it displays a current-voltage (I-V) characteristics specific of rectifying diodes which is claimed to imply that Sb implantation has induced p-type conductivity in the film [167]. These different behaviors, under two different annealing ambiences implies that the annealing in the air may reduce the V_O, which is the cause of arising p-type conductivity. In contrast, in another report [168], the authors have claimed to achieve p-type ZnO with a resistivity of 0.042 Ω.cm by implanting 1×10^{16} ions/cm^2 Sb into ZnO thin films and subsequent annealing at 500 °C in vacuum. However, more systematic investigations are needed for acquiring a more complete picture and a deeper understanding of the defect evolution in P and Sb implanted ZnO. Further various research groups have employed co-implantation technique to achieve stable p-type ZnO aiming to compensate the n-type defect donors and to increase the solubility of the acceptors. The co-implantation of N with O [169], Li [170], Na [171], and P [172] has been reported to show stable p-type conductivity. Apart from group V elements, it has been claimed that implantation with Ag ions of fluence 0.25×10^{17} ions/cm^2 into ZnO nanocrystalline films causes a change in the type of conductivity from n-type to p-type in ZnO films [84]. This points to the fact that a part of the Ag ions implanted into the ZnO lattice form acceptor impurities.

Critical analyses of the reported electrical data

From a structural viewpoint, the ion implantation into a ZnO creates a defect-rich cluster which may be either spontaneously converted into an amorphous phase or may be relaxed by defect diffusion. From an electrical standpoint, the implantation-induced defects act as carrier trapping centres. Thus, a decrease in the conductivity is expected to be observed in an implanted sample. However, by employing post-implantation annealing, these problems can

be avoided. However, residual damages retain in the implanted samples, which may participate in the alteration of electrical properties. If the implanted ions are of light in mass, the concentration of implantation-induced defects would be lower as observed for B in Fig. 2.12. Assuming the mass of Al, Ga and In as of intermediate (or higher) mass, the implantation-produced defects (as depicted in Fig. 2.12) are confined more nearly to a region of space surrounding the ion track. The density of the trap state may become quite high within this region, which causes a high resistivity in the material. The value of S_n for 50 keV B is 0.0057 keV/Å, which is much less than that of Al, Ga and In (0.039, 0.15, 0.24 keV/Å, respectively). If the projection of ions is taken as perpendicular to (0002) planes of ZnO, it is seen that the average energy loses per lattice plane for B ion is only about ~15 eV, whereas for Al, Ga, and In, it is 102, 390, 629 eV respectively. It can be expected that the majority of this energy is transferred to the primary recoil atom, so the average recoil atom has energy ~15 eV for B ions, which is less enough than those of Al, Ga, and In ions. From this point of view, the B implanted ZnO should exhibit enhanced electrical properties as compared to Al, Ga, and In implanted ZnO thin films. However, the experimental electrical data of B implanted ZnO is not at par with the above-mentioned prediction. Indeed, lower resistivity has been achieved at higher fluences ($>10^{15}$ ions/cm^2) of Al and Ga ions. To explain this, the electronegativity of the elements has to be considered. The trend in the degree of conductivity enhancement (Ga>In>Al>>B) depends on the electronegativity of these atoms [125]. From the reported data discussed in section 2.7.2.1, one interesting thing has been observed that the resistivity becomes high for lower fluences ($<10^{15}$ ions/cm^2) Ga implanted ZnO films. An increase in the resistivity at lower fluences of Ga ions suggests that the implanted Ga ions are incorporated in the interstitial sites instead of Zn sites. According to the SRIM calculations, Ga implantation induce more V_{Zn} than V_O at any given fluence (Fig. 2.12). Thus, the V_{Zn} acts as a compensating defect and leads to a deterioration in electrical properties. But at higher fluences, Ga ions are successfully placed into the Zn^{2+} sites. It is quite obvious that some complicated defect complexes are formed at higher fluence. However, due to post-implantation annealing treatment, these defects are annealed out and improved electrical properties appear. Thus, the electrical properties of group III elements implanted ZnO thin films are dominated by proper inclusion on dopant in the Zn^{2+} site.
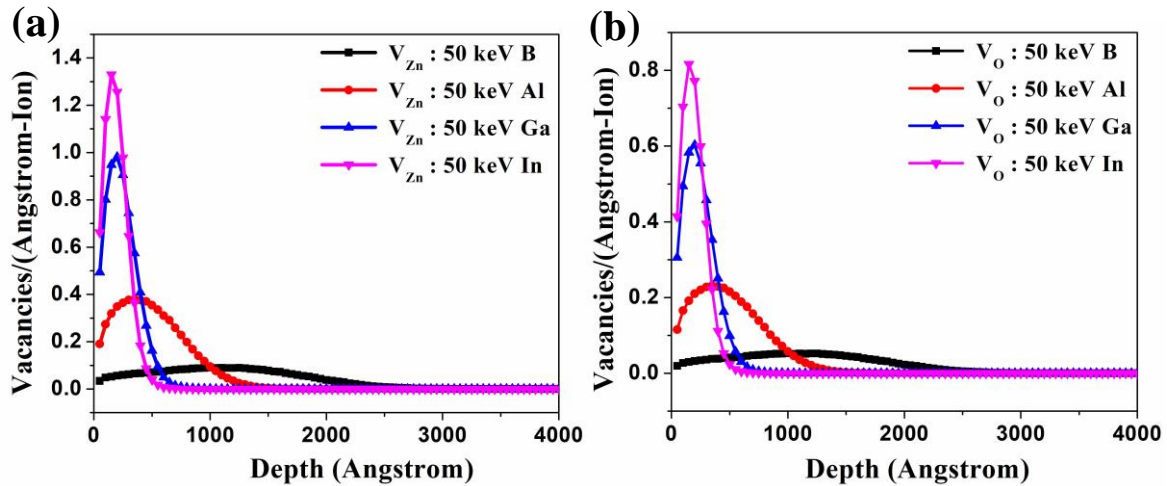
Fig. 2.12 SRIM predicted distribution of (a) V_{Zn} and (b) V_O defects for B, Al, Ga and In ions of energy 50 keV.

In the case of acceptor doping in ZnO, the defect complexes play a crucial role in p-type conductivity. Fig. 2.13 shows the SRIM predicted defect distribution for 50 keV N, As, P and Sb ions implanted ZnO thin films, respectively. As seen in Fig. 2.13, the defect concentration for N implanted ZnO thin films is lower than that of other group V elements. The value of S_n for 50 keV N is 0.011 keV/Å, which is much less than that of P, As, and Sb (0.05, 0.163, 0.251 keV/Å respectively). If the penetration of the ions is considered as perpendicular to (0002) planes of ZnO, the average energy loss per lattice plane for N ion should be ~29 eV, whereas for P, As and Sb, it would be ~132, 423, and 653 eV respectively. The majority of this energy is transferred to the primary recoil atom, so the average of the recoil atom is approaching only 29 eV for N atoms, which is less enough than that of the above-mentioned values for P, As, and Sb ions. Thus, N produces a lower defect concentration in ZnO than that of others. As a result, the probability of production of stable complexes with N acceptor dopants in ZnO is very low. Therefore, N implanted ZnO thin films have shown comparatively stable p-type conductivity under certain annealing temperatures. As the ion mass increases, the defect concertation for P, As, and Sb increases (Fig. 2.13). The produced simple defects migrate with other defects and produce defect clusters. Instead of an increase in acceptor concertation, these defect clusters convert them to an electrically inactive state and thus p-type conductivity is suppressed. In such heavy ion implantation, low energy, low fluence, and appropriate annealing temperature should be taken to achieve p-type ZnO. Further, more methodical and in-depth investigation are necessary in this area.

(a)

(b)
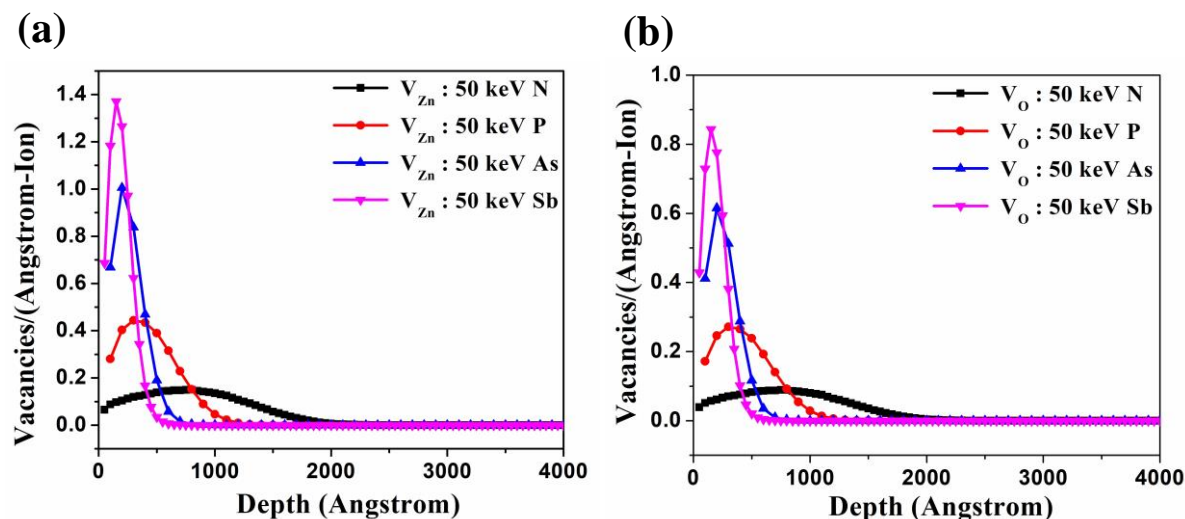
Fig. 2.13 (a) SRIM predicted distribution of (a) V_{Zn} and (b) V_O defects for 50 keV N, P, As and Sb ion implanted ZnO thin films.

2.8 Optoelectronic applications of ion implanted ZnO

2.8.1 Photoelectrochemical water splitting

ZnO nanostructures exhibit a good performance of H_2 production via PEC water splitting because of their high surface area, better crystallinity, excellent pathway for carrier transport, reduced charge recombination rate, and low charge transfer resistance [173]. However, there is a limitation related to its chemical stability to use ZnO as photoanodes in PEC water splitting. In presence of alkaline electrolyte solutions, the surface of ZnO nanostructures is converted into $Zn(OH)_2$, and the rate of conversion increases with an increase in the pH of the solution [174, 175]. Furthermore, the photostability of ZnO decreases in the presence of prolonged light irradiation due to photocorrosion mechanisms [176, 177]. The stability can significantly be improved by controlling the pH of the electrolyte and by doping, however it is expected to be highly variable even for the same dopant depending on the sample preparation method [175, 178, 179]. In this regard, doping of either metal or non-metal ions via ion implantation has been theoretically and experimentally proved to reduce the band gap of ZnO by introducing acceptor or donor levels in the forbidden band, which makes ZnO responsive to visible light ($\lambda > 420$ nm) PEC water splitting. Implantation of V, Cu, and W ions create the impurity levels in the forbidden band of ZnO, which reduce the band gap of ZnO NRs and extend the optical absorption edges into the visible light region [116, 120, 121]. The absorption edges of these implanted samples have been seen to be red-shifted

gradually as the implantation fluence increases. The proposed schematics of band structure of V, Cu, and W ion implanted ZnO NRs (Fig. 2.14) shows the impurity levels introduced by the respective ions such as V^{4+} and V^{5+} states for V [120], Cu^{2+} and Cu^+ states for Cu [121], and W^{6+} states for W ions implantation [116] acting either as electron donor and/or acceptor levels, leading to the visible light assisted charge carrier generation and transition. Afterward, the excited electrons can follow the 1D pathway of ZnO NRs and move efficiently to the external circuit. These impurities-assisted charge transfer processes lead to the appearance of substantial PEC water splitting activity in Cu, V, and W ions implanted ZnO NRs under visible light irradiation.
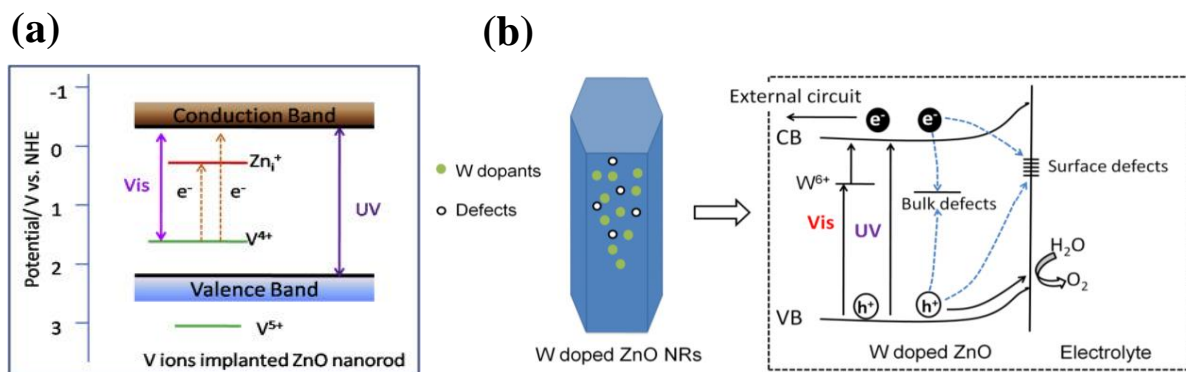
Fig. 2.14 The proposed microstructure and energy band diagram of (a) V [120] and (b) W [116] ions implanted ZnO NRs.

In Fig. 2.15, it is shown that the Cu, V, and W ions implanted ZnO NRs display an enhanced and quite stable photocurrent density as compared to that of pristine ZnO under visible light illumination (λ> 420 nm). The value of maximum photocurrent density 10.5 $\mu A/cm^2$ at 0.8 V (vs. Ag/AgCl) for the V ion implanted ZnO NRs has been achieved at the implantation fluence 2.5 $\times 10^{15}$ ions/cm^2. This maximum photocurrent density is about four times higher than that of undoped ZnO NRs [120]. In case of Cu ion implantation, the maximum photocurrent density 18 $\mu A/cm^2$ at 0.8 V (vs. a saturated calomel electrode) is achieved at the implantation fluence 2×10^{16} ions/cm^2, which is about eleven times higher than that of undoped ZnO NRs [121]. For W implanted ZnO NRs, the photocurrent density is increased by seven times as compared to the undoped ZnO NRs, reaching 15.2 $\mu A/cm^2$ at 1.0 V (vs. Ag/AgCl) [116]. Although the PEC performance of V, Cu, and W implanted ZnO NRs is still low, Wang et al. [122] have reported that N implantation induces a significantly

improved PEC water splitting activity in ZnO NRs. At 1×10^{15} ions/cm^2 N ion fluence, the implanted ZnO NRs exhibit a maximum photocurrent density as high as ~160 µA/cm^2 at 1.1 V (vs. SCE), which is almost two order of magnitudes higher than that of undoped ZnO NRs. The highly enhanced PEC performance of N implanted ZnO NRs is not only due to the extension of the optical absorption edges into the visible region but also due to the formation of terraced band structure as formed by the gradient distribution of N ion along the vertical <001> direction of ZnO NRs. The band structures of undoped ZnO, N implanted ZnO, and N gradient-implanted ZnO are depicted in Fig. 2.16. The relative positions of CB, VB, and Fermi level of the undoped ZnO are shown in Fig. 2.16(a). Generally, an acceptor level above the VB is introduced after N implantation, which lowers the Fermi level of ZnO (Fig. 2.16(b)). In case of undoped ZnO/N-ZnO homojunction, the electron is transferred from undoped ZnO to N-ZnO and equilibrate the Fermi levels, which results the formation of band bending (Fig. 2.16(c)). For N gradient-implanted ZnO, the concentration of N dopant is the highest (3.5%) at the top surfaces of ZnO NRs and thereafter it decreases steadily with the increase in the depth along ZnO NRs and thus terraced band structure is obtained in N gradient-implanted ZnO homojunction (Fig. 2.16(d)). The terraced band structure is assumed to induce a built-in electric field for effective charge separation and promoted charge transfer under visible light illumination. The pictorial representation of N gradient-implanted ZnO NRs and the formation of terraced band structure with promoted charge separation are shown in Fig. 2.16(e).
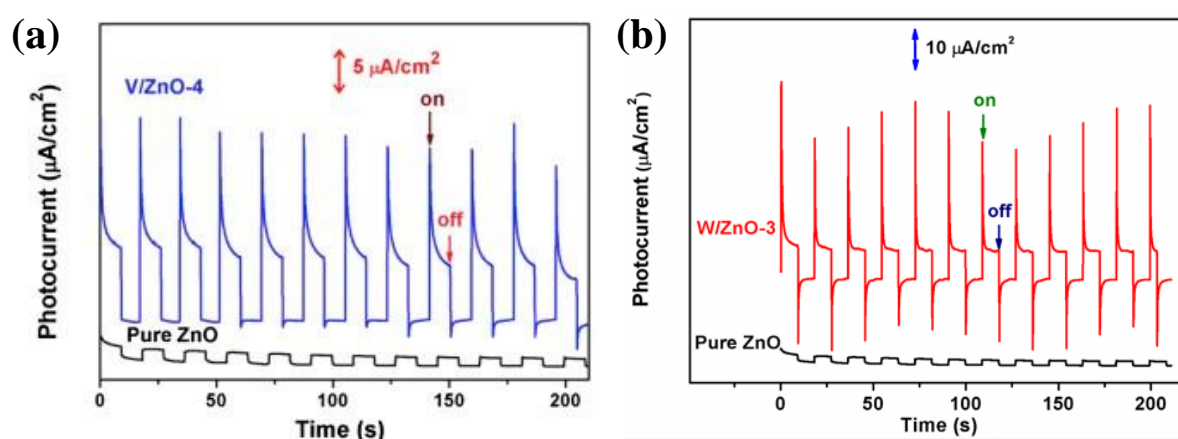
Fig. 2.15 Photocurrent plots of (a) V [120] and (b) W [116] ions implanted ZnO NRs under visible light (λ> 420 nm) illumination. The ZnO NRs implanted with the V ion fluence of 2.5×10^{15} ions/cm^2 has been marked as V/ZnO-4. Similarly, the ZnO NRs implanted with the W ion fluence of 5×10^{15} ions/cm^2 has been marked as W/ZnO-3.
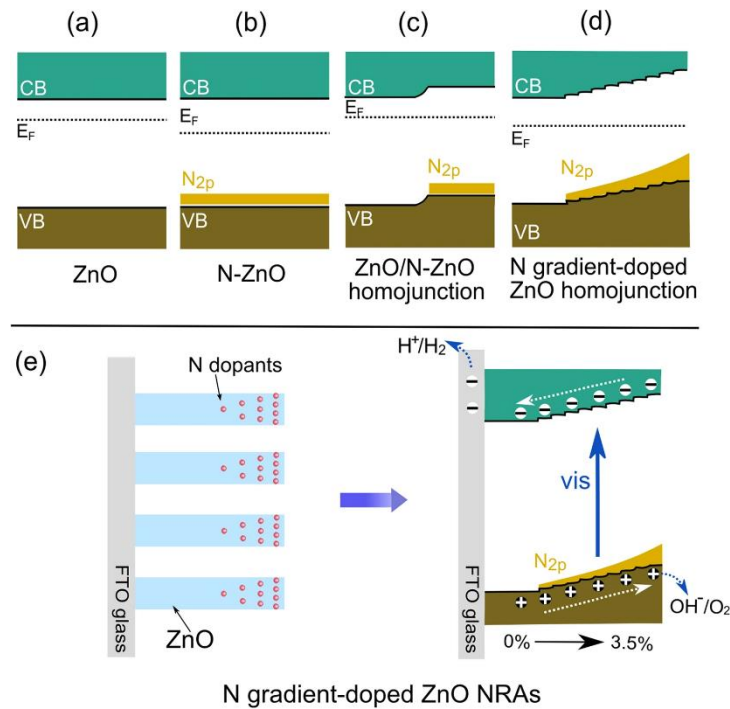
Fig. 2.16 The energy band diagram of (a) undoped ZnO, (b) N-ZnO, (c) undoped ZnO/N-ZnO homojunction, (d) N gradient-implanted ZnO homojunction, and (e) N gradient-implanted ZnO NRs and the formation of terraced band structure with promoted charge separation [122].

Critical analyses of the reported PEC water splitting data

From the above reported data, it is seen that the PEC performance of N implanted ZnO NRs is better than that of V, Cu and W implanted NRs. This difference in the efficiency in PEC can be analysed by the ion implantation-induced defects. The damages produced by the ions at their reported energies have been calculated to compare light (N ion) and heavy ions (V, Cu, and W ions) on an equal basis. Fig. 2.17 shows the SRIM predicted distribution of V_{Zn} and V_O for 30 keV N, 50 keV V, 30 keV Cu, and 50 keV W ion implanted ZnO NRs. From Fig. 2.17, it is clear that the ion-induced defects are always lower for N implanted ZnO than that of others. At the beginning of ion trajectory, the S_e for N implanted ZnO NRs is about 0.014 keV/Å, while the S_n is only 0.013 keV/ Å. Therefore, initially, S_e controls the stopping process and the N ions lose a significant amount of total energy in the form of S_e, which is not responsible for damage production. Subsequently, the primary recoil atoms with much less energy are produced and therefore they create much less damage. The majority of the displacements and subsequent damages are produced near the end of the track where the S_n dominates the stopping process. The damages in N implanted ZnO, therefore, consist of

primarily of simple Frenkel defects whose density increases to only near the end of the track. On the other hand, the estimated value of S_n is one order higher than that of S_e for V, Cu and W implanted ZnO NRs. Hence in the course of their stopping, the implanted V, Cu, and W ions transfer a significant amount of energy to primary recoil atoms via S_n. These high-energy recoiling atoms then move deeper inside the crystal and produce significant damages. To understand a more typical situation, 50 keV W implantation into vertically grown ZnO NRs is considered along <002> direction. The value of S_n for 50 keV W is about 0.32 keV/Å, where the interplanar distance between [0002] planes is 2.602 Å. As the implantation is carried out along the NRs orientation, the projected W ions lose about 832 eV per lattice plane on average. It can be expected that the majority of this energy is transferred to the primary recoil atoms, so the average recoil atom will have an energy ~832 eV, which is high enough than that of the above-mentioned values for N ions (420 eV). Thus, it is reasonable to assume that the heavy or intermediate V, Cu and W ions more likely to produce damage containing both simple defects and heavily disordered and overlapping cluster zones. If the overlap is adequately enough, the most of the damages can be assumed to lie within one large disordered region. Many of the target atoms are found to be displaced from their original lattice position within this region. When the defect density reaches a critical value, the cluster may result in the accumulation and recombination of holes at the electrode/electrolyte interface and thereby retarding the surface water oxidation reaction. Therefore, a significant low photocurrent density is observed for these V, Cu, and W implanted ZnO NRs.
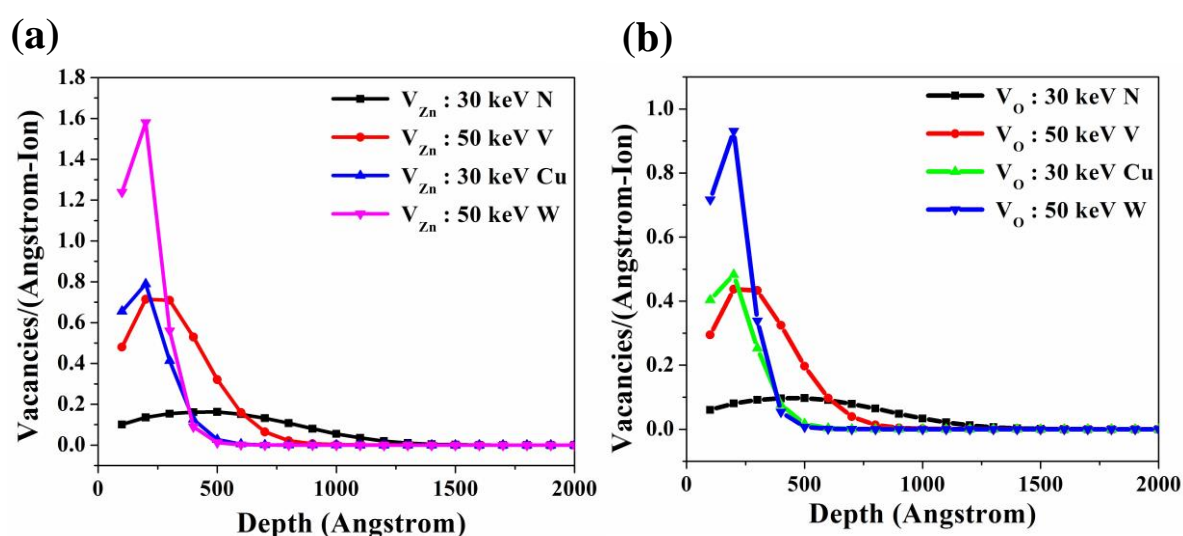
Fig. 2.17 SRIM predicted distribution of (a) V_{Zn} and (b) V_O defects in 30 keV N, 50 keV V, 30 keV Cu, and 50 keV W ion implanted ZnO thin films.

2.8.2 Light emitting diodes

Due to difficulty in achieving stable and high p-type conducting ZnO, initially, ZnO-based LEDs have been fabricated using various heterojunctions. The performance of those heterojunctions is not remotely close to the performance levels of competitive technologies [180-182]. Thus, an important challenge is to avoid the use of heterojunction as well as to overcome the surface-mediated non-radiative and deep-level recombination channels in order to improve device performance [183]. The successful p-type doping of ZnO using ion implantation technique has already been discussed in the section 2.7.2.2. Therefore, p-type doping via ion implantation can be an initial solution for getting an efficient ZnO-based LEDs. However, the reports on the fabrication of ZnO NWs based homojunction LEDs, in which p-type dopants are introduced by ion implantation are very few [184, 185]. Yang et al. [184] have reported stable and repeatable UV and red electroluminescence (EL) from ZnO NRs array LEDs, where a thin p-type layer was formed on top of the vertically aligned ZnO NRs by 50 and 180 keV As ion implantation at a fluence of 10^{14} or 10^{15} ions/cm^2. The device architecture of the p-ZnO: As NRs/n-ZnO NRs homojunction LEDs are shown in Fig. 2.18.
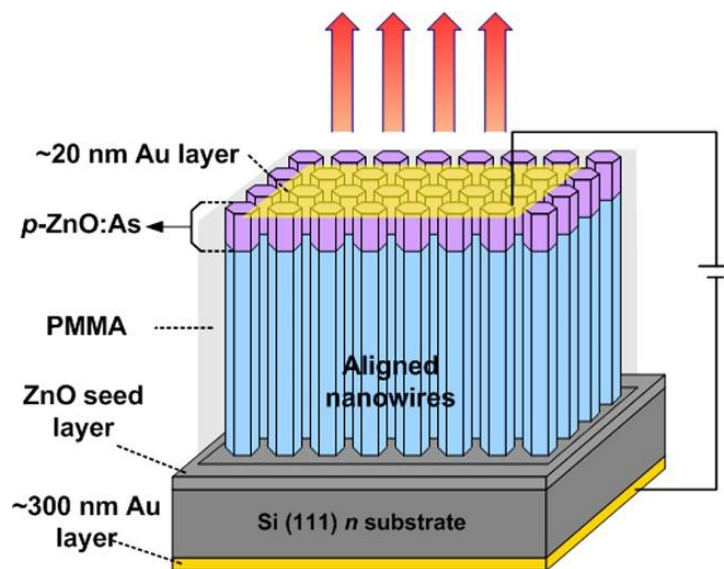
Fig. 2.18 The schematic diagram of p-ZnO: As/n-ZnO NRs homojunction device grown on Si substrate [184].
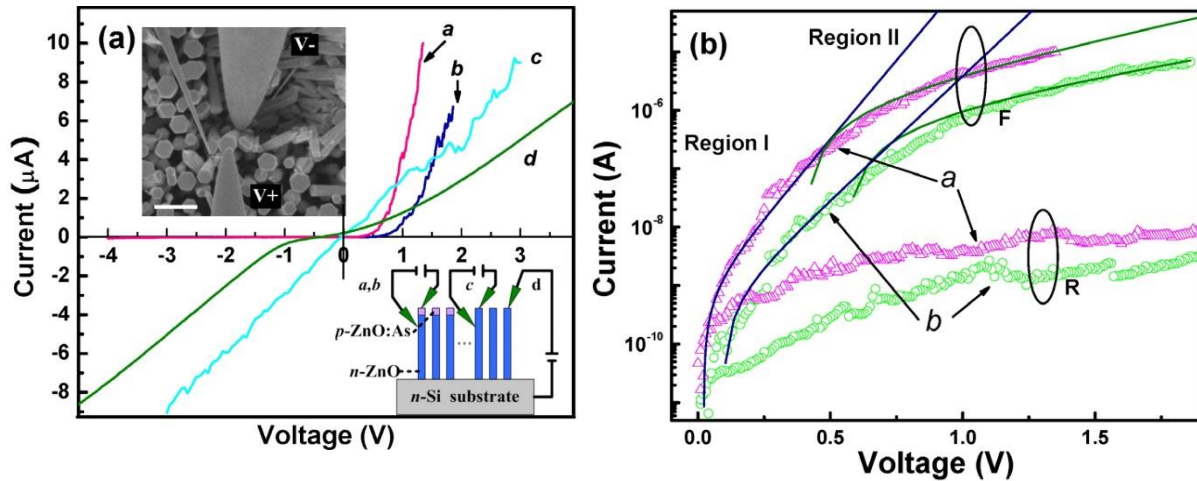
Fig. 2.19 (a) The I-V characteristics of a single NR at RT. The schematic diagram and a top view scanning electron microscope image of probing are shown in the bottom inset and in the upper inset respectively. (b) Semilogarithmic plot of curves a and b, where F indicates the forward bias and R indicates the reverse bias [184].

The typical I-V characteristics of the vertically aligned NRs-based p-ZnO: As/n-ZnO homojunction shown in Fig. 2.19(a) (curves a and b) indicate the formation of a typical p-n junction. The forward current is around two orders greater than the reverse current in the low bias voltage range. Fig. 2.19(b) shows the semilogarithmic plots of the I-V curves, in which two regions are observed in the positive biased region. The ideality factors (η) derived from the curve "a" in Fig. 2.19(b) are 3.9 and 22 respectively for the regions I (V<0.6 V) and region II (0.6<V<1.3 V). The values of η derived from curve "b" show small variations from the curve "a", which are 3.0 and 16.6 respectively for the regions I (V<0.5 V) and region II (0.5 <V<1.8 V). Very high values of η indicate large deviations probably due to unusual recombination mechanisms.

The EL spectra of the ZnO NRs homojunction diode at RT for different forward injection currents at ion fluence 10^{15} and 10^{14} ions/cm^2 are shown in Fig. 2.20(a) and Fig. 2.20(b) respectively. The variation of the peak intensities with respect to the injection current are shown in the insets. In the Fig. 2.20(a), a broad red band peaked at 630 nm has been appeared. The intensity of the red EL emission increases drastically with an increase in the forward bias voltage from 4 to 5 V. It is assumed that the donor-acceptor pair recombination is responsible for the observed red luminescence which is closely related to the implantation-induced defects. As shown in the inset of Fig. 2.20(a), the intensity of the red band increases exponentially with an increase in the injected current, indicating an increase in emission

efficiency at higher injection current. In contrast to Fig 2.20(a), the EL spectrum of the ZnO NR diode implanted with 10^{14} ions/cm^2 ions as depicted in Fig. 2.20(b) is consist of a strong UV band (at 380 nm) and a weak broad red band (at 630 nm). The difference in the intensity of emission peak at 630 nm for both cases indicates that a sufficient As implantation fluence (10^{15} ions/cm^2) is necessary to emerge the emission of 630 nm. The high fluence of As ion most probably induces an acceptor level in between the band gap and the transition of excitons from CB to this energy level appears as the emission of 630 nm.
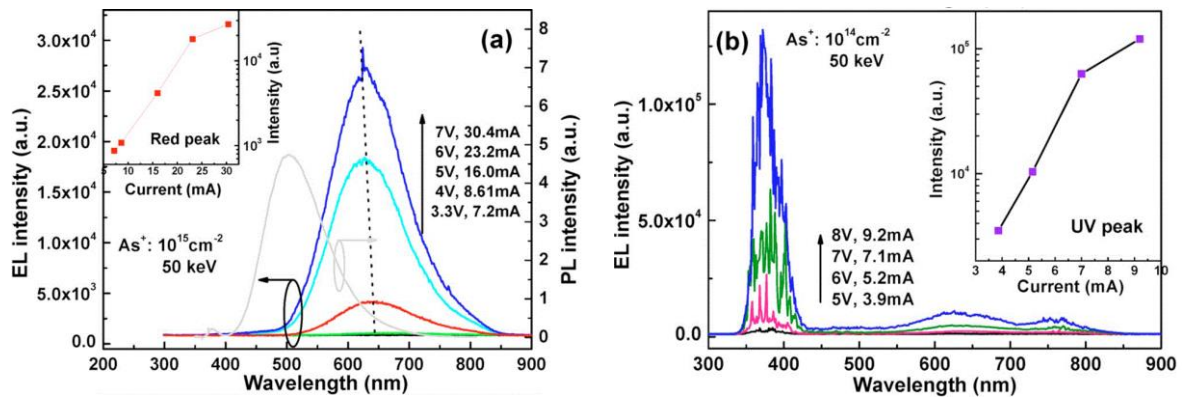
Fig. 2.20 EL spectra of 50 keV As implanted ZnO NRs homojunction having fluence (a) 10^{15} cm^{-2} and (b) 10^{14} cm^{-2} respectively. A typical PL spectrum of the homojunction is also shown in (a) (right side) for comparison. The semilogarithmic plots of the intensities of (a) red peak and (b) UV peak as a function of current is shown in the insets of corresponding figures [184].

In another study, p-type doping in ZnO NRs via P ion implantation, and p-n homojunction LEDs with UV light emission at RT have been reported [185]. The typical I-V measurement of the LEDs shows the p-n homojunction characteristics with a low turn-on voltage of ~0.8 V. The EL spectra of both the devices I, (wherein 50 keV P ions were implanted with fluence 10^{14} ions/cm^2), and II (wherein 100 keV P ions were implanted with fluence 10^{14} ions/cm^2) measured at different injection currents show a strong UV emission under the forward bias. The intensities of the UV emission increase linearly with beyond a threshold injection current (I =18.6, and 23.5 mA for devices I and II respectively). However, again these performances are far from the performance levels of the presently used LEDs. In addition to the UV emission, the device I shows a comparatively weak and broad emission band in the visible region, which corresponds to the deep defect level emission. The defect

emission becomes stronger in device II, which has predominantly two components, a green emission at ~510 nm and a near-infrared emission at ~800 nm.

Critical analyses of the reported LEDs data

Comparing the diode characteristics of As and P implanted ZnO NRs and the appearance of new visible emission peaks, it can be said that the performance of LEDs is influenced by the number of defects produced during implantation as well as the success of acceptor doping. As discussed in the section 2.7.2.2, As prefers to substitute on the Zn Site and forms As_{Zn}–$2V_{Zn}$ defect complexes in ZnO, which is responsible for the p-type conductivity in As implanted ZnO. In the case of P implantation, P may sit in the O site and/or in the Zn site forming deep P_O and shallow P_{Zn}-$2V_{Zn}$ acceptors respectively. Thus, depending on different types of acceptor states, the performance of LEDs differs which are observed in the above-reported results. Though the As and P implantation in ZnO NRs exhibits diode characteristics, a far deviation from the ideal case (η =1) has been observed. The deviations may be attributed to various possible reasons such as high contact resistance, deep-level assisted tunnelling or parasitic rectifying junctions within the diode, imperfections in making the abrupt p-n junction using implantation technique.

2.9 Conclusions

In this chapter, an overview of the recent developments on ion implantation in ZnO has been presented. With a brief introduction to the properties of ZnO, defects in ZnO, and ion implantation, the chapter illustrates the defect interaction and their distribution in implanted ZnO. Then, the recent works using ion implantation techniques in tuning the electrical and optical properties of ZnO and their application in optoelectronic devices have been discussed. Detailed analyses on the reported data show that in addition to the insertion of a foreign atom into the ZnO lattice, the formation of defects and their interaction alter the electrical, and optical properties of ZnO significantly. Crystal damage by ion implantation becomes prominent under the following conditions, when the other conditions are unchanged: (a) heavy ion mass, (b) high energy (>250 keV), (c) high fluence (> 10^{16} ions/cm^2), (d) high beam current, (e) shorter irradiation interval, (f) longer irradiation time. In such situation, the crystal damages cannot be fully repaired by post-implantation annealing. To achieve considerably better device performance, one should choose moderately low energy and low fluence of implanted ions. However, these ion implanted ZnO can be used in the field of

optoelectronic applications, especially in PEC water splitting and LED. Critical correlation of the reported properties with the implantation-induced defects as evaluated by the theoretical SRIM simulation have been established, which supports the reported experimental results in most of the cases.

2.10   References

[1] L.A. Larson, J.M. Williams, M.I. Current, t. Environment, Ion implantation for semiconductor doping and materials modification, Reviews Of Accelerator Science and Technology, 4 (2011) 11-40.

[2] J.R. Conrad, J.L. Radtke, R.A. Dodd, F.J. Worzala, N.C. Tran, Plasma source ion-implantation technique for surface modification of materials, J. Appl. Phys., 62 (1987) 4591-4596.

[3] M. Erman, J. Theeten, P. Chambon, S. Kelso, D. Aspnes, Optical properties and damage analysis of GaAs single crystals partly amorphized by ion implantation, J. Appl. Phys., 56 (1984) 2664-2671.

[4] J. Kennedy, A. Markwitz, Z. Li, W. Gao, C. Kendrick, S. Durbin, R. Reeves, Modification of electrical conductivity in RF magnetron sputtered ZnO films by low-energy hydrogen ion implantation, Curr. Appl. Phys., 6 (2006) 495-498.

[5] J. Kennedy, D. Carder, A. Markwitz, R. Reeves, Properties of nitrogen implanted and electron beam annealed bulk ZnO, J. Appl. Phys., 107 (2010) 103518.

[6] J. Kennedy, J. Leveneur, G. Williams, D. Mitchell, A. Markwitz, Fabrication of surface magnetic nanoclusters using low energy ion implantation and electron beam annealing, Nanotechnology, 22 (2011) 115602.

[7] H. Shen, L. Mi, P. Xu, W. Shen, P.-N. Wang, Visible-light photocatalysis of nitrogen-doped TiO2 nanoparticulate films prepared by low-energy ion implantation, Appl. Surf. Sci., 253 (2007) 7024-7028.

[8] P. Willke, J.A. Amani, A. Sinterhauf, S. Thakur, T. Kotzott, T. Druga, S. Weikert, K. Maiti, H. Hofsäss, M. Wenderoth, Doping of graphene by low-energy ion beam implantation: structural, electronic, and transport properties, Nano letters, 15 (2015) 5110-5115.

[9] S.O. Aisida, R. Obodo, M. Arshad, I. Mahmood, I. Ahmad, F. Ezema, T.-k. Zhao, M. Malik, Irradiation-induced structural changes in ZnO nanowires, Nuclear Instruments Methods in Physics Research Section B: Beam Interactions with Materials Atoms, 458 (2019) 61-71.

[10] J. Kotakoski, A. Krasheninnikov, Y. Ma, A.S. Foster, K. Nordlund, R.M. Nieminen, B and N ion implantation into carbon nanotubes: insight from atomistic simulations, Physical Review B, 71 (2005) 205408.

[11] A. Chrissanthopoulos, S. Baskoutas, N. Bouropoulos, V. Dracopoulos, P. Poulopoulos, S. Yannopoulos, Synthesis and characterization of ZnO/NiO p–n heterojunctions: ZnO nanorods grown on NiO thin film by thermal evaporation, Photonics Nanostructures-Fundamentals Applications, 9 (2011) 132-139.

[12] T. Sum, A. Bettiol, H. Seng, I. Rajta, J. Van Kan, F. Watt, Proton beam writing of passive waveguides in PMMA, Nuclear Instruments Methods in Physics Research Section B: Beam Interactions with Materials Atoms, 210 (2003) 266-271.

[13] A. Bettiol, S. Chiam, E. Teo, C. Udalagama, S. Chan, S. Hoi, J. Van Kan, M. Breese, F.J.N.I. Watt, Advanced applications in microphotonics using proton beam writing, Nuclear Instruments Methods in Physics Research Section B: Beam Interactions with Materials Atoms, 267 (2009) 2280-2284.

[14] F. Meng, Z. Li, X. Liu, Synthesis of tantalum thin films on titanium by plasma immersion ion implantation and deposition, Surface Coatings Technology, 229 (2013) 205-209.

[15] D.K. Avasthi, G.K. Mehta, Swift heavy ions for materials engineering and nanostructuring, Springer Science & Business Media, 2011.

[16] S. Chandramohan, R. Sathyamoorthy, P. Sudhagar, D. Kanjilal, D. Kabiraj, K. Asokan, Swift heavy ion beam irradiation induced modifications in structural, morphological and optical properties of CdS thin films, Nuclear Instruments Methods in Physics Research Section B: Beam Interactions with Materials Atoms, 254 (2007) 236-242.

[17] W. Wesch, A. Kamarou, E. Wendler, Effect of high electronic energy deposition in semiconductors, Nuclear Instruments Methods in Physics Research Section B: Beam Interactions with Materials Atoms, 225 (2004) 111-128.

[18] Z. Zhou, K. Kato, T. Komaki, M. Yoshino, H. Yukawa, M. Morinaga, K. Morita, Effects of dopants and hydrogen on the electrical conductivity of ZnO, Journal of the European Ceramic Society, 24 (2004) 139-146.

[19] A. Das, G. Das, D. Kabiraj, D. Basak, High conductivity along with high visible light transparency in Al implanted sol-gel ZnO thin film with an elevated figure of merit value as a transparent conducting layer, J. Alloy. Compd., 835 (2020) 11.

[20] A. Macková, P. Malinský, A. Jagerová, R. Mikšová, P. Nekvindová, J. Cajzl, E. Rinkevičiūtė, S. Akhmadaliev, Damage formation and Er structural incorporation in m-plane and a-plane ZnO, Nuclear Instruments Methods in Physics Research Section B: Beam Interactions with Materials Atoms, 460 (2019) 38-46.

[21] A. Turos, P. Jóźwik, M. Wójcik, J. Gaca, R. Ratajczak, A. Stonert, Mechanism of damage buildup in ion bombarded ZnO, Acta Materialia, 134 (2017) 249-256.

[22] A. Macková, P. Malinský, A. Jagerová, R. Mikšová, P. Nekvindová, J. Cajzl, R. Böttger, S. Akhmadaliev, Au incorporation into various ZnO crystallographic cuts realised by ion implantation–ZnO damage characterization, Vacuum, 169 (2019) 108892.

[23] A.Y. Azarov, E. Wendler, A.Y. Kuznetsov, B.G. Svensson, Crucial role of implanted atoms on dynamic defect annealing in ZnO, Appl. Phys. Lett., 104 (2014) 052101.

[24] A.Y. Azarov, A. Hallén, X.L. Du, P. Rauwel, A.Y. Kuznetsov, B.G. Svensson, Effect of implanted species on thermal evolution of ion-induced defects in ZnO, J. Appl. Phys., 115 (2014) 073512.

[25] A. Azarov, E. Wendler, K. Lorenz, E. Monakhov, B.G. Svensson, Effect of buried extended defects on the radiation tolerance of ZnO, Appl. Phys. Lett., 110 (2017) 172103.

[26] S.O. Kucheyev, J.S. Williams, C. Jagadish, J. Zou, C. Evans, A.J. Nelson, A.V. Hamza, Ion-beam-produced structural defects in ZnO, Physical Review B, 67 (2003) 094115.

[27] K. Lorenz, E. Alves, E. Wendler, O. Bilani, W. Wesch, M. Hayes, Damage formation and annealing at low temperatures in ion implanted ZnO, Appl. Phys. Lett., 87 (2005) 191904.

[28] J. Lv, X. Li, Defect evolution in ZnO and its effect on radiation tolerance, Physical Chemistry Chemical Physics, 20 (2018) 11882-11887.

[29] Ü. Özgür, Y.I. Alivov, C. Liu, A. Teke, M. Reshchikov, S. Doğan, V. Avrutin, S.-J. Cho, Morkoç, H.J.J.o.a. physics, A comprehensive review of ZnO materials and devices, 98 (2005) 11.

[30] U. Ozgur, Y.I. Alivov, C. Liu, A. Teke, M.A. Reshchikov, S. Dogan, V. Avrutin, S.J. Cho, H. Morkoc, A comprehensive review of ZnO materials and devices, J. Appl. Phys., 98 (2005) 041301.

[31] K. Ellmer, A. Bikowski, Intrinsic and extrinsic doping of ZnO and ZnO alloys, J. Phys. D-Appl. Phys., 49 (2016) 413002.

[32] U. Rössler, Energy Bands of Hexagonal II-VI Semiconductors, Physical Review, 184 (1969) 733-738.

[33] D. Langer, C.J.P.R.B. Vesely, Electronic core levels of zinc chalcogenides, 2 (1970) 4885.

[34] R. Powell, W. Spicer, J.J.P.R.L. McMenamin, Location of the Zn 3 d States in ZnO, 27 (1971) 97.

[35] L. Ley, R. Pollak, F. McFeely, S.P. Kowalczyk, D.J.P.R.B. Shirley, Total valence-band densities of states of III-V and II-VI compounds from x-ray photoemission spectroscopy, 9 (1974) 600.

[36] J.E. Jaffe, J.A. Snyder, Z. Lin, A.C. Hess, LDA and GGA calculations for high-pressure phase transitions in ZnO and MgO, Physical Review B, 62 (2000) 1660-1665.

[37] P. Erhart, K. Albe, A. Klein, First-principles study of intrinsic point defects in ZnO: Role of band structure, volume relaxation, and finite-size effects, Physical Review B, 73 (2006) 205203.

[38] K. Ellmer, A. Klein, B. Rech, Transparent Conductive Zinc Oxide: Basics and Applications in Thin Film Solar Cells, Springer Berlin Heidelberg, 2010.

[39] J.R. Chelikowsky, An oxygen pseudopotential: Application to the electronic structure of ZnO, Solid State Communications, 22 (1977) 351-354.

[40] P. Schröer, P. Krüger, J. Pollmann, First-principles calculation of the electronic structure of the wurtzite semiconductors ZnO and ZnS, Physical Review B, 47 (1993) 6971-6980.

[41] M.A. Borysiewicz, ZnO as a Functional Material, a Review, 9 (2019) 505.

[42] D. Seghier, H.P. Gislason, Shallow and deep donors in n-type ZnO characterized by admittance spectroscopy, Journal of Materials Science: Materials in Electronics, 19 (2008) 687-691.

[43] F.H. Leiter, H.R. Alves, A. Hofstaetter, D.M. Hofmann, B.K. Meyer, The Oxygen Vacancy as the Origin of a Green Emission in Undoped ZnO, physica status solidi (b), 226 (2001) R4-R5.

[44] D.C. Look, J.W. Hemsky, J.R. Sizelove, Residual native shallow donor in ZnO, Phys. Rev. Lett., 82 (1999) 2552-2555.

[45] A. Janotti, C.G.V.d. Walle, Oxygen vacancies in ZnO, Appl. Phys. Lett., 87 (2005) 122102.

[46] A. Janotti, C.G. Van de Walle, Oxygen vacancies in ZnO, Appl. Phys. Lett., 87 (2005) 122102.

[47] A. Janotti, C.G. Van de Walle, Native point defects in ZnO, Physical Review B, 76 (2007) 165202.

[48] L.S. Vlasenko, G.D. Watkins, Optical detection of electron paramagnetic resonance for intrinsic defects produced in ZnO by 2.5-MeV electron irradiation in situ at 4.2 K, Phys. Rev. B, 72 (2005) 12.

[49] A. Janotti, C.G. Van de Walle, Native point defects in ZnO, Phys. Rev. B, 76 (2007) 22.

[50] A. Travlos, N. Boukos, C. Chandrinou, H.-S. Kwack, L.S. Dang, Zinc and oxygen vacancies in ZnO nanorods, J. Appl. Phys., 106 (2009) 104307.

[51] F. Fabbri, M. Villani, A. Catellani, A. Calzolari, G. Cicero, D. Calestani, G. Calestani, A. Zappettini, B. Dierre, T. Sekiguchi, G. Salviati, Zn vacancy induced green luminescence on non-polar surfaces in ZnO nanostructures, Scientific Reports, 4 (2014) 5158.

[52] D. Sett, S. Sarkar, D. Basak, A successive photocurrent transient study to probe the sub-band gap electron and hole traps in ZnO nanorods, RSC Advances, 4 (2014) 58553-58558.

[53] O. Fumiyasu, T. Atsushi, T. Isao, Point defects in ZnO: an approach from first principles, Sci. Technol. Adv. Mater, 12 (2011) 034302.

[54] P. Erhart, K. Albe, First-principles study of migration mechanisms and diffusion of oxygen in zinc oxide, Phys. Rev. B, 73 (2006) 9.

[55] M.D. McCluskey, 1 - Defects in ZnO, in: J. Stehr, I. Buyanova, W. Chen (Eds.) Defects in Advanced Electronic Materials and Novel Low Dimensional Structures, Woodhead Publishing, 2018, pp. 1-25.

[56] D.C. Look, G.C. Farlow, P. Reunchan, S. Limpijumnong, S. Zhang, K. Nordlund, Evidence for native-defect donors in n-type ZnO, Physical review letters, 95 (2005) 225502.

[57] C.G. Van de Walle, Hydrogen as a cause of doping in zinc oxide, Physical review letters, 85 (2000) 1012.

[58] E. Lavrov, J. Weber, F. Börrnert, C.G. Van de Walle, R. Helbig, Hydrogen-related defects in ZnO studied by infrared absorption spectroscopy, Physical Review B, 66 (2002) 165205.

[59] D.M. Hofmann, A. Hofstaetter, F. Leiter, H. Zhou, F. Henecker, B.K. Meyer, S.B. Orlinskii, J. Schmidt, P.G. Baranov, Hydrogen: A Relevant Shallow Donor in Zinc Oxide, Physical Review Letters, 88 (2002) 045504.

[60] W.-W. Feng, S. Cho, M.-S. Wang, D.D. Dung, Co-contribution of hydrogen impurities and native defects might be the answer for the n-type conductivity in ZnO, Physics Letters A, 380 (2016) 480-484.

[61] S.F.J. Cox, E.A. Davis, S.P. Cottrell, P.J.C. King, J.S. Lord, J.M. Gil, H.V. Alberto, R.C. Vilão, J. Piroto Duarte, N. Ayres de Campos, A. Weidinger, R.L. Lichti, S.J.C. Irvine, Experimental Confirmation of the Predicted Shallow Donor Hydrogen State in Zinc Oxide, Physical Review Letters, 86 (2001) 2601-2604.

[62] B. El-Kareh, Ion Implantation, in: Fundamentals of Semiconductor Processing Technology, Springer, 1995, pp. 353-466.

[63] H. Ryssel, I. Ruge, Ion implantation, (1986).

[64] W.Q. Li, X.H. Xiao, A.L. Stepanov, Z.G. Dai, W. Wu, G.X. Cai, F. Ren, C.Z. Jiang, The ion implantation-induced properties of one-dimensional nanomaterials, Nanoscale research letters, 8 (2013) 1-13.

[65] J. Williams, Ion implantation of semiconductors, Materials Science Engineering: A, 253 (1998) 8-15.

[66] J. Wood, G. Majumdar, Ion Implantation, in: Reference Module in Materials Science and Materials Engineering, Elsevier, 2016.

[67] M. Goorsky, Ion implantation, BoD–Books on Demand, 2012.

[68] S. Chattopadhyay, S. Dutta, D. Jana, S. Chattopadhyay, A. Sarkar, P. Kumar, D. Kanjilal, D.K. Mishra, S.K. Ray, Interplay of defects in 1.2 MeV Ar irradiated ZnO, J. Appl. Phys., 107 (2010) 8.

[69] T. Wu, A. Wang, L. Zheng, G. Wang, Q. Tu, B. Lv, Z. Liu, Z. Wu, Y. Wang, Evolution of native defects in ZnO nanorods irradiated with hydrogen ion, Scientific Reports, 9 (2019) 17393.

[70] A.J. McKenna, T. Trevethan, C.D. Latham, P.J. Young, M.I. Heggie, Threshold displacement energy and damage function in graphite from molecular dynamics, Carbon, 99 (2016) 71-78.

[71] R.E. Smallman, A.H.W. Ngan, Chapter 6 - Point Defect Behaviour, in: R.E. Smallman, A.H.W. Ngan (Eds.) Modern Physical Metallurgy (Eighth Edition), Butterworth-Heinemann, Oxford, 2014, pp. 251-285.

[72] Y. Zhang, W.J. Weber, Ion irradiation and modification: The role of coupled electronic and nuclear energy dissipation and subsequent nonequilibrium processes in materials, Applied Physics Reviews, 7 (2020) 041307.

[73] M. Linnarsson, A. Hallén, L. Vines, Intentional and unintentional channeling during implantation of 51V ions into 4H-SiC, Semiconductor Science Technology, 34 (2019) 115006.

[74] L.C. Feldman, J.W. Mayer, S.T. Picraux, Materials analysis by ion channeling: submicron crystallography, Academic Press, 2012.

[75] G. Hobler, Critical angles and low-energy limits to ion channeling in silicon, Radiation effects defects in solids, 139 (1996) 21-85.

[76] J.F. Ziegler, M.D. Ziegler, J.P. Biersack, SRIM - The stopping and range of ions in matter (2010), Nuclear Instruments and Methods in Physics Research Section B: Beam Interactions with Materials and Atoms, 268 (2010) 1818.

[77] Z. Huang, H.B. Ruan, H. Zhang, D.P. Shi, W.J. Li, G.P. Qin, F. Wu, L. Fang, C.Y. Kong, Investigation on the p-type formation mechanism of nitrogen ion implanted ZnO thin films induced by rapid thermal annealing, Opt. Mater. Express, 9 (2019) 3098-3108.

[78] A. Mondal, S. Pal, A. Sarkar, T.S. Bhattacharya, A. Das, N. Gogurla, S.K. Ray, P. Kumar, D. Kanjilal, K.D. Devi, A. Singha, S. Chattopadhyay, D. Jana, Raman spectroscopic analysis on Li, N and (Li,N) implanted ZnO, Materials Science in Semiconductor Processing, 80 (2018) 111-117.

[79] H. Gupta, J. Singh, R. Dutt, S. Ojha, S. Kar, R. Kumar, V. Reddy, F. Singh, Defect-induced photoluminescence from gallium-doped zinc oxide thin films: influence of doping and energetic ion irradiation, Physical Chemistry Chemical Physics, 21 (2019) 15019-15029.

[80] F. Schmidt, S. Müller, R. Pickenhain, H. von Wenckstern, S. Geburt, C. Ronning, M. Grundmann, Defect studies on Ar-implanted ZnO thin films, physica status solidi (b), 251 (2014) 937-941.

[81] A. Jagerova, P. Malinsky, R. Miksova, P. Nekvindova, J. Cajzl, P. Rysanek, A. Mackova, High energy Au+ ion implantation of polar and nonpolar ZnO-Structure modification and optical properties, Surf. Interface Anal., 52 (2020) 1083-1088.

[82] Z.Q. Chen, A. Kawasuso, Y. Xu, H. Naramoto, X.L. Yuan, T. Sekiguchi, R. Suzuki, T. Ohdaira, Production and recovery of defects in phosphorus-implanted ZnO, J. Appl. Phys., 97 (2005) 013528.

[83] Z.Q. Chen, M. Maekawa, A. Kawasuso, R. Suzuki, T. Ohdaira, Interaction of nitrogen with vacancy defects in N+-implanted ZnO studied using a slow positron beam, Appl. Phys. Lett., 87 (2005) 091910.

[84] N.M. Lyadov, A.I. Gumarov, V.F. Valeev, V.I. Nuzhdin, R.I. Khaibullin, I.A. Faizrakhmanov, Optical and electrical studies of ZnO thin films heavily implanted with silver ions, in: N.S. Averkiev, S.A. Poniaev, G.S. Sokolovskii (Eds.) 16th Russian Youth Conference on Physics and Astronomy, Iop Publishing Ltd, Bristol, 2014.

[85] N.M. Lyadov, A.I. Gumarov, R.N. Kashapov, A.I. Noskov, V.F. Valeev, V.I. Nuzhdin, V.V. Bazarov, R.I. Khaibullin, I.A. Faizrakhmanov, Structure and optical properties of ZnO with silver nanoparticles, Semiconductors, 50 (2016) 43-49.

[86] N.M. Lyadov, A.I. Gumarov, V.F. Valeev, V.I. Nuzhdin, V.A. Shustov, V.V. Bazarov, I.A. Faizrakhmanov, Effect of Implantation Regimes of Silver Ions on the Structure and Optical Properties of Zinc-Oxide Nanocrystalline Films, Tech. Phys., 61 (2016) 1237-1243.

[87] K. Kono, S.K. Arora, N. Kishimoto, Modification in optical properties of negative Cu ion implanted ZnO, Nucl. Instrum. Methods Phys. Res. Sect. B-Beam Interact. Mater. Atoms, 206 (2003) 291-294.

[88] T. Karali, N. Can, L. Valberg, A.L. Stepanov, P.D. Townsend, C. Buchal, R.A. Ganeev, A.I. Ryasnyansky, H.G. Belik, M.L. Jessett, C. Ong, Optical properties and luminescence of metallic nanoclusters in ZnO : Cu, Physica B, 363 (2005) 88-95.

[89] A. Cetin, R. Kibar, M. Ayvaclkh, N. Can, C. Buchal, P.D. Townsend, A.L. Stepanov, T. Karah, S. Selvi, Optical properties of Cu implanted ZnO, Nucl. Instrum. Methods Phys. Res. Sect. B-Beam Interact. Mater. Atoms, 249 (2006) 474-477.

[90] X.D. Zhang, P. Wu, Y.Y. Shen, L.H. Zhang, Y.H. Xue, F. Zhu, D.C. Zhang, C.L. Liu, Structural and optical properties of Au-implanted ZnO films, Appl. Surf. Sci., 258 (2011) 151-157.

[91] J. Cajzl, K. Jenickova, P. Nekvindova, A. Michalcova, M. Vesely, A. Mackova, P. Malinsky, A. Jagerova, R. Miksova, S. Akhmadaliev, Creation of Gold Nanoparticles in ZnO by Ion Implantation-DFT and Experimental Studies, Nanomaterials, 10 (2020) 21.

[92] P. Rauwel, M. Salumaa, A. Aasna, A. Galeckas, E. Rauwel, A Review of the Synthesis and Photoluminescence Properties of Hybrid ZnO and Carbon Nanomaterials, Journal of Nanomaterials, 2016 (2016) 5320625.

[93] J. Petersen, C. Brimont, M. Gallart, O. Crégut, G. Schmerber, P. Gilliot, B. Hönerlage, C. Ulhaq-Bouillet, J.L. Rehspringer, C. Leuvrey, S. Colis, H. Aubriet, C. Becker, D. Ruch, A. Slaoui, A. Dinia, Structural and photoluminescence properties of ZnO thin films prepared by sol-gel process, J. Appl. Phys., 104 (2008) 113539.

[94] M. Mahanti, T. Ghosh, D. Basak, Enhanced near band edge luminescence of Ti/ZnO nanorod heterostructures due to the surface diffusion of Ti, Nanoscale, 3 (2011) 4427-4433.

[95] R.B.M. Cross, M.M.D. Souza, E.M.S. Narayanan, A low temperature combination method for the production of ZnO nanowires, Nanotechnology, 16 (2005) 2188-2192.

[96] J. Hsu, D. Tallant, R. Simpson, N. Missert, R. Copeland, Luminescent properties of solution-grown ZnO nanorods, Appl. Phys. Lett., 88 (2006) 252103.

[97] N.H. Alvi, K. ul Hasan, O. Nur, M. Willander, The origin of the red emission in n-ZnO nanotubes/p-GaN white light emitting diodes, Nanoscale Research Letters, 6 (2011) 130.

[98] L.E. Greene, M. Law, J. Goldberger, F. Kim, J.C. Johnson, Y. Zhang, R.J. Saykally, P. Yang, Low-Temperature Wafer-Scale Production of ZnO Nanowire Arrays, Angewandte Chemie International Edition, 42 (2003) 3031-3034.

[99] Y.I. Alivov, M.V. Chukichev, V.A. Nikitenko, Green luminescence band of zinc oxide films copper-doped by thermal diffusion, Semiconductors, 38 (2004) 31-35.

[100] R. Dingle, Luminescent Transitions Associated With Divalent Copper Impurities and the Green Emission from Semiconducting Zinc Oxide, Physical Review Letters, 23 (1969) 579-581.

[101] D.C. Reynolds, D.C. Look, B. Jogai, H. Morkoç, Similarities in the bandedge and deep-centre photoluminescence mechanisms of ZnO and GaN, Solid State Commun., 101 (1997) 643-646.

[102] A. Bera, T. Ghosh, D. Basak, Enhanced photoluminescence and photoconductivity of ZnO nanowires with sputtered Zn, ACS applied materials interfaces, 2 (2010) 2898-2903.

[103] K. Vanheusden, C.H. Seager, W.L. Warren, D.R. Tallant, J.A. Voigt, Correlation between photoluminescence and oxygen vacancies in ZnO phosphors, Appl. Phys. Lett., 68 (1996) 403-405.

[104] V. Quemener, L. Vines, E.V. Monakhov, B.G. Svensson, Evolution of deep electronic states in ZnO during heat treatment in oxygen- and zinc-rich ambients, Appl. Phys. Lett., 100 (2012) 112108.

[105] R. Bhaskar, A. Lakshmanan, S. Marimuthu, T. Ravishankar, M.T. Jose, L. Nariangadu, Mechanism of green luminescence in ZnO, Indian Journal of Pure and Applied Physics, 47 (2009) 772-774.

[106] K. Vanheusden, W.L. Warren, C.H. Seager, D.R. Tallant, J.A. Voigt, B.E. Gnade, Mechanisms behind green photoluminescence in ZnO phosphor powders, J. Appl. Phys., 79 (1996) 7983-7990.

[107] D.C. Reynolds, D.C. Look, B. Jogai, J.E. Hoelscher, R.E. Sherriff, M.T. Harris, M.J. Callahan, Time-resolved photoluminescence lifetime measurements of the Γ5 and Γ6 free excitons in ZnO, J. Appl. Phys., 88 (2000) 2152-2153.

[108] Ü. Özgür, Y.I. Alivov, C. Liu, A. Teke, M.A. Reshchikov, S. Doğan, V. Avrutin, S.-J. Cho, H. Morkoç, A comprehensive review of ZnO materials and devices, J. Appl. Phys., 98 (2005) 041301.

[109] Y. Zhao, X. Chen, L.G. Fang, L.F. Yang, H.H. Li, Y.F. Gao, Effects of Annealing on the Structural and Photoluminescent Properties of Ag-Doped ZnO Nanowires Prepared by Ion Implantation, Plasma Sci. Technol., 15 (2013) 817-820.

[110] C.O. Kim, D.H. Shin, S.H. Choi, K. Belay, R.G. Elliman, Strong enhancement of ultraviolet emission from ZnO films by V implantation, J. Vac. Sci. Technol. B, 29 (2011) 4.

[111] C.O. Kim, D.H. Shin, S.H. Choi, Strongly-enhanced near-band-edge photoluminescence of Nb-implanted ZnO films, J. Cryst. Growth, 326 (2011) 42-44.

[112] S. Muller, M.J. Zhou, Q. Li, C. Ronning, Intra-shell luminescence of transition-metal-implanted zinc oxide nanowires, Nanotechnology, 20 (2009) 8.

[113] S. Muller, M. Lorenz, C. Czekalla, G. Benndorf, H. Hochmuth, M. Grundmann, H. Schmidt, C. Ronning, Intense white photoluminescence emission of V-implanted zinc oxide thin films, J. Appl. Phys., 104 (2008) 7.

[114] H.B. Liu, Q.Y. Lu, H.P. He, K.W. Wu, S.L. Li, J.Y. Huang, Y.F. Lu, X.H. Pan, Z.Z. Ye, P.K. Chu, Effects of annealing temperature on excitonic emissions from Na-implanted ZnO nanorods, Mater. Lett., 90 (2013) 76-78.

[115] Z. Wang, H.B. Liu, H.P. He, J.Y. Huang, L.X. Chen, Z.Z. Ye, Determination of Na acceptor level in Na+ ion-implanted ZnO single crystal, Appl. Phys. A-Mater. Sci. Process., 118 (2015) 1229-1232.

[116] L. Cai, W. Zhou, F. Ren, J. Chen, G.X. Cai, Y.C. Liu, X.J. Guan, S.H. Shen, W ion implantation boosting visible-light photoelectrochemical water splitting over ZnO nanorod arrays, J. Photonics Energy, 7 (2017) 11.

[117] P.P. Murmu, R.J. Mendelsberg, J. Kennedy, D.A. Carder, B.J. Ruck, A. Markwitz, R.J. Reeves, P. Malar, T. Osipowicz, Structural and photoluminescence properties of Gd implanted ZnO single crystals, J. Appl. Phys., 110 (2011) 6.

[118] F. Otieno, M. Airo, E.G. Njoroge, R. Erasmus, T. Ganetsos, A. Quandt, D. Wamwangi, D.G. Billing, Effect of implantation of Sm+ ions into RF sputtered ZnO thin film, AIP Adv., 9 (2019) 7.

[119] A. Cetin, R. Kibar, K. Ayvacikli, Y. Tuncer, C. Buchal, P.D. Townsend, T. Karali, S. Selvi, N. Can, Optical propel-ties of Tb implantation into ZnO, Surf. Coat. Technol., 201 (2007) 8534-8538.

[120] L. Cai, F. Ren, M. Wang, G.X. Cai, Y.B. Chen, Y.C. Liu, S.H. Shen, L.J. Guo, V ions implanted ZnO nanorod arrays for photoelectrochemical water splitting under visible light, Int. J. Hydrog. Energy, 40 (2015) 1394-1401.

[121] M. Wang, F. Ren, G.X. Cai, Y.C. Liu, S.H. Shen, L.J. Guo, Activating ZnO nanorod photoanodes in visible light by Cu ion implantation, Nano Res., 7 (2014) 353-364.

[122] M. Wang, F. Ren, J. Zhou, G. Cai, L. Cai, Y. Hu, D. Wang, Y. Liu, L. Guo, S. Shen, N Doping to ZnO Nanorods for Photoelectrochemical Water Splitting under Visible Light: Engineered Impurity Distribution and Terraced Band Structure, Scientific Reports, 5 (2015) 12925.

[123] T. Matsuda, M. Furuta, T. Hiramatsu, H. Furuta, T. Hirao, Sheet resistance and crystallinity of Ga- and Al-implanted zinc oxide thin films with postannealing, J. Vac. Sci. Technol. A, 25 (2007) 706-710.

[124] T. Matsuda, M. Furuta, T. Hiramatsu, H. Furuta, T. Hirao, Crystallinity and resistivity of ZnO thin films with indium implantation and postannealing, J. Vac. Sci. Technol. A, 28 (2010) 135-138.

[125] S. Kohiki, M. Nishitani, T. Wada, T. Hirao, ENHANCED CONDUCTIVITY OF ZINC-OXIDE THIN-FILMS BY ION-IMPLANTATION OF HYDROGEN-ATOMS, Appl. Phys. Lett., 64 (1994) 2876-2878.

[126] M. Arita, H. Konishi, K. Matsuda, M. Masuda, Y. Hayashi, Effects of hydrogen introduction on electrical and optical properties of Cd-doped Ge oxide and Zn oxide thin films, Mater. Trans., 43 (2002) 1142-1145.

[127] G.S. Heo, S.J. Hong, J.W. Park, B.H. Choi, J.H. Lee, D.C. Shin, Decrease in work function of boron ion-implanted ZnO thin films, J. Nanosci. Nanotechnol., 7 (2007) 4021-4024.

[128] J. Kennedy, P.P. Murmu, J. Leveneur, G.V.M. Williams, R.L. Moody, T. Maity, S.V. Chong, Enhanced Power Factor and Increased Conductivity of Aluminum Doped Zinc Oxide Thin Films for Thermoelectric Applications, J. Nanosci. Nanotechnol., 18 (2018) 1384-1387.

[129] H. Lee, K. Sivashanmugan, C.Y. Kao, J.D. Liao, Fabrication of highly transparent Al-ion-implanted ZnO thin films by metal vapor vacuum arc method, Jpn. J. Appl. Phys., 56 (2017) 4.

[130] T. Viseu, J.A. de Campos, A.G. Rolo, T. de Lacerda-Aroso, M.F. Cerqueira, E. Alves, ZnO Thin Films Implanted with Al, Sb and P: Optical, Structural and Electrical Characterization, J. Nanosci. Nanotechnol., 9 (2009) 3574-3577.

[131] J. Lee, J. Metson, P.J. Evans, R. Kinsey, D. Bhattacharyya, Implanted ZnO thin films: Microstructure, electrical and electronic properties, Appl. Surf. Sci., 253 (2007) 4317-4321.

[132] S. Kohiki, M. Nishitani, T. Wada, Enhanced electrical conductivity of zinc oxide thin films by ion implantation of gallium, aluminum, and boron atoms, J. Appl. Phys., 75 (1994) 2069-2072.

[133] D. Weissenberger, M. Duerrschnabel, D. Gerthsen, F. Perez-Willard, A. Reiser, G.M. Prinz, M. Feneberg, K. Thonke, R. Sauer, Conductivity of single ZnO nanorods after Ga implantation in a focused-ion-beam system, Appl. Phys. Lett., 91 (2007) 3.

[134] W. Liu, F. Xiu, K. Sun, Y.-H. Xie, K.L. Wang, Y. Wang, J. Zou, Z. Yang, J. Liu, Na-Doped p-Type ZnO Microwires, Journal of the American Chemical Society, 132 (2010) 2498-2499.

[135] M. Jin, Z. Li, F. Huang, Y. Xia, X. Ji, W. Wang, Critical conditions for the formation of p-type ZnO with Li doping, RSC advances, 8 (2018) 30868-30874.

[136] Z.-N. Ng, K.-Y. Chan, S. Muslimin, D. Knipp, P-Type Characteristic of Nitrogen-Doped ZnO Films, Journal of Electronic Materials, 47 (2018) 5607-5613.

[137] X.H. Pan, J. Jiang, Y.J. Zeng, H.P. He, L.P. Zhu, Z.Z. Ye, B.H. Zhao, X.Q. Pan, Electrical and optical properties of phosphorus-doped p-type ZnO films grown by metalorganic chemical vapor deposition, J. Appl. Phys., 103 (2008) 023708.

[138] J. Li, S.-H. Wei, S.-S. Li, J.-B. Xia, Design of shallow acceptors in ZnO: First-principles band-structure calculations, Physical Review B (Condensed Matter and Materials Physics), 74 (2006) 081201.

[139] C.H. Park, S. Zhang, S.-H. Wei, Origin of p-Type Doping Difficulty in ZnO: The Impurity Perspective, Phys. Rev. B, 66 (2002) 073202.

[140] A.N. Georgobiani, A.N. Gruzintsev, V.T. Volkov, M.O. Vorobiev, V.I. Demin, V.A. Dravin, p-Type ZnO : N obtained by ion implantation of nitrogen with post-implantation annealing in oxygen radicals, Nucl. Instrum. Methods Phys. Res. Sect. A-Accel. Spectrom. Dect. Assoc. Equip., 514 (2003) 117-121.

[141] M.A. Myers, M.T. Myers, M.J. General, J.H. Lee, L. Shao, H. Wang, P-type ZnO thin films achieved by N+ ion implantation through dynamic annealing process, Appl. Phys. Lett., 101 (2012) 5.

[142] Z. Huang, H.B. Ruan, H. Zhang, D.P. Shi, W.J. Li, G.P. Qin, F. Wu, L. Fang, C.Y. Kong, Conversion mechanism of conductivity and properties of nitrogen implanted ZnO single crystals induced by post-annealing, J. Mater. Sci.-Mater. Electron., 30 (2019) 4555-4561.

[143] A. Kumar, S. Keshri, B. Pandey, J.B.M. Krishna, D. Das, Impact of N5+ ion implantation on optical and electrical properties of polycrystalline ZnO film, Radiat. Eff. Defects Solids, 169 (2014) 965-979.

[144] C.C. Lin, S.Y. Chen, S.Y. Cheng, H.Y. Lee, Properties of nitrogen-implanted p-type ZnO films grown on Si3N4/Si by radio-frequency magnetron sputtering, Appl. Phys. Lett., 84 (2004) 5040-5042.

[145] Y.J. Zeng, Z.Z. Ye, W.Z. Xu, B. Liu, Y. Che, L.P. Zhu, B.H. Zhao, Study on the Hall-effect and photoluminescence of N-doped p-type ZnO thin films, Mater. Lett., 61 (2007) 41-44.

[146] J.G. Reynolds, C.L.R. Jr., A. Mohanta, J.F. Muth, J.E. Rowe, H.O. Everitt, D.E. Aspnes, Shallow acceptor complexes in p-type ZnO, Appl. Phys. Lett., 102 (2013) 152114.

[147] J.L. Lyons, A. Janotti, C.G.V.d. Walle, Why nitrogen cannot lead to p-type conductivity in ZnO, Appl. Phys. Lett., 95 (2009) 252105.

[148] J.E. Stehr, S.L. Chen, W.M. Chen, L. Cai, S. Shen, I.A. Buyanova, Identification of a Nitrogen-related acceptor in ZnO nanowires, Nanoscale, 11 (2019) 10921-10926.

[149] L. Liu, J. Xu, D. Wang, M. Jiang, S.-p. Wang, B. Li, Z. Zhang, D. Zhao, C.-X. Shan, B. Yao, D. Shen, p-Type conductivity in N-doped ZnO: the role of the N(Zn)-V(O) complex, Physical Review Letters, 108 (2012) 215501.

[150] W. Li, H. Zhang, X. Zhang, G. Qin, H. Li, Y. Xiong, L. Ye, H. Ruan, C. Tong, C. Kong, L. Fang, Non-axial NO-VZn shallow acceptor complexes in nitrogen implanted p-type ZnO thin films, Appl. Surf. Sci., 529 (2020) 147168.

[151] M.N. Amini, R. Saniz, D. Lamoen, B. Partoens, The role of the VZn–NO–H complex in the p-type conductivity in ZnO, Physical Chemistry Chemical Physics, 17 (2015) 5485-5489.

[152] A. Das, D. Basak, Interplay of defects in low energy nitrogen implanted ZnO nanorods, Appl. Surf. Sci., 564 (2021) 150424.

[153] W. Li, C. Wang, J. Ma, H. Zhang, Y. Xiong, H. Li, L. Ye, H. Ruan, G. Qin, L. Fang, C. Kong, Effect of thermal evolution of point defects on the electrical properties of nitrogen-implanted ZnO thin films, Journal of Materials Science: Materials in Electronics, 31 (2020) 4208-4213.

[154] M. Schmidt, M. Ellguth, F. Schmidt, T. Lüder, H.v. Wenckstern, R. Pickenhain, M. Grundmann, G. Brauer, W. Skorupa, Defects in a nitrogen-implanted ZnO thin film, physica status solidi (b), 247 (2010) 1220-1226.

[155] C.H. Kwak, Y.B. Lee, S.Y. Seo, S.H. Kim, C.I. Park, B.H. Kim, D.W. Jeong, J.J. Kim, Z. Jin, S.W. Han, Structural and electrical properties of nitrogen-ion implanted ZnO nanorods, Curr. Appl. Phys., 11 (2011) S328-S332.

[156] W.J. Li, C.N. Wang, J.W. Ma, H. Zhang, Y.Q. Xiong, H.L. Li, L.J. Ye, H.B. Ruan, G.P. Qin, L. Fang, C.Y. Kong, Effect of thermal evolution of point defects on the electrical properties of nitrogen-implanted ZnO thin films, J. Mater. Sci.-Mater. Electron., 31 (2020) 4208-4213.

[157] M. Ying, S. Wang, T. Duan, B. Liao, X. Zhang, Z. Mei, X. Du, F.M. Gerriu, A.M. Fox, G.A. Gehring, The structure, optical and magnetic properties of arsenic implanted ZnO films prepared by molecular beam epitaxy, Mater. Lett., 171 (2016) 121-124.

[158] H.H. Wang, M.Y. Yuan, Effect of doping concentration on point defect structure in As-implanted ZnO, Solid State Commun., 261 (2017) 41-45.

[159] G. Braunstein, A. Muraviev, H. Saxena, N. Dhere, V. Richter, R. Kalish, p type doping of zinc oxide by arsenic ion implantation, Appl. Phys. Lett., 87 (2005) 3.

[160] W.-J. Lee, J. Kang, K.-J. Chang, Defect properties and p-type doping efficiency in phosphorus-doped ZnO, Physical Review B, 73 (2006) 024117.

[161] P. Li, S.-H. Deng, J. Huang, First-principles studies on the dominant acceptor and the activation mechanism of phosphorus-doped ZnO, Appl. Phys. Lett., 99 (2011) 111902.

[162] W.J. Lee, J. Kang, K.J. Chang, The origin of p-type conductivity in P-doped ZnO, Journal of the Korean Physical Society, 50 (2007) 602-607.

[163] B. Panigrahy, D. Bahadur, p-type Phosphorus doped ZnO nanostructures: an electrical, optical, and magnetic properties study, RSC Advances, 2 (2012) 6222-6227.

[164] F.X. Xiu, Z. Yang, L.J. Mandalapu, J.L. Liu, Donor and acceptor competitions in phosphorus-doped ZnO, Appl. Phys. Lett., 88 (2006) 152116.

[165] V. Vaithianathan, S. Hishita, J.Y. Park, S.S. Kim, Photoluminescence in phosphorous-implanted ZnO films, J. Appl. Phys., 102 (2007) 086107.

[166] H. Xie, T. Liu, J. Liu, K. Cao, Z. Dong, J. Yang, Y. Zhao, Implantation induced defects and electrical properties of Sb-implanted ZnO, Science China Technological Sciences, 58 (2015) 1333-1338.

[167] S. Millesi, M.R. Catalano, G. Impellizzeri, I. Crupi, G. Malandrino, F. Priolo, A. Gulino, Sb-implanted ZnO ultra-thin films, Materials Science in Semiconductor Processing, 69 (2017) 32-35.

[168] J. Ayres de Campos, T. Viseu, A.G. Rolo, N. Barradas, E. Alves, T. de Lacerda-Arôso, M. Cerqueira, Electrical and Raman scattering studies of ZnO: P and ZnO: Sb thin films, Journal of nanoscience nanotechnology, 10 (2010) 2620-2623.

[169] Z.Y. Zhang, J.Y. Huang, S.S. Chen, X.H. Pan, L.X. Chen, Z.Z. Ye, P-type single-crystalline ZnO films obtained by (N,O) dual implantation through dynamic annealing process, Superlattices Microstruct., 100 (2016) 468-473.

[170] Z.Y. Zhang, J.Y. Huang, S.S. Chen, X.H. Pan, L.X. Chen, Z.Z. Ye, P-type single-crystalline ZnO films obtained by (Li, N) dual implantation through dynamic annealing process, J. Mater. Sci.-Mater. Electron., 28 (2017) 16215-16219.

[171] Z.Y. Zhang, J.Y. Huang, S.S. Chen, X.H. Pan, L.X. Chen, Z.Z. Ye, P-type single-crystalline ZnO films obtained by (Na,N) dual implantation through dynamic annealing process, J. Cryst. Growth, 483 (2018) 236-240.

[172] Y.T. Chuang, J.W. Liou, W.Y. Woon, Formation of p-type ZnO thin film through co-implantation, Nanotechnology, 28 (2017) 7.

[173] M.A. Desai, A.N. Vyas, G.D. Saratale, S.D. Sartale, Zinc oxide superstructures: recent synthesis approaches and application for hydrogen production via photoelectrochemical water splitting, Int. J. Hydrog. Energy, 44 (2019) 2091-2127.

[174] S.B.A. Hamid, S.J. Teh, C.W. Lai, Photocatalytic water oxidation on ZnO: a review, Catalysts, 7 (2017) 93.

[175] C.-F. Liu, Y.-J. Lu, C.-C. Hu, Effects of Anions and pH on the Stability of ZnO Nanorods for Photoelectrochemical Water Splitting, ACS Omega, 3 (2018) 3429-3439.

[176] A.L. Rudd, C.B. Breslin, Photo-induced dissolution of zinc in alkaline solutions, Electrochimica acta, 45 (2000) 1571-1579.

[177] R. Sapkal, S. Shinde, T. Waghmode, S. Govindwar, K. Rajpure, C. Bhosale, Photo-corrosion inhibition and photoactivity enhancement with tailored zinc oxide thin films, Journal of Photochemistry Photobiology B: Biology, 110 (2012) 15-21.

[178] A.A. Aboud, M. Shaban, N. Revaprasadu, Effect of Cu, Ni and Pb doping on the photo-electrochemical activity of ZnO thin films, RSC advances, 9 (2019) 7729-7736.

[179] M. Samadi, M. Zirak, A. Naseri, E. Khorashadizade, A.Z. Moshfegh, Recent progress on doped ZnO nanostructures for visible-light photocatalysis, Thin Solid Films, 605 (2016) 2-19.

[180] D.-K. Kwon, Y. Porte, J.-M. Myoung, Fabrication of ZnO nanorods p–n homojunction light-emitting diodes using Ag film as self-doping source for p-type ZnO nanorods, The Journal of Physical Chemistry C, 122 (2018) 11993-12001.

[181] G.C. Park, S.M. Hwang, S.M. Lee, J.H. Choi, K.M. Song, H.Y. Kim, H.-S. Kim, S.-J. Eum, S.-B. Jung, J.H. Lim, Hydrothermally grown in-doped ZnO nanorods on p-GaN films for color-tunable heterojunction light-emitting-diodes, Scientific reports, 5 (2015) 1-10.

[182] Y. Zhang, L. Ge, M. Li, M. Yan, S. Ge, J. Yu, X. Song, B. Cao, Flexible paper-based ZnO nanorod light-emitting diodes induced multiplexed photoelectrochemical immunoassay, Chemical Communications, 50 (2014) 1417-1419.

[183] C. Zhang, Y. Qiu, W. Liu, H. Xu, L. Yang, C. Wang, Y. Liu, Improved near-UV electroluminescence of ZnO nanorod array LEDs by coupling with a graphene plasmon layer, Nanophotonics, 8 (2019) 2203-2213.

[184] Y. Yang, X.W. Sun, B.K. Tay, G.F. You, S.T. Tan, K.L. Teo, A p-n homojunction ZnO nanorod light-emitting diode formed by As ion implantation, Appl. Phys. Lett., 93 (2008) 3.

[185] X.W. Sun, B. Ling, J.L. Zhao, S.T. Tan, Y. Yang, Y.Q. Shen, Z.L. Dong, X.C. Li, Ultraviolet emission from a ZnO rod homojunction light-emitting diode, Appl. Phys. Lett., 95 (2009) 3.

CHAPTER-3

Experimental methods: Growth and characterization techniques of ZnO nanostructures

3.1 Introduction

This chapter presents an overview of the key experimental growth and characterization techniques used in this thesis work. The first two sections are devoted to sample preparation, while the rest are characterization techniques. The latter is arranged from structural, microstructural, morphological, compositional, optical, and lastly electrical techniques, respectively.

3.2 Growth of ZnO nanostructures

There are basically two categories of the growth techniques of ZnO nanostructures: (1) physical vapor deposition (PVD) and (2) chemical solution deposition. The chemical solution growth techniques have better control over the morphology and optical properties of ZnO nanostructures besides the advantages of large-scale fabrication. Moreover, the chemical solution deposition is a low-cost fabrication method. Keeping in mind these issues, in this thesis work, two chemical solution growth techniques namely sol-gel and aqueous chemical growth (ACG) have been used to synthesize the nanostructured ZnO. In the subsequent sections, these two methods have been described in details.

3.2.1 Sol-gel

Sol-gel synthesis is a very well-known wet chemical technique to synthesize metal oxide nanostructures [1, 2]. Basically, nanoparticle thin films are grown by this method. Here, a colloidal solution of metal-salt (known as 'sol') is taken as a precursor that can produce an integrated network (known as 'gel') of either discrete particles or network polymers. The mechanism of sol-gel processing follows four basic steps: the formation of the sol, gelation, drying, and annealing. The sol is basically a colloidal dispersion of very small particles of suitable precursors such as metal alkoxides salts some metal salts (like chlorides, nitrates, and acetates). To improve the stability of the precursor sol some chelating agents such as diethanolamine (DEA) and monoethanolamine (MEA) are used. In a typical sol-gel process the precursor is subjected to the following hydrolysis and polycondensation reactions.

$$M - X + H_2O \rightarrow M - OH + HX \ldots\ldots\ldots\ldots\ldots\ldots\ldots\ldots\ldots (3.1)$$
$$M - OH + X - M \rightarrow M - O - M + HX \ldots\ldots\ldots\ldots\ldots\ldots (3.2)$$
$$M - OH + HO - M \rightarrow M - O - M + H_2O \ldots\ldots\ldots\ldots\ldots.. (3.3)$$
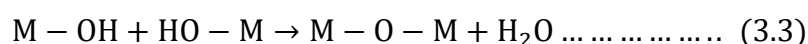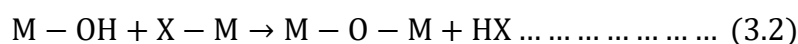
Here, M = metal or Si, X = reactive ligands like halogen, O-R, NR$_2$, acetate etc. The eqn. (3.1) represents the hydrolysis reaction and both eqn. (3.2) and eqn. (3.3) represent the condensation process. For a multi-component system, the hydrolysis rate depends on the type of precursor and thus metal hydroxides are produced at different rates which in turn control the condensation reactions. Metal hydroxides react further to produce metal oxide particles. In proper chemical and the thermal environment, these metal oxide particles create a three-dimensional continuous network which is known as gel. Finally drying of the gel is carried out in an oven so that the pore volume collapses as a result of the viscous flow of the gel network. This gel is deposited on the substrates to form the films. These films are annealed at high temperature to remove the chelating agent as well as the organic residue and finally the metal oxide films are produced. There are different types of coating techniques to form the sol-gel films. These are:

(i) **Dip coating**: This is the technique where ultrasonically cleaned substrates are immersed in the sol and then withdrawn at a particular rate under the specified temperature and atmospheric conditions. The thickness of the film can be regulated by varying the withdrawal speed, sol concentration, viscosity of the solvent, and number of dipping.

(ii) **Drain coating**: Here, the cleaned substrates are kept stationary and the sol is passed through the substrates and consequently drained out through an outlet. Here also, the thickness can be controlled by changing of sol flow, flow rate, viscosity, the surface tension of the sol, sol concentration, and the atmospheric condition around the substrate.

(iii) **Spin coating**: This is the most popular and widely used technique where the substrate is kept on a holder which can rotate at a certain rotation per minute (RPM) around an axis perpendicular to the substrate surface. The substrate surface is completely rinsed with few drops of the sol and rotated at required speed for few seconds and then subsequently annealed. Rotation speed, number of coatings, viscosity, and concentration of the sol determine the film thickness. There are some other techniques such as spray coating, capillary coating and roll coating which are mainly used in industries for large area coating.

In this thesis work, ZnO thin films have been prepared using sol-gel spin coating method on soda-lime glass substrates cleaned thoroughly by ultrasonication using chromic solution, de-ionized water, HCl, KOH solution, acetone, and methanol sequentially. ZnO sol of concentration 0.1 M was first prepared by adding the required amount of zinc acetate-2-hydrate [(CH$_3$COO)$_2$Zn·2H$_2$O] with dehydrated isopropyl alcohol containing DEA as a sol stabilizer followed by a thorough mixing at RT for 2 h using a magnetic stirrer, and then the sol was kept for 48 h for aging. Next, the cleaned substrates were spin coated with the aged sol

at 2500 rpm repeatedly. After each coating process, the films were first dried at 120 °C for 10 minutes in hot oven and then annealed at 500 °C in a furnace for another 30 minutes to get crystalline ZnO films. This process of coating and subsequent heat treatment was repeated exactly similar way for 20 times to achieve the desired thickness of the films. The entire process can be summarized by the following schematic diagram in Fig. 3.1. The sin coating unit (Apex instruments, model: spinNXG-P1) used for this present thesis work is shown in Fig. 3.2.
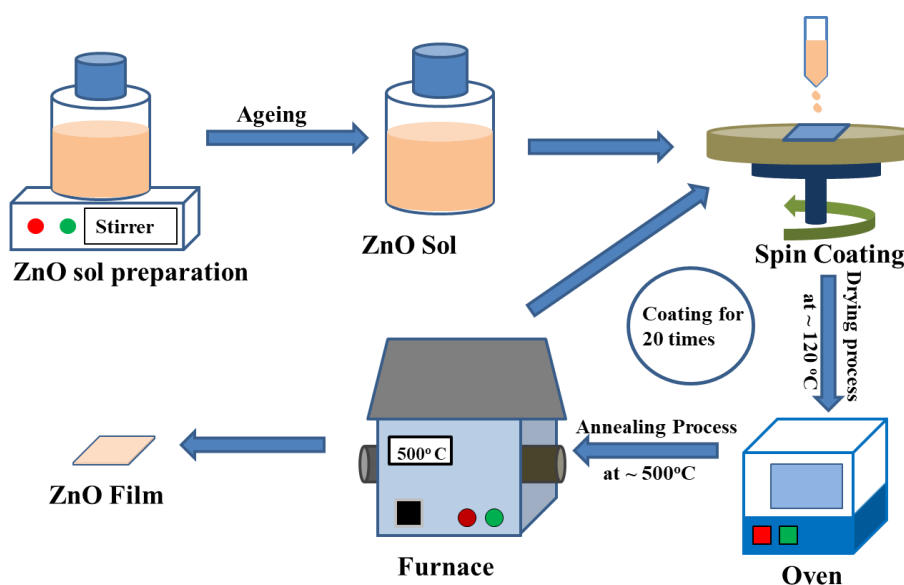
Fig. 3.1 Schematic diagram of sol-get spin coating process for ZnO thin film deposition.
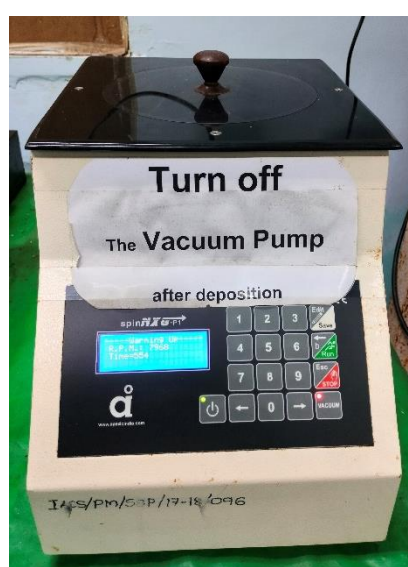
Fig. 3.2 Digital image of sol-gel spin coating unit (Apex instruments, model: spinNXG-P1).

3.2.2 Aqueous chemical growth (ACG)

Aqueous chemical growth of ZnO NRs is a simple but most popular and versatile synthesis technique to obtain highly aligned, vertically oriented nanostructures with excellent crystallinity [3, 4], which has been used in this thesis work. The chemical reactions in ACG method are carried out at ambient pressure and in aqueous medium. Here, the cleaned glass substrates were spin coated by 0.1 M solution of $(CH_3COOH)_2Zn \cdot 2H_2O$ to obtain seed layer of ZnO of a desired thickness. Then, the ZnO seeded substrates were immersed into a mixed aqueous solution of $(CH_3COO)_2Zn \cdot 2H_2O$ (20 mM) and hexamethylenetetramine $((CH_2)_6N_4)$ (20 mM) in a beaker, which was kept at 80 °C for 1 h for growing ZnO NRs on the substrates. The substrate containing ZnO NRs were then removed from the solution, rinsed in de-ionized water and dried. The reaction mechanism can be understood by following equations.

$$(CH_2)_6N_4 + 6H_2O \leftrightarrow 6HCHO + 4NH_3 \dots \dots \dots \dots (3.4)$$
$$NH_3 + H_2O \leftrightarrow NH_4{}^+ + OH^- \dots \dots \dots \dots \dots \dots \dots (3.5)$$
$$Zn^+ + 2OH^- \rightarrow ZnO\ (s) + H_2O \dots \dots \dots \dots \dots \dots \dots (3.6)$$
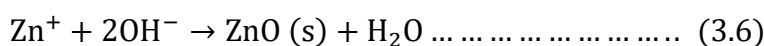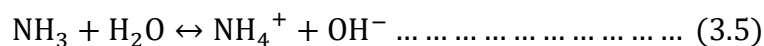
The particular experimental details of the ACG method used for this thesis have been described in the respective chapters.

3.2.3 Other techniques

Apart from the above discussed methods, there are several techniques to synthesize ZnO nanostructures. Among them, Hydrothermal method is very popular method for growing 1D ZnO NRs [5, 6]. This method is nearly similar to ACG except that a higher pressure than the ambient is maintained during the reaction. Various PVD methods are taken for the deposition of high quality ZnO thin films. In this method, the material undergoes from a condensed phase to a vapor phase and then comes back to the condensed phase again and form thin films. The most common PVD methods are sputtering [7, 8], pulsed laser deposition [9, 10], molecular beam epitaxy [11, 12].

3.3 Post-growth doping: Ion implantation

This section is based on the references by Campbell [13] and Morgan [14]. The ion implantation equipment generally comprises of a source of ion, an accelerator, a mass spectrometer, and a target chamber. Fig. 3.3 illustrates the basic elements required for an ion

implantation setup. Ions are made from a feed gas, or vapor from a solid source, by running it through a voltage difference, making a plasma. The ions are then accelerated into the apparatus with an even higher voltage difference. Thereafter, a mass spectrometer is employed at the bend in the setup to separate the incoming ions, only letting the ones with the right velocity, mass and charge. It is even possible to separate different isotopes of the ion. Finally, the ion beam is focused by the electromagnetic lenses over the target mounted on a sample holder.
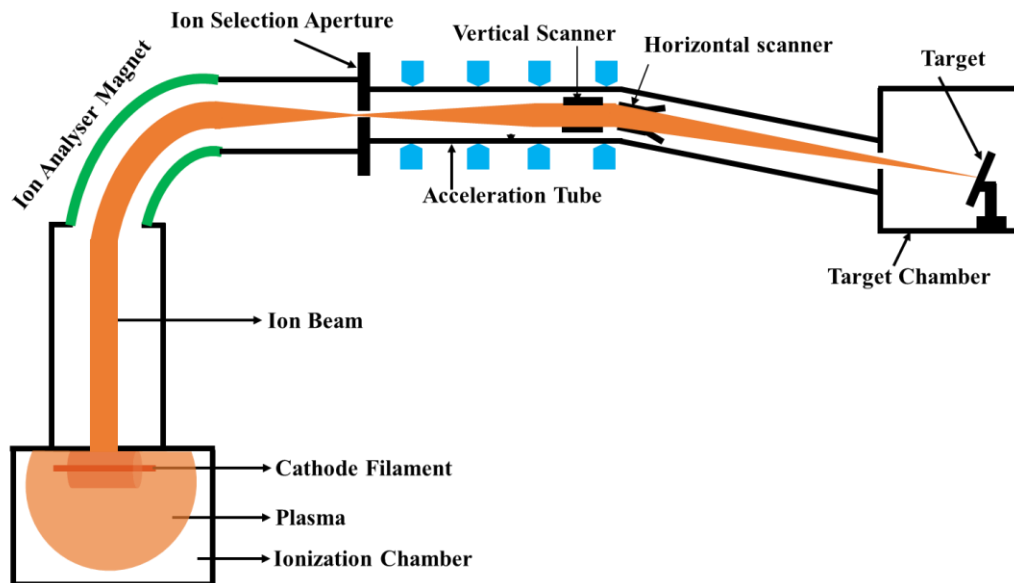
Fig. 3.3 Schematic diagram of an ion implanter.

Fig. 3.4 Digital image of the implantation unit of LEIBF at IUAC, New Delhi.

In this thesis work, the as-grown ZnO nanoparticle thin films as well as 1D NRs were implanted with various ions (both the positive and negative ions) using the low energy ion beam facility (LEIBF) at Inter-University Accelerator Centre (IUAC), New Delhi. The particular experimental details of each implantation have been described in the respective chapters. The digital image of the implantation unit installed at LEIBF is shown in Fig. 3.4.

3.4   Characterization techniques

3.4.1   Simulation of ion implantation: SRIM

To predict the ion distributions, energy loss, vacancy distributions and other implantation parameters inside the ion implanted ZnO nanostructures, SRIM-2008 simulation code has been used in this thesis work. The basics of the SRIM have been discussed in the chapter 2 already. The particular simulation details of each ion implantation have been described in the respective chapters.

3.4.2   X-ray diffractometry (XRD)

XRD is one of the most important structural characterization tools to determine the crystal structure, crystal phase, lattice parameter, grain size and some other physical properties of the thin film or powder materials using X-ray of the wavelength of atomic distance (~Å) [15, 16]. This technique basically collects the diffracted X-ray beam intensity as a function of the incident or scattered angle that is getting reflected from the sample of interest, which is shown by a schematic diagram in Fig. 3.5
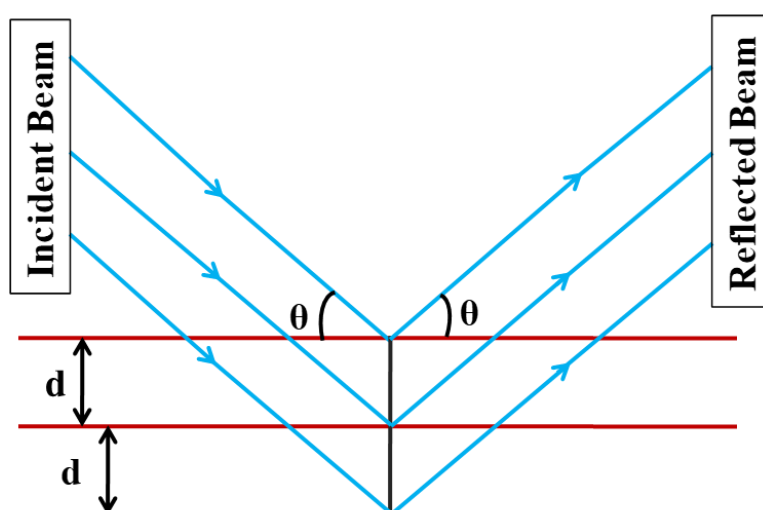
Fig. 3.5 Schematic diagram of XRD.

The basic principle of XRD follows Bragg's law of diffraction (eqn.3.7) [17].

$$2d\sin\theta = n\lambda \ldots \ldots \ldots \ldots \ldots \ldots \ldots \ldots \ldots \quad (3.7)$$

where n = 1, 2, 3……..., d is the spacing between the crystal planes, and λ is the wavelength of the X-ray. According to Bragg's law of diffraction, solid crystals are consisting of parallel sets of planes where atoms are arranged in a periodic manner. When X-rays are incident on a solid crystal at an angle θ with respect to the crystal plane, they are reflected from the crystal plane. These reflected rays produce a diffraction pattern and the diffracted rays are detected as a function of angle (2θ) as shown in the above schematic diagram in the Fig. 3.5. Comparing the peak positions (or 2θ values) of the recorded diffraction pattern with the standard joint committee on powder diffraction standards (JCPDS) data file, one can identify the structure of the sample and the reflection planes. Lattice parameters for example, 'a' (a-axis length) and 'c' (c-axis length) can be calculated by applying the standard equations. For a hexagonal wurtzite crystal structure, the equation can be written as:

$$\sin^2\theta = \frac{\lambda^2}{4}\left[\frac{4}{3}\cdot\frac{(h^2 + hk + l^2)}{a^2} + \frac{l^2}{c^2}\right] \ldots \ldots \ldots. (3.8)$$

where h, k, l are the Miller indices of the corresponding plane from where the diffraction occurs. The full width at half maximum (FWHM) value (β) of a certain XRD peak gives an idea about the crystalline quality of the thin film, where the smaller β value indicates better crystalline quality. An estimation of the average crystallite size (D) can be made using the following Scherrer equation [18]:

$$D = \frac{k\lambda}{\beta\cos\theta} \ldots \ldots \ldots \ldots \ldots \ldots \ldots \ldots \ldots. . \ldots \ldots \quad (3.9)$$

where, k is the shape factor determined by the geometry of the crystallites. The value of k is generally taken as 0.94. By knowing the value of D, the dislocation density (δ) in the material can be calculated by the following equation.

$$\delta = \frac{1}{D^2} \ldots \ldots \ldots \ldots \ldots \ldots \ldots \ldots \ldots \ldots. . \ldots \quad (3.10)$$

The dislocation density is a measure of the number of dislocations in a unit volume of a crystalline material. In this thesis work, the structural characterization of unimplanted and implanted ZnO NRs was carried out by Rigaku Smart Lab X-ray diffractometer (Fig. 3.6) using Cu K_α radiation of $\lambda = 1.5406$ Å. On the other hand, for the nanoparticle thin films, XRD was executed at Indian beamline (BL-18B), Photon Factory, Japan using the synchrotron radiation of $\lambda = 0.7749$ Å.
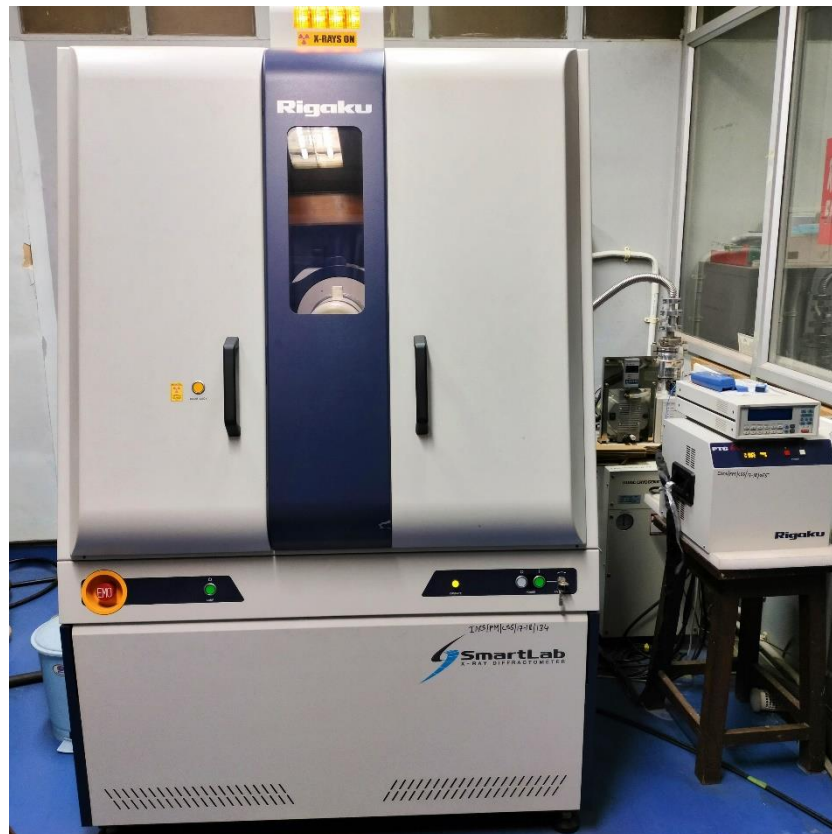
Fig. 3.6 Digital image of Rigaku Smart Lab X-ray diffractometer.

3.4.3   Scanning electron microscopy (SEM)

The microstructure and morphology of the nanostructure thin films are characterized by SEM [19, 20]. The working principle of the SEM is equivalent to an optical microscope where the electron beam is used instead of light. As the wavelength of an electron is much shorter than that of wavelength of visible light (photon), electron microscopes have a higher resolving power than optical microscopes and can reveal the structure of smaller objects, which has been described by a schematic diagram in Fig. 3.7.
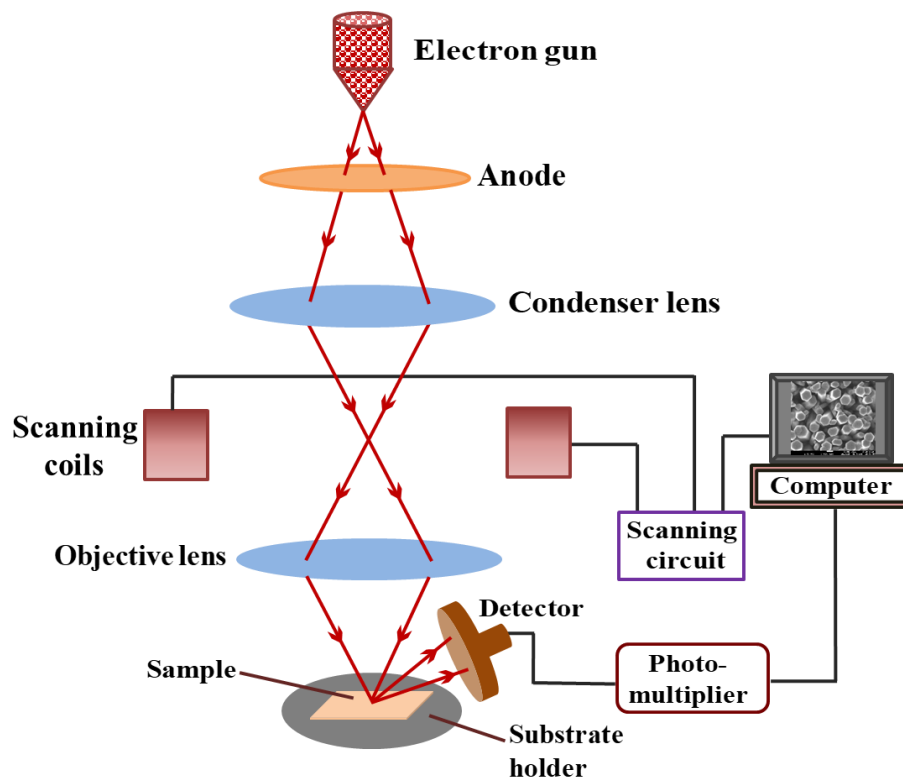
Fig. 3.7 Schematic diagram of SEM.

In a SEM setup, the electron beam is produced at the top of the microscope by heating a metal-filament known as electron gun. The electrons having typically an energy ranging from 0.2 keV to 40 keV follow a vertical path consists of a number of electromagnetic condenser lenses and scanning coils. As the electrons' beam hits the sample, various types of electrons (such as secondary electrons, reflected or back-scattered electrons, characteristic X-rays, transmitted electrons, etc.) are ejected from the sample. Mainly back-scattered and secondary electrons are collected by the detector that converts them to a signal which is sent to the viewing screen for producing an image. The secondary electrons basically provide the morphology and topography of the samples while the contrasts in the composition of multiphase samples are offered by the back-scattered electrons. It has been found that a field-emission cathode in the electron gun of an SEM (often called FESEM) provides narrower probing beam at low as well as high electron energy which can provide an improved spatial resolution as well as highest possible magnification. Use of field-emission cathode can also trim downs the possibility of sample charging which sometime may damage the sample. Sometimes an additional arrangement is attached to the FESEM for energy dispersive X-ray spectroscopy (EDS)

analysis. The elemental composition of the material for all elements with atomic number greater than B can be recognized using EDS analysis. This depends on the generation of the X-ray fluorescence from the atoms which are struck by the scanning beam. The X-ray photon is a characteristic of the element from which it is produced. These photons are collected and analyzed to identify the element. Fig. 3.8 shows the digital image of the FESEM instrument (JEOL, model: JSM-7500F) used in this thesis work.

Fig. 3.8 Digital image of FESEM instrument (JEOL, model: JSM-7500F).

3.4.4 Transmission electron microscopy (TEM)

Transmission electron microscopy (TEM) is popularly used for the microstructural and morphological characterizations of any material [21, 22]. In TEM, the electron beam is produced from a tungsten filament, or a lanthanum hexaboride source by thermionic or field emission technique. Then the electrons are accelerated to the specimen by an electric field of the order of 100 kV to 1000 kV which means that the corresponding wavelengths are of the order of 0.04 Å to 0.008 Å. When this high energy electron beam is passed through the ultrathin dispersion of the specimen on Cu grid, the intensity of the transmitted electron beam is spatially distributed. From the spatial distribution of the intensity of the transmitted electron beam,

images are formed. The operating principle of TEM can be described with the help of a schematic diagram shown in Fig. 3.9.
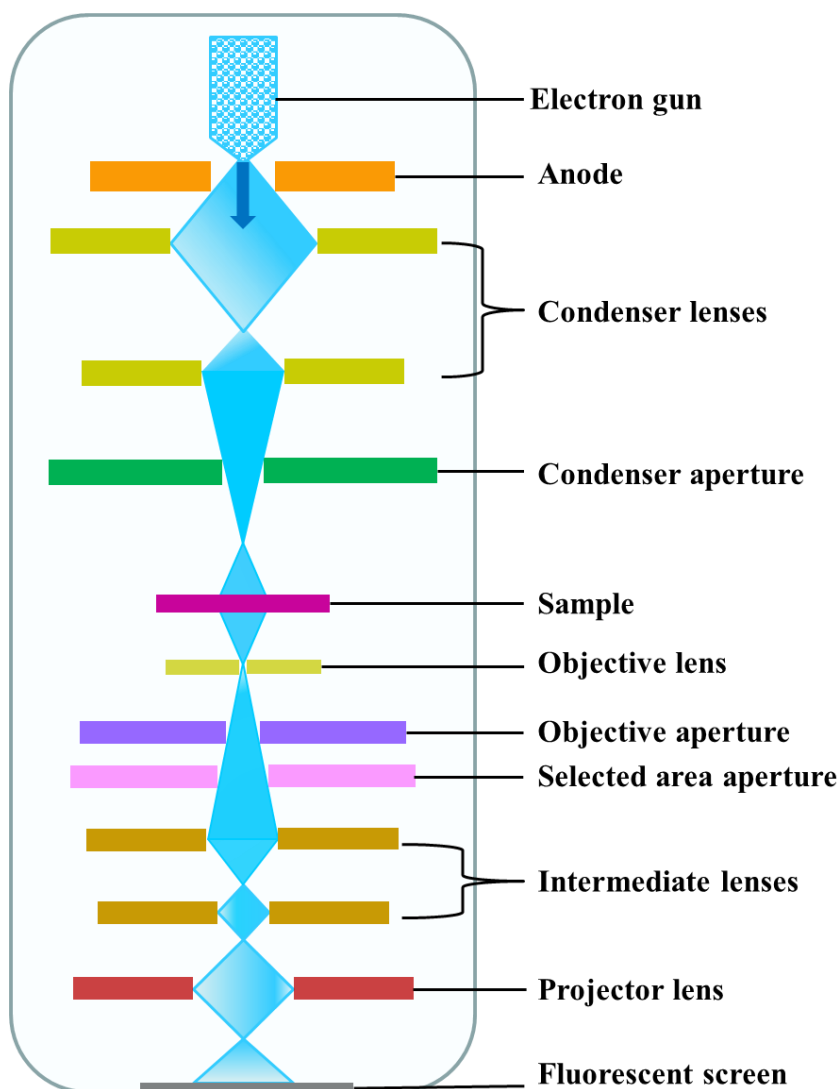
Fig. 3.9 Schematic diagram of TEM.

As shown in the above schematic diagram (Fig. 3.9), there are essentially three types of lenses used to form the final image in the TEM. These are condenser, objective, and projector lenses. The main function of condenser lens is to concentrate and focus the beam of electrons coming of the filament on to the sample for uniform illumination. The objective lens and its associated pole pieces are the heart of the TEM and the most critical of all the lenses. It forms the initial enlarged image of the illuminated portion of the specimen in a plane that is suitable for further enlargement. Finally, the projector lens is used to project the final magnified image onto a fluorescent screen. Thus, the total magnification is a product of the objective and projector

magnifications. The magnification of a TEM image depends on the ratio of the distances between the specimen and the objective lens' image plane. The most general mode of TEM operation is the bright field imaging mode. There is another mode for TEM imaging, which is called dark field mode. However, in both modes, the constructive and destructive interferences between the scattered beams provide an image with a periodicity related to the inter-planer spacing, d, of the specimen. The fringes in the image must match to an array of spots in the diffraction pattern of the specimen and can be related to each other via Fast-Fourier-transformation. Similar to the way that the diffraction spot does not have any direct relation with the position of atom in the specimen, the lattice fringes are not the direct image of the structure, but give the lattice spacing information. Selected area diffraction pattern can be used to recognize crystal structures and to observe the crystal defects. The digital image of High-Resolution Transmission electron microscopy (HRTEM) setup (model JEOL_JEM – 2010) used for this thesis work is shown in Fig. 3.10.

Fig. 3.10 Digital image of TEM instrument (model JEOL_JEM – 2010).

3.4.5   Atomic force microscopy (AFM)

Atomic force microscopy (AFM) is another tool for the microstructure and morphology analyses of the thin films of any material [23, 24]. It is a very high-resolution scanning probe microscopy with resolution in the order of fractions of nm, which is more than 1000 times better compared to the optical diffraction limit. The basic working principle of AFM is shown by a schematic diagram in Fig. 3.11.
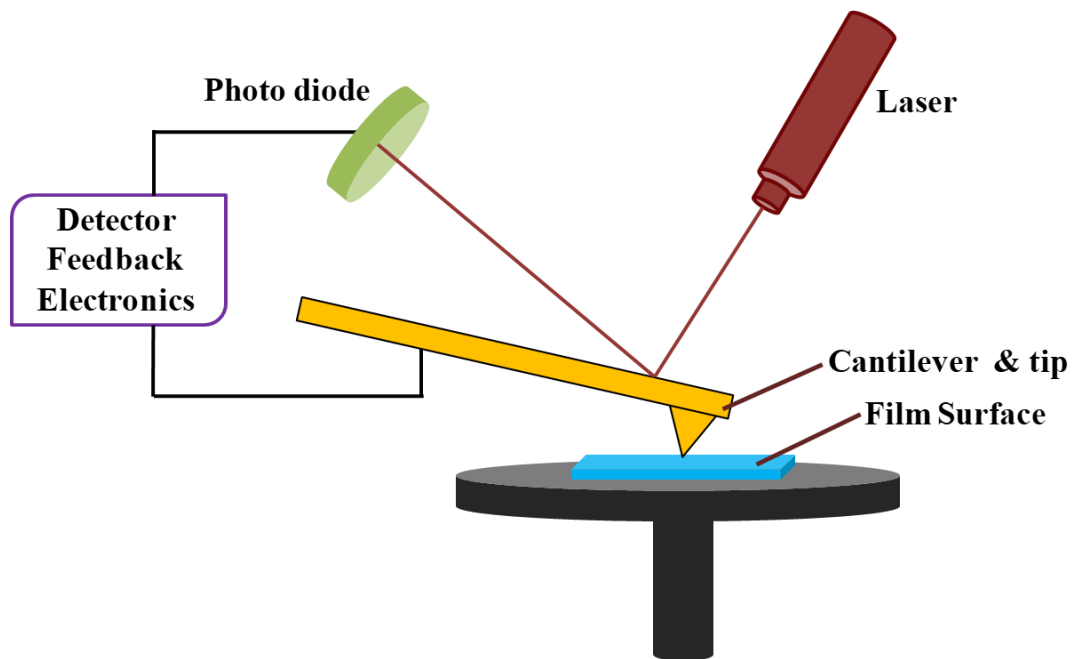
Fig. 3.11 Schematic diagram of AFM.

It operates by measuring the force between a probe that includes a sharp tip of approximately 10-20 nm in diameter, mounted on a micromachined cantilever and the sample surface. As the tip scans the surface, the inter-atomic forces between the tip and the sample surface induce a displacement of the tip that bends the cantilever which is then measured using a laser beam that gets reflected from the moving cantilever. A position-sensitive detector is used to sense the reflected laser beam which then feeds to a computer to process the data that provide a topographical image of the surface with atomic range resolution. Generally, an AFM is operated in two basic modes: contact and tapping mode. In the contact mode, the AFM tip is in continuous contact with the sample surface, while in the tapping mode, the AFM cantilever is vibrated above the sample surface in such a way that the tip is only in alternating contact with the sample surface. This process is quite helpful to reduce the shear forces associated with

the tip movement. The tapping mode is normally used for AFM imaging. The contact mode is used for some specific applications, such as force curve measurements. On the variety of the sample surfaces, the AFM is used to image and manipulate atoms and structures. The tip senses the individual atoms on the underlying sample surface. A position-sensitive detector is used to sense the reflected signal from sample surfaces, which provides a topographical image of the sample surface by computing processing with atomic range resolution. The digital image of the AFM instrument (VEECO, model: diCP-II) used for this thesis work is shown in Fig. 3.12.
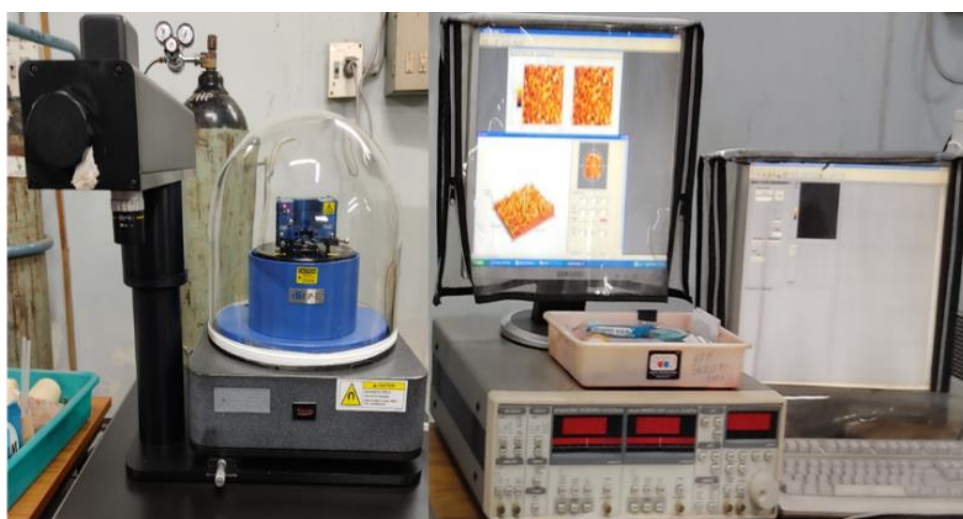
Fig. 3.12 Digital image of AFM instrument (VEECO, model: diCP-II).

3.4.6 X-ray photoelectron spectroscopy (XPS)

XPS identifies the elemental composition along with the chemical and electronic states of any material [25-27]. The working principle of XPS is based on the photoelectric effect. Each atom on the surface of a material has core electron with the characteristic binding energy (E_b) ideally equal to the ionization energy of that electron. When the monochromatic X-ray falls on the sample, the energy of the X-ray photon (hv) is completely absorbed by the core electron of the surface atom. If the incoming photon energy is more than E_b of the core electron, then it will escape from the atom as well as the surface with some kinetic energy (E_k). The kinetic energy of the core electron can be determined using the famous Einstein photoelectric equation:

$$E_k = h\nu - E_b - \varphi \dots \dots \dots \dots \dots \dots \dots \dots \quad (3.11)$$

where φ is the work function of the material induced by the analyzer. This basic working principle of XPS is shown by a schematic diagram in Fig. 3.13.
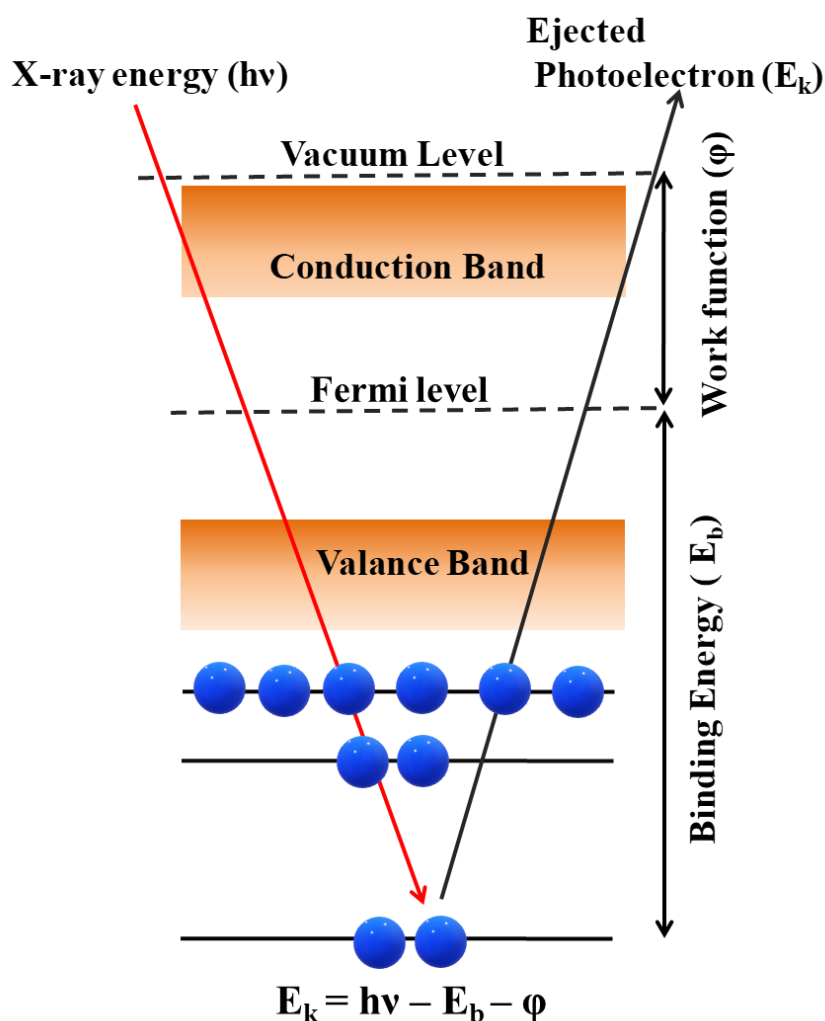
Fig. 3.13 Schematic diagram of XPS.

The constituent element, chemical bonding, and quantitative amount of an element can be determined from the peak shape, exact peak position, and intensity of a photoelectron peak. As the tool is surface sensitive, it only provides information of elemental composition of the top 80-100 Å of the sample surface [27] because electron below this depth cannot reach outside of the surface due to collision with the atoms and electrons lying above them. Fig. 3.14 shows a digital image of the XPS instrument (Omicron, serial no: 0571) used in this thesis work.
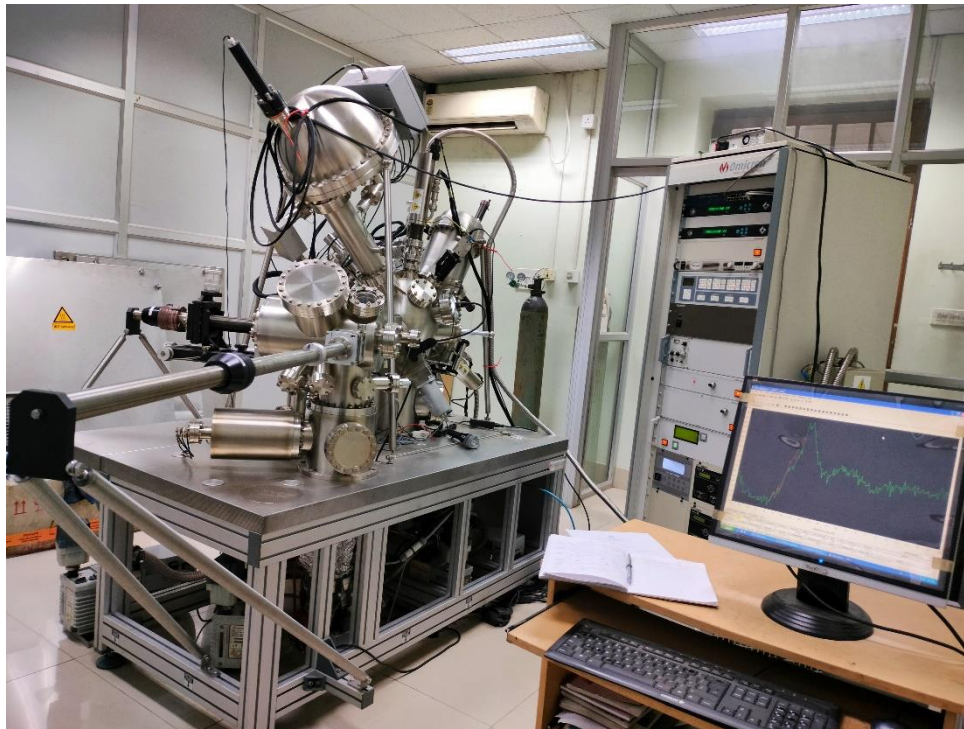
Fig. 3.14 Digital image of XPS instrument (Omicron, serial no: 0571).

3.4.7   UV-VIS transmission spectroscopy

UV-VIS transmission spectroscopy is one of the most useful tools to know the transmission, absorption, and reflection of a material [28, 29]. When a light beam falls on a material, a part of the beam is transmitted, another part is reflected, and the rest is absorbed by the material. The ability of absorption of any material depends on the concentration as well the absorption coefficient of the absorbing material. The absorbed beam intensity for a particular wavelength, $I(\lambda)$ as a function of the thickness 'd' of a film can be written according to the Lambert-Bouguer law [30]:

$$I(\lambda) = I_0(\lambda)e^{-\alpha(\lambda)d} \ldots\ldots\ldots\ldots\ldots\ldots\ldots\ldots \ (3.12)$$

where $I_0(\lambda)$ is the incident beam intensity, d is the film thickness and $\alpha(\lambda)$ is the absorption coefficient. The change in the α with λ is called the absorption spectrum of the medium. The schematic diagram of UV-VIS transmission spectroscopy is presented in Fig. 3.15.
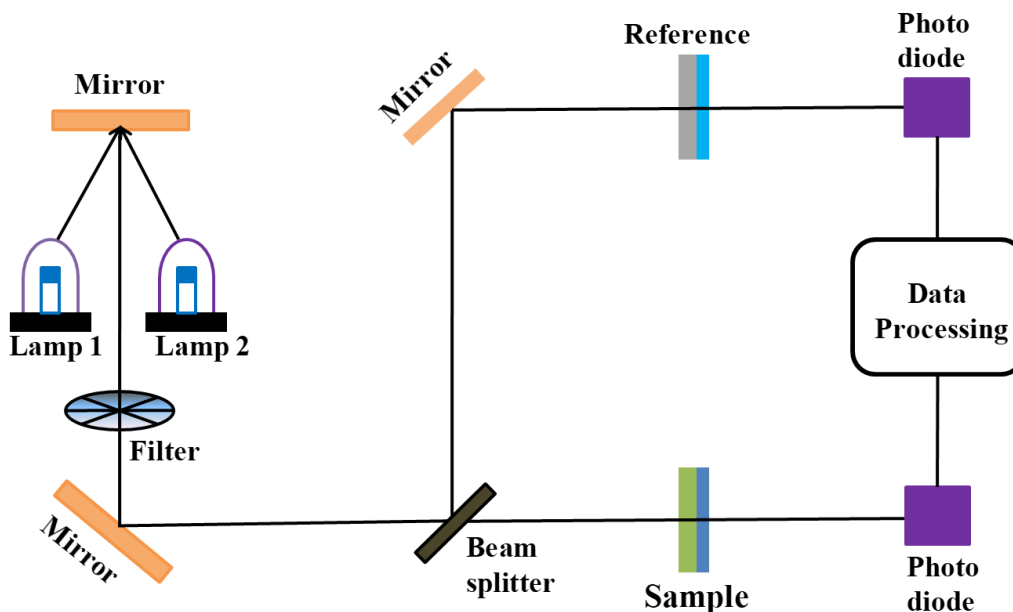
Fig. 3.15 Schematic diagram of UV-VIS transmission spectroscopy.

According to classical electromagnetic theory, the absorption coefficient can be written as the following equation:

$$\alpha = {}^{4\pi k}/_{c} \ldots\ldots\ldots\ldots\ldots\ldots\ldots\ldots\ldots. (3.13)$$

where k is the imaginary part of the complex index of refraction and it is also called extinction coefficient and c is the speed of the light in free space. Now considering that the reflection is insignificant for any material, then the transmittance, T(λ) is equal to the ratio of the intensity of the transmitted beam to that of the incident beam and given by,

$$T(\lambda) = {}^{I(\lambda)}/_{I_0(\lambda)} \ldots\ldots\ldots\ldots\ldots.. (3.14)$$

From the eqn. (3.12), one can write

$$\alpha(\lambda) = \frac{1}{d}\ln\frac{I_0(\lambda)}{I(\lambda)} \ldots\ldots\ldots\ldots\ldots.. (3.15)$$

Using eqn. (3.14) in eqn. (3.15), one can obtain

$$\alpha(\lambda) = \frac{1}{d} \ln \frac{1}{T(\lambda)} \quad ……………… \quad (3.16)$$

By putting the value of 'd' in the eqn. (3.16), one can easily find out the value of absorption coefficient from its transmission value. From the Tauc plot [$(\alpha h v)^n$ vs $h v$] [31, 32], the optical band gap can be calculated where n is 2 for direct band gap and n is 1/2 for indirect band gap materials. Fig. 3.16 shows the digital image of a UV-VIS spectrophotometer (Perkin elmer, model: Lambda 35) used in this thesis work.

Fig. 3.16 Digital image of UV-VIS spectrophotometer (Perkin elmer, model: Lambda 35).

3.4.8 Photoluminescence (PL)

PL is the emission of light from any form of matter after the absorption of photons (electromagnetic radiation). By measuring the PL spectrum it is possible to observe material imperfections (defects) and impurities [33, 34]. Due to the irradiation by a monochromatic light, once a photon gets absorbed by a material, the electrons are excited to the higher energy state and then fall to the lower energy state with the emission of a radiation of smaller frequency than the absorbed frequency. Emission causes due to the transition of a molecule from the lowest vibrational level of an excited singlet state to the ground state is known as fluorescence. Whereas in the case of phosphorescence, the absorbed energy is released relatively slowly in the form of light and transition occurs through a forbidden state. The decay time constant is

~10^{-9}-10^{-5} s for the fluorescence and 10^{-3} s for phosphorescence. In a typical PL measurement instrument, the essential components are: (i) Excitation source, (ii) Monochromator, and (iii) Detector. The the sample is generally excited by a monochromatic source. Then the emission from the sample is focused by a lens and feed to a monochromator. After that, the output is sent to a photomultiplier tube and finally the emission intensity is recorded at the detector. Fig. 3.17 shows the schematic diagram of PL measurements.
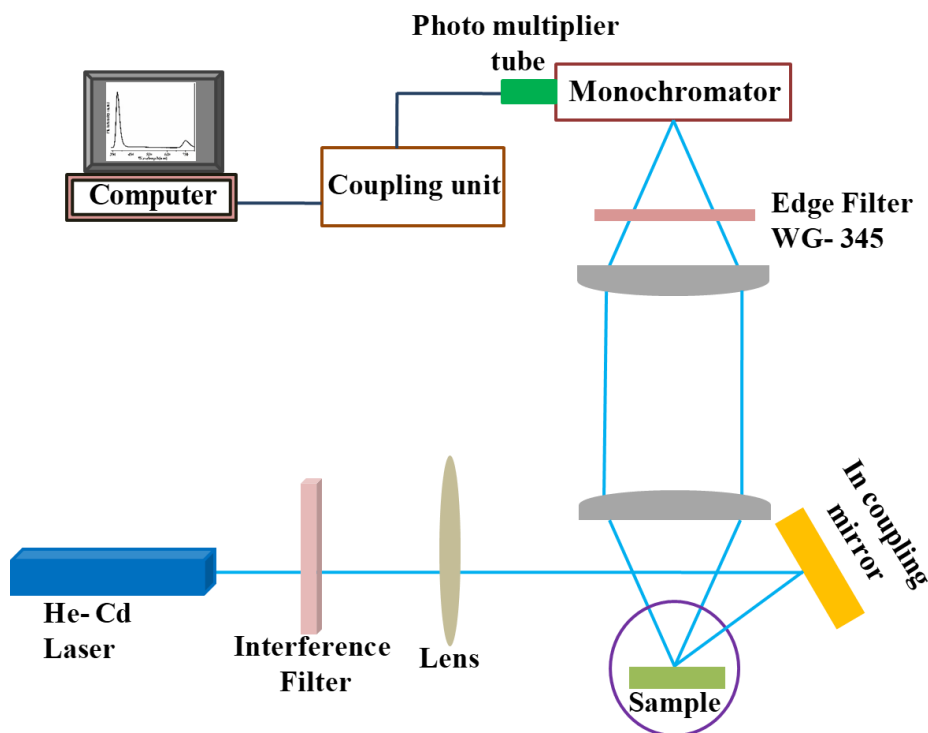
Fig. 3.17 Schematic diagram of PL measurement.

Fig. 3.18 Digital image of the PL measurement system.

In this thesis work, the RT PL spectra with 1 nm resolution has been measured by exciting the samples with a He-Cd LASER (Kimmon Koha Co. Ltd., model: KR1801C) as 325 nm excitation source and recording the luminescence using a spectrometer (Horiba Jobin Yvon, model: iHR 320) together with a photomultiplier tube. The digital image of the PL measurement setup used in this thesis work is shown in Fig. 3.18.

3.4.9 Raman spectroscopy

Raman spectroscopy belongs into the category of vibrational spectroscopy [35]. This means that it analyses a sample chemically by using light to create molecular vibration, and interpreting the interaction of light with the chemical bonds of the substance. These yields detailed information about chemical structure, polymorphism, defects in crystal, crystallinity and molecular dynamics. The basic principle of Raman spectroscopy is based on the inelastic scattering of light that occurs when a sample is irradiated by light. A very small part of scattered lights changes its wavelength after the light interacts with the sample. This usually happens in relation to molecular vibration. This scattered light is then collected and is used to gain information about the sample. This scattering phenomenon, which was predicted by Adolf Smekal in 1923 and discovered by C.V. Raman in 1930, is called the Raman effect. Fig. 3.19 shows the schematic diagram of Raman effect measurement.
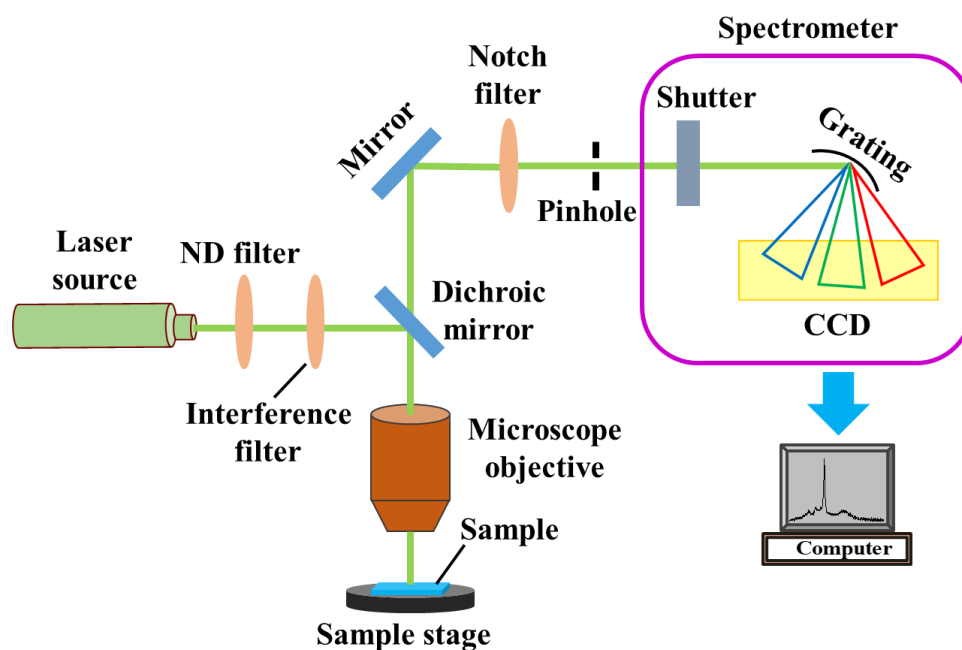
Fig. 3.19 Schematic diagram of Raman effect measurement.

As the change of wavelength is very small compared to the wavelength of the irradiating light, the change of wavelength is most easily observed when using monochromatic light sources. Therefore, in Raman spectrometer, a laser beam is generally focused onto the sample we want to investigate. That sample however, must not be showing fluorescence to the laser used for excitation. If that is the case, the fluorescence will cover most of the Raman effect, since it is so weak in comparison. After the laser light has irradiated the sample, the scattered light is passed through a notch filter (to get rid of any light from the excitation laser). Then it is directed onto a grating, which distributes the inelastic parts like a prism and according to wavelength. At the end these rays are directed to a CCD sensor which then outputs a spectrum depending on the intensity. In this thesis work, Raman measurements were carried out using a Lab RAM HR800 spectrometer (Horiba Jobin Yvon) with 458 nm Argon-ion laser as the excitation source, which is shown in Fig. 3.20.
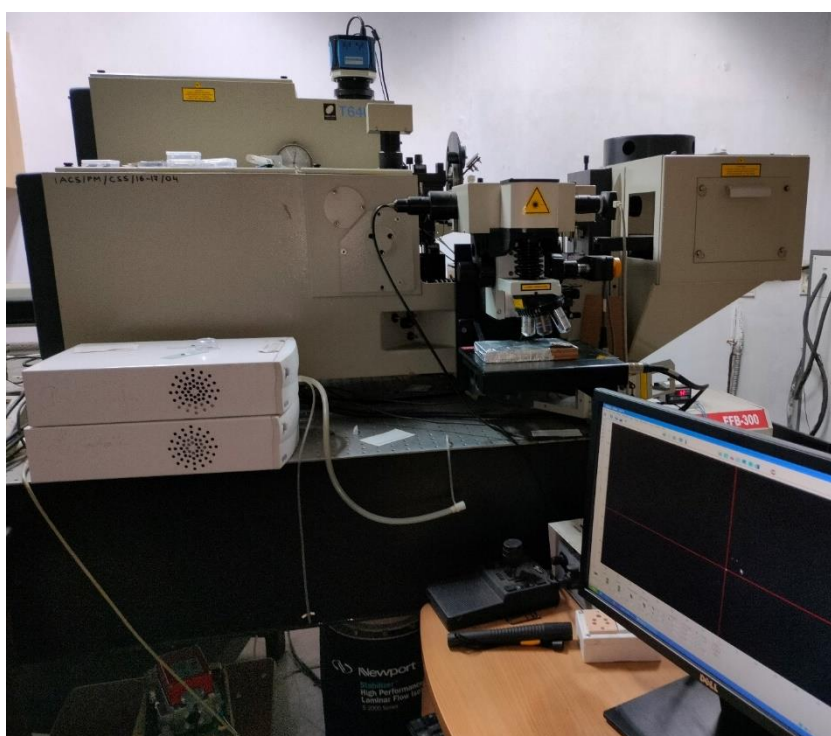
Fig. 3.20 Digital image of Raman setup (Horiba Jobin Yvon, model: Lab RAM HR800).

3.4.10 Current-voltage (I-V) measurement

The I-V characteristic between two Ohmic contacts on the semiconductor surface provides data on current magnitude at a particular applied voltage to judge the electronic transportation behavior of the material. In this thesis work, two circular electrodes (diameter 2 mm) Au or Al

were deposited on the sample surface having a separation of 2 mm to measure the the typical I-V characteristics of the samples. The data was recorded using a programmable source meter (Keithley, model: 2400).

3.4.11 Hall effect measurement

Hall measurement is one of the most popular methods for electrical characterization of any material [36, 37]. Hall effect principle says that when a conductor or semiconductor with current flowing in one direction is introduced perpendicular to a magnetic field, a voltage (known as Hall voltage) is developed at right angles to the current path. The basic principle of this phenomenon has been demonstrated in Fig. 3.21.
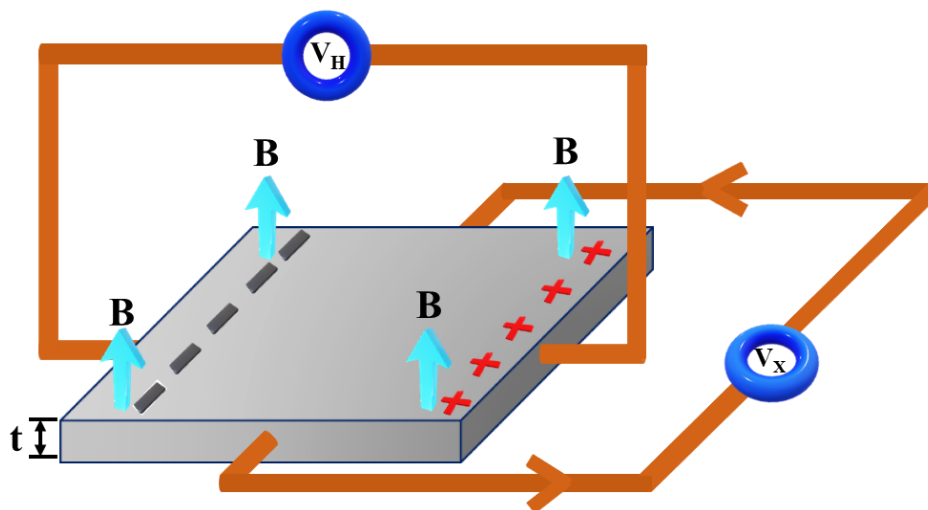
Fig. 3.21 Schematic diagram of Hall effect measurement.

In this thesis work, four-probe technique in Van der Pauw geometry has been used in hall measurement to measure the electrical resistivity (ρ), carrier concentration (n), sheet resistance (R_s), and hall mobility (μ) of the thin films. The advantages of this technique are: (i) It can eliminate the measurement errors due to the probe resistance or contact resistance between each metal probe and the non-homogeneity of the thin film materials. (ii) It has the ability to measure the electrical parameters of any arbitrarily shaped sample as long as the thickness is very less compared to the area and the metal contact pads are deposited at the perimeter of the films. For the experiment, first, four Ohmic contacts i.e., metal pads of same size having the proper work function matching with the thin film material are deposited at the corner most area of a square thin film by using the vacuum coating. The voltage drop between two contacts (1

and 3) is measured while a current is passed through the other two contacts (2 and 4). Fig. 3.22 shows the digital image of the Hall measurement system (Nano Magnetic Instruments) used in this thesis work.

Fig. 3.22 Digital image of the Hall measurement system (Nano Magnetic Instruments).

There are some basic equations involved in Hall measurement. The resistivity is calculated using the following formula:

$$\rho = \frac{\pi t}{\ln 2} \frac{V}{I} \ldots \ldots \ldots \ldots \ldots \ldots \ldots (3.17)$$

where t is the thickness of the thin film, ln2 is the correction factor, I is the applied electric current and V is the voltage drop. The mathematical Expression for Hall voltage is (V_H) is:

$$V_H = \frac{BI}{\rho t} \ldots \ldots \ldots \ldots \ldots \ldots \ldots (3.18)$$

where B is the magnetic field. The Hall coefficient can be determined from the flowing relation:

$$R_H = \frac{1}{qn} \quad ………………… \quad (3.19)$$

where q is the charge of majority carrier and n is the carrier concentration. The mobility of the majority carrier can also be calculated from the following equation:

$$\mu = \frac{1}{\rho q n} \quad ………………… \quad (3.20)$$

Using the eqn. (3.18), one can write

$$\mu = \frac{|R_H|}{\rho} \quad ……………… \quad (3.21)$$

3.4.12 Photoconductivity measurement

Photoconductivity is an optical and electrical phenomenon in which a semiconducting material becomes more electrically conductive due to the absorption of electromagnetic radiation [38, 39]. A photoconductivity set-up basically consists of a light source, a monochromator along with an electrometer for current measurements. The arrangement for the photoconductivity measurement used in the thesis work is given by a schematic diagram in Fig. 3.23.
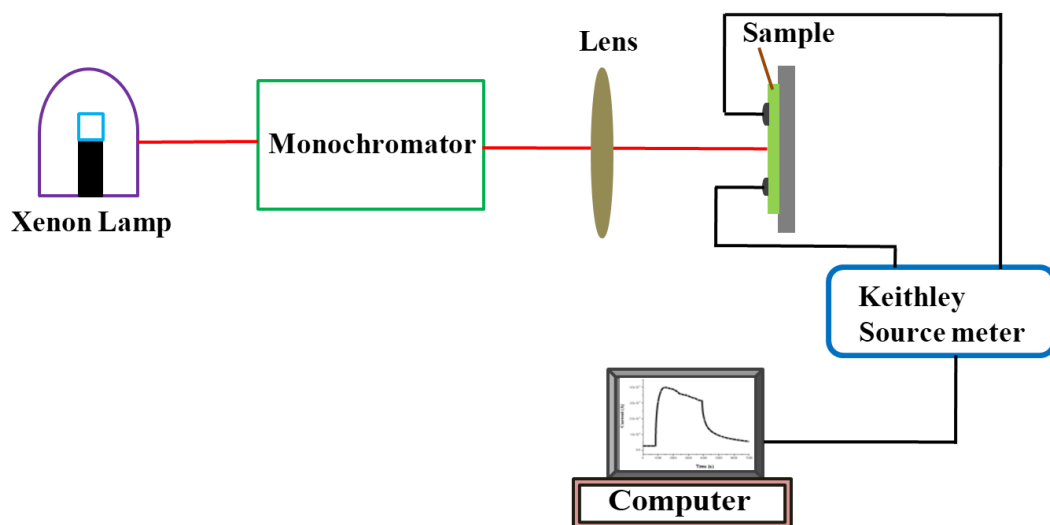
Fig. 3.23 Schematic diagram of photoconductivity measurement.

When the light with suitable energy is absorbed by a semiconducting material, its electron jumps from the VB or from any in-gap defects state to the CB, leading to the generation of electron-hole pairs. The excess charge carriers formed in this process is transported to the electrode and the growth of the photocurrent is observed consequently. Photoconductivity is very much affected by the trapping process and depending upon the depth of the trapping centre, it can be classified as (i) shallow trapping level and (ii) deep trapping level. In photogeneration process, the electron-hole pairs are continuously generated and at the same time recombined too. Assuming there are no trap state or recombination centres except direct band to band recombination, the rate equation for the transient photo current in an ideal semiconductor can be written as

$$\frac{dn(t)}{dt} = G - \frac{n(t)}{\tau} \dots \dots \dots \dots \dots \dots \dots \dots (3.22)$$

where n(t) is the photogenerated carrier concentration at any instant, G is the rate of generation of carriers due to illumination and τ the free carrier life time. At a particular instant during the growth of photo current, the number of photogenerated carriers are given by

$$n(t) = n_s(1 - e^{-\frac{t}{\tau}}) \dots \dots \dots \dots \dots \dots \dots \dots (3.23)$$

where n(s) is the saturated photocarrier concentration When the illumination is turned off, the current starts to decay due to recombination. The carrier concentration at the time t during decay can be written as

$$n(t) = n_s e^{-\frac{t}{\tau}} \dots \dots \dots \dots \dots \dots \dots \dots \dots . (3.24)$$

Substituting t = τ in the eqn. (3.23) and eqn. (3.24), the growth and decay equations become

$$n(\tau) = n_s \left(1 - \frac{1}{e}\right) \dots \dots \dots \dots \dots \dots \dots \dots (3.25)$$

$$n(\tau) = \frac{n_s}{e} \dots \dots \dots \dots \dots \dots \dots \dots \dots \dots . . (3.26)$$

This means that the free carrier lifetime can be calculated easily from the growth or decay equation. In this thesis work, to obtain the photocurrent transient spectra, the NRs were illuminated with a monochromatic light from a Xenon lamp (150 W) fitted with a spectral

illuminator system (New-port Corp., model: 9050). Fig. 3.24 shows the digital image of the photoconductivity measurement system used in this thesis work.

Fig. 3.24 Digital image of the photoconductivity measurement system.

3.5 References

[1] L.J.M.S. Znaidi, E. B, Sol–gel-deposited ZnO thin films: A review, 174 (2010) 18-30.

[2] M. Kamalasanan, S.J.T.s.f. Chandra, Sol-gel synthesis of ZnO thin films, 288 (1996) 112-115.

[3] L.J.A.M. Vayssieres, Growth of arrayed nanorods and nanowires of ZnO from aqueous solutions, 15 (2003) 464-466.

[4] Q. Li, V. Kumar, Y. Li, H. Zhang, T.J. Marks, R.P.J.C.o.M. Chang, Fabrication of ZnO nanorods and nanotubes in aqueous solutions, 17 (2005) 1001-1006.

[5] S. Baruah, J.J.S. Dutta, t.o.a. materials, Hydrothermal growth of ZnO nanostructures, (2009).

[6] D. Polsongkram, P. Chamninok, S. Pukird, L. Chow, O. Lupan, G. Chai, H. Khallaf, S. Park, A.J.P.B.C.M. Schulte, Effect of synthesis conditions on the growth of ZnO nanorods via hydrothermal method, 403 (2008) 3713-3717.

[7] W. Gao, Z.J.C.I. Li, ZnO thin films produced by magnetron sputtering, 30 (2004) 1155-1159.

[8] A. Hachigo, H. Nakahata, K. Higaki, S. Fujii, S.i.J.A.p.l. Shikata, Heteroepitaxial growth of ZnO films on diamond (111) plane by magnetron sputtering, 65 (1994) 2556-2558.

[9] F. Shan, B. Shin, S. Jang, Y.J.J.o.t.E.C.S. Yu, Substrate effects of ZnO thin films prepared by PLD technique, 24 (2004) 1015-1018.

[10] S. Venkatachalam, Y. Iida, Y.J.S. Kanno, Microstructures, Preparation and characterization of Al doped ZnO thin films by PLD, 44 (2008) 127-135.

[11] Y. Heo, D. Norton, S.J.J.o.A.P. Pearton, Origin of green luminescence in ZnO thin film grown by molecular-beam epitaxy, 98 (2005) 073502.

[12] M. Suja, S.B. Bashar, M.M. Morshed, J.J.A.A.m. Liu, interfaces, Realization of Cu-doped p-type ZnO thin films by molecular beam epitaxy, 7 (2015) 8894-8899.

[13] S.A. Campbell, Fabrication engineering at the micro-and nanoscale, 2008.

[14] D.V. Morgan, Channeling: theory, observation, and applications, (1973).

[15] A. Chauhan, P.J.J.A.B.T. Chauhan, Powder XRD technique and its applications in science and technology, 5 (2014) 1-5.

[16] J. Van Heerden, R.J.T.S.F. Swanepoel, XRD analysis of ZnO thin films prepared by spray pyrolysis, 299 (1997) 72-77.

[17] W.H.B. Bragg, W.L., The Reflexion of X-rays by Crystals, Göttinger Nachrichten Gesell, 88 (1913) 428-438.

[18] A.L. Patterson, The Scherrer Formula for X-Ray Particle Size Determination, Physical Review, 56 (1939) 978-982.

[19] S. Aksoy, Y. Caglar, S. Ilican, M.J.J.o.A. Caglar, Compounds, Sol–gel derived Li–Mg co-doped ZnO films: Preparation and characterization via XRD, XPS, FESEM, 512 (2012) 171-178.

[20] D. Read, Y. Cheng, R.J.M.E. Geiss, Morphology, microstructure, and mechanical properties of a copper electrodeposit, 75 (2004) 63-70.

[21] M.A. Rubin, I. Jasiuk, J. Taylor, J. Rubin, T. Ganey, R.P.J.B. Apkarian, TEM analysis of the nanostructure of normal and osteoporotic human trabecular bone, 33 (2003) 270-282.

[22] R. Brayner, S.A. Dahoumane, C. Yéprémian, C. Djediat, M. Meyer, A. Couté, F.J.L. Fiévet, ZnO nanoparticles: synthesis, characterization, and ecotoxicological studies, 26 (2010) 6522-6528.

[23] S.N. Magonov, M.-H. Whangbo, Surface Analysis with STM and AFM, VCH, 1996.

[24] Z. Fang, Z. Yan, Y. Tan, X. Liu, Y.J.A.s.s. Wang, Influence of post-annealing treatment on the structure properties of ZnO films, 241 (2005) 303-308.

[25] M.J.S. Seah, I. Analysis, The quantitative analysis of surfaces by XPS: a review, 2 (1980) 222-239.

[26] E.J.S. Paparazzo, I. Analysis, XPS analysis of oxides, 12 (1988) 115-118.

[27] J.F. Watts, J. Wolstenholme, An introduction to surface analysis by XPS and AES, John Wiley & Sons, 2019.

[28] Z. Chen, T.G. Deutsch, H.N. Dinh, K. Domen, K. Emery, A.J. Forman, N. Gaillard, R. Garland, C. Heske, T.F. Jaramillo, UV-vis Spectroscopy, in: Photoelectrochemical Water Splitting, Springer, 2013, pp. 49-62.

[29] S. Talam, S.R. Karumuri, N.J.I.S.R.N. Gunnam, Synthesis, characterization, and spectroscopic properties of ZnO nanoparticles, 2012 (2012).

[30] H.C. Lee, Introduction to Color Imaging Science, Cambridge University Press, 2005.

[31] J. Kennedy, P.P. Murmu, J. Leveneur, A. Markwitz, J. Futter, Controlling preferred orientation and electrical conductivity of zinc oxide thin films by post growth annealing treatment, Appl. Surf. Sci., 367 (2016) 52-58.

[32] J. Tauc, Optical properties and electronic structure of amorphous Ge and Si, Materials Research Bulletin, 3 (1968) 37-46.

[33] H. Kaftelen, K. Ocakoglu, R. Thomann, S. Tu, S. Weber, E.J.P.R.B. Erdem, EPR and photoluminescence spectroscopy studies on the defect structure of ZnO nanocrystals, 86 (2012) 014113.

[34] L. Cao, M.J. Meziani, S. Sahu, Y.-P.J.A.o.C.R. Sun, Photoluminescence properties of graphene versus other carbon nanomaterials, 46 (2013) 171-180.

[35] R.J.A.i.P. Loudon, The Raman effect in crystals, 13 (1964) 423-482.

[36] R. Karplus, J.J.P.R. Luttinger, Hall effect in ferromagnetics, 95 (1954) 1154.

[37] S.E.J.P.R. Harrison, Conductivity and Hall effect of ZnO at low temperatures, 93 (1954) 52.

[38] Q. Li, T. Gao, Y. Wang, T.J.A.P.L. Wang, Adsorption and desorption of oxygen probed from ZnO nanowire films by photocurrent measurements, 86 (2005) 123117.

[39] D. Basak, G. Amin, B. Mallik, G. Paul, S.J.J.o.C.G. Sen, Photoconductive UV detectors on sol–gel-synthesized ZnO films, 256 (2003) 73-77.

Chapter-4

Optical and electrical properties of Al implanted ZnO thin films

4.1 Introduction

As discussed in chapter 2, the as-grown ZnO thin films always shows strong n-type electrical conductivity. To further improve the n-type conductivity, ZnO is normally doped with a group III elements, such as B, Ga, In and Al [1-4]. Among group III elements, Al is superior to Ga and In, and is the most effective donor dopant for ZnO due to its low cost and high abundance. Moreover, Al doped ZnO (AZO) films has better thermal, chemical, mechanical stability, and non-toxicity. Their high optical transparency in the visible region makes them a promising candidate as an alternative of costly Indium Tin oxide (ITO) in the field of transparent conducting oxide (TCO) layers. However, majority of the previous studies on AZO films [3, 5, 6] deal with Al dopant incorporation into ZnO during the process of thin film growth, which typically allows a certain degree of control over the doping level. In contrast to these studies, very few post-growth Al doping via ion implantation technique have been followed for ZnO thin films [7-12], which have already been reviewed in the chapter 2. Further, among these, most of the hand on literatures studying Al implantation [7-13] have dealt with either RF magnetron and ion beam sputtered ZnO thin films or ZnO single crystal. To the best of our knowledge, a high-performance (Figure of merit, FOM) Al ion implanted sol-gel ZnO thin films as transparent conducting films has not been reported till date. On the other hand, the sol-gel process of ZnO film deposition has many advantageous properties as described in chapter 3. Therefore, the issue being in mind, the effect of Al ion implantation on the electrical and optical transmittance properties correlated to the implantation-induced structural defects in sol-gel grown ZnO thin films has been discussed in this chapter to use the later as TCO layers.

4.2 Experimental details

ZnO thin films were deposited on glass substrates using the sol-gel spin coating method as described in the chapter 3. The as-grown ZnO films were then implanted with 100 keV Al ions having various fluences ranging from 1×10^{13} to 6×10^{15} ions/cm^2 [14]. The implantation process was executed at RT and in vacuum at pressure of $\sim5\times10^{-7}$ Torr. During implantation, the ion beam was scanned over one cm^2 area of the sample and the beam current was fixed at 130 nA. After Al implantation, the implanted ZnO films were finally annealed at 450 °C for 1 h in Ar ambient. The as-grown ZnO films, which were not implanted by Al, were also annealed using similar conditions and have been considered as the pristine sample in this

work. A second set of implanted films were annealed in excess Zn ambient at 450 °C for 1 h just to understand the effect of defects on the observed optical and electrical properties. The nomenclature of the samples in this study is given in Table 4.1.

Table 4.1 Nomenclature of the samples with their specifications.

Fluence (ions/cm^2)	Sample name (Annealed in Ar)	Sample name (Annealed in excess Zn)
0	Pristine	Zn_Pristine
1×10^{13}	AZO113	Zn_AZO113
5×10^{13}	AZO513	Zn_AZO513
1×10^{14}	AZO114	Zn_AZO114
5×10^{14}	AZO514	Zn_AZO514
1×10^{15}	AZO115	Zn_AZO115
5×10^{15}	AZO515	Zn_AZO515
6×10^{15}	AZO615	Zn_AZO615

The structural, morphological, compositional, optical, and electrical analyses of the samples have been carried out using XRD, FESEM, AFM, EDS, XPS, UV-VIS transmission, PL and Hall effect measurements respectively as described in chapter-3. Here, XRD measurement as performed at Indian beamline (BL-18B), Photon Factory, Japan as described in chapter-3. The Hall measurement was carried out at RT by applying a magnetic field of 1.50 T.

4.3 Results and discussion

4.3.1   Characterizations of Al implanted and subsequently Ar annealed ZnO films

Fig. 4.1(a) shows the XRD patterns of pristine and Al implanted and subsequently Ar annealed ZnO thin films exhibiting the presence of sharp, narrow and well distinct diffraction peaks which correspond to $(10\bar{1}0)$, (0002), $(10\bar{1}1)$, $(10\bar{1}2)$, $(11\bar{2}0)$, $(10\bar{1}3)$, and $(11\bar{2}2)$ reflection planes of hexagonal wurtzite structure of ZnO (JCPDS card No. 36-1451). The existence of several peaks indicated a mixed orientation of the crystallites in all the films. However, the random changes in the intensities of the (002) and (101) peaks are not understood at this moment. No diffraction peak from Al-related secondary phase or

impurities have been detected within the sensitivity of the XRD [15]. The inclusion of Al donors in ZnO has two distinctive effects on the lattice parameters: The first effect is related to the difference between the ionic radii of Al and the host Zn ions. The ionic radii of Al^{3+} and Zn^{2+} with a coordination number of 6 are 53 and 74 pm respectively, which indicates to the fact that a decrease in the lattice parameter should occur. The second effect is related to the deformation potentials. The occupation of Al in the antibonding state is likely to result in a repulsive force between Zn and O, which lowers the total energy of the crystal structure, thereby inducing expansion in the lattice [16]. Analyses of the data of the (002) diffraction peak of the implanted films (Fig. 4.1(b)) show a shift towards lower 2θ value as compared to the pristine. A small but a gradual lower angle shift of the (002) peak indicates that the c-axis lattice parameter (c) gradually increases (Fig. 4.1(c)) due to Al implantation [17]. Similar lower angle shift of the (002) peak after Al doping in ZnO thin films has also been reported in the previous studies [17-19]. Ab initio electronic band structure calculations based on the density functional theory shows that the average bond length along the c-axis between O and Zn locating at the second-nearest neighbor of Al replacing Zn atoms, the total number of which is 12, is 2.04 Å, which is larger than 1.98 Å of the Zn-O bond length in undoped ZnO crystal, resulting in a larger c-axis length than that of undoped ZnO crystal [16]. To compensate the increase in c, the stress (σ) parallel to c-axis can be decreased. Based on the biaxial strain model [20], the value of σ along c-axis has been calculated. As shown in Fig. 4.1(c), the positive value of σ indicates the presence of tensile stress in all the samples [20]. The value of σ is maximum for the pristine and with an increase in Al ion fluence, the value decreases with a 29% drop for AZO615. The variation of FWHM of the (002) peak with Al ion fluences in Fig. 4.1(d) shows that the FWHM remains almost unchanged till 1×10^{15} ions/cm^2 and then increases sharply with an increase in the fluence. The average crystallite size (D) calculated using the eqn. 3.9 is 41.94 nm for pristine. As shown in Fig. 4.1(d), the value of D decreases gradually with an increase in Al fluence up to 1×10^{15} ions/cm^2, and then sharply falls to a value of 22.24 nm at the fluence of 6×10^{15} ions/cm^2. The dislocation density (δ) as calculated using the eqn. 3.10 shows an increasing trend with an increase in the Al ion fluence as expected (Fig. 4.1(d)). Turos et al. [21] have shown that an increase in the dislocation loop concentration causes lattice strain resulting in plastic deformation of the implanted layer. However, the structural changes as compared to the pristine are modest up to the ion fluence of 1×10^{15} ions/cm^2, and beyond 1×10^{15} ions/cm^2, are significant.
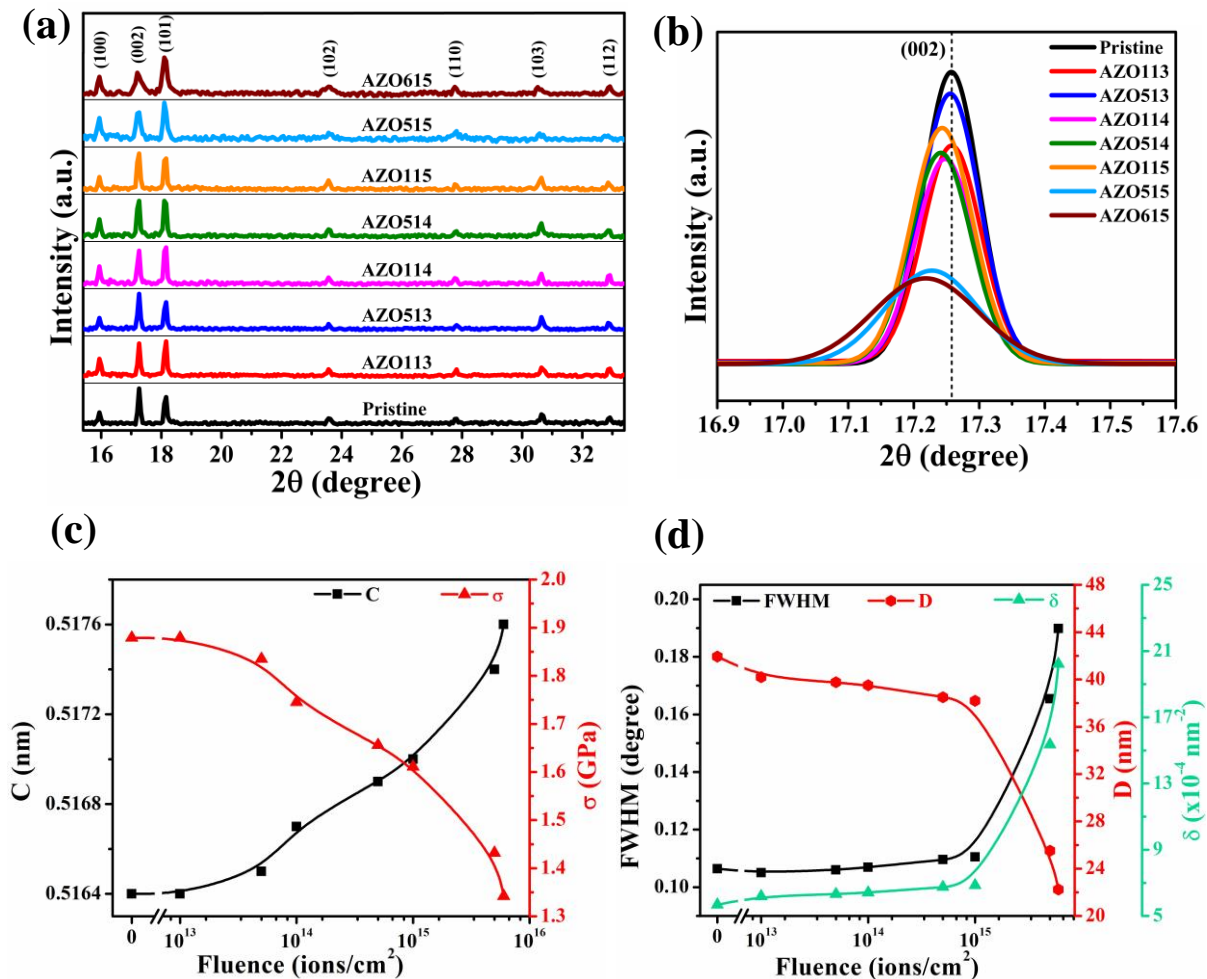
Fig. 4.1 (a) XRD patterns, (b) enlarged view of (002) peak of pristine and Al implanted ZnO films, (c) variation of c-axis lattice parameter and stress with fluence, and (d) variation of FWHM of (002) peak, crystallite size and dislocation density with Al ion fluence.

As the microstructure has an influence on the electrical and optical properties, it is very important to investigate the surface morphologies of the films. Fig. 4.2(a)-(c) shows the top view FESEM images of pristine and two representatives implanted ZnO films. As seen in Fig. 4.2(a)-(c), the surfaces of the films with uniform distribution of the grains are not much affected by the ion implantation. The cross-sectional FESEM image of pristine in the inset in Fig. 4.2(a) reveals that the grains are columnar in structure and a film thickness is of ~350 nm. The elemental analysis of AZO615 performed using the EDS as shown in Fig. 4.2(d) confirms the presence of Al besides Zn and O with an average Al atomic concentration of 0.63 at.%.

(a)

(b)

(c)

(d)

Element	at.%
Zn	41.93
O	57.44
Al	0.63
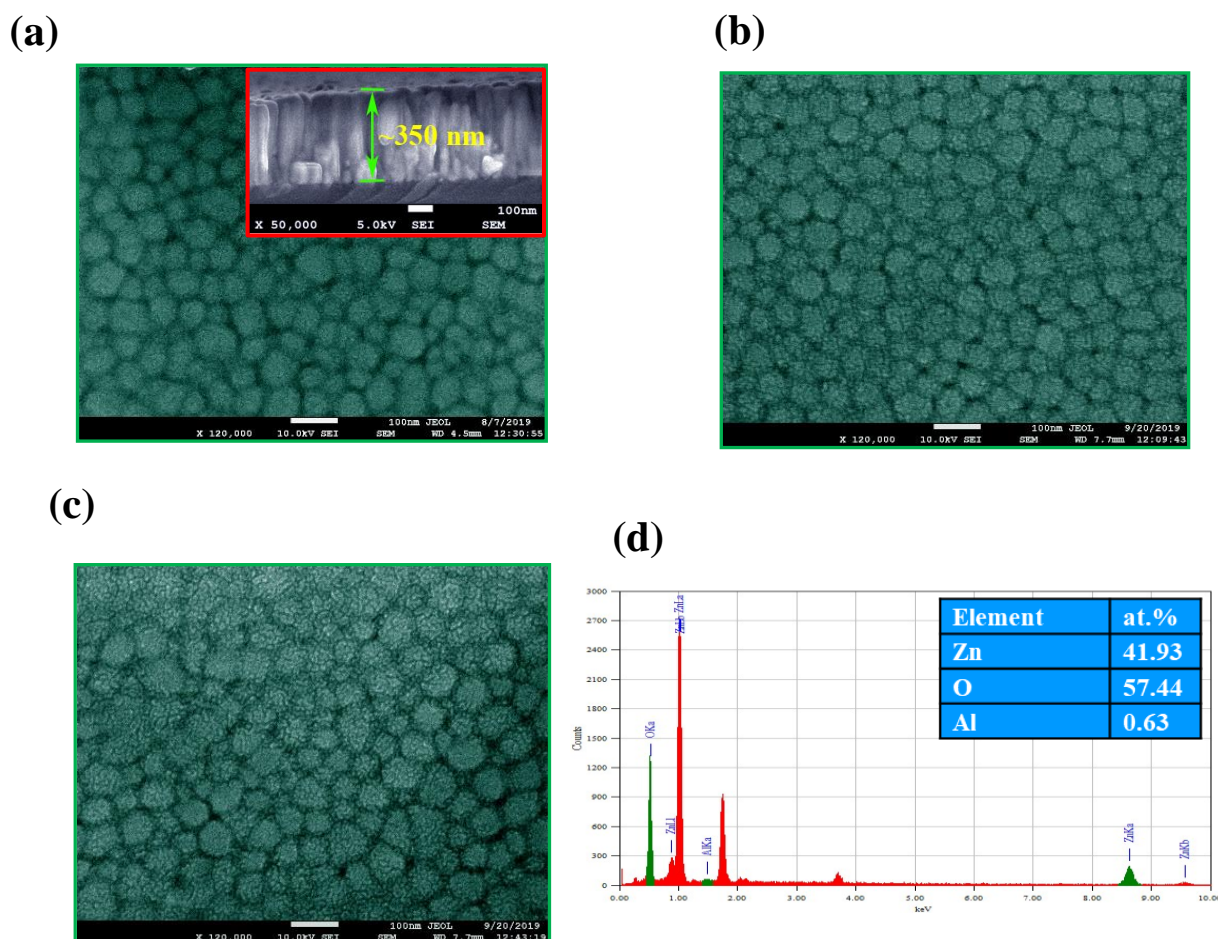
Fig. 4.2 (a)-(c) Top view FESEM images of pristine, AZO513, and AZO615 respectively, (d) EDS spectrum of AZO615. The inset in the Fig. 4.2(a) is the cross-sectional FESEM of pristine.

The 3D AFM micrographs (2×2 μm^2) of selected samples depicted in Fig. 4.3(a)-(c) elucidate an influence of Al ions on the roughness of ZnO thin films surfaces. The value of RMS roughness (R_{rms}) of pristine has been found to be 5.49 nm and with an increase in Al ion fluence, the value of R_{rms} decreases and it reaches to a minimum value of ~1.65 nm for AZO615.
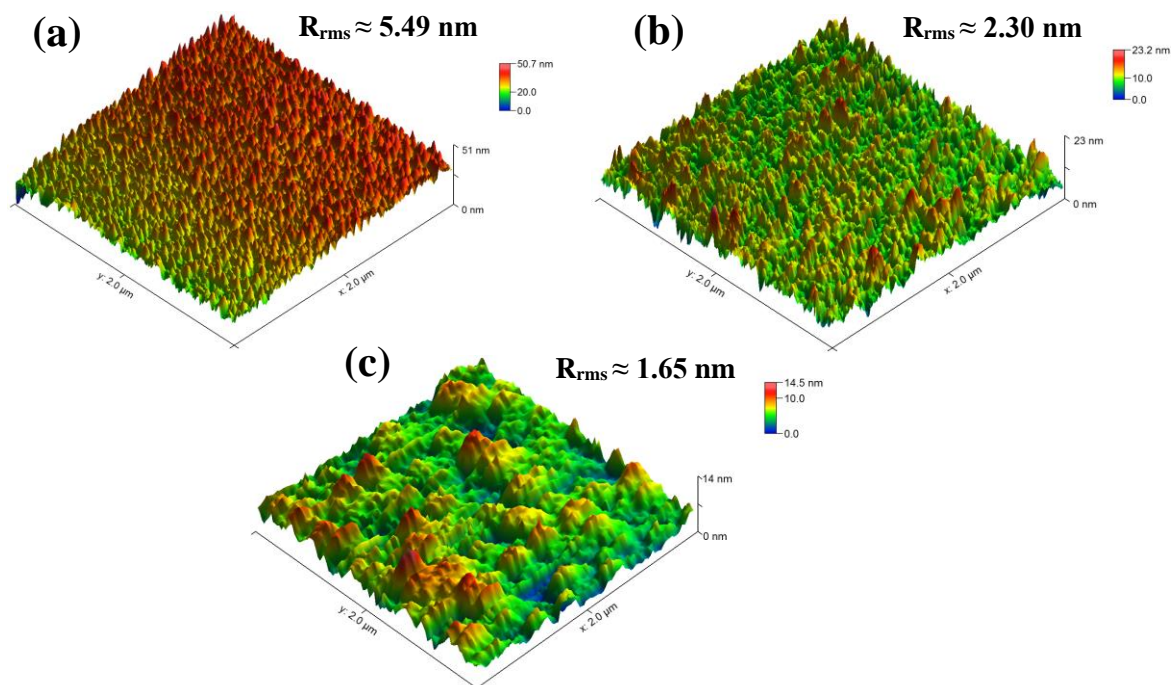
Fig. 4.3 (a)-(c) AFM micrographs of pristine, AZO513, and AZO615 respectively.

The XPS survey scan of pristine and AZO615 in Fig. 4.4(a) shows the well resolved peaks corresponding to different core levels of O and Zn. The appearance of Al 2p peak as shown in the inset in the Fig. 4.4(a) confirms the presence of Al in AZO615. The broad Al 2p peak can be deconvoluted into two Gaussian peaks, where the first peak (P_1) at 74.65 eV is ascribed to the stoichiometric Al–O bond, confirming the successful incorporation of Al into Zn^{2+} sites of ZnO [22, 23], and the second peak (P_2) at 73.76 eV is attributed to the formation of non-stoichiometric Al_xO_y [24]. Being asymmetric in nature, the O 1s XPS spectra of pristine and AZO615 can be deconvoluted into three Gaussian components, as shown in Fig. 4.4(b)-(c). The O_a peak on the lower binding energy side of the O 1s spectra located at around 530.6 eV can be attributed to the O^{2-} ions of wurtzite hexagonal ZnO [25]. The O_c peak towards the higher binding energy located at 532.6 eV is usually associated with the loosely bound surface absorbed O atoms and the middle component (O_b) at 531.9 eV is related to oxygen-deficient regions within the ZnO matrix, namely V_O [25, 26]. The contributions of O_a, O_b, and O_c have been computed from the measured peak area, which reveals that the concentration of V_O increases due to Al implantation. Considering the peak area and relative sensitivity factor of three main peaks namely Zn $2p_{3/2}$, O 1s and Al 2p [27], the calculated atomic concentration of Al is 0.40 at.% for AZO615, which is quite at par with the EDS results and SRIM calculations (shown later).

(a)

(b)

(c)
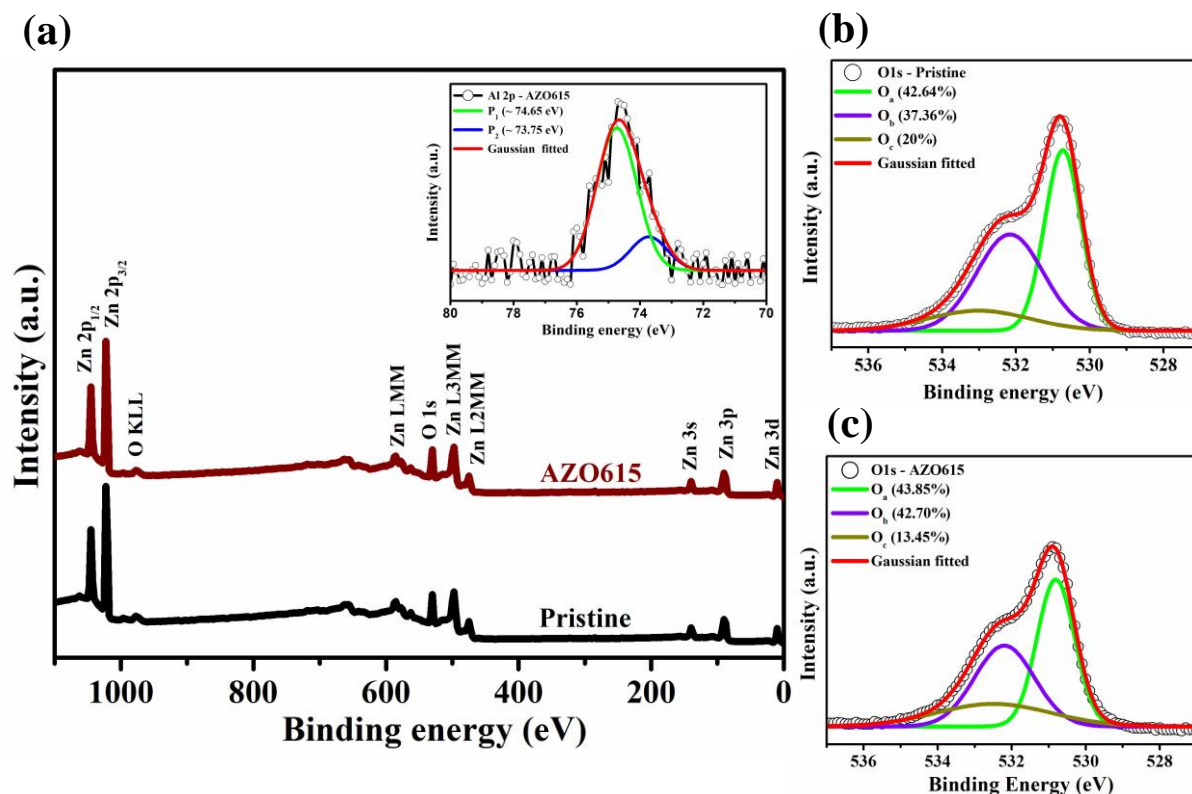
Fig. 4.4 (a) XPS survey scan of pristine and AZO615. The inset shows the Al 2p peak and its deconvolution, (b) and (c) O 1s peak fittings of pristine and AZO615 respectively.

As high transparency is an important factor in the application of Al implanted ZnO thin films to TCOs, the optical transmittance has been recorded for pristine and implanted samples in the wavelength range of 325-1100 nm as shown in Fig. 4.5(a). All the films exhibit sharp band-edge absorption below 390 nm. The pristine ZnO film exhibits a very high optical transmission in the visible range having average transparency (T_{av}) of ~92% and the value decreases as the Al ion fluence increases (Table 4.2) with the lowest value of 82% for the highest fluence of 6×10^{15} ions/cm^2. The value of T_{av} over 80% in the visible region indicates a quite good transmission quality of the films under study. The decrease in the visible transmittance at higher fluences may be due to optical scattering from crystal defects generated by the incorporation of Al in ZnO lattice, which is in good agreement with the XRD results [28, 29]. The optical direct band gap energy (E_g) of the films has been estimated in Fig. 4.5(b) by employing the well-known relation described in chapter 3. A plot of ln(α) vs. hν in Fig. 4.5(c) for the films show the presence of the so-called Urbach tail, related to the disorder in the films as $\alpha = \alpha_0 e^{\left(\frac{h\nu}{E_u}\right)}$, where α$_0$ is the pre–exponential factor and E_u is the Urbach energy) [30]. The variation in the values of E_g with Al ion fluence in Fig. 4.5(d)

[95]

shows that the value of E_g for the pristine is about 3.293 eV and increases significantly beyond the fluence of 1×10^{15} ions/cm^2 and reaches to a value of 3.393 eV at 6×10^{15} ions/cm^2. An increase in the value of E_g with an increase in the fluence is attributed to the well-known BM effect and is consistent with the previous reports [31, 32]. This indicates that the implanted Al is substituted in the Zn sites. The Fig. 4.5(d) reveals that the value of E_u increases with fluence, indicating creation of localized states within the band gap. A jump in the E_u value from AZO115 indicates the formation of more disorder in the lattice of ZnO due to higher Al ion fluences. This result is at par with the structural changes as observed from the XRD data.
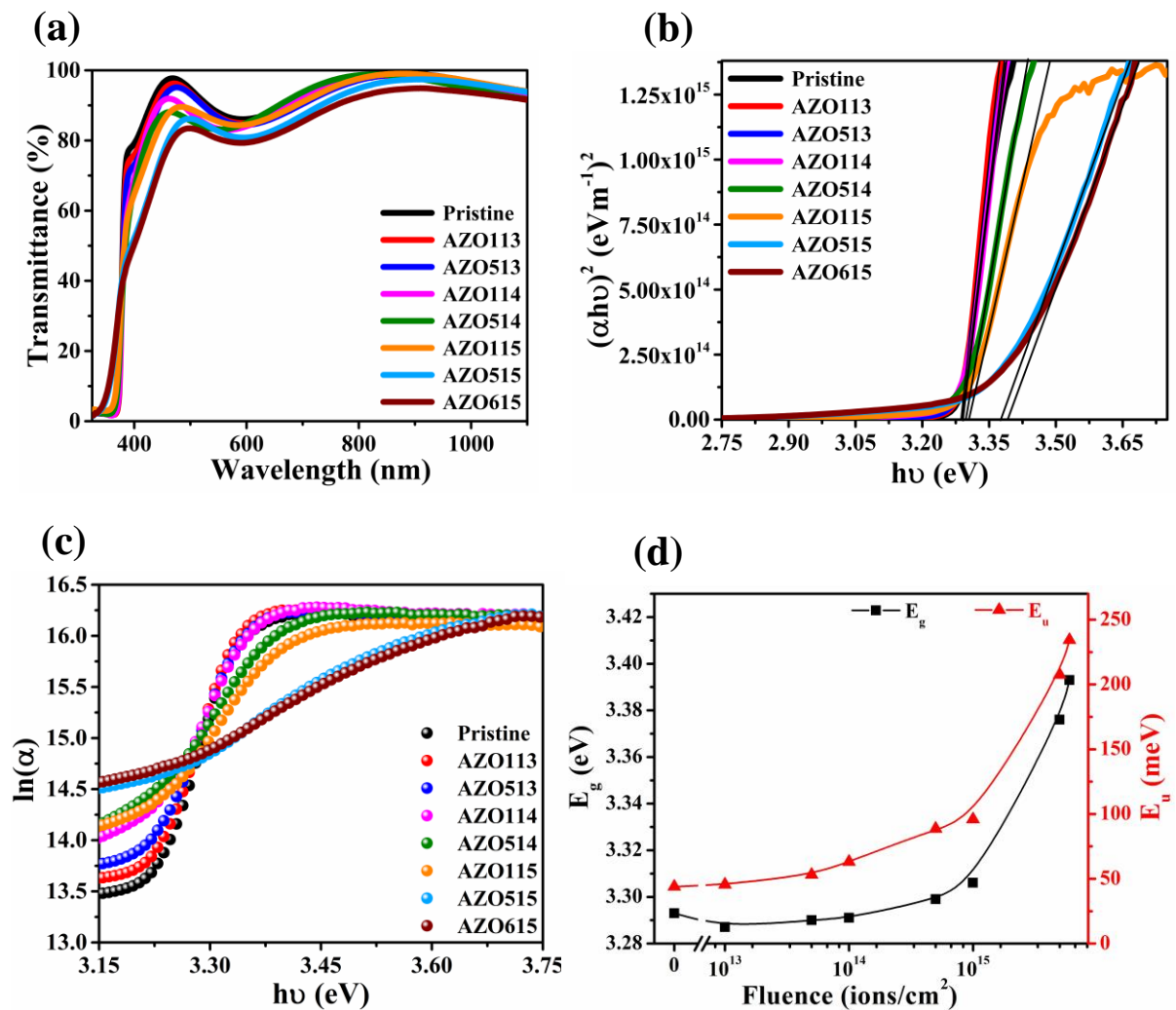
Fig. 4.5 (a) Transmittance spectra, (b) Tauc plots, (c) E_u for pristine and Al implanted samples and (d) variation of E_g and E_u with Al ion fluence

Based on the Hall measurements, the impact of Al ion fluences on the electrical parameters such as resistivity (ρ), carrier concentration (n), and Hall mobility (μ_h) of the implanted samples are shown in Fig. 4.6. The pristine ZnO film exhibits a ρ value of ~ 6.81×10^{-2} Ω.cm with n and μ_h values are of ~1.29×10^{19} cm^{-3} and 7.08 cm^2/V.s respectively. Interestingly, as soon as the film is implanted with an Al ion fluence of 1×10^{13} ions/cm^2, the values of n and μ_h are decreased and subsequently the value of ρ is increased. Further deterioration in the electrical properties occurs for an Al ion fluence of 5×10^{13} ions/cm^2. The minimum values of n and μ_h have been observed for AZO513, which are 1.64×10^{18} cm^{-3} and 1.52 cm^2/V.s respectively, while the value of ρ is maximum (2.52 Ω.cm). An increase in the ρ and decrease in n values at initial fluences suggest that the implanted Al ions do not act as donors and probably are incorporated in the inappropriate sites as observed by Jannane et al. [33] and Kim et al. [34]. Instead of occupying the Zn sites with the tetrahedral coordination of hexagonal wurtzite, the Al ions probably occupy the interstitial sites with octahedral voids [33]. Also, Al ions may gather at the grain boundaries, leading to an enhanced grain boundary scattering, which is manifested in an almost 4.6 times degradation in the μ_h value for AZO513 [33]. According to the SRIM calculations, at a fixed fluence, Al implantation induces more V_{Zn} than V_O, as indicated in Fig. 4.7(b). The V_{Zn} can act as a donor compensating defect and may lead to the deterioration in electrical properties of Al implanted samples at initial fluences. As the fluence increases beyond 5×10^{13} ions/cm^2, both μ_h and n increases and subsequently the value of ρ decreases. However, till an Al ion fluence of 1×10^{15} ions/cm^2, the value of ρ remains higher and the values of n and μ_h remain lower than that of the pristine, indicating implanted Al ions are rather producing defects. Beyond the fluence of 1×10^{15} ions/cm^2, the ρ decreases and n and μ_h increases with an increase in the fluence. This is in corroboration with the structural changes. For AZO615, ρ as low as 5.46×10^{-3} Ω.cm and n as high as 2.81×10^{20} cm^{-3} have been achieved. This trend of increase in n and decrease in the ρ value indicates successful incorporation of Al ions in the Zn sites. For a highest fluence (AZO615), a decrease in the μ_h is seen which may probably be due to an ionized impurity scattering. To calculate the FOM value of the samples, the important electrical parameter sheet resistance (R_s) has also been determined in Table 4.2. The lower R_s value of 186 and 156 Ω/sq respectively has been observed for AZO515 and AZO615, which indicates a prospective application of this Al implanted sol-gel film as TCO.
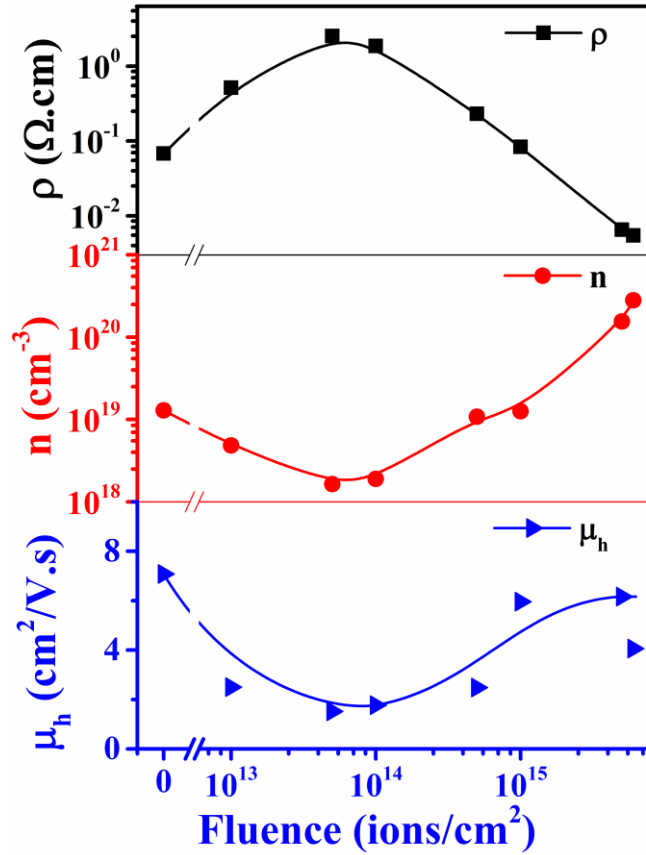
Fig. 4.6 Variation of ρ, n, and μ_h values with Al ion fluence after annealing in Ar.

To evaluate the performance of the implanted films as TCO, the well-known parameter FOM can be calculated by employing Haacke formula [35]: $FOM = {T_{av}^{10}}/{R_s}$. Using the values of T_{av} and R_s presented in Table 4.2, the FOM values have been estimated for all the samples and noted in the same table. The FOM value gets better than that of pristine at higher Al ion fluences (beyond 1×10^{15} ions/cm^2). The highest FOM value of $9.57\times10^{-4}\,\Omega^{-1}$ has been achieved for AZO515, which is almost 4.4 times greater than that of the value of pristine. The typical reported values of electrical and optical parameters of Al doped ZnO thin films deposited by sol-gel techniques are summarized in Table 4.3. As compared to these reported values, it is seen that the FOM value for AZO515 in our study with the dopant concentration of 0.5 at% (as estimated by SRIM) is best; indicating to the fact that post growth doping of Al via ion implantation may be more effective for controlled doping to make the sol-gel grown films highly conducting and visible light transparent.

[98]

Table 4.2 T_{av}, R_s, and FOM values of the Al implanted ZnO films.

Sample name	T_{av} (%)	R_s ($\times 10^3$ Ω/sq)	Haacke FoM (Ω^{-1})
Pristine	91.75	1.95	2.17×10^{-4}
AZO113	90.54	14.7	2.52×10^{-5}
AZO513	89.83	71.7	4.77×10^{-6}
AZO114	89.39	53.08	6.13×10^{-6}
AZO514	89.15	6.58	4.82×10^{-5}
AZO115	88.44	2.38	1.23×10^{-4}
AZO515	84.15	0.186	9.57×10^{-4}
AZO615	82.20	0.156	9.03×10^{-4}

Table 4.3 Al doping %, thickness, ρ, R_s, n, μ_h, T_{av} or T_{max} in the visible region and Haacke FOM values of various reported sol-gel grown AZO films.

Doping % of Al	Thickness (nm)	ρ (Ω.cm)	R_s (Ω/sq)	n (cm^{-3})	μ_h	T_{av} or T_{max} (%)	Haacke FoM (Ω^{-1})	Ref.
1 mol%	-	2.95×10^{-1}	-	8.9×10^{19}	0.7*	50	-	[33]
0.8 mol%	571	9.89×10^{-4}	18.5	1.51×10^{20}	41.9	-	-	[36]
1 at%	-	1.49×10^{-2}	-	-	-	-	-	[37]
1 at%	12500	4.27×10^{-3}	3.42	5.21×10^{19}	16.2	-	-	[38]
2.7 at%	-	-	14.5×10^{6}	-	-			[39]
1.25 at%	-	1.6×10^{-3}	-	1.5×10^{20}	6.41			[40]
2 at%	550	5.9×10^{-1}	1.07×10^{4}	3.13×10^{17}	33.5	-	-	[41]
1 at%	-	2.5×10^{-3}	-	6.5×10^{19}*	7.6			[42]
1.5 at%	-	-	3.53×10^{6}	-	-	97.83	2.28×10^{-7}*	[43]
1 at%	101*	2.52×10^{-1}	2.49×10^{4}	~3×10^{18}	9	~70	1.13×10^{-6}*	[44]
1.6 mol%	-	-	1.54×10^{4}	-	-	87.5	1.71×10^{-5}*	[45]
0.53 mol%	300	-	1.32×10^{4}	-	-	94.79	4.43×10^{-5}*	[18]

Doping % of Al	Thickness (nm)	ρ (Ω.cm)	R_s (Ω/sq)	n (cm^{-3})	μ_h	T_{av} or T_{max} (%)	Haacke FoM (Ω^{-1})	Ref.
1 mol%	150	6.45×10^{-2}*	4.3×10^3	5.3×10^{19}*	2.9*	85	4.58×10^{-5}*	[46]
5 at%	525	4.5×10^{-1}	8.57×10^3	5.22×10^{16}	2.66	95	6.98×10^{-5}*	[47]
0.5 mol %	234*	3.77×10^{-2}	1.61×10^3	-	-	87.2	1.58×10^{-4}*	[48]
2 at%	200	4.4×10^{-2}	2.2×10^3	-	-	90	1.58×10^{-4}*	[49]
2 at%	108.5	5.9×10^{-3}	5.48×10^2	-	-	79.1	1.72×10^{-4}	[6]
1 at %	260	1.64×10^{-2}	6.31×10^2	2.7×10^{19}	-	85*	3.12×10^{-4}*	[31]
1 at%	780*	3.2×10^{-2}	4.10×10^2	-	-	83*	3.78×10^{-4}*	[50]
2 wt%	1030	2.14×10^{-4}	2.08	-	-	48.99	3.82×10^{-4}	[51]
2 at%	326	7.56×10^{-3}	2.32×10^2	2.76×10^{19}	29.73	80	4.62×10^{-4}	[52]
10 mol%	357	2.35×10^{-2}	6.58×10^2	6.78×10^{19}	3.92	91.4	6.18×10^{-4}*	[53]
1 at%	200	1.1×10^{-2}	5.5×10^2	-	-	90	6.33×10^{-4}*	[54]
0.5 at%	350	6.53×10^{-3}	1.86×10^2	1.55×10^{20}	6.16	84.15	9.57×10^{-4}	This work

*Calculated from the given data

4.3.2 Role of defects

4.3.2.1 Defect formation: SRIM calculation

Since the films at initial fluences of Al implantation is more resistive than that of the pristine, some structural changes in the implanted films are expected. To gain an understanding on these implantation-induced structural changes, SRIM-2008 full-cascade simulation code [55] has been used. The main parameters [56-58] used in this numerical computation are shown in Table 4.4. Fig. 4.7(a) shows the Gaussian distribution of 100 keV Al ions along the depth of ZnO films. The estimated total penetration depth of the Al ions is about 300 nm, where the maximum concentration of implanted Al atoms is observed at a depth of 138 nm (projected range, R_p). The estimated Al concentrations at R_p are about 0.001

at.% for the lowest fluence of 1×10^{13} ions/cm^2 and 0.6 at.% at the highest fluence of 6×10^{15} ions/cm^2, which is consistent with our EDS and XPS results. The at.% of Al in our samples is very low as compared to other reports on Al doped sol-gel grown ZnO films as shown in Table 4.3. As discussed in the chapter 2, the energy loss process is executed via both the electronic energy loss (S_e) and nuclear energy loss (S_n), when the implanted Al ions move inside the films [57]. The energy loss through S_n knocks out the target atoms from their lattice positions and produces large concentration of point defects, vacancies etc., inside the target material. Fig. 4.7(b) shows the SRIM simulated distribution of V_{Zn} and V_O due to 100 keV Al implantation into ZnO films. It clearly reveals that the number of implantation-induced V_{Zn} is always greater as compared to V_O at any fluence of Al implantation. It can also be inferred from Fig. 4.7(b) that the implantation generated vacancies are extended from the surface to 250 nm depth

Table 4.4 Parameters used in SRIM calculation

Ion	Al	
Energy of the ion (keV)	100	
Incident angle of the ion (degrees)	0	
Number of ions	99999	
Density of ZnO target	4 g/cm^3	
Displacement energy (eV)	Zn	O
	34	44
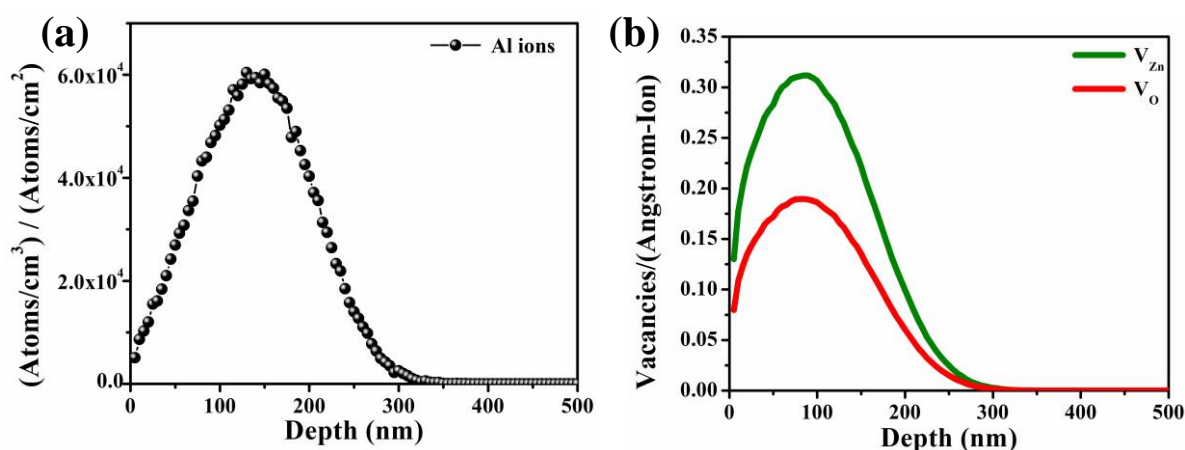
Fig. 4.7 SRIM calculated distribution of (a) Al ions and (b) V_{Zn} and V_O defects.

4.3.2.2 Annealing in excess Zn

As observed in the above SRIM calculation that Al implantation leads to the formation of more V_{Zn} defects, one another set of Al implanted samples was annealed in excess Zn ambient in order to understand the influence of these V_{Zn} defects on the electrical properties. The values of ρ, n, and μ_h for Zn annealed Al implanted ZnO films have been compared with those of the Ar annealed films in Fig. 4.8. It is seen that ρ for Zn annealed films is much less than those of the Ar annealed films up to the Al fluence of 1×10^{15} ions/cm^2, beyond which the value is almost same (Fig. 4.8(a)). On the other hand, the values of n for Zn annealed films are greater than those of Ar annealed films up to the same fluence of 1×10^{15} ions/cm^2 and thereafter however, the values become less (Fig. 4.8(b)). Due to annealing in excess Zn, it is expected that Zn would diffuse into the ZnO lattice and sits in the V_{Zn} positions and/or creates Zn_i defects. In both cases, the n-type conductivity is supposed to be increased. Since the values of μ_h for Zn annealed films are larger than those of the Ar annealed films (Fig. 4.8(c)), Zn_i defects are not likely to be formed in this case because Zn_i defects would otherwise increase the ionized impurity scattering and thus decrease the value of μ_h. Moreover, Zn_i defects have a very low diffusion barrier, so it is highly improbable to find these defects in annealed ZnO films. Therefore, the results indicate that V_{Zn} defects most probably are reduced as a result of Zn diffusion to the V_{Zn} sites [59]. From this point of view, it is confirmed that the vacancies like point defects are created as a result of implantation and are increased as the fluence of Al is increased, which have already been predicted from the SRIM calculation. The degree of repairing of V_{Zn} with either by incident Al ion or by recoiled Zn atoms at initial fluences is very low, rather Al ions occupy the interstitial positions, which causes the degradation in the electrical properties for Ar annealed samples. Due to annealing with Zn, V_{Zn} defects are recovered resulting in restoration of the electrical properties. As the fluence increases, a huge number of Al ions incident on the samples resulting in more Al in the Zn sites. The plot of the ratio of carrier concentration of Zn annealed samples, n(Zn) to the carrier concentration of Ar annealed samples, n(Ar) with the Al ion fluences in Fig. 4.8(d) signifies the increment of carrier concentration after annealing in excess Zn. The ratio n(Zn)/n(Ar) increases up to Al ion fluence of $\sim1\times10^{14}$ ions/cm^2 beyond which the ratio starts to decrease. The effect of Al ion implantation and subsequent annealing treatment on the ZnO lattice structure can be explained with a schematic presented in Fig. 4.9.
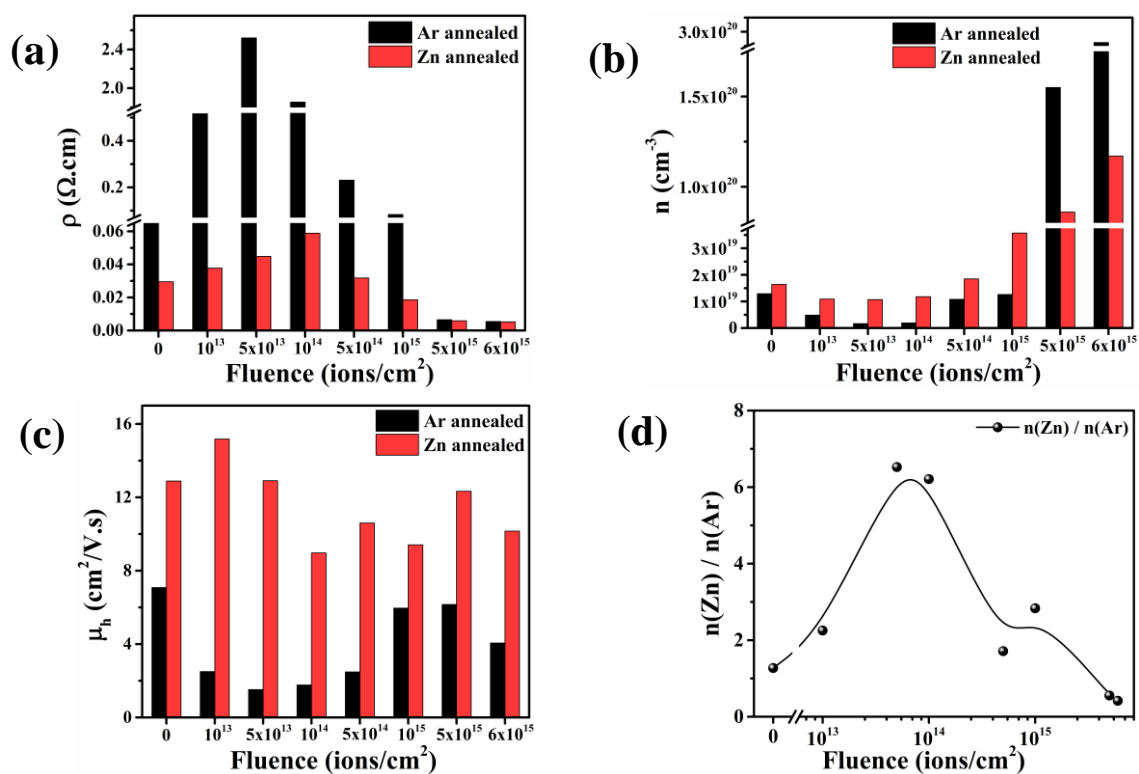
Fig. 4.8 Comparison of (a) ρ, (b) n, (c) μ_h values between Ar annealed and Zn annealed samples, (d) ratio of n(Zn) to n(Ar).
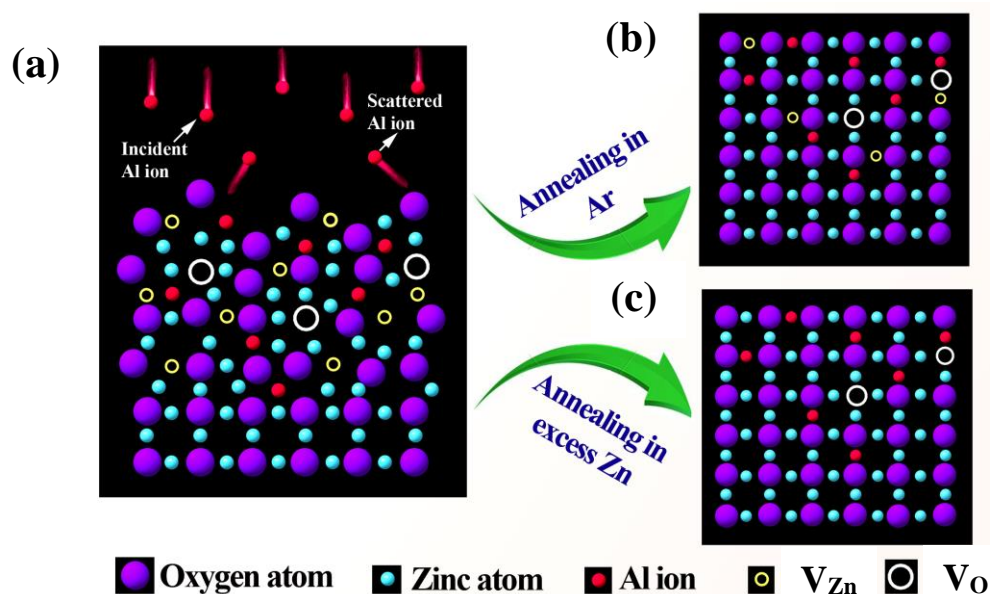
Fig. 4.9 (a) illustrates the distorted lattice positions and the formation of intrinsic defects due to energetic Al ion implantation, (b) shows the recovery of V_{Zn} and inclusion of Al ions in Zn sites due to annealing in Ar ambient, (c) elucidates the recovery of V_{Zn} as well as proper incorporation of Al in Zn sites after annealing in excess Zn ambient.

4.3.2.3 PL properties

The RT PL spectra of pristine and Al implanted and subsequently Ar annealed samples are shown in Fig. 4.10(a). The pristine ZnO film exhibits a strong NBE emission in UV region at around 3.28 eV, mainly due to the free exciton (FX) recombination and a broad DL emission in the visible region ranging from 1.75 to 2.85 eV peaking at around 2.40 eV [14, 60, 61]. With an increase in the Al ion fluence the intensities of both NBE and DL emissions are reduced monotonically. Interestingly, the NBE peak is broadened gradually and merges with the DL emission peak with an increase in the fluence. V_{Zn} defects are mostly known to be responsible for the DL emission at around 2.40 eV [62, 63]. With an increase in the fluence, V_{Zn} and their complexes as well as other defects dominate in the films and form radiative and non-radiative recombination centres [64]. The energy levels of which are spread right from the beneath of CBM to deep into the band gap. Thus, the band edge and DL emission peaks broaden and merge with each other. The RT PL spectra of Zn annealed samples in Fig. 4.10(b) as compared to the spectra in Fig. 4.10(a) show that after annealing with Zn, the nature and intensity of the UV PL peak intensity is recovered to some extent and enhanced for the samples up to a fluence of 1×10^{14} ions/cm^2. The reason behind the enhancement in the UV PL peak may be attributed to a reduced contribution from the recombination involving V_{Zn} due to diffusion of Zn in V_{Zn} sites. This is at par with the electrical transport data for the Zn annealed films.
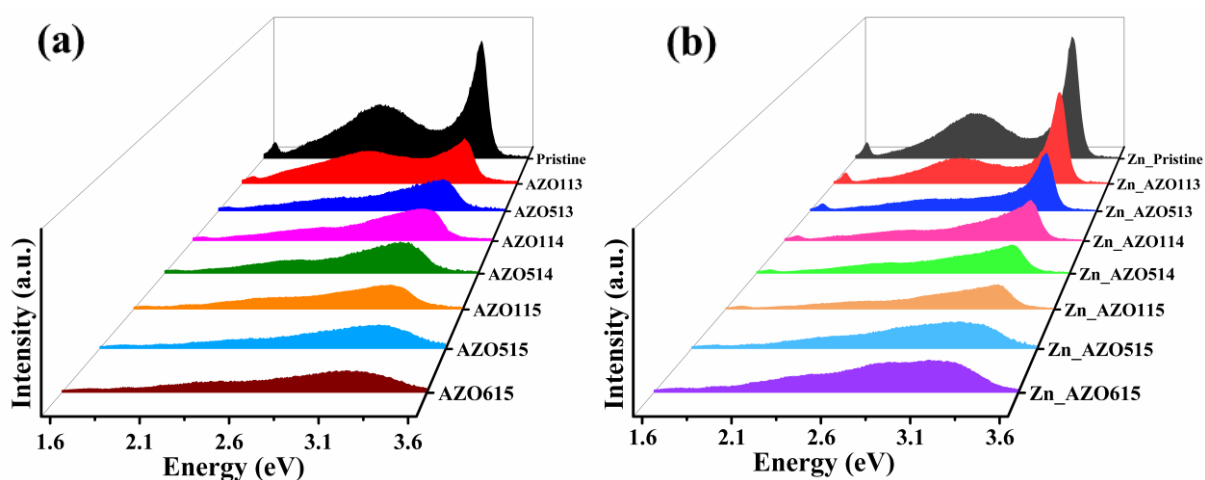
Fig. 4.10 RT PL spectra of pristine and Al implanted samples after annealing in (a) Ar and (b) excess Zn ambient.

4.4 Conclusions

In summary, implantation in sol–gel ZnO films with Al ions with various fluences lead to the formation of structural defects causing modification in the electrical and optical transmission properties. The implantation-induced V_{Zn} defects play a crucial role in controlling the electrical transport mechanism. For the highest fluence of 6×10^{15} ions/cm^2, the R_s is found to be 156 Ω/sq with an average visible transmission of 82%. The FOM value of our ZnO film implanted is the highest as compared to the FOM values of the reported Al doped sol-gel ZnO films indicating not only a probable use of the film as a TCO layer but also offers an opportunity to control the conductivity along with its transparency. Our study also provides an in-depth understanding on the mechanism of the implantation induced modification in the electrical transport properties.

4.5 References

[1] J. Steinhauser, S. Fay, N. Oliveira, E. Vallat-Sauvain, C. Ballif, Transition between grain boundary and intragrain scattering transport mechanisms in boron-doped zinc oxide thin films, Appl. Phys. Lett., 90 (2007).

[2] A. Sarkar, S. Ghosh, S. Chaudhuri, A.K. Pal, STUDIES ON ELECTRON-TRANSPORT PROPERTIES AND THE BURSTEIN-MOSS SHIFT IN INDIUM-DOPED ZNO FILMS, Thin Solid Films, 204 (1991) 255-264.

[3] S. Ghosh, A. Mallick, B. Dou, M. Van Hest, S.M. Garner, D. Basak, A novel blanket annealing process to achieve highly transparent and conducting Al doped ZnO thin films: Its mechanism and application in perovskite solar cells, Sol. Energy, 174 (2018) 815-825.

[4] P.S. Shewale, S.H. Lee, Y.S. Yu, Pulse repetition rate dependent structural, surface morphological and optoelectronic properties of Ga-doped ZnO thin films grown by pulsed laser deposition, Journal of Alloys and Compounds, 725 (2017) 1106-1114.

[5] J. Mass, P. Bhattacharya, R.S. Katiyar, Effect of high substrate temperature on Al-doped ZnO thin films grown by pulsed laser deposition, Mater. Sci. Eng. B-Solid State Mater. Adv. Technol., 103 (2003) 9-15.

[6] M.H. Nateq, R. Ceccato, Enhanced Sol-Gel Route to Obtain a Highly Transparent and Conductive Aluminum-Doped Zinc Oxide Thin Film, Materials, 12 (2019).

[7] J. Lee, J. Metson, P.J. Evans, R. Kinsey, D. Bhattacharyya, Implanted ZnO thin films: Microstructure, electrical and electronic properties, Appl. Surf. Sci., 253 (2007) 4317-4321.

[8] T. Viseu, J.A. de Campos, A.G. Rolo, T. de Lacerda-Aroso, M.F. Cerqueira, E. Alves, ZnO Thin Films Implanted with Al, Sb and P: Optical, Structural and Electrical Characterization, J. Nanosci. Nanotechnol., 9 (2009) 3574-3577.

[9] J. Kennedy, P.P. Murmu, J. Leveneur, G.V.M. Williams, R.L. Moody, T. Maity, S.V. Chong, Enhanced Power Factor and Increased Conductivity of Aluminum Doped Zinc Oxide Thin Films for Thermoelectric Applications, J. Nanosci. Nanotechnol., 18 (2018) 1384-1387.

[10] H. Lee, K. Sivashanmugan, C.Y. Kao, J.D. Liao, Fabrication of highly transparent Al-ion-implanted ZnO thin films by metal vapor vacuum arc method, Jpn. J. Appl. Phys., 56 (2017).

[11] T. Matsuda, M. Furuta, T. Hiramatsu, H. Furuta, T. Hirao, Sheet resistance and crystallinity of Ga- and Al-implanted zinc oxide thin films with postannealing, J. Vac. Sci. Technol. A, 25 (2007) 706-710.

[12] Z.Q. Chen, M. Maekawa, S. Yamamoto, A. Kawasuso, X.L. Yuan, T. Sekiguchi, R. Suzuki, T. Ohdaira, Evolution of voids in Al+-implanted ZnO probed by a slow positron beam, Physical Review B, 69 (2004).

[13] S. Kohiki, M. Nishitani, T. Wada, Enhanced electrical conductivity of zinc oxide thin films by ion implantation of gallium, aluminum, and boron atoms, J. Appl. Phys., 75 (1994) 2069-2072.

[14] A. Das, S. Ghosh, A.D. Mahapatra, D. Kabiraj, D. Basak, Highly enhanced ultraviolet to visible room temperature photoluminescence emission ratio in Al implanted ZnO nanorods, Appl. Surf. Sci., 495 (2019) 143615.

[15] M. Kumar, R. Singh, S. Nandy, A. Ghosh, S. Rath, T. Som, Tunable optoelectronic properties of pulsed dc sputter-deposited ZnO:Al thin films: Role of growth angle, J. Appl. Phys., 120 (2016) 015302.

[16] J. Nomoto, K. Inaba, S. Kobayashi, T. Watanabe, H. Makino, T. Yamamoto, Characteristics of Carrier Transport and Crystallographic Orientation Distribution of Transparent Conductive Al-Doped ZnO Polycrystalline Films Deposited by Radio-Frequency, Direct-Current, and Radio-Frequency-Superimposed Direct-Current Magnetron Sputtering, Materials, 10 (2017).

[17] M.R. Islam, M. Rahman, S.F.U. Farhad, J. Podder, Structural, optical and photocatalysis properties of sol–gel deposited Al-doped ZnO thin films, Surfaces and Interfaces, 16 (2019) 120-126.

[18] G.H. Jo, S.H. Kim, J.H. Koh, Enhanced electrical and optical properties based on stress reduced graded structure of Al-doped ZnO thin films, Ceram. Int., 44 (2018) 735-741.

[19] X. Zi-qiang, D. Hong, L. Yan, C. Hang, Al-doping effects on structure, electrical and optical properties of c-axis-orientated ZnO:Al thin films, Materials Science in Semiconductor Processing, 9 (2006) 132-135.

[20] H.C. Wang, C.H. Liao, Y.L. Chueh, C.C. Lai, P.C. Chou, S.Y. Ting, Crystallinity improvement of ZnO thin film by hierarchical thermal annealing, Opt. Mater. Express, 3 (2013) 295-306.

[21] A. Turos, P. Jozwik, M. Wojcik, J. Gaca, R. Ratajczak, A. Stonert, Mechanism of damage buildup in ion bombarded ZnO, Acta Mater., 134 (2017) 249-256.

[22] R. Sankar ganesh, M. Navaneethan, G.K. Mani, S. Ponnusamy, K. Tsuchiya, C. Muthamizhchelvan, S. Kawasaki, Y. Hayakawa, Influence of Al doping on the structural, morphological, optical, and gas sensing properties of ZnO nanorods, Journal of Alloys and Compounds, 698 (2017) 555-564.

[23] J. Wang, Y. Li, Y. Kong, J. Zhou, J. Wu, X. Wu, W. Qin, Z. Jiao, L. Jiang, Non-fluorinated superhydrophobic and micro/nano hierarchical Al doped ZnO film: the effect of Al doping on morphological and hydrophobic properties, RSC Adv., 5 (2015) 81024-81029.

[24] N. Kumar, A.H. Chowdhury, B. Bahrami, M.R. Khan, Q. Qiao, M. Kumar, Origin of enhanced carrier mobility and electrical conductivity in seed-layer assisted sputtered grown Al doped ZnO thin films, Thin Solid Films, 700 (2020) 137916.

[25] M. Pal, S. Bera, S. Sarkar, S. Jana, Influence of Al doping on microstructural, optical and photocatalytic properties of sol–gel based nanostructured zinc oxide films on glass, RSC Adv., 4 (2014) 11552-11563.

[26] T. Basu, M. Kumar, S. Nandy, B. Satpati, C.P. Saini, A. Kanjilal, T. Som, Thickness-dependent blue shift in the excitonic peak of conformally grown ZnO:Al on ion-beam fabricated self-organized Si ripples, J. Appl. Phys., 118 (2015).

[27] J.F. Moulder, Handbook of X-Ray Photoelectron Spectroscopy, Physical Electronics, (1995) 230-232.

[28] A. Nakrela, N. Benramdane, A. Bouzidi, Z. Kebbab, M. Medles, C. Mathieu, Site location of Al-dopant in ZnO lattice by exploiting the structural and optical characterisation of ZnO:Al thin films, Results in Physics, 6 (2016) 133-138.

[29] C. Manoharan, G. Pavithra, M. Bououdina, S. Dhanapandian, P. Dhamodharan, Characterization and study of antibacterial activity of spray pyrolysed ZnO:Al thin films, Appl. Nanosci., 6 (2016) 815-825.

[30] S. Kumar, F. Singh, A. Kapoor, Study of valence band tailing effect induced by electronic excitations in nanocrystalline cadmium oxide thin films, Optik, 127 (2016) 2055-2058.

[31] S. Mridha, D. Basak, Aluminium doped ZnO films: electrical, optical and photoresponse studies, J. Phys. D-Appl. Phys., 40 (2007) 6902-6907.

[32] M. Baradaran, F.E. Ghodsi, C. Bittencourt, E. Llobet, The role of Al concentration on improving the photocatalytic performance of nanostructured ZnO/ZnO:Al/ZnO multilayer thin films, Journal of Alloys and Compounds, 788 (2019) 289-301.

[33] M. Chaik, A. Outzourhit, A. Almaggoussi, A. El Hichou, T. Jannane, Sol-gel Aluminum-doped ZnO thin films: synthesis and characterization, Journal of Materials and Environmental Science, 8 (2019) 160-168.

[34] H. Kim, S. Jin, L. Wen, Y.-s. Choi, I. Choi, M. Hori, J.G. Han, Study on change of electrical properties of ZnO thin films deposited in low temperature facing targets magnetron sputtering (FTS) system with H2 and O2 flow rate changes, Journal of Ceramic Processing Research, 14 (2013) 188-193.

[35] G. Haacke, New figure of merit for transparent conductors, J. Appl. Phys., 47 (1976) 4086-4089.

[36] L. Meng, X.G. Yang, T. Yang, Self-Flattened ZnO:Al Transparent Conductive Thin Films Derived by Sol-Gel Process, IEEE J. Photovolt., 8 (2018) 1149-1155.

[37] M. Maache, T. Devers, A. Chala, Al-doped and pure ZnO thin films elaborated by sol-gel spin coating process for optoelectronic applications, Semiconductors, 51 (2017) 1604-1610.

[38] M.U. Shahid, K.M. Deen, A. Ahmad, M.A. Akram, M. Aslam, W. Akhtar, Formation of Al-doped ZnO thin films on glass by sol-gel process and characterization, Appl. Nanosci., 6 (2016) 235-241.

[39] M. Yilmaz, D. Tatar, E. Sonmez, C. Cirak, S. Aydogan, R. Gunturkun, Investigation of Structural, Morphological, Optical, and Electrical Properties of Al Doped ZnO Thin Films Via Spin Coating Technique, Synth. React. Inorg. Met.-Org. Nano-Metal Chem., 46 (2016) 489-494.

[40] B. Hu, J. Xu, J. Wang, B. Liu, B. Du, Pressure effect on structural and electrical properties of AZO thin films annealed in N2/H2 atmosphere, Materials Letters, 232 (2018) 51-53.

[41] M. Dutta, T. Ghosh, D. Basak, N Doping and Al-N Co-doping in Sol-Gel ZnO Films: Studies of Their Structural, Electrical, Optical, and Photoconductive Properties, J. Electron. Mater., 38 (2009) 2335-2342.

[42] M.C. Jun, J.H. Koh, Effects of Annealing Temperature on Properties of Al-Doped ZnO Thin Films prepared by Sol-Gel Dip-Coating, J. Electr. Eng. Technol., 8 (2013) 163-167.

[43] M. Murugesan, D. Arjunraj, J. Mayandi, V. Venkatachalapathy, J.M. Pearce, Properties of Al-doped zinc oxide and In-doped zinc oxide bilayer transparent conducting oxides for solar cell applications, Materials Letters, 222 (2018) 50-53.

[44] L.B. Duan, X.R. Zhao, Y.Y. Zhang, H. Shen, R.D. Liu, Fabrication of flexible Al-doped ZnO films via sol-gel method, Materials Letters, 162 (2016) 199-202.

[45] S.Y. Kuo, W.C. Chen, F.I. Lai, C.P. Cheng, H.C. Kuo, S.C. Wang, W.F. Hsieh, Effects of doping concentration and annealing temperature on properties of highly-oriented al-doped ZnO films, J. Cryst. Growth, 287 (2006) 78-84.

[46] M.C. Jun, S.U. Park, J.H. Koh, Comparative studies of Al-doped ZnO and Ga-doped ZnO transparent conducting oxide thin films, Nanoscale Res. Lett., 7 (2012).

[47] G. El Hallani, S. Nasih, N. Fazouan, A. Liba, M. Khuili, M. Sajieddine, M. Mabrouki, L. Laanab, E.H. Atmani, Comparative study for highly Al and Mg doped ZnO thin films elaborated by sol gel method for photovoltaic application, J. Appl. Phys., 121 (2017).

[48] J. Kim, J.H. Ji, S.W. Min, G.H. Jo, M.W. Jung, M.J. Park, S.K. Lee, J.H. Koh, Enhanced conductance properties of UV laser/RTA annealed Al-doped ZnO thin films, Ceram. Int., 43 (2017) 3900-3904.

[49] W.M. Tsang, F.L. Wong, M.K. Fung, J.C. Chang, C.S. Lee, S.T. Lee, Transparent conducting aluminum-doped zinc oxide thin film prepared by sol-gel process followed by laser irradiation treatment, Thin Solid Films, 517 (2008) 891-895.

[50] V. Balaprakash, P. Gowrisankar, S. Sudha, R. Rajkumar, Aluminum doped ZnO transparent conducting thin films prepared by sol-gel dip coating technique for solar cells and optoelectronic applications, Mater. Technol., 33 (2018) 414-420.

[51] K.N. Tonny, R. Rafique, A. Sharmin, M.S. Bashar, Z.H. Mahmood, Electrical, optical and structural properties o transparent conducting Al doped ZnO (AZO) deposited by sol-gel spin coating, AIP Adv., 8 (2018).

[52] W.L. Liu, Y.F. Zhang, Blueshift of absorption edge and photoluminescence in Al doped ZnO thin films, Integr. Ferroelectr., 188 (2018) 112-120.

[53] L. Luo, M.D. Rossell, D. Xie, R. Erni, M. Niederberger, Microwave-Assisted Nonaqueous Sol-Gel Synthesis: From Al:ZnO Nanoparticles to Transparent Conducting Films, ACS Sustain. Chem. Eng., 1 (2013) 152-160.

[54] J.H. Lee, B.O. Park, Transparent conducting ZnO : Al, In and Sn thin films deposited by the sol-gel method, Thin Solid Films, 426 (2003) 94-99.

[55] J.F. Ziegler, J.P. Biersack, The Stopping and Range of Ions in Matter, in: D.A. Bromley (Ed.) Treatise on Heavy-Ion Science: Volume 6: Astrophysics, Chemistry, and Condensed Matter, Springer US, Boston, MA, 1985, pp. 93-129.

[56] A. Mondal, S. Pal, A. Sarkar, T.S. Bhattacharya, A. Das, N. Gogurla, S.K. Ray, P. Kumar, D. Kanjilal, K.D. Devi, A. Singha, S. Chattopadhyay, D. Jana, Raman spectroscopic analysis on Li, N and (Li,N) implanted ZnO, Mater. Sci. Semicond. Process, 80 (2018) 111-117.

[57] S. Chattopadhyay, S. Dutta, D. Jana, A. Sarkar, P. Kumar, D. Kanjilal, D.K. Mishra, S.K. Ray, Interplay of defects in 1.2 MeV Ar irradiated ZnO, J. Appl. Phys., 107 (2010).

[58] D.C. Look, G.C. Farlow, P. Reunchan, S. Limpijumnong, S.B. Zhang, K. Nordlund, Evidence for native-defect donors in n-type ZnO, Phys. Rev. Lett., 95 (2005).

[59] T. Ghosh, D. Basak, Enhanced mobility in visible-to-near infrared transparent Al-doped ZnO films, Sol. Energy, 96 (2013) 152-158.

[60] J. Kennedy, P.P. Murmu, E. Manikandan, S.Y. Lee, Investigation of structural and photoluminescence properties of gas and metal ions doped zinc oxide single crystals, Journal of Alloys and Compounds, 616 (2014) 614-617.

[61] P.P. Murmu, R.J. Mendelsberg, J. Kennedy, D.A. Carder, B.J. Ruck, A. Markwitz, R.J. Reeves, P. Malar, T. Osipowicz, Structural and photoluminescence properties of Gd implanted ZnO single crystals, J. Appl. Phys., 110 (2011).

[62] F. Fabbri, M. Villani, A. Catellani, A. Calzolari, G. Cicero, D. Calestani, G. Calestani, A. Zappettini, B. Dierre, T. Sekiguchi, G. Salviati, Zn vacancy induced green luminescence on non-polar surfaces in ZnO nanostructures, Sci Rep, 4 (2014).

[63] D. Sett, S. Sarkar, D. Basak, A successive photocurrent transient study to probe the sub-band gap electron and hole traps in ZnO nanorods, RSC Adv., 4 (2014) 58553-58558.

[64] P.K. Giri, S. Kumari, D.K. Goswami, Low energy oxygen implantation induced improved crystallinity and optical properties of surface modified ZnO single crystals, Appl. Surf. Sci., 256 (2009) 384-388.

CHAPTER-5

Role of defects in photoluminescence property of Al implanted ZnO nanorods

5.1 Introduction

In the chapter 1, it has been already described that besides incorporating impurities, the main feature of ion implantation is the creation of point defects (vacancies/interstitials) inside the target material due to the energetic ion collisions [1] and these implantation-indued defects are not completely restored with subsequent post-implantation annealing treatments [2]. It is well known that PL emission property of any material strongly depends on these intrinsic defects as well as doping impurities. To understand the change in the defect chemistry in ZnO NRs due to ion implantation, the PL characterization is, therefore, very much essential. Though, a significant amount of study on the optical and electrical properties of ion implanted ZnO thin films has been performed over the last decades [3-12] and some of which have already been discussed in the chapter 2, studies on ion implantation on ZnO NRs are seldom done [13-15], while these are appropriate for utilization in various nanoscale solid state devices. Second thing is that Al ion implantation may leads to the formation of highly conductive and highly visible light transparent ZnO films, which can be used as a TCO (as discussed in the previous chapter). Therefore, in this chapter, we have described the effect of Al ion implantation in the RT PL properties of ZnO NRs. The implanted ZnO NRs have been complementarily characterized to reveal the simultaneous modifications in the structural, microstructural, electrical, and photoconductivity properties. Being chemically inert, Ar is believed to occupy no lattice site, but creates structural damages and therefore, Ar implantation into ZnO NRs has also been carried out as a reference to eliminate the influence of implantation damage [16, 17].

5.2 Experimental details

First, ZnO NRs were grown on glass substrates by ACG method. The chemical reactions involved in ACG method has already been described in chapter 3. One set of as-grown ZnO NRs were then implanted with 100 keV Al ions having various fluences with ranging from 1×10^{13} to 1×10^{16} ions/cm^2. The details of the implantation have been described in the previous chapter. After Al implantation, the implanted ZnO NRs were annealed in Ar ambient at 450 °C for 1 h. Another set of as-grown ZnO NRs were implanted by Ar ions and subsequently annealed under similar conditions as it was for Al implanted samples. The nomenclature of the samples in this study is given in Table 5.1 with their detailed specifications. The unimplanted ZnO NRs were also annealed and have been considered as the pristine sample in this work.

Table 5.1 Nomenclature with detailed specifications of various ZnO NRs Samples.

Sample name	Specifications		
	Implanted Ion	Fluence (ions/cm^2)	Annealing condition
Pristine	unimplanted	0	Annealed in Ar ambient at temperature 450 °C for 1 h
Al/ZnO113	Al	1×10^{13}	
Al/ZnO513		5×10^{13}	
Al/ZnO114		1×10^{14}	
Al/ZnO514		5×10^{14}	
Al/ZnO115		1×10^{15}	
Al/ZnO515		5×10^{15}	
Al/ZnO116		1×10^{16}	
Ar/ZnO513	Ar	5×10^{13}	
Ar/ZnO114		1×10^{14}	
Ar/ZnO514		5×10^{14}	
Ar/ZnO115		1×10^{15}	

The structural, morphological, compositional, optical, and electrical analyses of the samples have been carried out using XRD, FESEM, TEM, EDS, XPS, PL, I-V, and photoconductivity measurements, respectively as described in the chapter 3. EDS and the elemental mapping were carried out using an equipment attached with the same TEM system.

5.3 Results and discussion

The XRD patterns of the pristine and ZnO NRs implanted with different fluences of Al as presented in Fig. 5.1(a) show the presence of sharp, narrow and well distinct peaks, which can be assigned to the diffractions from the respective (10$\bar{1}$0), (0002), (10$\bar{1}$1), (10$\bar{1}$2), (10$\bar{1}$3), and (11$\bar{2}$0) planes of hexagonal wurtzite ZnO (JCPDS card No. 36-1451). The diffraction peak originating from 0002 plane is the strongest among all the peaks, which implies that all of the samples share the same preferred orientation along the <002> direction and the wurtzite ZnO structure has not been destroyed after Al implantation. No extra diffraction peak from Al-related secondary phase or impurities is observed within the sensitivity of the XRD. Fig. 5.1(b) shows an enlarged view of the (002) peak of the pristine

and Al implanted ZnO NRs. Similar to the previous chapter, the (002) peak position has been shifted towards the lower 2θ value for Al implanted NRs as compared to the pristine. Though the shift is irregular at lower fluences, a clear peak shift towards the lower angle is observed at higher fluences. The values of c and FWHM of the (002) peak have been tabulated in Table 5.2. It is observed that the value of c slightly increases as the fluence of Al increases. The calculated values of FWHM of (002) peak of Al implanted samples are also slightly larger than that of the pristine and the change is quite significant at higher fluences. Fig. 5.1(c) shows the similar XRD patterns for Ar implanted NRs. Similar enlarged view of (002) peak for Ar implanted NRs has been shown in Fig. 5.1(d). The (002) diffraction peak of ZnO NRs has also been shifted towards lower 2θ value as compared to the pristine due to Ar implantation. The values of c and FWHM of (002) peak (Table 5.2) for Ar implanted NRs is also larger than that of the pristine. Now, the lower angle shift in both Al and Ar implanted NRs can be assigned to the existence of the tensile stress introduced by the lattice distortion [18]. However, an increment in c may be due to the broadening effect in (002) diffraction peak as described by Thandavan et al. [19]. The larger FWHM values of (002) peak for higher Al and Ar implanted NRs indicate to the deterioration of the crystallinity of the NRs [20], which is an obvious effect of ion implantation at higher fluences.

Table 5.2 Variation of the values of c and FWHM of (002) peak of pristine and Al ion implanted ZnO NRs.

Sample name	c (Å)	FWHM (002) (degree)
Pristine	5.213	0.184
Al/ZnO113	5.214	0.184
Al/ZnO513	5.215	0.187
Al/ZnO114	5.213	0.189
Al/ZnO514	5.214	0.187
Al/ZnO115	5.214	0.189
Al/ZnO515	5.217	0.189
Al/ZnO116	5.217	0.202
Ar/ZnO513	5.217	0.197
Ar/ZnO114	5.215	0.184
Ar/ZnO514	5.217	0.197
Ar/ZnO115	5.217	0.197
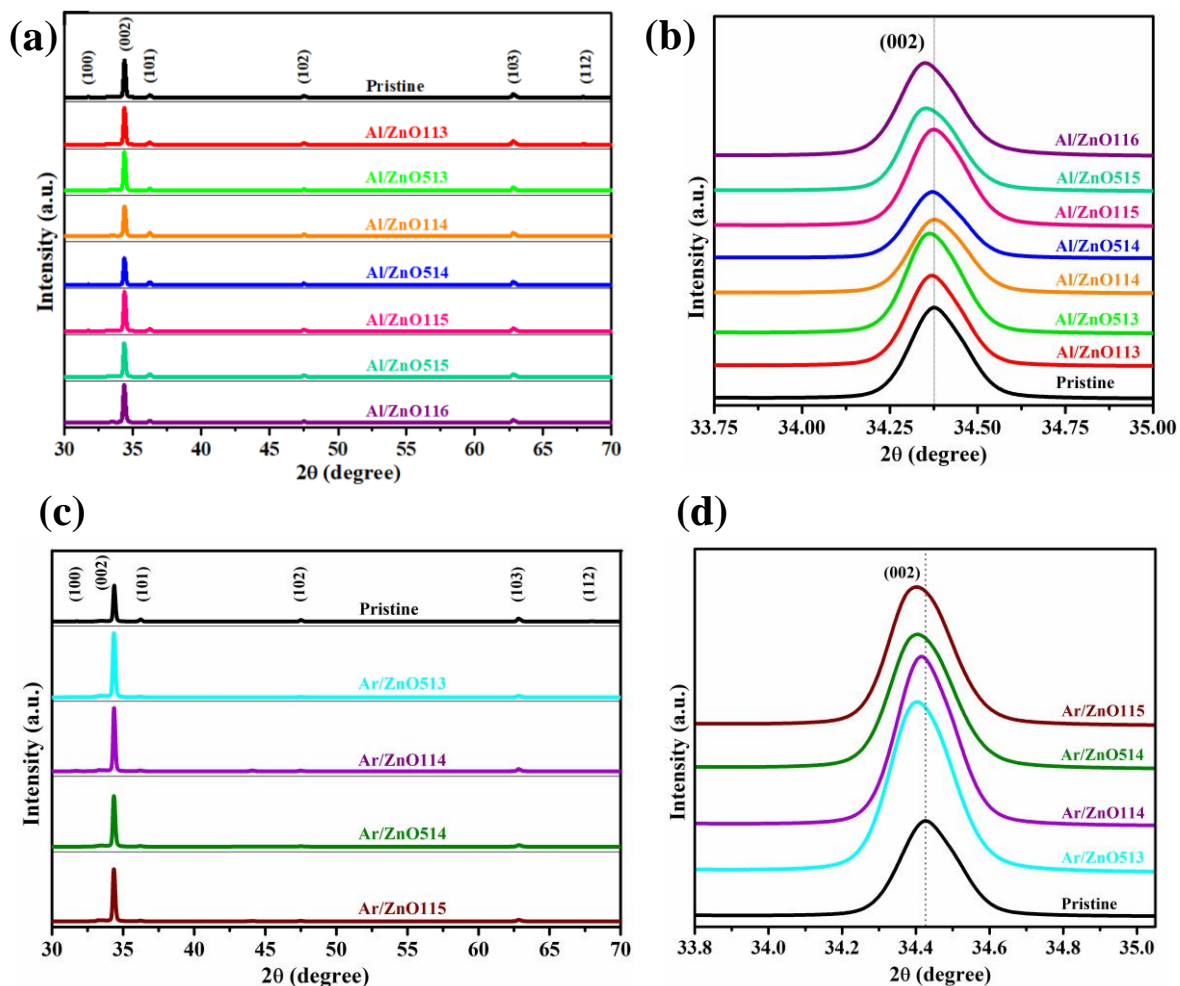
Fig. 5.1 (a) XRD patterns, (b) enlarged view of (002) peak of pristine and Al implanted ZnO NRs, (c) XRD patterns, (d) enlarged view of (002) peak of pristine and Ar implanted ZnO NRs.

Fig. 5.2(a)-(d) show the top view FESEM images of pristine and some representative ion implanted samples (Al/ZnO513, Al/ZnO116, and Ar/ZnO115). As seen in Fig. 5.2(a)-(d), the hexagonal ZnO NRs have been grown vertically on the seeded glass substrate, which is at par with the XRD results. The diameter and length (the inset in the Fig. 5.2(a), cross-sectional view) of the NRs are in the approximate range of 130 ± 20 nm and 750 ± 20 nm respectively. The top and side surfaces of pristine ZnO NRs are smooth (Fig. 5.2(a)). After implantation with Al and Ar, the rod-like structure of ZnO NRs is well maintained as shown in Fig. 5.2(b)-(d), suggesting ion implantation method have not destroyed the overall morphology and arrangement of the ZnO NRs array. The top surfaces of lower fluence Al implanted NRs (Al/ZnO513) are also as smooth as the pristine (Fig. 5.2(b)). However, the tips of the NRs are agglomerated to some extent (indicated by yellow arrows in Fig. 5.2(c)) for higher

fluence Al implantation (Al/ZnO116). This is probably due to dynamic annealing effect, resulting in an agglomeration and production of surface irregularities [21]. For Ar implanted NRs, such type of changes in the morphology have not been observed in the FESEM micrograph at the same magnification (Fig. 5.2(d)). However, this is in contrast with a previous report [22], where the tips of ZnO NRs have been modified due to Ar implantation.
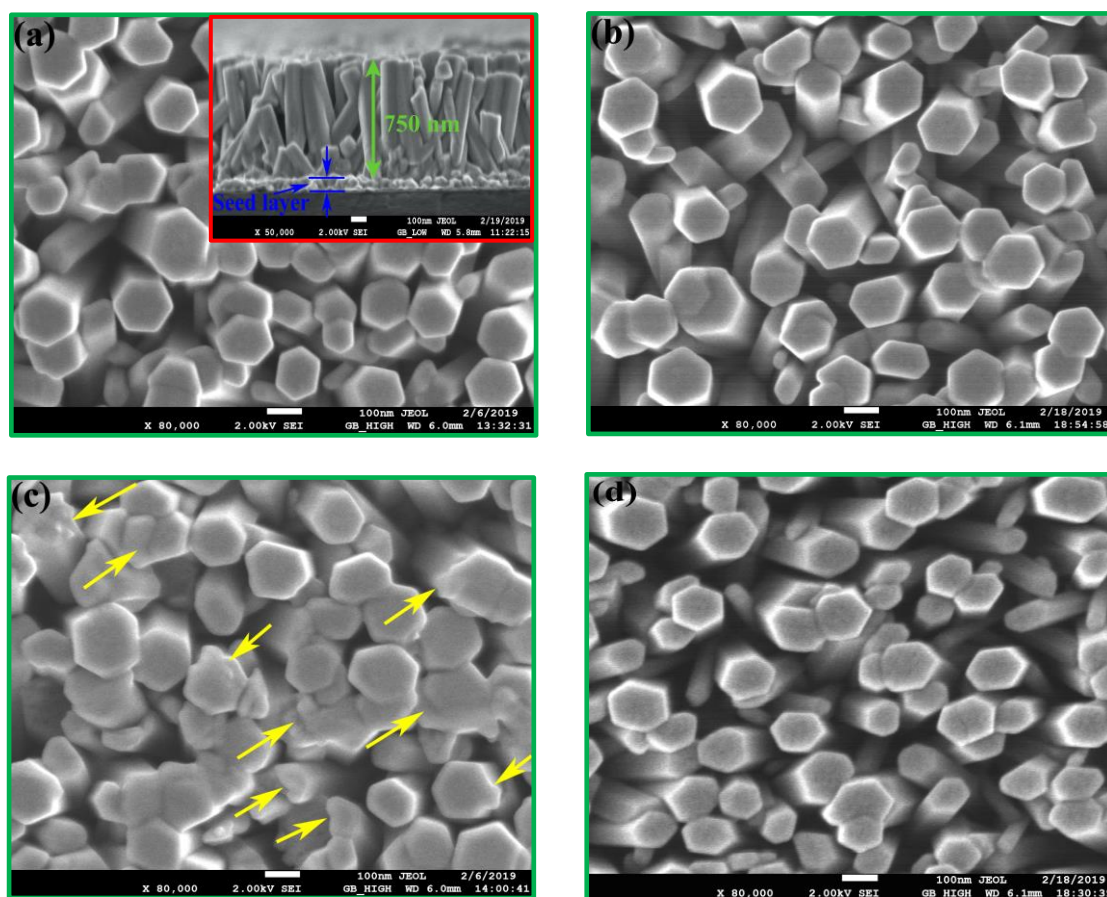
Fig. 5.2 FESEM images of (a) pristine and ion implanted ZnO NRs: (b) Al/ZnO513, (c) Al/ZnO116, (d) Ar/ZnO115.

The precise nature of the local morphological changes brought about by energetic Al and Ar ion bombardment is again manifested in TEM images of individual NR as shown in the insets of Fig. 5.3(a)-(d). It is noted that the mean diameter of the NRs is ~125 nm. The 1D structure of NRs has not been destroyed for the implantation of both Al and Ar ions, even at higher fluence of implantation (the insets in the Fig. 5.3(b)-(d)). Instead, rough surfaces are observed for the implanted NRs as compared to the pristine. The surface roughening is prominent in Al/ZnO116, and Ar/ZnO115. The nature of the surface modification caused by the ion bombardment is further studied at the atomic scale using HRTEM. The HRTEM

image of the pristine (Fig. 5.3(a)) shows that the rods are typically single crystalline and the outer walls are almost atomically flat with (0002) crystal planes. The clear observation of the lattice fringes in the HRTEM image indicates that the pristine ZnO NRs are free of extended defects such as dislocations, stacking faults, defect clusters, and so on [23]. The lattice spacing of pristine as calculated from HRTEM image (Fig. 5.3(a)) is about 0.26 nm, which corresponds to the interplanar distance of (0002) crystal plane of wurtzite ZnO [24, 25]. Any aggregated nanoparticles or lattice fringes related to Al or its oxide species are hardly found in Al implanted ZnO NRs, maybe due to the high dispersion of Al dopants in ZnO phase [24]. The HRTEM image (Fig. 5.3(b)) of lower Al implanted NRs is similar to that of pristine, which indicates the complete recovery of implantation induced structural damages in lower Al implanted NRs due to annealing at 450 °C. With an increase in the implantation fluence, the density of point defects increases because of a large number of collision cascades. Due to their high local concentration, point defects agglomerate to form extended defects [23], which in turns produce strain inside the ZnO lattice. As a result, the ordered lattice arrangement of (0002) planes get distorted as indicated by yellow circle in the HRTEM images of Al/ZnO116 sample in the Fig. 5.3(c). The lattice distortion in the outer part of ZnO NRs has also been observed for higher Ar implanted sample Ar/ZnO115 (marked by yellow circle in Fig. 5.3(d)).
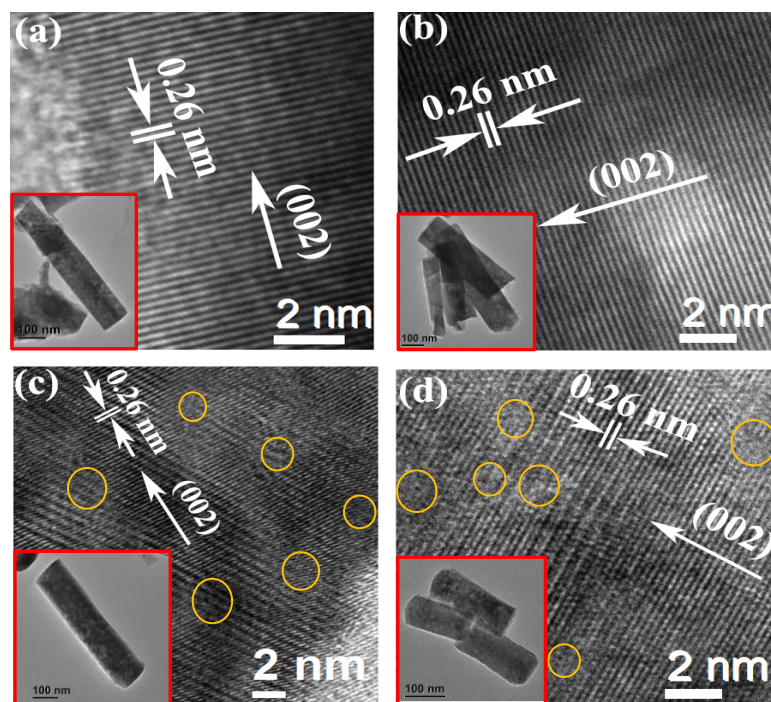
Fig. 5.3 HRTEM images of (a) pristine, (b) Al/ZnO513, (c) Al/ZnO116, and (d) Ar/ZnO115. The inset in each figure is the corresponding TEM image.

The EDS spectra for lower (5×10^{13} ions/cm^2) and higher fluence (1×10^{16} ions/cm^2) Al implanted ZnO NRs are shown in Fig. 5.4 (a)-(b), confirming the presence of Al, Zn, and O in the NRs with the average Al atomic concentration of 0.16 at.% and 1.30 at.%, respectively. It indicates indeed an increase in Al concentration with an increase in the implantation fluence. No trace of Ar was found in EDS spectra of Ar/ZnO115 (Fig. 5.4(c), though, a weak EDS peak for Ar has been reported for Ar bombarded ZnO NRs by Chatterjee et al. [22]. The insets in the Fig. 5.4 (a)-(b) show the elemental mapping of the Al/ZnO513 and Al/ZnO116 samples, which demonstrate that Al ions are distributed uniformly over the entire NRs. The uniformity of Al over an entire length of the NRs can be assigned to the diffusion of Al due to post implantation annealing treatment.
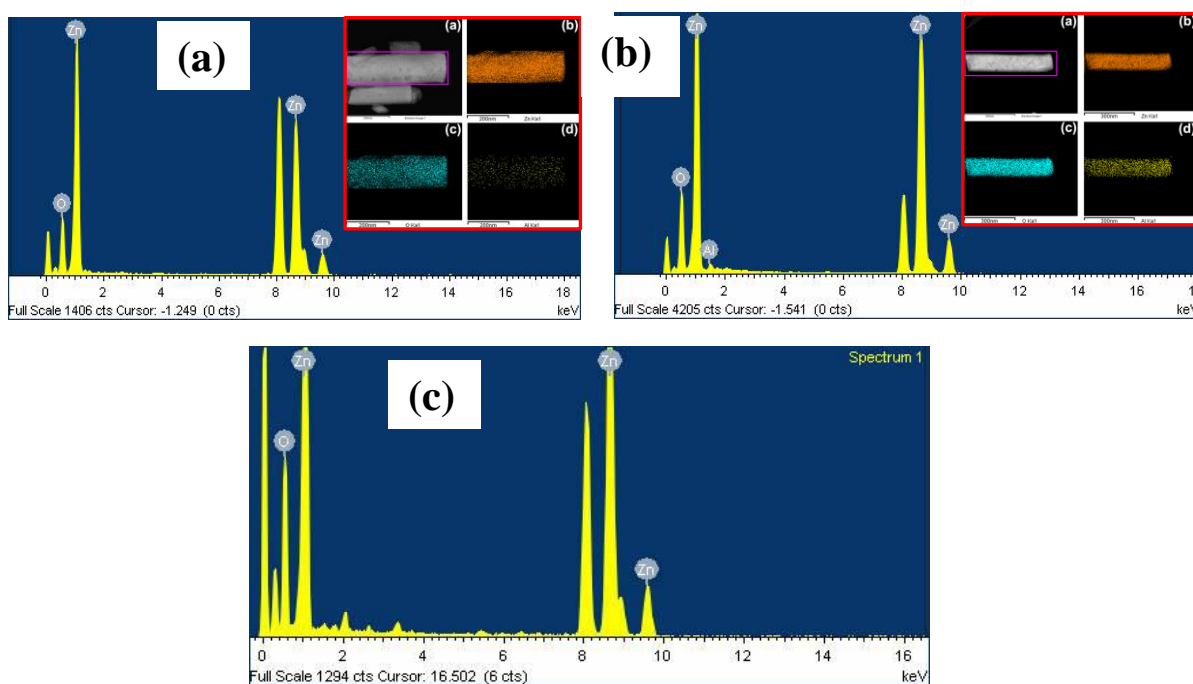
Fig. 5.4 EDS spectra of (a) Al/ZnO513, (b) Al/ZnO116, and (c) Ar/ZnO115. The insets are elemental mapping of (a) a single rod and distribution of (b) Zn, (c) O, (d) Al along the NR.

In order to show the effect on the optical emission properties ZnO NRs due to both Al and Ar ion implantations (before annealing treatments), the RT PL spectra of three representative samples has been illustrated in Fig. 5.5(a)-(c). As evident from the Fig. 5.5(a), as-grown NRs show a strong NBE emission in UV region at around 3.28 eV, mainly due to FX recombination and a broad DL emission in the visible region ranging from 1.75 to 2.85 eV peaking at around 2.20 eV. The ratio of NBE to DL emission intensity (I_{NBE} / I_{DL}) for as-

grown NRs is ~ 9. The broad yellow-orange emission at 2.20 eV is a commonly observed feature in the emission spectrum of ZnO nanostructures grown via solution-based methods which is resulted from the surface regions or near surface regions of the NRs [26, 27]. Yellow-orange emission is mainly attributed to excess O_2/OH adsorbed on the surface of NRs [28, 29]. After implantation even with a lower fluence (5×10^{13} ions/cm^2) of either Al or Ar, I_{NBE} is highly reduced for both cases (Fig. 5.5(b) and Fig. 5.5(c)), indicating a large onset of structural damage in the crystal lattice due to energetic ion implantation. I_{DL} also gets suppressed and the centroid is seen to be shifted towards higher energy at around 2.40 eV, which indicates that the visible emission shifts from yellow-orange to green one, implying the change in intrinsic defect chemistry mediated by the implanted ions. The ratio I_{NBE} / I_{DL} has been calculated for the as-implanted Al/ZnO513 and Ar/ZnO513 samples and the values are found to be ~2 and ~4 respectively, which are much lower than that of the as-grown NRs. The decreased value of the I_{NBE} / I_{DL} can be correlated to implantation induced surface defects which give rise to non-radiative recombination paths.
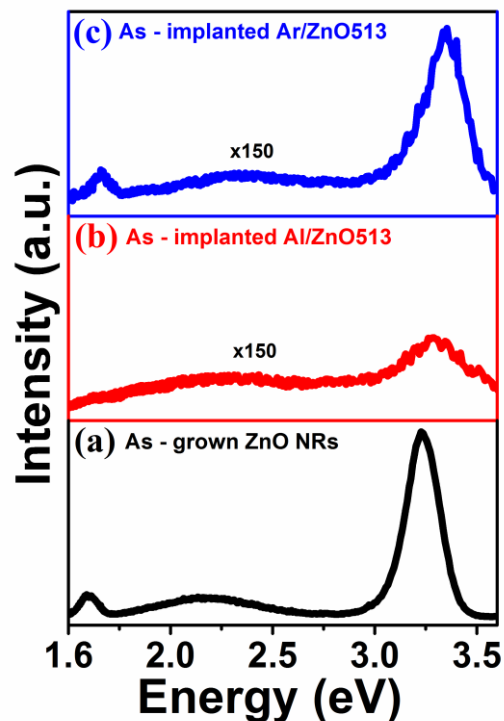
Fig. 5.5 RT PL spectra of (a) as-grown NRs, (b) as-implanted Al/ZnO513, and (c) as-implanted Ar/ZnO513 before annealing.

Fig. 5.6(a) shows the RT PL spectra of the annealed samples. As the as-grown NRs are annealed at 450 °C in Ar ambient, the I_{NBE} is increased by almost 8.5 times as compared to the as-grown NRs signifying the good crystallinity due to just annealing. For the Al implanted samples, post-implantation annealing activates the luminescent centers causing an enhancement in the intensities of both NBE and DL emissions. This is the reason why the PL peak intensities of Al implanted and subsequently annealed NRs have always been compared with the unimplanted but annealed NRs (pristine). Fig. 5.6(a) interestingly shows that the I_{NBE} is maximum for the NRs implanted with Al fluence of 1×10^{13} ions/cm^2 and the enhancement is almost 2.3 times higher than that of the pristine. With further increase in the Al fluence, the I_{NBE} again starts to decrease. However, a blue shift of around 53 meV is found in the NBE peak position for the higher fluence (1×10^{16} ions/cm^2) Al implanted NRs. The blue shift in NBE emission peak can be assigned to the BM effect due to Al incorporation inside ZnO lattice [30]. When a high fluence of Al is implanted into ZnO, the carrier concentration becomes high enough and thus the Fermi level moves into the CB due to the filling of the CB by electrons [31]. Then the recombination only occurs between the valence band and about or above the Fermi level, which leads to a blue shift of the UV peak [30]. Similar to I_{NBE}, initially an increase and then a decrease in the I_{DL} are found as the fluence increases. The DL emission center is also seen to be shifted to ~2.4 eV (green emission) as compared to the pristine. The highly enhanced I_{NBE} for lower fluence can reasonably be assigned to a recovery of the lattice damages by the annealing treatment, which is supported by our HRTEM results. As the implantation fluence increases, the number of structural damages as well as the density of the point defects are increased, which on annealing are not restored completely for higher fluences. The large concentration of the point defects forms extended defects, (discussed earlier) which act as non-radiative recombination centers reducing the intensity of the NBE PL emission. In order to make a comparison of the emissive properties, the ratio I_{NBE} / I_{DL} has been calculated as shown as a bar diagram in Fig. 5.6(b). It is observed that the ratio for the pristine is 54, while the ratio is highly enhanced to 73 and 75 for the lower fluences of 1×10^{13} and 5×10^{13} ions/cm^2 respectively. As the fluence increases, beyond 5×10^{13} ions/cm^2, the ratio I_{NBE}/I_{DL} decreases gradually and for 1×10^{16} ions/cm^2 it becomes 47, which is even lower than that of the pristine. To understand the role of Al in the enhancement of PL properties of ZnO NRs at lower fluence, similar analyses of PL emission spectra have been carried out for the Ar implanted ZnO NRs. It is seen from the Fig. 5.7(a) that as soon as Ar is implanted even with a fluence as low as 5×10^{13} ions/cm^2, the I_{NBE} steeply decreases as compared to the pristine and it decreases more and more as the fluence increases. However, in contrast to Al implantation, there is no NBE peak shift in case of Ar implantation, which indicates Al ions cause different type of change in the exitonic emission. The Fig. 5.7(a)

further shows that the DL emission intensity first increases and then decreases and its peak position is shifted towards higher energy side (~2.4) as compared to pristine, which is similar to Al implantation. Fig. 5.7(b) shows a drastic decrease in the ratio I_{NBE} / I_{DL} as soon as Ar is implanted in ZnO NRs, reaching a value as low as ~8 for the fluence 1×10^{15} ions/cm^2, which is about 7.6 times lower to that of the Al implanted sample for a similar fluence. Therefore, a comparison of the PL spectra of Al and Ar implanted samples suggests that a different recombination mechanism is involved in the PL emission for the Al implanted samples.
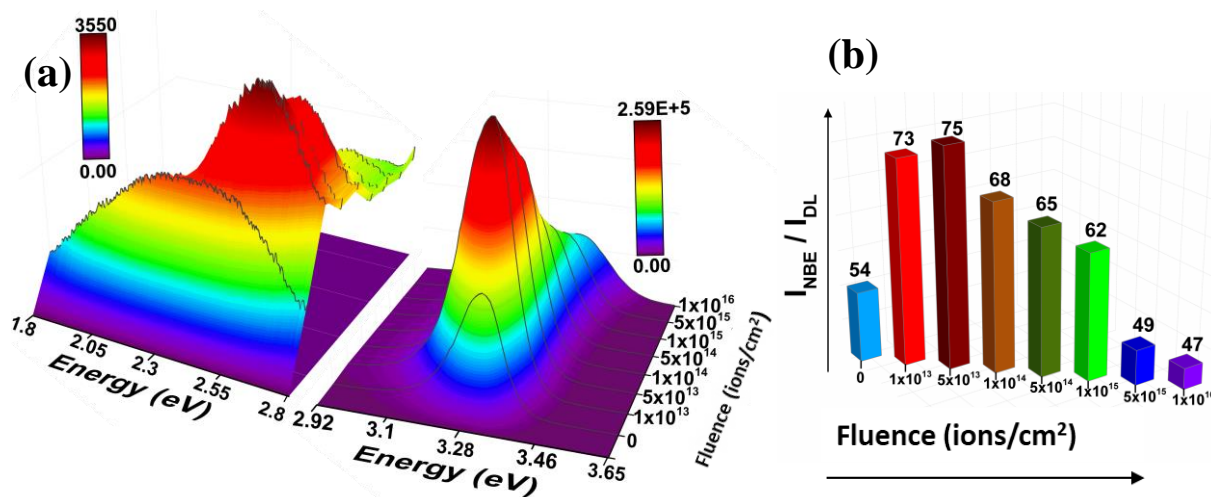
Fig. 5.6 (a) RT PL spectra and (b) the corresponding ratio I_{NBE} / I_{DL} of pristine and Al implanted ZnO NRs samples after annealing.
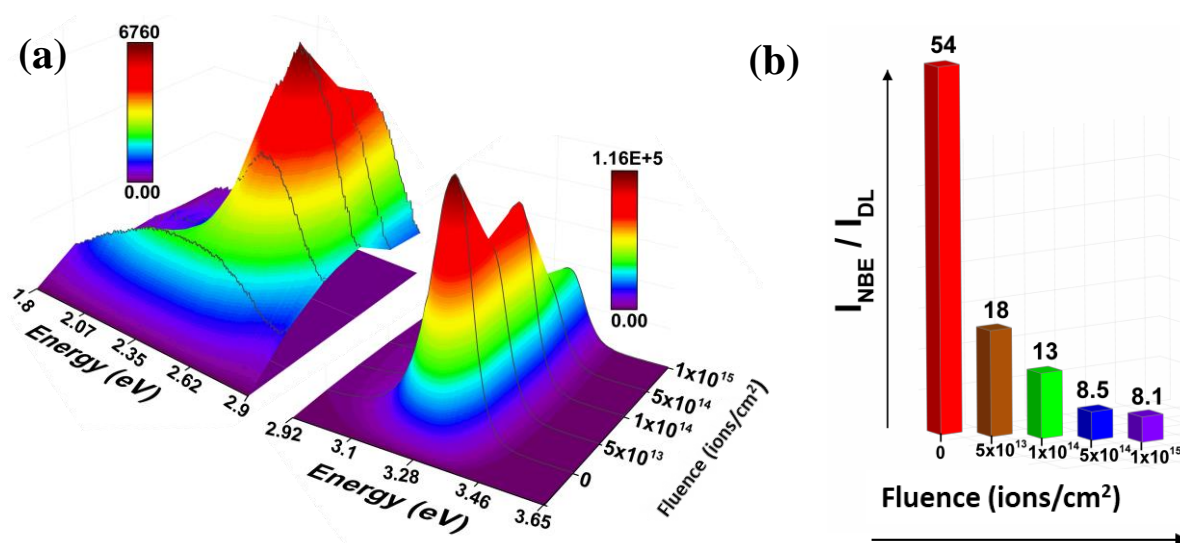
Fig. 5.7 (a) RT PL spectra and (b) the corresponding ratio I_{NBE} / I_{DL} of pristine and Ar implanted ZnO NRs samples after annealing.

In order to understand the carrier recombination mechanisms in pristine and ion implanted ZnO NRs, the excitation power dependence of I_{NBE} at RT has been measured, which is shown in Fig. 5.8. The variation of I_{NBE} with the excitation power (P) follows a power law: $I = \eta P^{\alpha}$, where η is the emission efficiency, and the exponent α represents the radiative recombination mechanism [32-34]. If the excitation energy is higher than the band gap value, the value of α falls into one of the following ranges: $1 < \alpha < 2$ for recombination of bound-excitons; For band-to-band transition, the value of α has been reported to be ~2; $0 < \alpha < 1$ for impurity or defect-related emission [33, 34]. As shown in Fig. 5.8(a), the value of α is 1.02 for pristine, indicating a recombination of bound excitons. Being an n-type material, the donor bound excitons dominates in ZnO. Previous reports [35, 36] suggest that the neutral donor bound excitons (D^0X) dominate the NBE PL spectra of ZnO at 10 K and beyond this temperature D^0X gradually loses its intensity and FX becomes intense due to the thermal-induced conversion from D^0X to FX [35]. Therefore, the observed RT NBE peak in the pristine can be assigned to the recombination of FX. For the samples Al/ZnO513 and Al/ZnO514, the values of α are 1.24 and 1.23, respectively (Fig. 5.8(b) and Fig. 5.8(c)), indicating bound excitonic recombination. Neglecting acceptor concentration in Al implanted ZnO NRs, it is more likely that the origin of UV emission is dominated by donor bound excitons, specifically these are the excitons bound to neutral Al donors (Al D^0X). The existence of bound excitons corresponding to the shallow Al donor has been conclusively demonstrated by a various implantation and back-doping experiments [37, 38]. The energy position of the neutral Al donor state is about 3.32 eV [10]. For lower fluence Al implanted samples, besides FX, Al D^0X takes the dominant role in the recombination process, which leads to the significant enhancement in the NBE emission. As the fluence of Al increases, the value of α for Al/ZnO515 becomes 0.971 (Fig. 5.8(d)). For Ar/ZnO513 and Ar/ZnO514, the values of α are found to be 0.996 and 0.959 respectively (Fig. 5.8(e) and Fig. 5.8(f)) and are similar to the value found for Al/ZnO515, implying similar structural changes for both cases. Neglecting the contribution from impurity related emission in Ar implanted samples, the excitons bound to defect states (DBX) at the particle surface can be assumed to play a dominant role in the recombination process for all Ar implanted as well as for higher fluence of Al implanted samples. Thonke et al. [39] suggest that the extended defects particularly stacking faults are responsible for non-radiative defect states. With the increase in fluence of Al and Ar, the density of extended defect increases and produces the non-radiative defect

centers. For higher fluence Al implanted samples, the Al D^0X and for Ar implanted samples, the FX migrates at these non-radiative centers, resulting in the reduction of I_{NBE}/I_{DL} ratio.
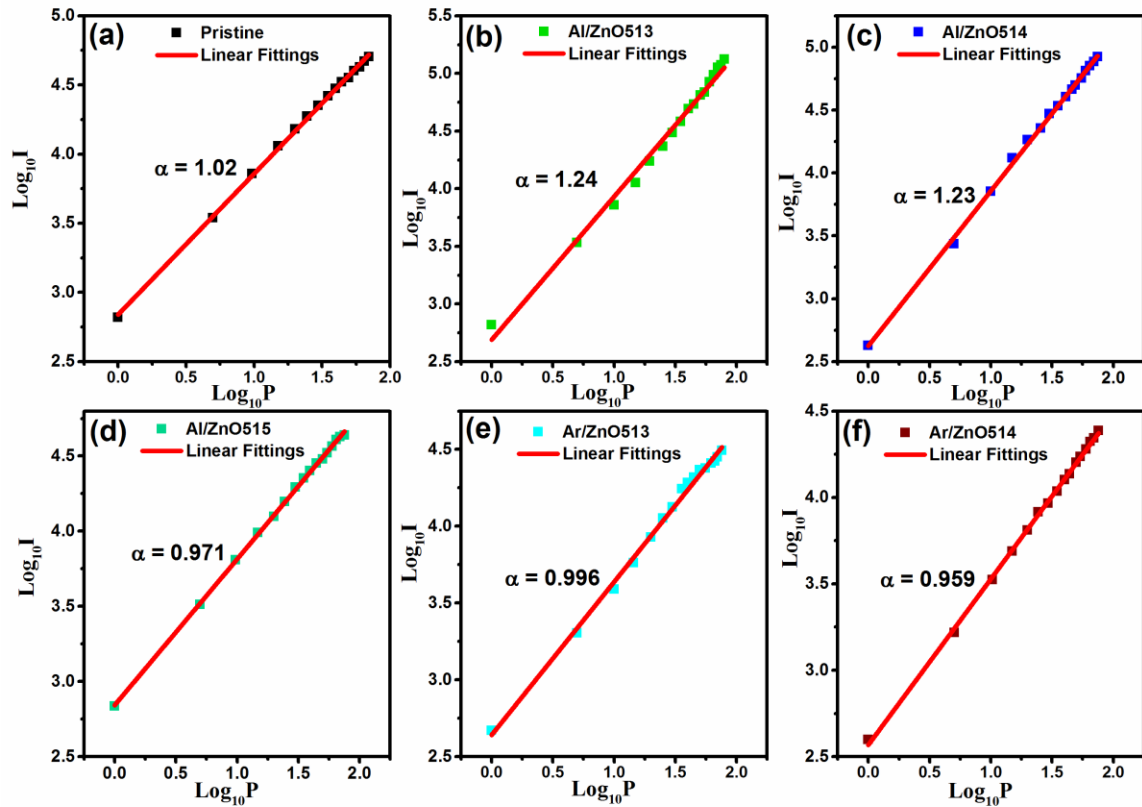
Fig. 5.8 Excitation power dependence of UV emission of (a) pristine, (b) Al/ZnO513, (c) Al/ZnO514, (d) Al/ZnO515, (e) Ar/ZnO513 and (f) Ar/ZnO514.

The NBE peaks being an asymmetric have been deconvoluted into two Gaussian peaks for all the samples. Fig. 5.9 shows three representative peak fittings. The estimated peak positions and corresponding FWHM values have been noted in Table 5.3. For pristine (Fig. 5.9(a)), P_1 can be assigned to the radiative transition of FX, whereas P_2 is related to the surface states localized at band tail [40]. The estimated energy difference between P_1 and P_2 peaks as shown in Table 5.3 is 61 meV, which is actually the localization energy of DBX. For Al implanted sample (Fig. 5.9(b)), the peak P_1 is probably the superposition of FX and Al D^0X, whereas P_2 is related DBX. As the Al implantation carried out, the localization energy of DBX vary from 67 to 115 meV with an increase in Al fluence (Table 5.3). As this value exceeds the excitonic binding energy of 60 meV, it is expected that along with the excitonic luminescence, the DBX would also play a major role in the UV PL emission [41]. The

gradual shift towards higher energy side and an increase in the FWHM of P_1 and P_2 as shown in Table 5.3 further indicates to the BM effect due to incorporation of Al donors. The energy difference between D^0X (or DBX) and the corresponding peaks at lower energy side is about an integer multiple of 72 meV, which is in consistent with the characteristic energy of longitudinal optical (LO)-phonon replicas in ZnO [42]. The estimated energy differences between P_1 and P_2 peak as shown in Table 5.3 are around 71 meV for all Ar implanted samples. From this fact, the peak P_1 of Ar implanted samples (Fig. 5.9(c)) can be assigned to DBX emission overlapping with FX and the peak P_2 to the corresponding LO - phonon replicas as supported by the reports on the existence of DBX emission and its phonon replicas in ZnO at RT [41, 42]. Most notably, no appreciable shift in the peak position as well as change in the FWHM values of P_1 and P_2 for Ar implanted samples indicate to the fact of no influence of donor defects in the excitonic recombination. In this case, only the creation of implantation-induced surface defects is responsible for the deterioration of the NBE. In both implantation cases, surface defects are modified and increased and thus the nature of the emission changes from yellow-orange to an enhanced green emission. V_{Zn} defects are mostly known to be responsible for the green emissions [43-45]. Recent diffusion studies of Al [46] in ZnO suggest that the migration of Al occurs via an intermediate substitutional dopant-vacancy complex (Al_{Zn}-V_{Zn}), and if this be the case, diffusion of implanted Al in ZnO NRs happens to be via dopant-vacancy complex, the net effect of V_{Zn} in green emission is expected to decrease. Indeed, the green emission intensity shows a decreasing trend as the Al implantation fluence increases (Fig. 5.6(a)). However, the possibility of creation of other non-radiative recombination paths cannot be ruled out.
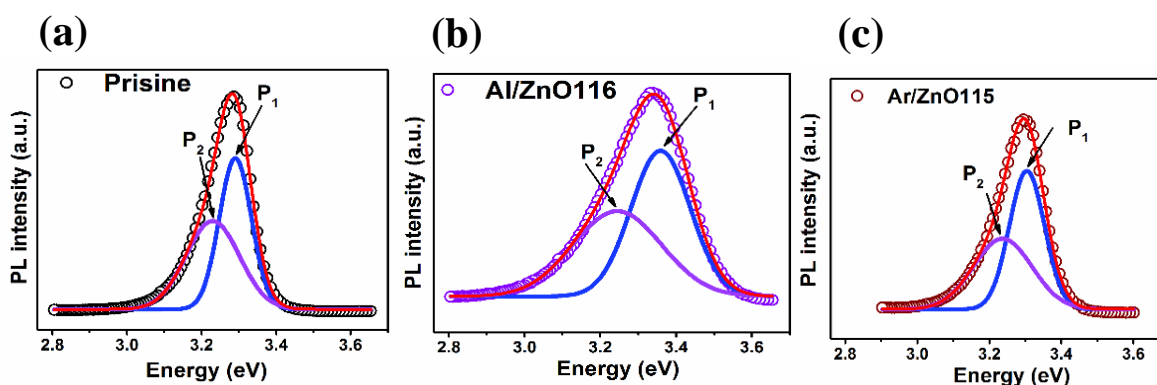
Fig. 5.9 Gaussian multi-peak fittings of the NBE peaks of (a) pristine, (b) Al/ZnO116, and (c) Ar/ZnO115 samples.

Table 5.3 The position and FWHM of NBE fitted peaks P_1 and P_2 and energy their energy separation.

Sample name	Peak P_1 at higher energy side		Peak P_2 at lower energy side		Energy difference between P_1 and P_2 (meV)
	Peak position (eV)	FWHM	Peak position (eV)	FWHM	
Pristine	3.291	0.114	3.230	0.176	61
Al/ZnO113	3.294	0.103	3.227	0.173	67
Al/ZnO513	3.296	0.108	3.231	0.180	65
Al/ZnO114	3.297	0.117	3.228	0.188	69
Al/ZnO514	3.303	0.129	3.229	0.201	74
Al/ZnO115	3.318	0.138	3.239	0.211	79
Al/ZnO515	3.337	0.144	3.249	0.231	88
Al/ZnO116	3.359	0.185	3.244	0.278	115
Ar/ZnO513	3.299	0.116	3.227	0.183	72
Ar/ZnO114	3.300	0.111	3.230	0.178	70
Ar/ZnO514	3.304	0.116	3.232	0.183	72
Ar/ZnO115	3.304	0.115	3.233	0.185	71

Fig. 5.10(a) shows the XPS survey scan of pristine, Al/ZnO513, and Al/ZnO116. Well resolved XPS peaks correspond to different core levels of O and Zn are found for all the samples (Fig. 5.10(a)). The Gaussian fittings of the Al 2p core line as shown in the Fig. 5.10(b) and Fig. 5.10(c) exhibits only one component with a binding energy around 74.37 eV, indicating the successful substitution of Zn^{2+} ions by Al^{3+} ions in the ZnO lattice of both Al/ZnO513 and Al/ZnO116 samples after implantation and subsequent annealing process [12, 47]. The centroid at around 74.37 eV is basically a slightly shifted position towards lower binding energies compared to the 74.60 eV peak position of Al $2p_{3/2}$ of stoichiometric Al_2O_3, indicating an O deficient ZnO matrix [48]. The increasing intensity of Al 2p peaks (Fig. 5.10(a) and Fig. 5.10(b)) indicates that the concentration of Al increases as the fluence increases, which is at par with the EDS data as discussed earlier.
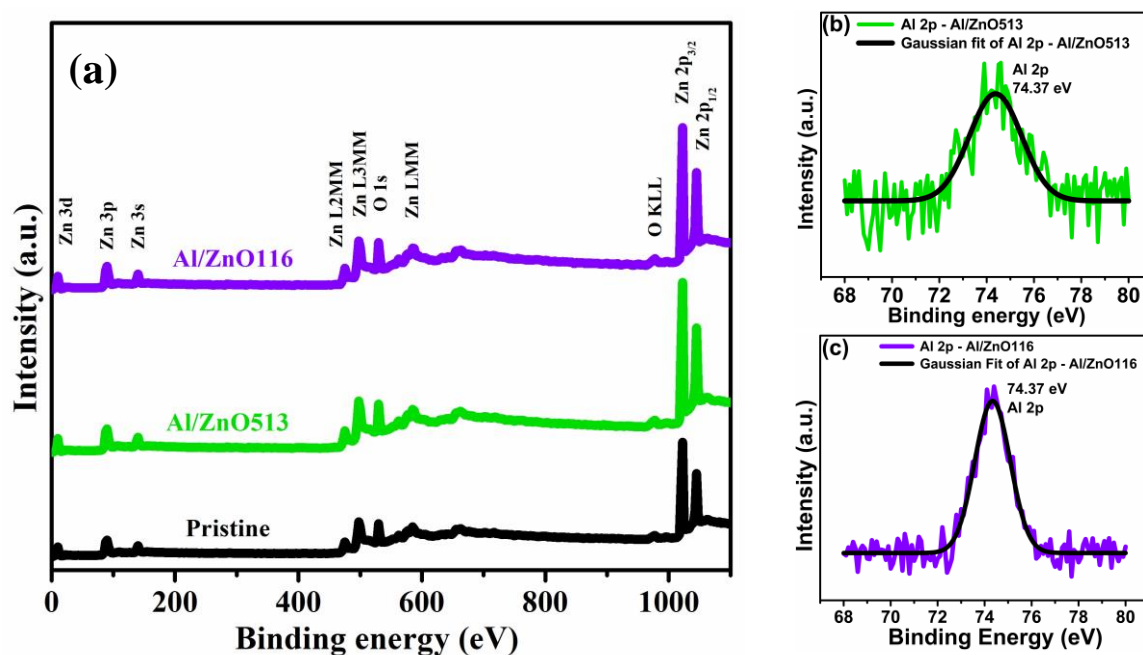
Fig. 5.10 (a) XPS survey scan of pristine, Al/ZnO513 and Al/ZnO116 samples. (b) and (c) are Al 2p, confirming the presence of Al in Al/ZnO513 and Al/ZnO116 respectively

The O 1s XPS spectra of pristine and implanted samples exhibit the asymmetric nature. Similar to the previous chapter, the O 1s spectra is coherently fitted by three Gaussian components, centered at around 530.6 eV (O_a), 531.9 eV (O_b) and 532.6 eV (O_c), respectively, as shown in Fig. 5.11. The contributions of stoichiometric O (O_a), V_O (O_b) and excess O (O_c) were computed from the measured peak area and the numerical values are given in Table 5.4. It is clear that V_O increases both in Al and Ar implanted samples, though at a higher rate for the later which supports our PL results.
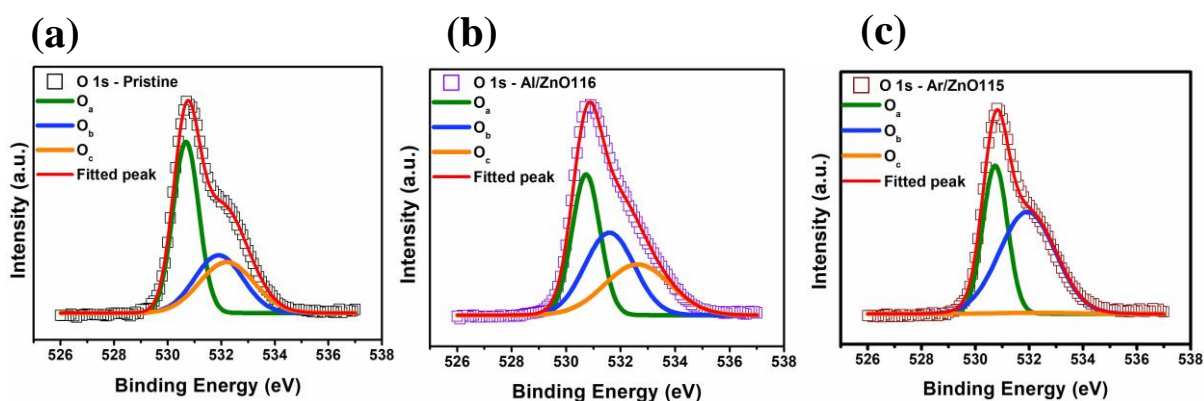
Fig. 5.11 O 1s peak fitting for (a) pristine, (b) Al/Zn116 and (c) Ar/ZnO115.

Table 5.4 Areal contribution of fitted O_a, O_b and O_c peaks in O1s peak for pristine and ion implanted samples.

Sample name	O_a (%)	O_b (%)	O_c (%)
Pristine	46.18	30.08	23.74
Al/ZnO513	41.61	34.61	23.78
Al/ZnO116	29.55	38.62	31.82
Ar/ZnO513	38.64	43.03	18.32
Ar/ZnO115	38.70	60.34	0.96

The I-V measurements results in Fig. 5.12 indicate that the rate of increase in the current for Al implanted samples is higher than Ar implanted samples indicating incorporation of Al donor dopants in the lattice sites, which further supports the BM effect in the PL spectra. However, an increase in the current also in case of Ar ion implanted samples indicates formation of more donor defects (V_O) supporting XPS result.
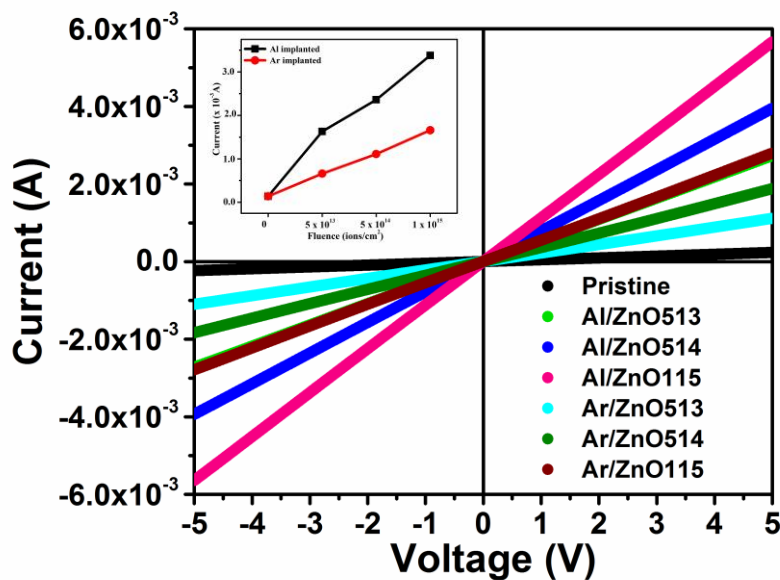
Fig. 5.12 The I-V characteristics of pristine, and some representative of Al and Ar implanted ZnO NRs. The inset shows the variation of current at 3 V with fluence of Al and Ar.

It is well known that UV photoconductivity (PC) in ZnO NRs is influenced highly by the surface defects [49] and therefore, PC studies on both Al and Ar implanted samples would certainly provide us an idea about generation of surface defects. To realize the reproducible

measurement starting conditions and to eliminate the uncontrolled influence of light on the samples, each sample was kept in the dark for a long time and then photocurrent rise and fall were measured in air ambient by illuminating the NRs with an UV illumination (370 nm) for a time during of 50 minutes each (Fig. 5.13). The measurements were performed on a long-time scale so that the photo-excitation led to a persistent photoconductivity (PPC) with long photocurrent decay times and very low contribution of short time decay processes. There are some controversial opinions about the origin of PPC; some authors have assigned it to the presence of metastable conductive states corresponds to V_O [50-52], whereas others have attributed it to the O_2 adsorption and desorption processes on the surface [53-55]. The percentage of maximum photocurrent (I_{ph}) decayed after 50 minutes of light turned off has been calculated in Table 5.5 to get an idea about the PPC. However, Table 5.5 depicts rather a faster decay of the pristine, whereas slower decay for the implanted samples. Among, the implanted samples, the PPC is more pronounced for Al implanted samples than that of Ar implanted samples. Madel et al. [56] have reported that V_O is responsible for the fast decay of the photocurrent after turning off the light, whereas adsorption and desorption processes of O_2 on the ZnO NWs surface are related to the slow one. The surface absorbed O_2 dominate the slower decay of the I_{ph} for Al implanted samples, whereas V_O takes the main role in the faster decay for Ar implanted samples, which is supported by the XPS results (Table 5.4).
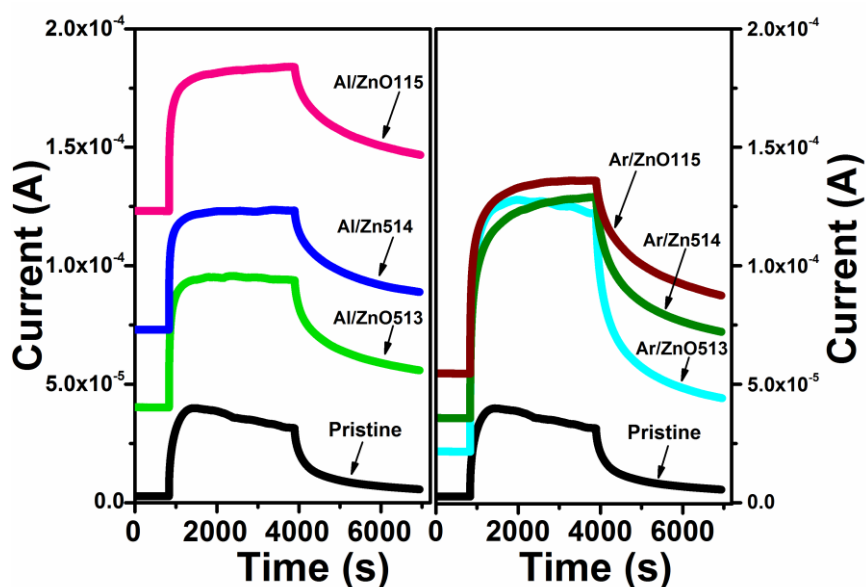
Fig. 5.13 Photocurrent transient spectra of pristine, Al implanted and Ar implanted ZnO NRs (Al/ZnO513, Al/ZnO514, Al/ZnO115 and Ar/ZnO513, Ar/ZnO514, Ar/ZnO115).

Table 5.5 PPC for various doses for both Al and Ar implantations.

Fluence (ions/cm^2)	% of I_{ph} decayed after 50 mins of light turned off	
	Al implanted	Ar implanted
Pristine	82	82
5×10^{13}	41	63
5×10^{14}	27	44
1×10^{15}	20	35

5.4 Conclusions

In summary, the effect of Al ion implantation on the RT PL properties of ZnO NRs by varying ion fluences by three orders of magnitude has been demonstrated in details. A comparative study with the effect of Ar ion implantation in ZnO NRs for similar ion fluences helps to understand the mechanisms and the role of defects behind the change in the PL properties. A dramatic improvement in the PL properties has been observed due to the formation of neutral Al donor bound excitonic recombination centers for the lower fluence Al implanted ZnO NRs. For higher fluences of Al and for all fluences of Ar implanted NRs, the non-radiative recombination centers on the surfaces of ZnO NRs are formed causing reduced PL properties. The comprehensive study provides a significant novel route for utilizing the Al implanted ZnO NRs in a large variety of optical devices such as solid-state lighting.

5.5 References

[1] K.S. Ranjith, L.R. Nivedita, K. Asokan, S. Krishnamurthy, R. Pandian, M. Kamruddin, D.K. Avasthi, R.T.R. Kumar, Robust water repellent ZnO nanorod array by Swift Heavy Ion Irradiation: Effect of Electronic Excitation Induced Local Chemical State Modification, Sci Rep, 7 (2017).

[2] T. Shimogaki, K. Okazaki, D. Nakamura, M. Higashihata, T. Asano, T. Okada, Effect of laser annealing on photoluminescence properties of Phosphorus implanted ZnO nanorods, Opt. Express, 20 (2012) 15247-15252.

[3] T. Matsuda, M. Furuta, T. Hiramatsu, H. Furuta, T. Hirao, Sheet resistance and crystallinity of Ga- and Al-implanted zinc oxide thin films with postannealing, J. Vac. Sci. Technol. A, 25 (2007) 706-710.

[4] N.M. Lyadov, A.I. Gumarov, V.F. Valeev, V.I. Nuzhdin, V.A. Shustov, V.V. Bazarov, I.A. Faizrakhmanov, Effect of Implantation Regimes of Silver Ions on the Structure and Optical Properties of Zinc-Oxide Nanocrystalline Films, Tech. Phys., 61 (2016) 1237-1243.

[5] M.J. Ying, S.D. Wang, T. Duan, B. Liao, X. Zhang, Z.X. Mei, X.L. Du, F.M. Gerriu, A.M. Fox, G.A. Gehring, The structure, optical and magnetic properties of arsenic implanted ZnO films prepared by molecular beam epitaxy, Mater. Lett., 171 (2016) 121-124.

[6] P.P. Murmu, J. Kennedy, B.J. Ruck, G.V.M. Williams, A. Markwitz, S. Rubanov, A.A. Suvorova, Effect of annealing on the structural, electrical and magnetic properties of Gd-implanted ZnO thin films, J. Mater. Sci., 47 (2012) 1119-1126.

[7] Y.H. Xue, X.D. Zhang, X.L. Zhang, Y.Y. Shen, F. Zhu, L.H. Zhang, J. Wang, C.L. Liu, Room temperature magnetic properties of Fe and C implanted ZnO films, Appl. Surf. Sci., 257 (2011) 10329-10332.

[8] P.K. Giri, S. Kumari, D.K. Goswami, Low energy oxygen implantation induced improved crystallinity and optical properties of surface modified ZnO single crystals, Appl. Surf. Sci., 256 (2009) 384-388.

[9] D. Li, D.K. Li, H.Z. Wu, F. Liang, W. Xie, C.W. Zou, L.X. Shao, Defects related room temperature ferromagnetism in Cu-implanted ZnO nanorod arrays, J. Alloy. Compd., 591 (2014) 80-84.

[10] T. Oga, Y. Izawa, K. Kuriyama, K. Kushida, A. Kinomura, Origins of low resistivity in Al ion-implanted ZnO bulk single crystals, J. Appl. Phys., 109 (2011).

[11] T. Nakagawa, I. Sakaguchi, K. Matsumoto, M. Uematsu, H. Haneda, N. Ohashi, Observation of Diffusion Behavior in Al-implanted ZnO Single Crystal, in: T. Takenaka, H. Haneda, K. Kato, M. Takata, K. Shinozaki (Eds.) Asian Ceramic Science for Electronics Iii and Electroceramics in Japan Xii, Trans Tech Publications Ltd, Durnten-Zurich, 2010, pp. 197-+.

[12] H. Lee, K. Sivashanmugan, C.Y. Kao, J.D. Liao, Fabrication of highly transparent Al-ion-implanted ZnO thin films by metal vapor vacuum arc method, Jpn. J. Appl. Phys., 56 (2017).

[13] H.B. Liu, Q.Y. Lu, H.P. He, K.W. Wu, S.L. Li, J.Y. Huang, Y.F. Lu, X.H. Pan, Z.Z. Ye, P.K. Chu, Effects of annealing temperature on excitonic emissions from Na-implanted ZnO nanorods, Mater. Lett., 90 (2013) 76-78.

[14] C.W. Zou, L.X. Shao, D.J. Fu, Effects of annealing temperature on the structure, photoluminescence and ferromagnetism properties of Cr-implanted ZnO nanowires, Appl. Phys. A-Mater. Sci. Process., 109 (2012) 163-168.

[15] Y. Yang, X.W. Sun, B.K. Tay, G.F. You, S.T. Tan, K.L. Teo, A p-n homojunction ZnO nanorod light-emitting diode formed by As ion implantation, Appl. Phys. Lett., 93 (2008).

[16] S. Muller, M. Lorenz, C. Czekalla, G. Benndorf, H. Hochmuth, M. Grundmann, H. Schmidt, C. Ronning, Intense white photoluminescence emission of V-implanted zinc oxide thin films, J. Appl. Phys., 104 (2008).

[17] P.T. Neuvonen, L. Vines, B.G. Svensson, A.Y. Kuznetsov, Intrinsic Point-Defect Balance in Self-Ion-Implanted ZnO, Phys. Rev. Lett., 110 (2013).

[18] F. Mouzaia, D. Djouadi, A. Chelouche, L. Hammiche, Al-Doping Effects on Structural and Morphological Properties of ZnO Aerogels Synthesized in Supercritical Ethanol, in, Springer International Publishing, Cham, 2018, pp. 81-88.

[19] T.M.K. Thandavan, C.S. Wong, S.M.A. Gani, R.M. Nor, Photoluminescence properties of un-doped and Mn-doped ZnO nanostructures, Mater. Express, 4 (2014) 475-482.

[20] K.R. Nandanapalli, D. Mudusu, Surface Passivated Zinc Oxide (ZnO) Nanorods by Atomic Layer Deposition of Ultrathin ZnO Layers for Energy Device Applications, ACS Applied Nano Materials, 1 (2018) 4083-4091.

[21] L. Cai, W. Zhou, F. Ren, J. Chen, G. Cai, Y. Liu, X. Guan, S. Shen, W ion implantation boosting visible-light photoelectrochemical water splitting over ZnO nanorod arrays, 2017.

[22] S. Chatterjee, A.K. Behera, A. Banerjee, L.C. Tribedi, T. Som, P. Ayyub, Nanometer-scale sharpening and surface roughening of ZnO nanorods by argon ion bombardment, Appl. Surf. Sci., 258 (2012) 7016-7020.

[23] L.D. Yao, D. Weissenberger, M. Durrschnabel, D. Gerthsen, I. Tischer, M. Wiedenmann, M. Feneberg, A. Reiser, K. Thonke, Structural and cathodoluminescence properties of ZnO nanorods after Ga-implantation and annealing, J. Appl. Phys., 105 (2009).

[24] M. Wang, F. Ren, J.G. Zhou, G.X. Cai, L. Cai, Y.F. Hu, D.N. Wang, Y.C. Liu, L.J.J. Guo, S.H. Shen, N Doping to ZnO Nanorods for Photoelectrochemical Water Splitting under Visible Light: Engineered Impurity Distribution and Terraced Band Structure, Sci Rep, 5 (2015).

[25] C.M. Pelicano, H. Yanagi, Enhanced charge transport in Al-doped ZnO nanotubes designed via simultaneous etching and Al doping of H2O-oxidized ZnO nanorods for solar cell applications, Journal of Materials Chemistry C, (2019).

[26] A. Bera, D. Basak, Pd-nanoparticle-decorated ZnO nanowires: ultraviolet photosensitivity and photoluminescence properties, Nanotechnology, 22 (2011).

[27] L.M. Trinca, A.C. Galca, A.G. Boni, M. Botea, L. Pintilie, Effect of Li doping on the electric and pyroelectric properties of ZnO thin films, Appl. Surf. Sci., 427 (2018) 29-37.

[28] J.W.P. Hsu, D.R. Tallant, R.L. Simpson, N.A. Missert, R.G. Copeland, Luminescent properties of solution-grown ZnO nanorods, Appl. Phys. Lett., 88 (2006).

[29] R.B.M. Cross, M.M. De Souza, E.M.S. Narayanan, A low temperature combination method for the production of ZnO nanowires, Nanotechnology, 16 (2005) 2188-2192.

[30] Y.H. Yang, X.Y. Chen, Y. Feng, G.W. Yang, Physical Mechanism of Blue-Shift of UV Luminescence of a Single Pencil-Like ZnO Nanowire, Nano Lett., 7 (2007) 3879-3883.

[31] T.N. Sky, K.M. Johansen, V. Venkatachalapathy, B.G. Svensson, L. Vines, F. Tuomisto, Influence of Fermi level position on vacancy-assisted diffusion of aluminum in zinc oxide, Phys. Rev. B, 98 (2018) 245204.

[32] R. Chen, Q.L. Ye, T.C. He, V.D. Ta, Y.J. Ying, Y.Y. Tay, T. Wu, H.D. Sun, Exciton Localization and Optical Properties Improvement in Nanocrystal-Embedded ZnO Core-Shell Nanowires, Nano Lett., 13 (2013) 734-739.

[33] X. Fang, Z.P. Wei, R. Chen, J.L. Tang, H.F. Zhao, L.G. Zhang, D.X. Zhao, D. Fang, J.H. Li, F. Fang, X.Y. Chu, X.H. Wang, Influence of Exciton Localization on the Emission and Ultraviolet Photoresponse of ZnO/ZnS Core-Shell Nanowires, ACS Appl. Mater. Interfaces, 7 (2015) 10331-10336.

[34] B.W. Zhang, Z.P. Wei, X.W. Wang, X. Fang, D.K. Wang, X. Gao, D. Fang, X.H. Wang, R. Chen, Effect of Post Thermal Annealing on the Optical Properties of InP/ZnS Quantum Dot Films, Nanoscale Res. Lett., 13 (2018).

[35] Y.M. Lu, X.P. Li, P.J. Cao, S.C. Su, F. Jia, S. Han, W.J. Liu, D.L. Zhu, X.C. Ma, Study of Ultraviolet Emission Spectra in ZnO Thin Films, J. Spectrosc., (2013) 1-7.

[36] B.K. Meyer, H. Alves, D.M. Hofmann, W. Kriegseis, D. Forster, F. Bertram, J. Christen, A. Hoffmann, M. Strassburg, M. Dworzak, U. Haboeck, A.V. Rodina, Bound exciton and donor-acceptor pair recombinations in ZnO, Phys. Status Solidi B-Basic Solid State Phys., 241 (2004) 231-260.

[37] K. Johnston, M.O. Henry, D. McCabe, E. McGlynn, M. Dietrich, E. Alves, M. Xia, Identification of donor-related impurities in ZnO using photoluminescence and radiotracer techniques, Phys. Rev. B, 73 (2006) 165212.

[38] S. Müller, D. Stichtenoth, M. Uhrmacher, H. Hofsäss, C. Ronning, J. Röder, Unambiguous identification of the PL-I9 line in zinc oxide, Appl. Phys. Lett., 90 (2007) 012107.

[39] K. Thonke, M. Schirra, R. Schneider, A. Reiser, G.M. Prinz, M. Feneberg, R. Sauer, J. Biskupek, U. Kaiser, The role of stacking faults and their associated 0.13 eV acceptor state in doped and undoped ZnO layers and nanostructures, Phys. Status Solidi B-Basic Solid State Phys., 247 (2010) 1464-1468.

[40] R.K. Biroju, P.K. Giri, Strong visible and near infrared photoluminescence from ZnO nanorods/nanowires grown on single layer graphene studied using sub-band gap excitation, J. Appl. Phys., 122 (2017) 044302.

[41] J. Fallert, R. Hauschild, F. Stelzl, A. Urban, M. Wissinger, H.J. Zhou, C. Klingshirn, H. Kalt, Surface-state related luminescence in ZnO nanocrystals, J. Appl. Phys., 101 (2007).

[42] X. Ding, Y.J. Fang, M. Zhao, W. Wang, J. Sha, Y.W. Wang, Influence of Al capping on the photoluminescence of ZnO, Opt. Mater. Express, 7 (2017) 1898-1905.

[43] F. Fabbri, M. Villani, A. Catellani, A. Calzolari, G. Cicero, D. Calestani, G. Calestani, A. Zappettini, B. Dierre, T. Sekiguchi, G. Salviati, Zn vacancy induced green luminescence on non-polar surfaces in ZnO nanostructures, Sci Rep, 4 (2014).

[44] H. Chen, S.L. Gu, K. Tang, S.M. Zhu, Z.B. Zhu, J.D. Ye, R. Zhang, Y.D. Zheng, Origins of green band emission in high-temperature annealed N-doped ZnO, J. Lumines., 131 (2011) 1189-1192.

[45] D. Sett, S. Sarkar, D. Basak, A successive photocurrent transient study to probe the sub-band gap electron and hole traps in ZnO nanorods, RSC Adv., 4 (2014) 58553-58558.

[46] K.M. Johansen, L. Vines, T.S. Bjorheim, R. Schifano, B.G. Svensson, Aluminum Migration and Intrinsic Defect Interaction in Single-Crystal Zinc Oxide, Phys. Rev. Appl., 3 (2015).

[47] C.M. Pelicano, H. Yanagi, Enhanced Charge Transport in Al-doped ZnO Nanotubes Designed via Simultaneous Etching and Al Doping of H2O-Oxidized ZnO Nanorods for Solar Cell Applications, 2019.

[48] M. Pal, S. Bera, S. Sarkar, S. Jana, Influence of Al doping on microstructural, optical and photocatalytic properties of sol–gel based nanostructured zinc oxide films on glass, RSC Adv., 4 (2014) 11552-11563.

[49] X. Li, J. Li, C. Cui, Z. Liu, Y. Niu, PbS Nanoparticle Sensitized ZnO Nanowire Arrays to Enhance Photocurrent for Water Splitting, The Journal of Physical Chemistry C, 120 (2016) 4183-4188.

[50] Y. Wang, Z.L. Liao, G.W. She, L.X. Mu, D.M. Chen, W.S. Shi, Optical modulation of persistent photoconductivity in ZnO nanowires, Appl. Phys. Lett., 98 (2011).

[51] S. Hullavarad, N. Hullavarad, D. Look, B. Claflin, Persistent Photoconductivity Studies in Nanostructured ZnO UV Sensors, Nanoscale Res. Lett., 4 (2009) 1421-1427.

[52] A. Janotti, C.G.V.d. Walle, Oxygen vacancies in ZnO, Appl. Phys. Lett., 87 (2005) 122102.

[53] J.M. Bao, I. Shalish, Z.H. Su, R. Gurwitz, F. Capasso, X.W. Wang, Z.F. Ren, Photoinduced oxygen release and persistent photoconductivity in ZnO nanowires, Nanoscale Res. Lett., 6 (2011).

[54] J.D. Prades, F. Hernandez-Ramirez, R. Jimenez-Diaz, M. Manzanares, T. Andreu, A. Cirera, A. Romano-Rodriguez, J.R. Morante, The effects of electron-hole separation on the photoconductivity of individual metal oxide nanowires, Nanotechnology, 19 (2008).

[55] A. Bera, D. Basak, Photoluminescence and Photoconductivity of ZnS-Coated ZnO Nanowires, ACS Appl. Mater. Interfaces, 2 (2010) 408-412.

[56] M. Madel, F. Huber, R. Mueller, B. Amann, M. Dickel, Y. Xie, K. Thonke, Persistent photoconductivity in ZnO nanowires: Influence of oxygen and argon ambient, J. Appl. Phys., 121 (2017).

CHAPTER-6

Interplay of defects in N implanted ZnO nanorods

6.1 Introduction

In chapter 2, the difficulties in achieving controllable and reproducible p-type ZnO have been described elaborately. But the formation of p-type ZnO is very much urgent for the practical applications of ZnO as p-n homojunction-based devices. In this context, the p-type conductivity in ZnO has been achieved to some extent by doping with group V elements [1-4]. As earlier said, N is regarded as the most suitable p-type dopant among group V elements for ZnO due to similar atomic radius and electronic structure between N and O [5]. Though, the incorporation of N atom into O sublattice (N_O) is generally believed as the acceptor and is the source of p-type conductivity in ZnO [6, 7], the complex of N_O and V_{Zn} (N_O-V_{Zn}) theoretically and experimentally has been recognized as shallow acceptor for stable p-type conductivity in N doped ZnO [8-11]. In addition to the acceptor like complexes, there are many donor defect complexes in N doped ZnO, which have been described in chapter 2. These donors compensate the effect of N related acceptors (e.g., N_O, N_O-V_{Zn}). Chiesa et al. [12] have shown that the insertion of N in various oxides dramatically drops the formation energy of V_O, which causes a parallel formation of shallow donors and frustrates the effect of low-lying N states. Therefore, as a possibility of achieving p-type conductivity in N doped ZnO NRs, it is important to introduce not only an effective shallow acceptor level but also to suppress donor concentration as much as possible. Therefore, the understanding of the interplay between point defects and N impurity is very much essential, which still remains alluring. Having all these issues in mind, in this chapter, the probable interactions between N and various point defects and the recovery process of implantation induced defects as a function of various implantation fluences as well as under different annealing ambiences have been discussed.

6.2 Experimental details

ZnO NRs were first grown on the glass substrates by ACG method. The details of the NRs preparation are described in chapter 3. The as-grown ZnO NRs were then implanted with 50 keV N ions at RT using fluences from 1×10^{14} to 1×10^{16} ions/cm^2. The irradiated area of the samples was one cm^2 and the beam current was fixed at 1μA. After N implantation, the samples were subjected to an annealing treatment at 450 °C for 1 h in Ar ambient. Next, the sample implanted with the fluence of 5×10^{15} ions/cm^2 was further annealed separately in O_2 and excess Zn ambiences under similar conditions with an expectation that annealing in O_2

and excess Zn ambiences would diminish the concentration of V_O and V_{Zn} defects respectively. The as-grown NRs annealed in Ar ambient has been marked as a control sample. The nomenclature of the samples in this study is given in the Table 6.1.

Table 6.1 Nomenclature of the samples with their corresponding fluences and annealing ambiences.

Fluence (ions/cm^2)	Annealing ambient	Sample name
0		ArP
1×10^{14}		ArN114
5×10^{14}		ArN514
1×10^{15}	Ar	ArN115
5×10^{15}		ArN515
1×10^{16}		ArN116
5×10^{15}	O$_2$	ON515
5×10^{15}	Zn	ZnN515

The structural, morphological, compositional, optical, and electrical analyses of the samples have been carried out using XRD, FESEM, XPS, PL, Raman, and electrical I-V measurements, respectively as described in chapter 3.

6.3 Results and discussion

6.3.1 Defect formation: SRIM calculation

The parameters described in the chapter 4 have been used again for the SRIM calculation in this chapter. The simulated N concentration displays a well-known Gaussian profile which is shown in Fig. 6.1(a), where the value of R_p is ~130 nm and the implanted N ions are extended upto a depth of ~250 nm from the surface of the NRs. The distributions of implantation-induced V_{Zn} and V_O are shown in Fig. 6.1(b), which implies that the implantation of low energy (50 keV) N ions can induce quite a bit of vacancy defects in ZnO lattice. These vacancy defects are also extended upto a ~250 nm depth from the surface. As indicated by Fig. 6.1(b), the number of implantation-induced V_{Zn} is always higher than that of V_O at any value of N ion fluence. Now, according to the theoretical calculations [8, 9], the

V_{Zn} defects are especially desired to realize the acceptor doping in N doped ZnO films. Under a certain condition, the V_O also contributes to form N_O. Fons et al. [13] have shown that V_O is the most preferred location for N in ZnO. Thus, the SRIM calculations indicate that the acceptor defects are produced in ZnO due to N ion implantation.

(a)   **(b)**
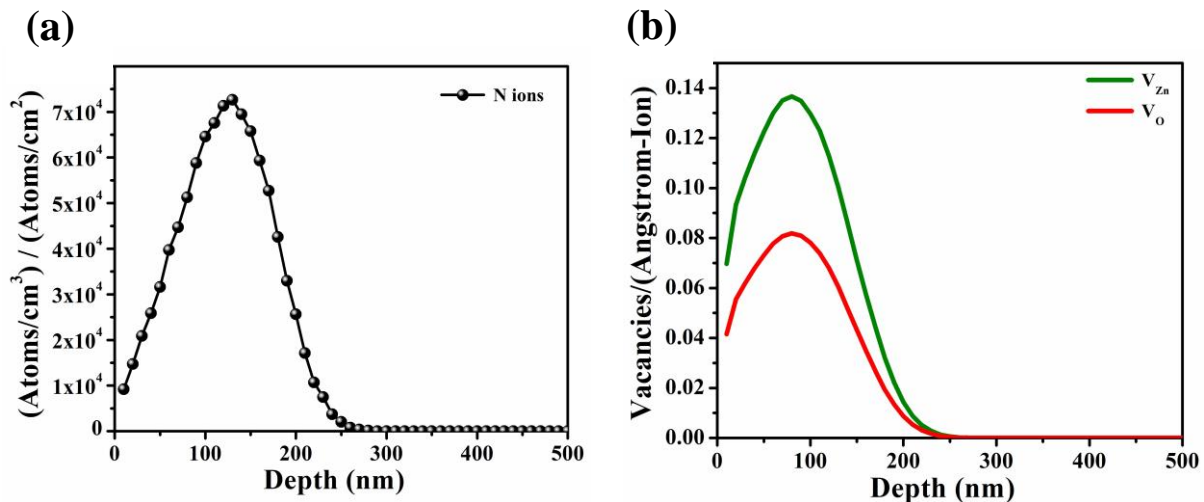
Fig. 6.1 SRIM predicted distributions of (a) N ions, and (b) defects (V_{Zn} and V_O).

6.3.2   Effect of N ion fluence

The XRD patterns of the control (ArP) as well as implanted and subsequently Ar annealed samples presented in Fig. 6.2(a) show the presence of well distinct, sharp and narrow peaks, which correspond to the diffractions from (0002), (10$\bar{1}$1), (10$\bar{1}$2), (10$\bar{1}$3) and (11$\bar{2}$0) planes of hexagonal wurtzite ZnO (JCPDS card No. 36-1451). The (002) diffraction peak corresponding to the (0002) plane is the strongest for all the samples. This indicates to the fact that the preferred orientation of ZnO NRs along the <002> direction remains unaffected after N implantation and all the samples maintain same wurtzite structure. Any extra diffraction peak due to N-related impurities or any secondary phase is not observed in the XRD patterns. The enlarged view of (002) peak of all the samples in Fig. 6.2(b) shows that the intensity of the (002) peak decreases distinctly and shifts towards higher 2θ value (as shown with a dashed line in Fig. 6.2(b)) as the implantation fluence increases. However, the gradual decrease in the (002) peak intensity implies that N implantation probably induces extra defects, which leads to a lattice distortion [14]. Since the atomic radius of N atom is greater than that of O atom, but smaller than that of Zn atom, the substitution of N at O sites

or the incorporation of N at interstitial sites in ZnO is likely to induce a peak shift towards lower angle [15-18]. In contrast, a shift towards higher 2θ value in our case probably indicates an appearance of the additional structural defects. Similar higher angle shift of the (002) diffraction peak after N implantation into ZnO NRs has also been reported earlier [19, 20]. The higher angle shift causes compressive strain (ε) as the c-axis lattice parameter (c) decreases (Fig. 6.2(c)) [19]. The value of ε is minimum for ArP and then it increases by 23% for ArN116 with an increase in the N fluence. In Fig. 6.2(d), it is seen that the value of FWHM of the (002) peak remains almost unchanged upto 5×10^{14} ions/cm^2 and beyond which it increases sharply with an increase in the fluence. The larger value of FWHM of the (002) peak for N implanted samples as compared to the control sample signifies the presence of dislocations and defects in the implanted NRs [21]. With an increase in the N fluence, the creation of point defects causes strain which causes change in the FWHM values of (002) diffraction peak. Considering the (002) peak, the average crystallite size (D) has been estimated using Debye-Scherrer's formula [22], described in the chapter 3. The value of D remains almost unchanged till 5×10^{14} ions/cm^2 and then it sharply decreases with an increase in the fluence (Fig. 6.2(d)), which is consistent with reported result [23]. The values of dislocation density (δ) have been calculated using the relation [24], described in the chapter 3. As shown in Fig. 6.2 (d), the value of δ increases as the N ion fluence increases. However, the structural changes of N implanted ZnO NRs as compared to the control sample (ArP) are modest up to the fluence 5×10^{14} ions/cm^2, and beyond which the change is significant (Fig. 6.2(c) and Fig. 6.2(d)).

Fig. 6.3(a)-(b) shows the top view FESEM images of ArP and a representative implanted sample ArN515. As seen in Fig. 6.3(a), the quasi-vertical alignment of the hexagonal ZnO NRs on the seeded glass substrate is consistent with the XRD results. The diameters of the NRs are in the range of 80 ± 15 nm. The top as well as the side surfaces of the NRs of ArP are smooth (Fig. 6.3(a)). After implantation, though the rod-like structure is well maintained (Fig. 6.3(b)), careful investigation shows that the top surfaces of the ion implanted NRs are not as smooth as that of the control sample as evident from the enlarged images in the insets in the Fig. 6.3(a) and Fig. 6.3(b). This indicates that some damages in the morphology of the ZnO NRs are produced at higher N ion fluence.
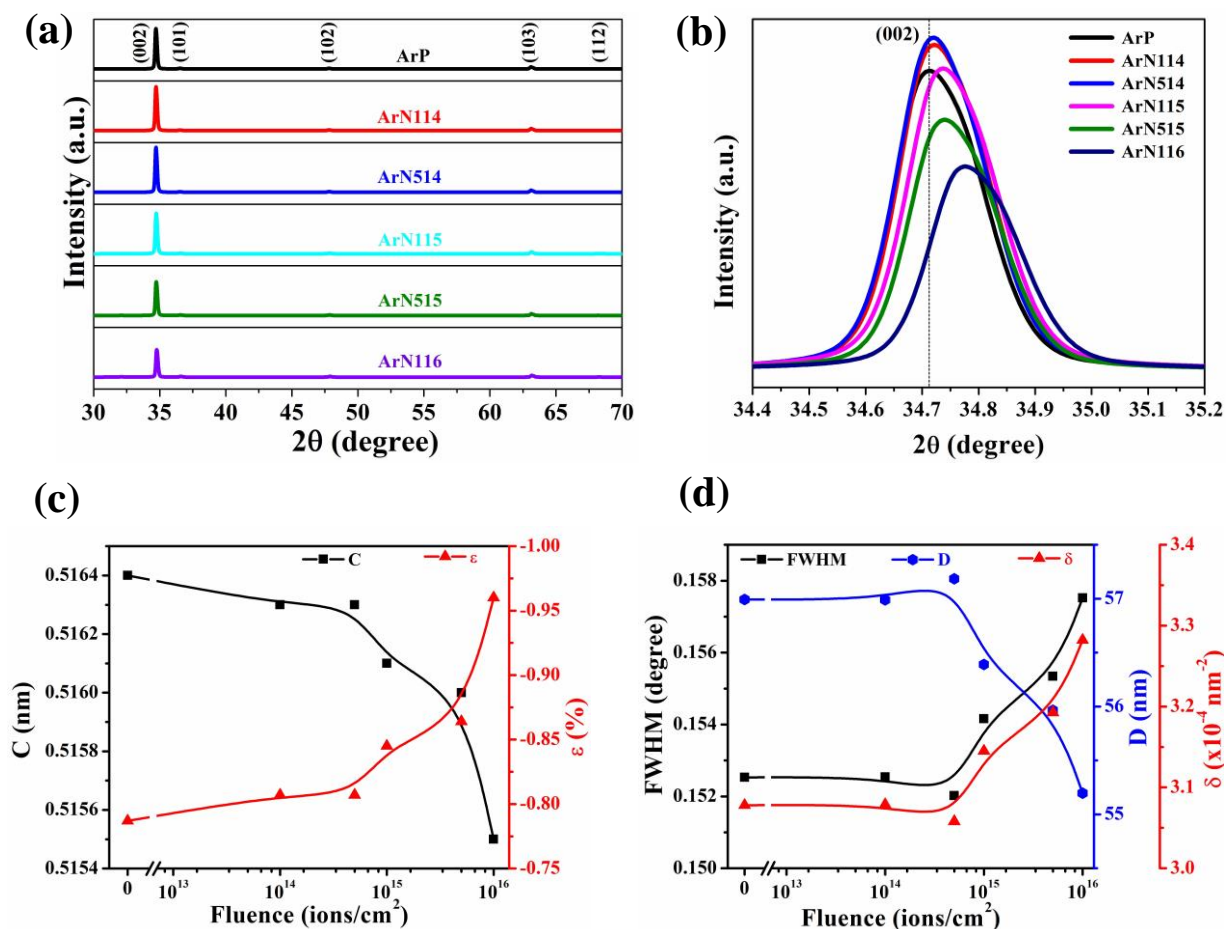
Fig. 6.2 (a) XRD patterns, (b) enlarged view of (002) peak of the samples, variation of (c) c-axis lattice parameter, strain, and (d) FWHM of (002) peak, crystallite size and dislocation density with N ion fluence.
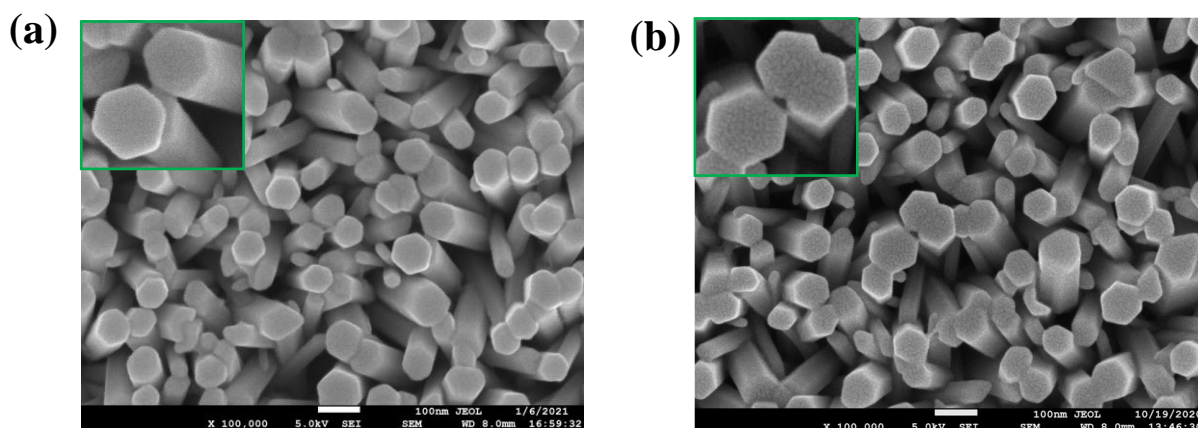
Fig. 6.3 Top view FESEM images of (a) ArP and (b) ArN515. The corresponding insets are the enlarged view of the NRs.

Fig. 6.4(a) shows the XPS full survey scans of ArP and a representative implanted sample ArN515. The XPS scans were taken after sputtering the samples for ~100 s to remove the undesired particles from the sample's surface. The XPS peaks corresponding to different core levels of O and Zn such as O 1s, Zn 2p are found clearly for all the samples in Fig. 6.4(a) [25]. The broad N 1s XPS peak of ArN515 as shown in Fig. 6.4(b) with ranging from 394 to 403 eV can be deconvoluted into two Gaussian peaks (N_I and N_{II}) having the binding energies at 396.5 ± 0.1 and 399.6 ± 0.1 eV respectively, which is similar with the earlier reported results [15, 26, 27]. The origins of both N_I (396.5 ± 0.1 eV) and N_{II} (399.6 ± 0.1 eV) peaks are generally ascribed to the N_O acceptor [15, 26, 28]. As previously reported [26], the local structure of N_O may be O-rich or N-rich and the O^{2-} ions have stronger attraction to electrons from the Zn cores than that of N^{3-} ions. Hence, it is reasonably assigned that the peak N_I at lower binding energy corresponds to N_O in N-rich environment (i.e., N-Zn-N bond), whereas the peak N_{II} at higher binding energy corresponds to N_O in O-rich (i.e., O-Zn-N bond) environment [15, 26, 28]. However, few previous reports [29, 30] have shown that a third peak (N_{III}) at around ~ 404 eV may appear in N 1s XPS spectra of N doped ZnO. The peak N_{III} is usually attributed to the $(N_2)_O$ donor [29, 30]. As seen in Fig. 6.4(b), the N_{III} peak is absent for the sample ArN515, which implies that the substitution of N_2 at an O site has not occurred after annealing in Ar ambient. As predicted from the SRIM calculation, the native acceptor defects V_{Zn} in ZnO are generated in large concentration due to N implantation. As the V_{Zn} and N_O both are present in N implanted ZnO NRs, one can believe that N_O-V_{Zn} complex is formed during post implantation annealing process. As described in the chapter 4, the asymmetric O 1s XPS peak of ArP and ArN515 can be deconvoluted by three Gaussian peaks, as shown in Fig. 6.4(c)-(d). The O_a peak in the lower energy side at ~531eV is ascribed to the O^{2-} ions of wurtzite hexagonal ZnO [31]. The O_c in the higher energy side at ~533 eV corresponds to the surface absorbed O atoms, whereas the middle component (O_b) at ~532.5 eV is assigned to the regions with oxygen-deficient namely V_O [31, 32]. The contributions of the fitted peaks have been calculated from their corresponding areas. As predicted by SRIM code, along with V_{Zn}, the concentration of V_O defects is increased due to implantation. In Fig. 6.4(c)-(d), it is seen that V_O defects in ArN515 is slightly higher than that of ArP, suggesting that excess V_O defects are produced due to implantation. The atomic concentration of N has been calculated considering the relative sensitivity factor and peak area of Zn 2p$_{3/2}$, O 1s and N 1s, which is about 0.85 at% [33]. The estimated dopant concentration is quite closer to that calculated from the SRIM (1.2 at%).
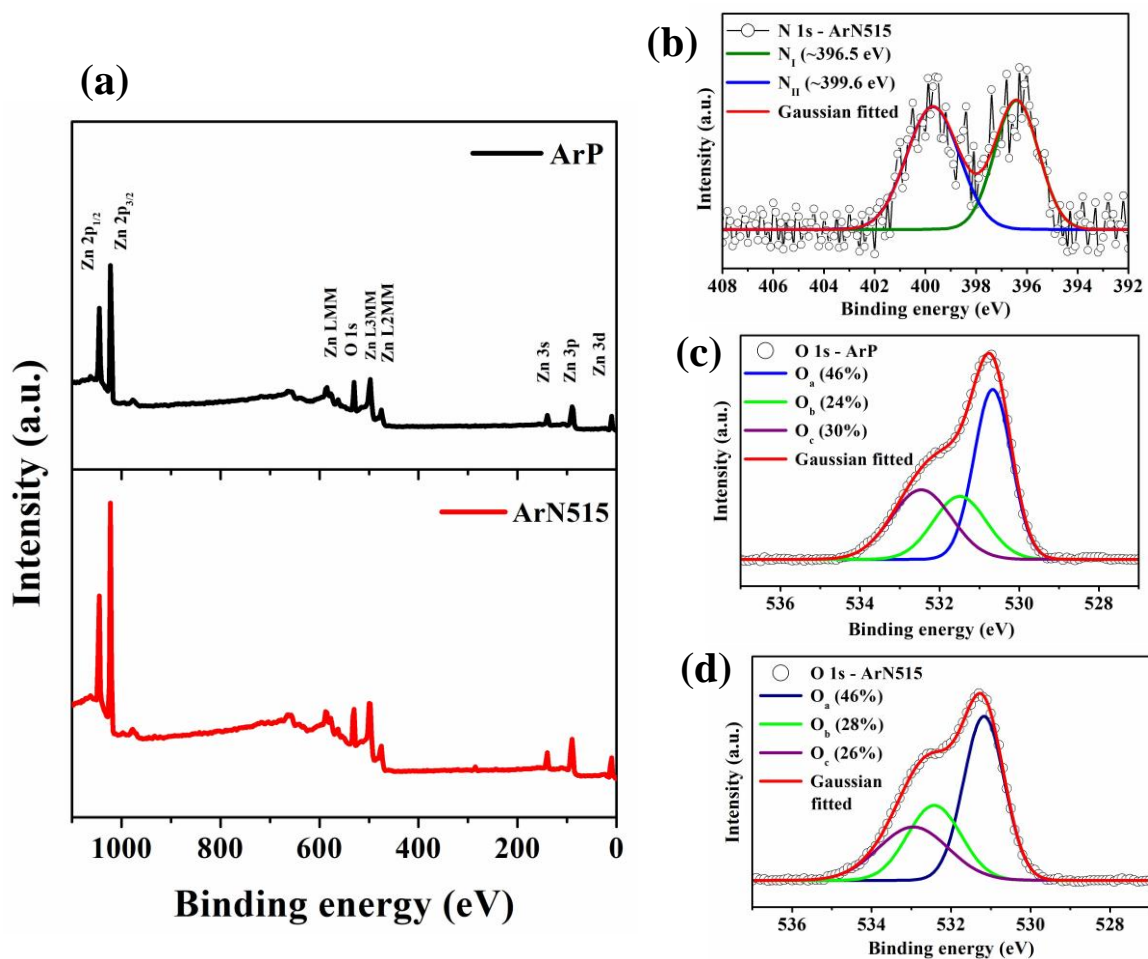
Fig. 6.4 (a) XPS survey scan of ArP and ArN515 respectively, (b) N 1s spectra of ArN515, and (c)-(d) Gaussian fittings of O 1s core line of ArP and ArN515 respectively.
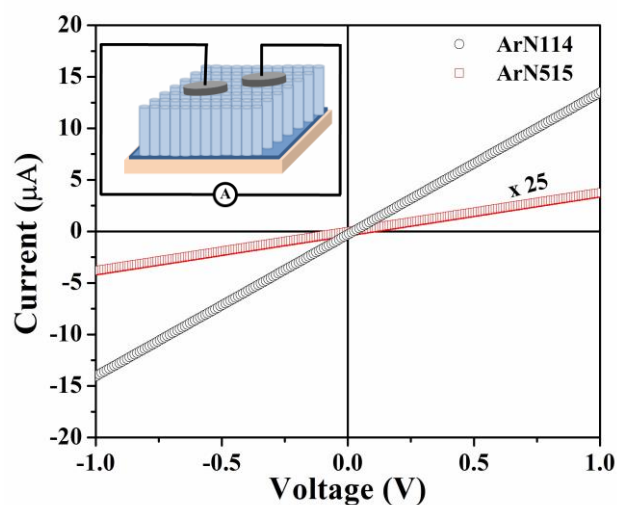
Fig. 6.5 I-V characteristic curves of ArN114 and ArN515 respectively. The inset shows schematic diagrams of the electrical I-V measurements.

The results of I-V measurements of ArN114 and ArN515 in Fig. 6.5 show lower current values at all bias voltages for a higher fluence as compared to a lower fluence. As the N ion fluence increases, the concentration of acceptor like N_O defects and the acceptor complexes N_O-V_{Zn} are expected to be increased. Meanwhile, the post implantation annealing also suppresses the Zn_i related shallow donors. Therefore, the measured electrical current should decrease with an increase in the fluence.

For the hexagonal wurtzite ZnO (C^4_{6v} space group), the optical phonons at the Γ point of the Brillouin zone can be represented as $\Gamma_{opt} = 1A_1 + 2B_1 + 1E_1 + 2E_2$ [34]. The modes A_1 and E_1 are polar and split into longitudinal (LO) and transverse (TO) optical phonons. The modes $A_1(TO)$, $E_1(TO)$, $A_1(LO)$, and $E_1(LO)$ are Raman and infrared active and are found at 380, 411, 579, 594 cm^{-1} respectively [34-36]. The two non-polar E_2 modes E_2^{Low} and E_2^{High} appear at 100, and 437 cm^{-1} respectively. The mode at 333 cm^{-1} is assigned to E_2^{High} - E_2^{Low} [34, 35, 37]. However, the B_1 modes are called silent modes because they are Raman and infrared inactive [34]. It is normally believed that the Raman signatures for ZnO above 300 cm^{-1} arise from the vibrations of O atoms and below due to Zn sublattice vibrations [38, 39]. Particularly, E_2^{High}, $A_1(LO)$, and $E_1(LO)$ modes are very much sensitive to the O site disorder in ZnO lattice [20, 40]. Fig. 6.6 presents the RT Raman scattering spectra (200–800 cm^{-1}) for all the samples, where the Raman modes E_2^{High} - E_2^{Low}, E_2^{High}, a broad band and different defect and N related modes have been appeared [37, 41]. E_2^{High} mode is correlated with O atom, which represents the high crystalline order in ZnO [42]. As seen from Fig. 6.6, the intensity of E_2^{High} Raman mode is gradually reduced with an increase in N ion fluence, indicating the reduction in crystallinity of the implanted samples as well as introduction of more lattice disorder, which are at par with the XRD results [43, 44]. A Raman mode at 275 cm^{-1} has been appeared for N implanted samples, while it is absent for the control sample (ArP). The origin of 275 cm^{-1} Raman Mode is controversial. It is believed that the native defects like Zn_i or Zn_i clusters or N related defects are responsible for 275 cm^{-1} Raman mode [36, 45-49]. However, N atoms being responsible for 275 cm^{-1} mode, Friedrich et al. [50] have reported that the vibrational mode at 275 cm^{-1} is due to the vibration of the Zn_i–N_O defect complex, where an Zn_i is bound to a N_O. Wu et al. [51] have also mentioned that 275 cm^{-1} Raman mode originates from N_O related complexes, likely to be in the form of Zn_i–N_O. As the N ion fluence increases, the concentration of N_O increases. As the concentration of N_O increases, the migration probability of isolated Zn_i with N_O also increases and therefore, the concentration of Zn_i–N_O defect complex increases. In fact, a sharp appearance of 275 cm^{-1}

Raman mode for higher influence has been observed. The origin of Raman modes at 511 cm^{-1} and 645 cm^{-1} are also controversial. Though, It has been reported that these two Raman modes correspond to the N-related local vibration [49], the presence of this mode has also been observed in Fe, Sb, and Al doped ZnO films [52]. However, Friedrich et al. [50] have confirmed that the presence of N in the ZnO lattice induces a local lattice distortion that favours the formation of Zn_i-related defect complexes (Zn_i–O_i), which is responsible for Raman mode of vibration at 511 cm^{-1}. In our case, low intense individual peaks at 511 cm^{-1} and 645 cm^{-1} respectively have only been appeared for ArN515 (Fig. 6.6). No trace of these modes has been observed for ArP and ArN114, which indicates that the defect complexes accompanied by N are produced only at higher ion fluence. In the range of 510–605 cm^{-1}, all the samples show a broad band Raman mode peaking at around 579 cm^{-1}. This broad peak is the cumulative effect of several Raman modes as reported by previous reports [53, 54]. Detailed deconvolution of the broad peak and assignment of the deconvoluted peaks to various Raman modes would be discussed in the next section. However, Fig. 6.6 shows the inverse-correlation between the intensities of 579 cm^{-1} and 437 cm^{-1} (E_2^{High}). It is clear that the intensity of 437 cm^{-1} Raman modes decreases as the fluence increases, whereas the intensity of 579 cm^{-1} mode increases. The reverse nature of the intensities of both 579 cm^{-1} and 437 cm^{-1} modes with an increase in N fluence is quite obvious because this broad band is composed of several disorder activated Raman modes [54].
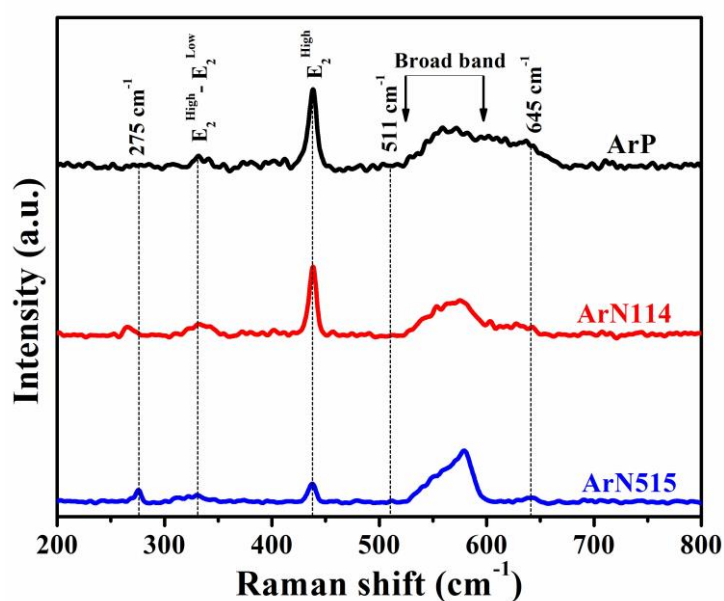
Fig. 6.6 Raman spectra of the control and N implanted ZnO NRs samples annealed in Ar.

The RT PL spectra of all the samples have been illustrated in Fig. 6.7(a), wherein a strong peak at ~3.28 eV corresponds to the NBE emission and a broad hump in the visible region from 1.75 to 2.85 eV corresponds to the DL emission [55, 56]. The I_{NBE} is maximum for the sample ArP. After N implantation and subsequently annealing in Ar, I_{NBE} decreases and the sample implanted with higher fluence (1×10^{16} ions/cm^2) owns minimum NBE emission intensity, indicating a large structural defect due to higher fluence of the energetic N ion implantation. In contrast to I_{NBE}, the value of I_{DL} is found to increase as compared to ArP just at an initial fluence. As the fluence increases, I_{DL} then starts to decrease. The DL emission in the visible region for ArP is observed ranging from ~1.75 to ~2.85 eV peaking at ~2.25 eV (yellow orange emission), while the peak of DL emission for N implanted samples is seen at ~2.4 eV (green emission). Therefore, the change of the yellow-orange emission for ArP to the green emission for N implanted samples is a clear indication of the changes in the structural defects as well [57]. The ratio I_{NBE} / I_{DL} has been presented using a bar diagram in Fig. 6.7(b) in order to compare the emission properties of ArP and N implanted ZnO NRs. It is seen from Fig. 6.7(b) that the ratio I_{NBE} / I_{DL} is maximum for ArP and the ratio decreases just after N is implanted with a fluence of 1×10^{14} ions/cm^2 and beyond which the ratio again increases till 5×10^{14} ions/cm^2 and thereafter the ratio again starts to decrease. The concentration of point defects is increased with an increase in the N ion fluence, which are not repaired completely even after annealing treatment for higher fluences. The large concentration of the point defects merges to larger open volumes defects, which act as non-radiative recombination centres and reduces the ratio I_{NBE} / I_{DL}.
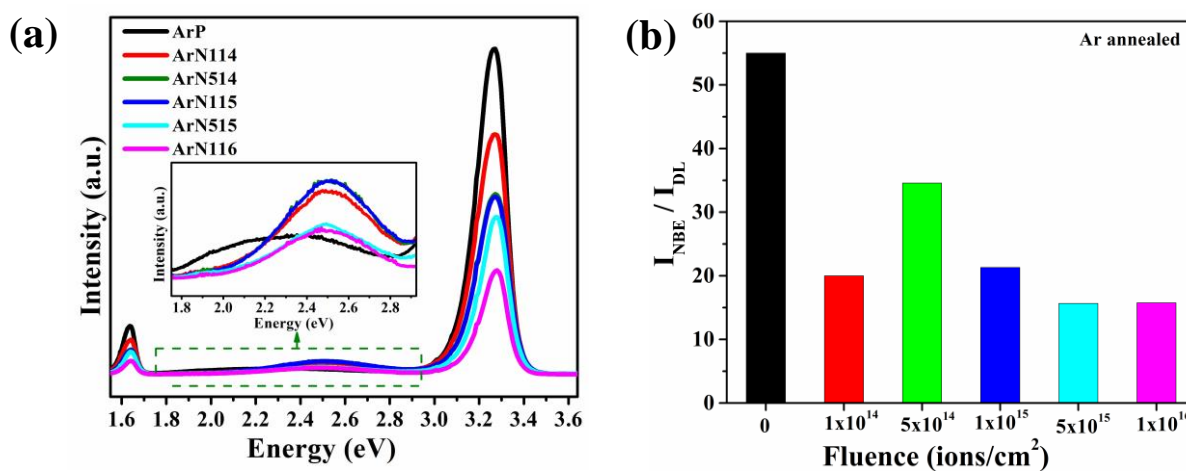
Fig. 6.7 (a) RT PL spectra of the control and N implanted ZnO NRs samples after annealing in Ar ambient, (b) variation of the ratio I_{NBE}/I_{DL} with N ion fluences.

To understand the possible defect energy levels contributing to DL emission, the visible emission spectrum has been deconvoluted with Gaussian fittings. The visible emission band of ArP and some representative N implanted samples have coherently been fitted with two Gaussian peaks P_1 and P_2 as shown in Fig. 6.8(a). The peak P_1 at ~2.5 eV corresponds to the green emission. V_{Zn} is mainly considered to be responsible for the green emissions [58-60]. The other peak P_2 ~2.2 eV is generally termed as yellow-orange emission which is due to surface adsorbed excess O_2/OH [61, 62]. By calculating the ratio of the area under P_1 and P_2 in Fig. 6.8(b), it is seen that, the green emission with respect to the yellow-orange emission increases with an increase in N ion fluence. Due to N implantation and subsequent annealing process, the surface defects are tailored and thus the characteristics of the emission changes from yellow-orange to a green. This is again in concordance with the XPS results revealing the contribution of surface adsorbed O is less for implanted samples than that of ArP. At the same time, according to SRIM prediction, excess V_{Zn} defects are induced due to N implantation, which aids to increase the green emission.
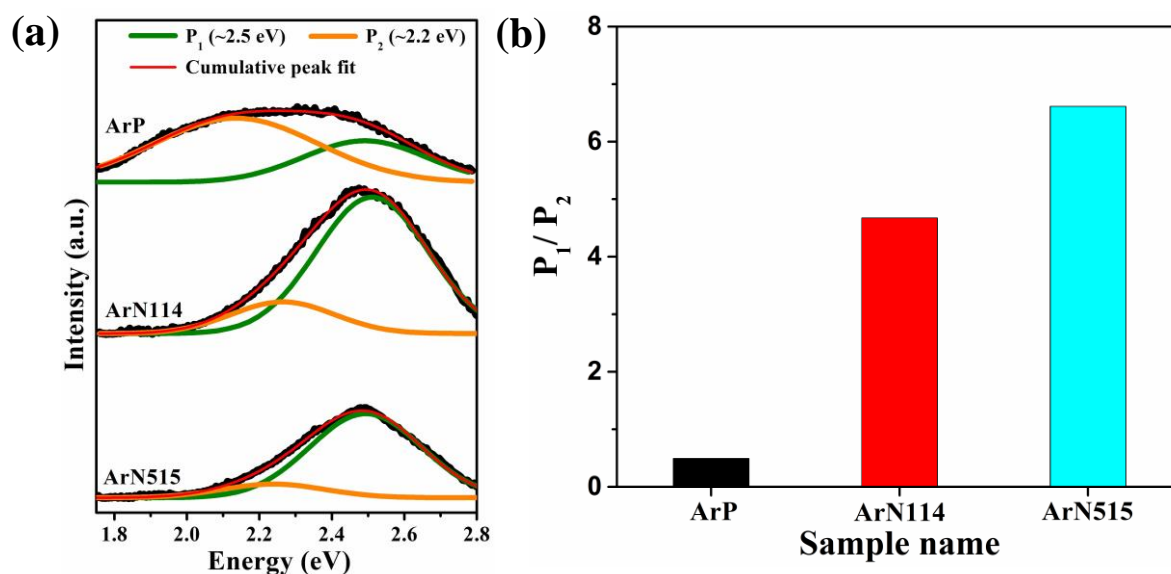
Fig. 6.8 (a) Gaussian fittings of the DL emission band, (b) bar diagram of the ratio of the area under the peak P_1 to P_2 of ArP, ArN14 and ArN515, respectively.

6.3.3 Influence of post-implantation annealing ambient

The XRD patterns of ArN515, ON515 and ZnN515 (Fig. 6.9(a)) show that the intensity of the (002) peak is the strongest for ZnN515 implying an excess Zn annealing ambient has a

great influence on the intensity of (002) peak. It indicates that due to annealing in excess Zn, a preferred orientation along c-axis of ZnO NRs further is strengthened. The enlarged view of (002) peaks in Fig. 6.9(b) indicates that the peak position is similar indicating similar lattice parameter of ZnO for all annealing conditions while a slight change in the FWHM of the (002) peak has been observed (Table 6.2). The lower FWHM value due to annealing in O_2 implies an achievement of better crystallinity. The average crystallite size of all the samples, as listed in Table 6.2 shows that the crystallite size is slightly larger for ON515 and ZnN515. Larger crystallite size implies lower dislocation density. The estimated value of dislocation density indicates that the number of defects in ON515 and ZnN515 are lower than that of ArN515 as expected. Thus, the XRD results partially support the prediction of better recovery of defects under annealing in O and Zn ambiences.
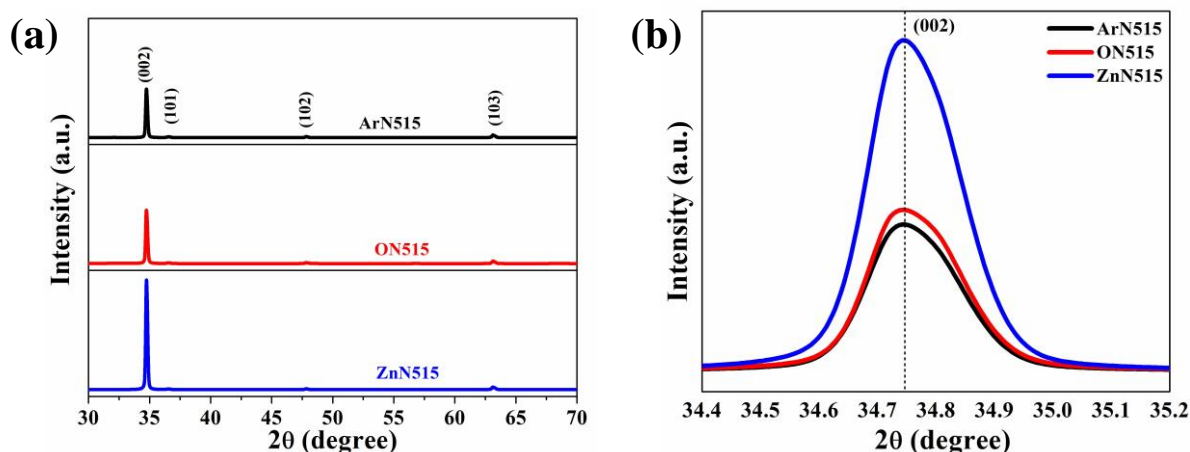
Fig. 6.9 (a) XRD patterns, (b) enlarged view of (002) peak of ArN515, ON515 and ZnN515 respectively.

Table 6.2 Values of c-axis lattice parameter, FWHM of (002) peak, crystallite size and dislocation density of ArN515, ON515 and ZnN515 respectively.

Sample name	c (nm)	FWHM (degree)	D (nm)	δ ($\times 10^{-4}$ nm^{-2})
ArN515	0.5160	0.1553	55.96	3.19
ON515	0.5160	0.1536	56.45	3.13
ZnN515	0.5160	0.1540	56.45	3.13

The full scan XPS spectra of ArN515, ON515 and ZnN515 in Fig. 6.10(a) show the XPS peaks, which correspond to the different core levels of O and Zn such as Zn 2p, O 1s [25]. The N 1s XPS spectra of the corresponding samples are shown in Fig. 6.10(b)-(d) respectively. Post-implantation annealing ambient particularly imparts a great influence on N 1s chemical state in ZnO. As observed in Fig. 6.10(b)-(d), the peaks N_I and N_{II} have been appeared at all annealing conditions. No additional peak is observed for ArN515 and ON515, while an additional peak N_{III} at ~404.3 eV has been appeared for ZnN515. As discussed in the earlier section, the emergence of N_{III} peak implies that some of N_O converts into the undesirable $(N_2)_O$ donors, because of annealing in excess Zn ambient, which is at par with the previous study [63]. The formation energy of $(N_2)_O$ is higher than N_O at O-rich condition, but lower at Zn-rich condition [63]. The lower formation energy of $(N_2)_O$ at Zn-rich condition boosts the N_O to convert into $(N_2)_O$ during annealing in excess Zn ambient [26]. This result implies that only N_O state is developed during annealing in O_2 and Ar ambient, whereas an additional donors of the type $(N_2)_O$ are produced under annealing in excess Zn ambient. Another aspect of annealing is that the N related defect complexes such as N_O-Zn_i, N_O-V_O and N_O-V_{Zn} are prone to be dissociated during thermal annealing treatment [64] and thus the concentration of isolated N_O is expected to be increased and at the same time some other defects may be annealed out. However, the dissociated defects again may migrate with each other at RT resulting in a very complex effect. For all annealing conditions, the isolated Zn_i defects formed from the dissociation of N_O-Zn_i or Zn_i clusters are annealed because of its low migration barrier [65]. In case of annealing in O_2, the isolated V_O is expected to be repaired and thus the concentration of donor N_O-V_O is reduced. Simultaneously the dissociated N_O and V_{Zn} again may migrate with each other, forming acceptor complex N_O-V_{Zn}. Thus, the isolated N_O is enhanced and N_O-V_{Zn} complex is maintained for annealing in O_2 ambient. In case of annealing in Zn ambient, the isolated V_{Zn} is likely to be repaired and the concentration of acceptor N_O-V_{Zn} is decreased. At the same time, the dissociated N_O and V_O again may migrate and form donor complex N_O-V_O. Thus, though the isolated N_O is enhanced, the concentration of N_O-V_{Zn} complex is reduced and N_O-V_O complex is maintained for annealing in Zn ambient. An annealing in Ar ambient has the effect on both V_{Zn} and V_O. It is expected that the concentration of both N_O-V_O and N_O-V_{Zn} defects are well maintained after annealing in Ar. Again, an insight into the O spectra (analyses done as described earlier by fitting the peak into three components) shows that the contribution of O_b for ZnN515 is higher than that of ArN515 and ON515 (Fig. 6.10(e)-(g)), which indicates that V_O defects are retained significantly after annealing in Zn ambient. From this discussion, it may be concluded that

the net effect of the acceptors is higher for ON515 and ArN515 as compared to ZnN515. Moreover, the contribution of O_a is better for annealing in O_2 ambient (Fig. 6.10(f)), which indicates that the stoichiometry of the implanted samples is well restored for annealing in O_2, which is in concord with the XRD results for ON515. From the above analyses, it may be inferred that post-implantation annealing in O_2 and Ar ambient can be effective to enhance the acceptors concentration in N implanted ZnO NRs.
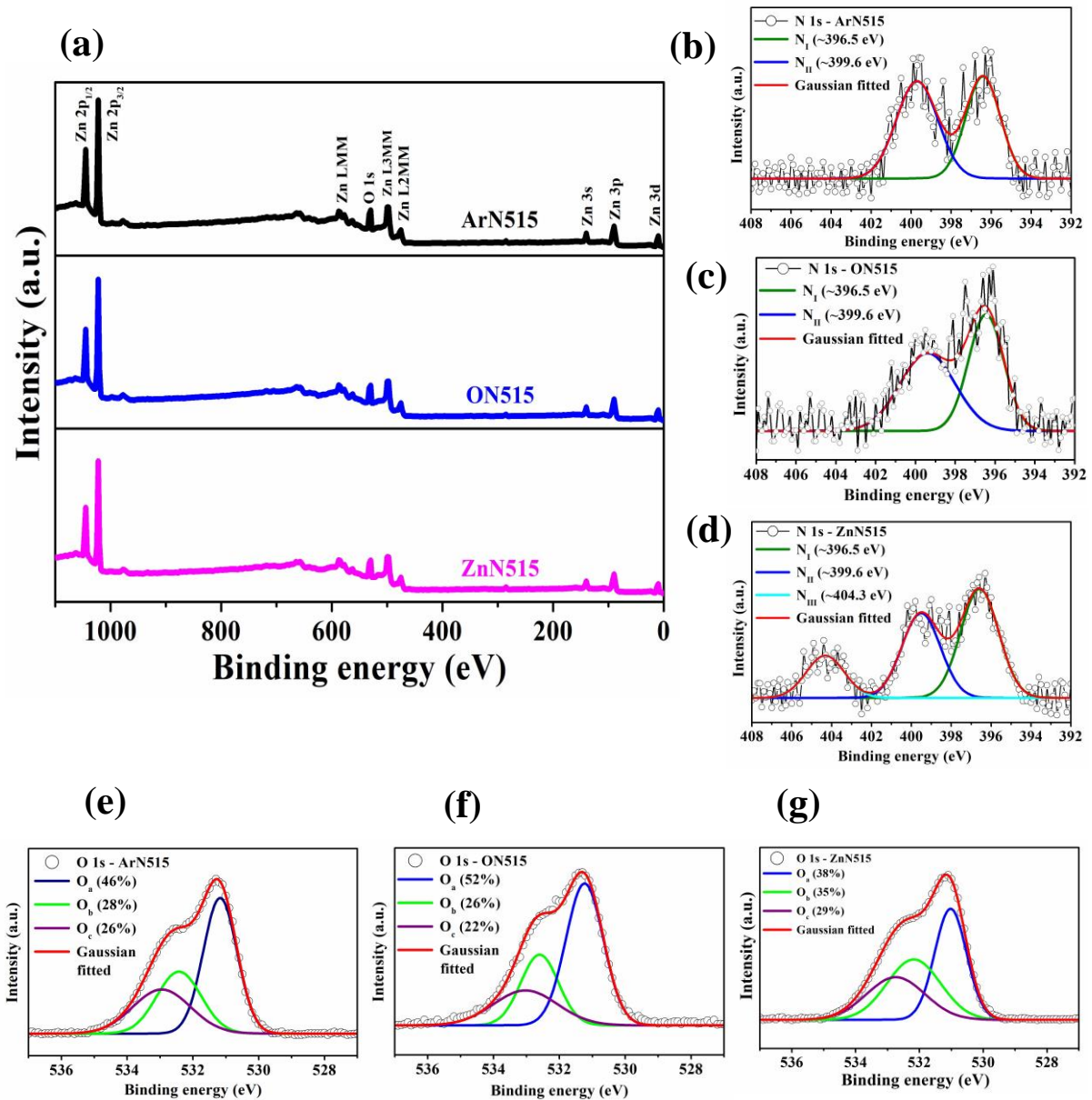
Fig. 6.10 (a) XPS survey scan, (b)-(d) N 1s spectra, (e)-(g) O 1s peak fittings of the samples ArN515, ON515 and ZnN515, respectively.

The electrical I-V characteristic curves of ArN515, ON515 and ZnN515 in Fig. 6.11 show that the current at all bias voltages is always lower for the samples annealed in Ar and O_2 ambiences as compared to that annealed in excess Zn ambient. The enhanced current in ZnN515 can be understood in terms of an increase in V_O and appearance of $(N_2)_O$ shallow donor, which is also at par with the XPS results. Simultaneously, the concentration of V_{Zn} is reduced due to annealing in Zn ambient, which seems to be another reason for an enhancement in the current in Zn annealed sample. However, lower current of ArN515 and ON515 at all bias voltages also suggest that N_O and N_O-V_{Zn} are effectively preserved during annealing in Ar and O_2 ambient. Further for ON515, the suppression or compensation of V_O may be another reason for lower current, which is again in accordance with the XPS results.
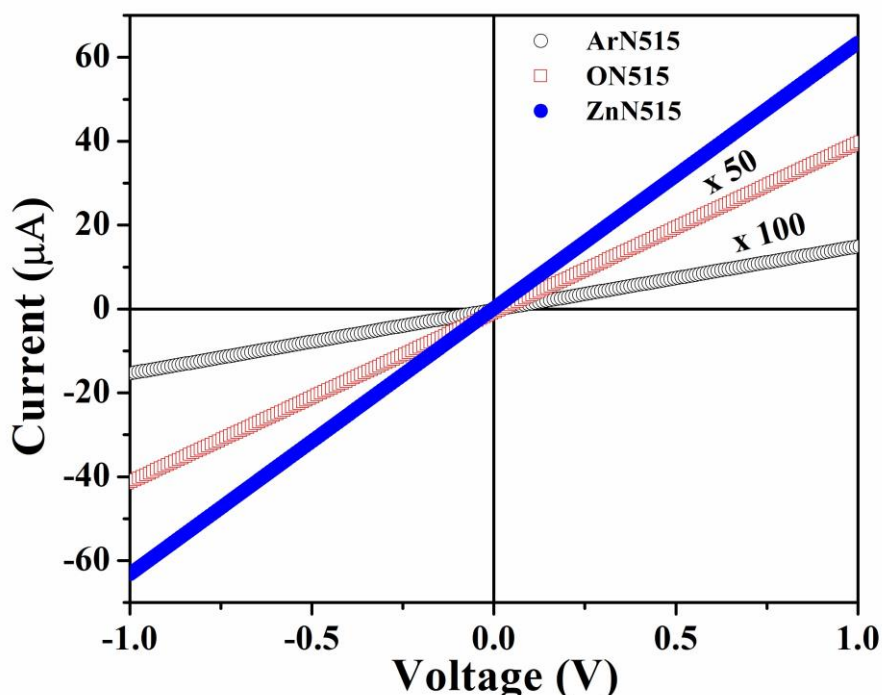
Fig. 6.11 I-V characteristic curves of ArN515, ON515 and ZnN515.

Fig. 6.12(a) presents the RT Raman scattering spectra in the range of 200–800 cm^{-1} for the ArN515, ON515 and ZnN515 respectively. It is seen that the intensity of E_2^{High} is always higher for O_2 and Zn annealing as compared to Ar annealing. This indicates to the fact that the crystallinity of implanted samples is restored for annealing in both O_2 and excess Zn ambiences, which is in agreement with the XRD results. The intensity of 275 cm^{-1} Raman

mode is through higher for annealing in O_2 and excess Zn ambiences, it is quite broader than that of Ar ambient. After annealing in O_2 and Zn ambiences, the decrease in the concentration of V_O and V_{Zn}, respectively may induce the N related defects to broaden 275 cm^{-1} mode. The broad Raman mode in the range of ~510 – 605 cm^{-1} for the samples ArN515, ON515 and ZnN515 is quite at par with the previous results [53, 54]. Though the evolution of the broad Raman mode has been investigated previously as a function of annealing temperature [54, 66, 67], here the evolution of the broad mode under various annealing ambiences has been investigated. It is seen that the shape of the broad band is quite different for annealing in excess Zn ambient than that of Ar and O_2. The reason behind this can be well understood considering the evolutions of the individual peaks under the broad mode which can coherently be deconvoluted into three Gaussians peaks centred at around 540, 560, and 579 cm^{-1} respectively in Fig. 6.12(b)-(d). The mode at 540 cm^{-1} is fundamentally a second order Raman mode (2B1^{Low}; 2LA), which usually dominates in existence of defects [53, 54, 68]. The physical origin of 560 cm^{-1} has been assigned to the surface optical (SO) phonon vibration induced by the interfacial defects at the grain boundaries in the ZnO shell [67]. In another report [69], it has been claimed that the SO phonon mode of vibration at 560 cm^{-1} occurs within thin ZnO coatings of Zn cores. Later on, Fan et al. [66] have revealed that such a Zn core/ZnO shell structure can be associated with the nanocrystallites, in which the existence of Zn cores is a result of incomplete oxidation of Zn at 450 °C. Thus, the mode at 560 cm^{-1} can reasonably be ascribed to Zn_i type defects. The implanted samples were annealed at 450 °C and thus logically, our assignment of the mode (560 cm^{-1}) to the Zn_i is in line with the previous observations [53, 54, 66]. The mode at 579 cm^{-1} is assigned to V_O type defects [53, 54, 68]. The areal contributions of 560 cm^{-1} and 579 cm^{-1} peaks for different annealing conditions plotted in Fig. 6.12(e) shows that the area under 560 cm^{-1} modes is lower for ZnN515 than that of ArN515 and ON515. This implies that the Zn_i defects in implanted samples can effectively be reduced after annealing in excess Zn ambient. The area under 579 cm^{-1} mode is lower for ArN515 and ON515, whereas it increases sharply for ZnN515. This implies that V_O related defects in N implanted samples are well recovered under annealing in Ar and O_2 ambiences, while these defects remain in appreciable quantity in Zn annealed sample. This result is in concordance with the XPS results.
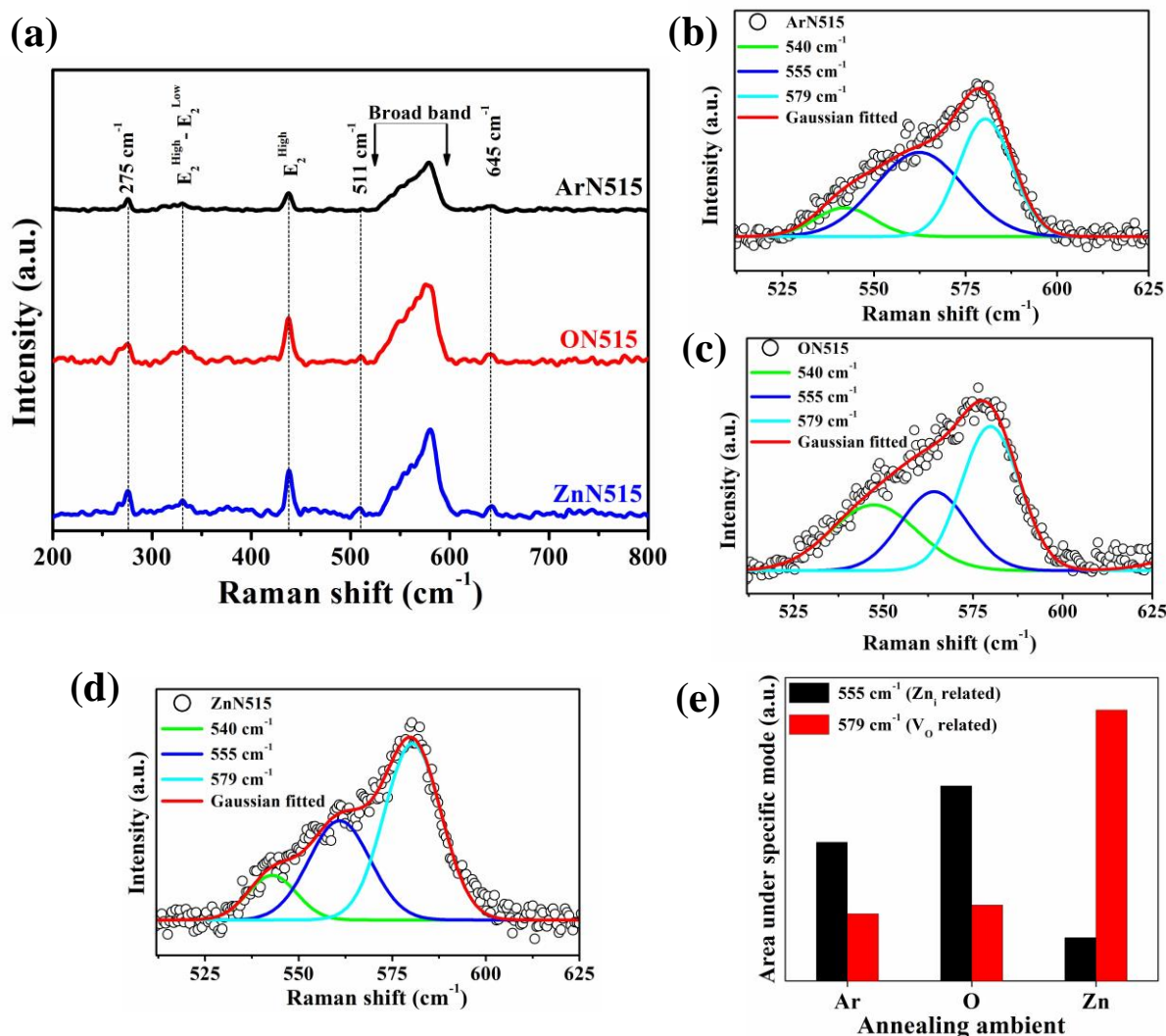
Fig. 6.12 (a) Raman spectra, (b)-(d) fittings of the broad band, and (e) the variation of area under 560 and 579 cm^{-1} mode for the samples ArN515, ON515 and ZnN515 respectively.

The RT PL spectra of ArN515, ON515 and ZnN515 has been illustrated in Fig. 6.13(a), where the strong peak at ~3.28 eV corresponds to NBE emission and a broad hump in the visible region from 1.75 to 2.85 eV indicates to the DL emission. In order to carry out a comparison, the ratio I_{NBE}/I_{DL} has been calculated in Fig. 6.13(b). It is seen that the ratio I_{NBE}/I_{DL} is maximum for ON515 and minimum for ZnN515. From this point of view, it may be inferred that the structural damages after annealing in O$_2$ ambient are well restored, which is in accordance with the XRD, XPS and Raman scattering results for ON515. The visible emission spectra have been deconvoluted with Gaussian's fittings in Fig. 6.13(c)-(e). By calculating the ratio of the area under P$_1$ to P$_2$, it is seen that for all annealing conditions, the green emission is higher than that of yellow-orange emission. Surprisingly, an intense green

emission is observed for Zn annealed sample as compared to others. After annealing in excess Zn, it is expected that Zn is diffused into ZnO lattice by sitting into V_{Zn} positions and/or create Zn_i defects. Zn_i has very low migration barrier of 0.56 eV [65] and it is therefore highly unlikely to get isolated Zn_i in annealed NRs. V_{Zn} defects most likely are reduced due to the diffusion of Zn into the V_{Zn} sites, which should give rise to a decrease in the green emission intensity in contrast to the observed emission properties. This confirms a probable involvement of N related defect complexes in the observed green emission, which may also be the cause of reduction in the ratio I_{NBE} / I_{DL} for ZnN515.
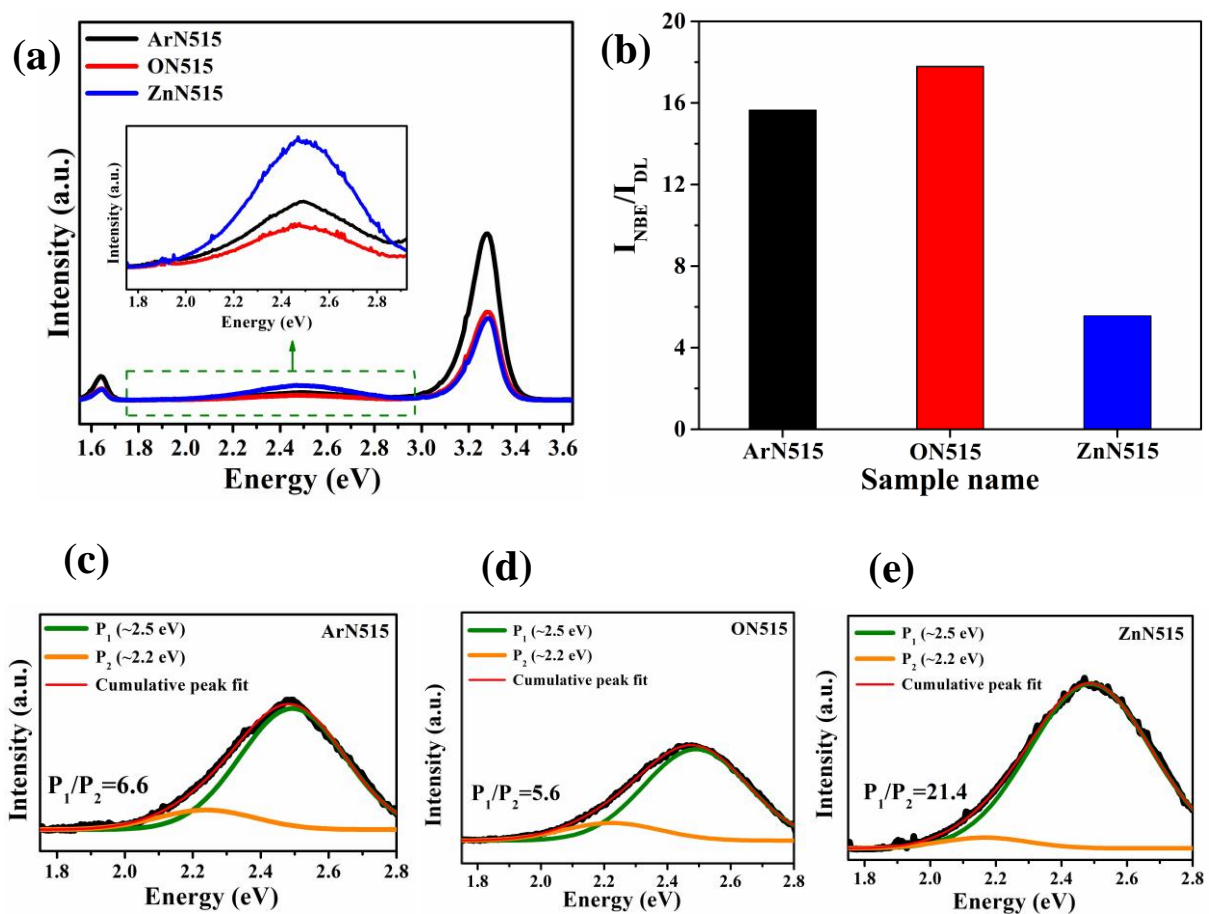
Fig. 6.13 (a) RT PL spectra, (b) comparison among the ratio I_{NBE}/I_{DL}, (c)-(e) Gaussian fittings of the DL emission band of the samples ArN515, ON515 and ZnN515 respectively.

6.4 Conclusions

In conclusion, the interaction of defects in 50 keV N implanted ZnO NRs by varying the ion fluences as well as annealing ambiences has been demonstrated. Ion induced structural

damages are increased sharply as the N ion fluence increases beyond 1×10^{15} ions/cm^2. These structural disorders have been seen to be related to various N related defect complexes. The incorporation of N at O sublattice induces the formation of N_O acceptor in N implanted NRs. In addition, the formation of N_O-V_{Zn} shallow acceptor complex has been predicted. Among various post-implantation annealing ambiences, an annealing separately in Ar and O$_2$ generates only N_O acceptor state, while an annealing in excess Zn ambient produces an unwanted $(N_2)_O$ donor state. In addition, O$_2$ and Ar play a key role to stabilize the N dopants in ZnO via suppressing V_O and/or preserving the concentration of N related acceptors in the ZnO NRs. These findings not only help one to enrich the microscopic understanding of interplay of defects but also demonstrate a way to tailor the nontrivial compensating point defects in case of p-type doping in ZnO which could be a potential component for electronic devices.

6.5 References

[1] D.C. Look, G.M. Renlund, R.H.B. II, J.R. Sizelove, As-doped p-type ZnO produced by an evaporation∕sputtering process, Applied Physics Letters, 85 (2004) 5269-5271.
[2] X.H. Pan, W. Guo, Z.Z. Ye, B. Liu, Y. Che, H.P. He, X.Q. Pan, Optical properties of antimony-doped p-type ZnO films fabricated by pulsed laser deposition, Journal of Applied Physics, 105 (2009) 113516.
[3] J.G. Lu, Z.Z. Ye, F. Zhuge, Y.J. Zeng, B.H. Zhao, L.P. Zhu, p-type conduction in N–Al co-doped ZnO thin films, Applied Physics Letters, 85 (2004) 3134-3135.
[4] X. Fang, J.H. Li, D.X. Zhao, D.Z. Shen, B.H. Li, X.H. Wang, Phosphorus-Doped p-Type ZnO Nanorods and ZnO Nanorod p-n Homojunction LED Fabricated by Hydrothermal Method, J. Phys. Chem. C, 113 (2009) 21208-21212.
[5] S.-L. Yao, J.-D. Hong, C.-T. Lee, C.-Y. Ho, D.-S. Liu, Determination of activation behavior in annealed Al–N codoped ZnO Films, Journal of Applied Physics, 109 (2011) 103504.
[6] Y.J. Zeng, Z.Z. Ye, W.Z. Xu, B. Liu, Y. Che, L.P. Zhu, B.H. Zhao, Study on the Hall-effect and photoluminescence of N-doped p-type ZnO thin films, Mater. Lett., 61 (2007) 41-44.
[7] J.G. Reynolds, C.L.R. Jr., A. Mohanta, J.F. Muth, J.E. Rowe, H.O. Everitt, D.E. Aspnes, Shallow acceptor complexes in p-type ZnO, Applied Physics Letters, 102 (2013) 152114.
[8] L. Liu, J.L. Xu, D.D. Wang, M.M. Jiang, S.P. Wang, B.H. Li, Z.Z. Zhang, D.X. Zhao, C.X. Shan, B. Yao, D.Z. Shen, p-Type Conductivity in N-Doped ZnO: The Role of the N-Zn-V-O Complex, Phys. Rev. Lett., 108 (2012).
[9] M.N. Amini, R. Saniz, D. Lamoen, B. Partoens, The role of the VZn–NO–H complex in the p-type conductivity in ZnO, Physical Chemistry Chemical Physics, 17 (2015) 5485-5489.
[10] Z. Huang, H. Ruan, H. Zhang, D. Shi, W. Li, G. Qin, F. Wu, L. Fang, C. Kong, Investigation on the p-type formation mechanism of nitrogen ion implanted ZnO thin films induced by rapid thermal annealing, Opt. Mater. Express, 9 (2019) 3098-3108.
[11] W.J. Li, H. Zhang, X.Y. Zhang, G.P. Qin, H.L. Li, Y.Q. Xiong, L.J. Ye, H.B. Ruan, C.Z. Tong, C.Y. Kong, L. Fang, Non-axial N-O-V-Zn shallow acceptor complexes in nitrogen implanted p-type ZnO thin films, Appl. Surf. Sci., 529 (2020).
[12] M. Chiesa, S. Livraghi, M.C. Paganini, E. Salvadori, E. Giamello, Nitrogen-doped semiconducting oxides. Implications on photochemical, photocatalytic and electronic properties derived from EPR spectroscopy, Chem. Sci., 11 (2020) 6623-6641.

[13] P. Fons, H. Tampo, A.V. Kolobov, M. Ohkubo, S. Niki, J. Tominaga, R. Carboni, F. Boscherini, S. Friedrich, Direct Observation of Nitrogen Location in Molecular Beam Epitaxy Grown Nitrogen-Doped ZnO, Phys. Rev. Lett., 96 (2006) 045504.

[14] C.C. Lin, S.Y. Chen, S.Y. Cheng, H.Y. Lee, Properties of nitrogen-implanted p-type ZnO films grown on Si3N4/Si by radio-frequency magnetron sputtering, Applied Physics Letters, 84 (2004) 5040-5042.

[15] M. Wang, F. Ren, J.G. Zhou, G.X. Cai, L. Cai, Y.F. Hu, D.N. Wang, Y.C. Liu, L.J.J. Guo, S.H. Shen, N Doping to ZnO Nanorods for Photoelectrochemical Water Splitting under Visible Light: Engineered Impurity Distribution and Terraced Band Structure, Sci Rep, 5 (2015).

[16] S.H. Park, Y.B. Lee, C.H. Kwak, S.Y. Seo, S.H. Kim, Y.D. Choi, S.W. Han, Structural and optical properties of nitrogen-ion-implanted ZnO nanorods, J. Korean Phys. Soc., 52 (2008) 954-959.

[17] Y.T. Chuang, J.W. Liou, W.Y. Woon, Formation of p-type ZnO thin film through co-implantation, Nanotechnology, 28 (2017).

[18] P. Kumar, H.K. Malik, A. Ghosh, R. Thangavel, K. Asokan, An insight to origin of ferromagnetism in ZnO and N implanted ZnO thin films: Experimental and DFT approach, J. Alloy. Compd., 768 (2018) 323-328.

[19] S. Ramasubramanian, R. Thangavel, M. Rajagopalan, A. Thamizhavel, K. Asokan, D. Kanjilal, J. Kumar, Study on the ferromagnetism in Co and N doped ZnO thin films, Curr. Appl. Phys., 13 (2013) 1547-1553.

[20] J.P. Lv, X.J. Li, Defect evolution in ZnO and its effect on radiation tolerance, Phys. Chem. Chem. Phys., 20 (2018) 11882-11887.

[21] K.R. Nandanapalli, D. Mudusu, Surface Passivated Zinc Oxide (ZnO) Nanorods by Atomic Layer Deposition of Ultrathin ZnO Layers for Energy Device Applications, ACS Appl. Nano Mater., 1 (2018) 4083-4091.

[22] P. Ariyakkani, L. Suganya, B. Sundaresan, Investigation of the structural, optical and magnetic properties of Fe doped ZnO thin films coated on glass by sol-gel spin coating method, J. Alloy. Compd., 695 (2017) 3467-3475.

[23] J.J. Macias-Sanchez, L. Hinojosa-Reyes, A. Caballero-Quintero, W. de la Cruz, E. Ruiz-Ruiz, A. Hernandez-Ramirez, J.L. Guzman-Mar, Synthesis of nitrogen-doped ZnO by sol-gel method: characterization and its application on visible photocatalytic degradation of 2,4-D and picloram herbicides, Photochem. Photobiol. Sci., 14 (2015) 536-542.

[24] P. Bindu, S. Thomas, Estimation of lattice strain in ZnO nanoparticles: X-ray peak profile analysis, Journal of Theoretical and Applied Physics, 8 (2014) 123-134.

[25] R. Al-Gaashani, S. Radiman, A.R. Daud, N. Tabet, Y. Al-Douri, XPS and optical studies of different morphologies of ZnO nanostructures prepared by microwave methods, Ceram. Int., 39 (2013) 2283-2292.

[26] X.H. Li, H.Y. Xu, X.T. Zhang, Y.C. Liu, J.W. Sun, Y.M. Lu, Local chemical states and thermal stabilities of nitrogen dopants in ZnO film studied by temperature-dependent x-ray photoelectron spectroscopy, Applied Physics Letters, 95 (2009).

[27] S. Karamat, R.S. Rawat, T.L. Tan, P. Lee, V. Springham, E. Ghareshabani, R. Chen, H.D. Sun, Nitrogen doping in pulsed laser deposited ZnO thin films using dense plasma focus, Appl. Surf. Sci., 257 (2011) 1979-1985.

[28] X. Yang, A. Wolcott, G. Wang, A. Sobo, R.C. Fitzmorris, F. Qian, J.Z. Zhang, Y. Li, Nitrogen-Doped ZnO Nanowire Arrays for Photoelectrochemical Water Splitting, Nano Lett., 9 (2009) 2331-2336.

[29] H. Zhang, W.J. Li, G.P. Qin, H.B. Ruan, D. Wang, J. Wang, Z. Huang, F. Wu, C.Y. Kong, L. Fang, Thermal evolution and migration behavior of ion-implanted nitrogen in ZnO:In-N films, Appl. Surf. Sci., 509 (2020).

[30] G.P. Qin, H. Zhang, W.J. Li, H.B. Ruan, J. Wang, D. Wang, L. Fang, C.Y. Kong, Investigation on the formation mechanism of p-type ZnO:In-N thin films: experiment and theory, Journal of Materials Science-Materials in Electronics, 30 (2019) 6059-6064.

[31] M. Pal, S. Bera, S. Sarkar, S. Jana, Influence of Al doping on microstructural, optical and photocatalytic properties of sol-gel based nanostructured zinc oxide films on glass, RSC Adv., 4 (2014) 11552-11563.

[32] T. Basu, M. Kumar, S. Nandy, B. Satpati, C.P. Saini, A. Kanjilal, T. Som, Thickness-dependent blue shift in the excitonic peak of conformally grown ZnO:Al on ion-beam fabricated self-organized Si ripples, Journal of Applied Physics, 118 (2015).

[33] D. Briggs, Handbook of X-ray Photoelectron Spectroscopy C. D. Wanger, W. M. Riggs, L. E. Davis, J. F. Moulder and G. E.Muilenberg Perkin-Elmer Corp., Physical Electronics Division, Eden Prairie, Minnesota, USA, 1979. 190 pp. $195, Surface and Interface Analysis, 3 (1981) v-v.

[34] R. Jothilakshmi, V. Ramakrishnan, R. Thangavel, J. Kumar, A. Sarua, M. Kuball, Micro-Raman scattering spectroscopy study of Li-doped and undoped ZnO needle crystals, J. Raman Spectrosc., 40 (2009) 556-561.

[35] A. Mondal, S. Pal, A. Sarkar, T.S. Bhattacharya, S. Pal, A. Singha, S.K. Ray, P. Kumar, D. Kanjilal, D. Jana, Raman investigation of N-implanted ZnO: Defects, disorder and recovery, J. Raman Spectrosc., 50 (2019) 1926-1937.

[36] J. Kennedy, B. Sundrakannan, R.S. Katiyar, A. Markwitz, Z. Li, W. Gao, Raman scattering investigation of hydrogen and nitrogen ion implanted ZnO thin films, Curr. Appl. Phys., 8 (2008) 291-294.

[37] S. Khachadorian, R. Gillen, S. Choi, C. Ton-That, A. Kliem, J. Maultzsch, M.R. Phillips, A. Hoffmann, Effects of annealing on optical and structural properties of zinc oxide nanocrystals, Phys. Status Solidi B-Basic Solid State Phys., 252 (2015) 2620-2625.

[38] R. Cusco, E. Alarcon-Llado, J. Ibanez, L. Artus, J. Jimenez, B.G. Wang, M.J. Callahan, Temperature dependence of raman scattering in ZnO, Phys. Rev. B, 75 (2007) 165202.

[39] V. Russo, M. Ghidelli, P. Gondoni, C.S. Casari, A.L. Bassi, Multi-wavelength Raman scattering of nanostructured Al-doped zinc oxide, J. Appl. Phys., 115 (2014) 073508.

[40] A. Jagerova, R. Miksova, O. Romanenko, I. Plutnarova, Z. Sofer, P. Slepicka, J. Mistrik, A. Mackova, Surface modification by high-energy heavy-ion irradiation in various crystalline ZnO facets, Phys. Chem. Chem. Phys., 23 (2021) 22673-22684.

[41] R. Cusco, E. Alarcon-Llado, J. Ibanez, L. Artus, J. Jimenez, B.G. Wang, M.J. Callahan, Temperature dependence of raman scattering in ZnO, Phys. Rev. B, 75 (2007).

[42] A. Kumar, S. Keshri, B. Pandey, J.B.M. Krishna, D. Das, Impact of N5+ ion implantation on optical and electrical properties of polycrystalline ZnO film, Radiat. Eff. Defects Solids, 169 (2014) 965-979.

[43] Z.Q. Chen, A. Kawasuso, Y. Xu, H. Naramoto, X.L. Yuan, T. Sekiguchi, R. Suzuki, T. Ohdaira, Production and recovery of defects in phosphorus-implanted ZnO, J. Appl. Phys., 97 (2005) 013528.

[44] Z. Huang, H.B. Ruan, H. Zhang, D.P. Shi, W.J. Li, G.P. Qin, F. Wu, L. Fang, C.Y. Kong, Conversion mechanism of conductivity and properties of nitrogen implanted ZnO single crystals induced by post-annealing, J. Mater. Sci.-Mater. Electron., 30 (2019) 4555-4561.

[45] J.B. Wang, H.M. Zhong, Z.F. Li, W. Lu, Raman study of N+-implanted ZnO, Applied Physics Letters, 88 (2006) 101913.

[46] R. Kobayashi, T. Kishi, Y. Katayanagi, T. Yano, N. Matsushita, Fabrication of nitrogen-doped ZnO nanorod arrays by hydrothermal synthesis and ambient annealing, RSC Adv., 8 (2018) 23599-23605.

[47] W.W. Liu, B. Yao, Z.Z. Zhang, Y.F. Li, B.H. Li, C.X. Shan, J.Y. Zhang, D.Z. Shen, X.W. Fan, Doping efficiency, optical and electrical properties of nitrogen-doped ZnO films, Journal of Applied Physics, 109 (2011) 093518.

[48] M.A. Gluba, N.H. Nickel, N. Karpensky, Interstitial zinc clusters in zinc oxide, Phys. Rev. B, 88 (2013).

[49] A. Kaschner, U. Haboeck, M. Strassburg, G. Kaczmarczyk, A. Hoffmann, C. Thomsen, A. Zeuner, H.R. Alves, D.M. Hofmann, B.K. Meyer, Nitrogen-related local vibrational modes in ZnO : N, Applied Physics Letters, 80 (2002) 1909-1911.

[50] F. Friedrich, M.A. Gluba, N.H. Nickel, Identification of nitrogen and zinc related vibrational modes in ZnO, Applied Physics Letters, 95 (2009).

[51] K.Y. Wu, Q.Q. Fang, W.N. Wang, M.A. Thomas, J.B. Cui, On the origin of an additional Raman mode at 275 cm(-1) in N-doped ZnO thin films, Journal of Applied Physics, 111 (2012).

[52] C. Bundesmann, N. Ashkenov, M. Schubert, D. Spemann, T. Butz, E.M. Kaidashev, M. Lorenz, M. Grundmann, Raman scattering in ZnO thin films doped with Fe, Sb, Al, Ga, and Li, Applied Physics Letters, 83 (2003) 1974-1976.

[53] A. Mondal, S. Pal, A. Sarkar, T.S. Bhattacharya, A. Das, N. Gogurla, S.K. Ray, P. Kumar, D. Kanjilal, K.D. Devi, A. Singha, S. Chattopadhyay, D. Jana, Raman spectroscopic analysis on Li, N and (Li,N) implanted ZnO, Mater. Sci. Semicond. Process, 80 (2018) 111-117.

[54] A. Mondal, S. Pal, A. Sarkar, T.S. Bhattacharya, A. Singha, S.K. Ray, P. Kumar, D. Kanjilal, D. Jana, Raman investigation of N-implanted ZnO: Defects, disorder and recovery, J. Raman Spectrosc., 50 (2019) 1926-1937.

[55] R. Ghosh, B. Mallik, S. Fujihara, D. Basak, Photoluminescence and photoconductance in annealed ZnO thin films, Chem. Phys. Lett., 403 (2005) 415-419.

[56] R.K. Biroju, P.K. Giri, Strong visible and near infrared photoluminescence from ZnO nanorods/nanowires grown on single layer graphene studied using sub-band gap excitation, Journal of Applied Physics, 122 (2017).

[57] H.P. He, Q.A. Yang, C. Liu, L.W. Sun, Z.Z. Ye, Size-Dependent Surface Effects on the Photoluminescence in ZnO Nanorods, J. Phys. Chem. C, 115 (2011) 58-64.

[58] F. Fabbri, M. Villani, A. Catellani, A. Calzolari, G. Cicero, D. Calestani, G. Calestani, A. Zappettini, B. Dierre, T. Sekiguchi, G. Salviati, Zn vacancy induced green luminescence on non-polar surfaces in ZnO nanostructures, Sci Rep, 4 (2014).

[59] H. Chen, S.L. Gu, K. Tang, S.M. Zhu, Z.B. Zhu, J.D. Ye, R. Zhang, Y.D. Zheng, Origins of green band emission in high-temperature annealed N-doped ZnO, J. Lumines., 131 (2011) 1189-1192.

[60] D. Sett, S. Sarkar, D. Basak, A successive photocurrent transient study to probe the sub-band gap electron and hole traps in ZnO nanorods, RSC Adv., 4 (2014) 58553-58558.

[61] J.W.P. Hsu, D.R. Tallant, R.L. Simpson, N.A. Missert, R.G. Copeland, Luminescent properties of solution-grown ZnO nanorods, Applied Physics Letters, 88 (2006).

[62] R.B.M. Cross, M.M. De Souza, E.M.S. Narayanan, A low temperature combination method for the production of ZnO nanowires, Nanotechnology, 16 (2005) 2188-2192.

[63] Y.F. Yan, S.B. Zhang, S.T. Pantelides, Control of doping by impurity chemical potentials: Predictions for p-type ZnO, Phys. Rev. Lett., 86 (2001) 5723-5726.

[64] W.J. Li, C.N. Wang, J.W. Ma, H. Zhang, Y.Q. Xiong, H.L. Li, L.J. Ye, H.B. Ruan, G.P. Qin, L. Fang, C.Y. Kong, Effect of thermal evolution of point defects on the electrical properties of nitrogen-implanted ZnO thin films, Journal of Materials Science-Materials in Electronics, 31 (2020) 4208-4213.

[65] A. Janotti, C.G. Van de Walle, Native point defects in ZnO, Phys. Rev. B, 76 (2007).

[66] H.J. Fan, R. Scholz, F.M. Kolb, M. Zacharias, U. Gösele, F. Heyroth, C. Eisenschmidt, T. Hempel, J. Christen, On the growth mechanism and optical properties of ZnO multi-layer nanosheets, Applied Physics A, 79 (2004) 1895-1900.

[67] H. Zeng, X. Ning, X. Li, An insight into defect relaxation in metastable ZnO reflected by a unique luminescence and Raman evolutions, Physical Chemistry Chemical Physics, 17 (2015) 19637-19642.

[68] M. Scepanovic, M. Grujic-Brojcin, K. Vojisavljevic, S. Bernik, T. Sreckovic, Raman study of structural disorder in ZnO nanopowders, J. Raman Spectrosc., 41 (2010) 914-921.

[69] J. Xu, G. Cheng, W. Yang, Y. Du, Raman scattering from surface phonons in fine Zn particles coated with ZnO, Journal of Physics B: Atomic, Molecular and Optical Physics, 29 (1996) 6227.

CHAPTER-7

Evolution of point defects in Li implanted ZnO nanorods

7.1 Introduction

The p-type conductivity in ZnO can theoretically be achieved by substituting group-I elements in Zn or group-V elements in O sites [1-3]. In the previous chapter, the substitution of group-V element in ZnO by implanting N ion in ZnO NRs have been explained. Now, in this chapter, the substitution group-I element taking Li ion implantation in ZnO NRs has been discussed. Though there are several reports on p-type ZnO, the results are not reproducible and still remain debatable [4-7]. In many cases, the group-I elements have shown better success rate in getting p-type ZnO as compared to the group-V elements. However, dopants belonging to the group-I often act as donors due to their tendency to occupy the interstitial sites [8-10]. Among the group-I elements, Li ion (Li^{1+}) has the smallest ionic radius (0.60 Å), which is very close to that of Zn ion (Zn^{2+}) (0.74 Å) [11, 12]. Therefore, Li can easily occupy the Zn^{2+} site and produces Li_{Zn} acceptors [11-13]. Besides, Li can also occupy an interstitial position (Li_i) due to its small ionic radius [11-13]. This Li_i defect acts as a donor and compensates the contribution of Li_{Zn} and V_{Zn} acceptors. Therefore, the introduction of an effective shallow acceptor level, as well as suppression of the donor concentration, are prerequisites to obtain p-type conductivity in Li doped ZnO NRs. Compared to other ion implantation [14-19], few pieces of literature are available which have focused on Li implantation in ZnO thin films [20-22]. In an attempt to make ZnO p-type, Nagar et al. [21] have shown that Li implantation into ZnO thin films displays n-type conductivity even after employing annealing treatment due to presence of donor defects. However, a free electron-acceptor peak at ~ 3.227 eV in PL spectra appears in the Li implanted films, which indicates that some Li ions act as shallow acceptors in ZnO [21]. Therefore, an interaction between Li impurity and the intrinsic defects as well as its influence on the physical properties of ZnO NRs must be understood clearly for realization of p-type ZnO for its applications in devices. Keeping these issues in mid, in this chapter, the formation and the evolution of various point defects due to Li ion implantation in ACG grown vertical ZnO NRs resulting in changes in the structural, optical, and electrical properties as a function of various fluences have been investigated experimentally as well as using SRIM simulation code [23].

7.2 Experimental details

ZnO NRs were first grown on the glass substrates by ACG method details of which are described in chapter 3. The as-grown ZnO NRs were then implanted with 100 keV Li ions at

RT with varying the fluences from 1×10^{14} to 7×10^{15} ions/cm^2. The implanted area of the samples was around one cm^2 with a beam current of 80 nA. The Li ion implantation in ZnO NRs can be illustrated with a schematic which is presented in Fig. 7.1. The nomenclatures of the samples in this study are given in Table 7.1.
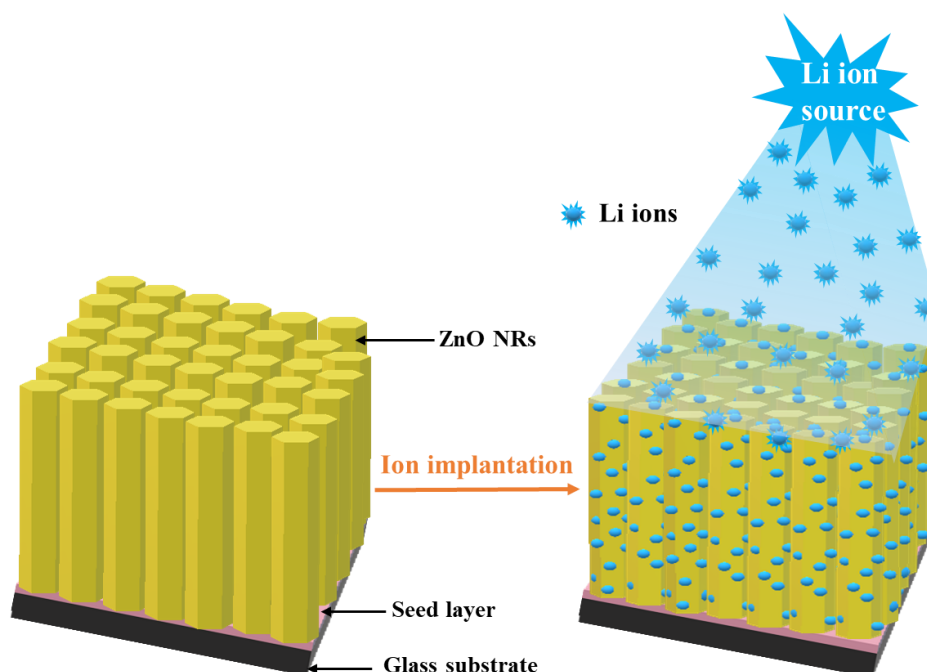
Fig. 7.1 Li ion implantation into aqueous chemically grown vertically aligned ZnO NRs.

Table 7.1 The nomenclature of the samples according to the corresponding Li ion fluences.

Fluence (ions/cm^2)	Sample name
0	Pristine
1×10^{14}	Li114
5×10^{14}	Li514
1×10^{15}	Li115
5×10^{15}	Li515
7×10^{15}	Li715

The structural, morphological, compositional, optical, and electrical analyses of the samples have been carried out using XRD, FESEM, XPS, Raman, PL, and electrical I-V measurements, respectively as described in the chapter 3.

7.3 Results and discussion

7.3.1 Experimental characterizations

The XRD patterns of pristine and Li implanted ZnO NRs presented in Fig. 7.2(a) show the narrow, sharp, and distinct peaks (according to the JCPDS card no. 36-1451), which correspond to the diffractions from the (0002), $(10\bar{1}1)$, $(10\bar{1}2)$, $(10\bar{1}3)$, $(10\bar{2}2)$ planes of hexagonal wurtzite ZnO. The (002) diffraction peak is the strongest among all the peaks, which indicates the preferential growth of the NRs along the <002> direction for all the samples. Any trace of Li-related impurities or secondary phase has not been detected by the XRD measurements (Fig. 7.2(a)). According to the enlarged view of the (002) peaks, as presented in Fig. 7.2(b), the intensity of the (002) peak though increases at the initial fluence as compared to the pristine, it decreases distinctly as the fluence increases. A decrease in the peak intensity indicates a deterioration in the crystal quality, which is probably a result of the formation of defect complexes at higher Li fluences [24]. Li doping in ZnO should lead to a shift in the XRD peak position towards a higher 2θ value because of the smaller ionic radius of Li^{1+} than that of Zn^{2+} [25-27]. In contrast, a gradual shift of the (002) peak position towards a lower 2θ value (Fig. 7.2(b)) with an increase in the Li fluence has been observed similar to the previous studies [20, 28]. Due to the lower angle shift, the c-axis lattice parameter (c) increases and a tensile strain (ε) arises (Fig. 7.2(c)). The value of ε is maximum for pristine and then it is released gradually with an increase in the Li fluence. A decrease in the residual strain in the system is likely to occur resulting from implantation-induced point defects, defects complexes, or even dislocations [24]. The value of FWHM of the (002) peak increases as the fluence increases (Fig. 7.2(d)) due to the appearance of structural disorders in the implanted NRs [29, 30]. The average crystallite size (D) as calculated from the well-known Debye-Scherrer's formula, described in chapter 3, decreases with an increase in the fluence, as shown in Fig. 7.2(d), which is at par with the previously reported results [25, 28]. The dislocation density (δ) increases drastically with an increase in Li ion fluence beyond 5×10^{14} ions/cm^2 (Fig. 7.2(d)) revealing the information on the evolution of structural defects in Li implanted ZnO NRs.
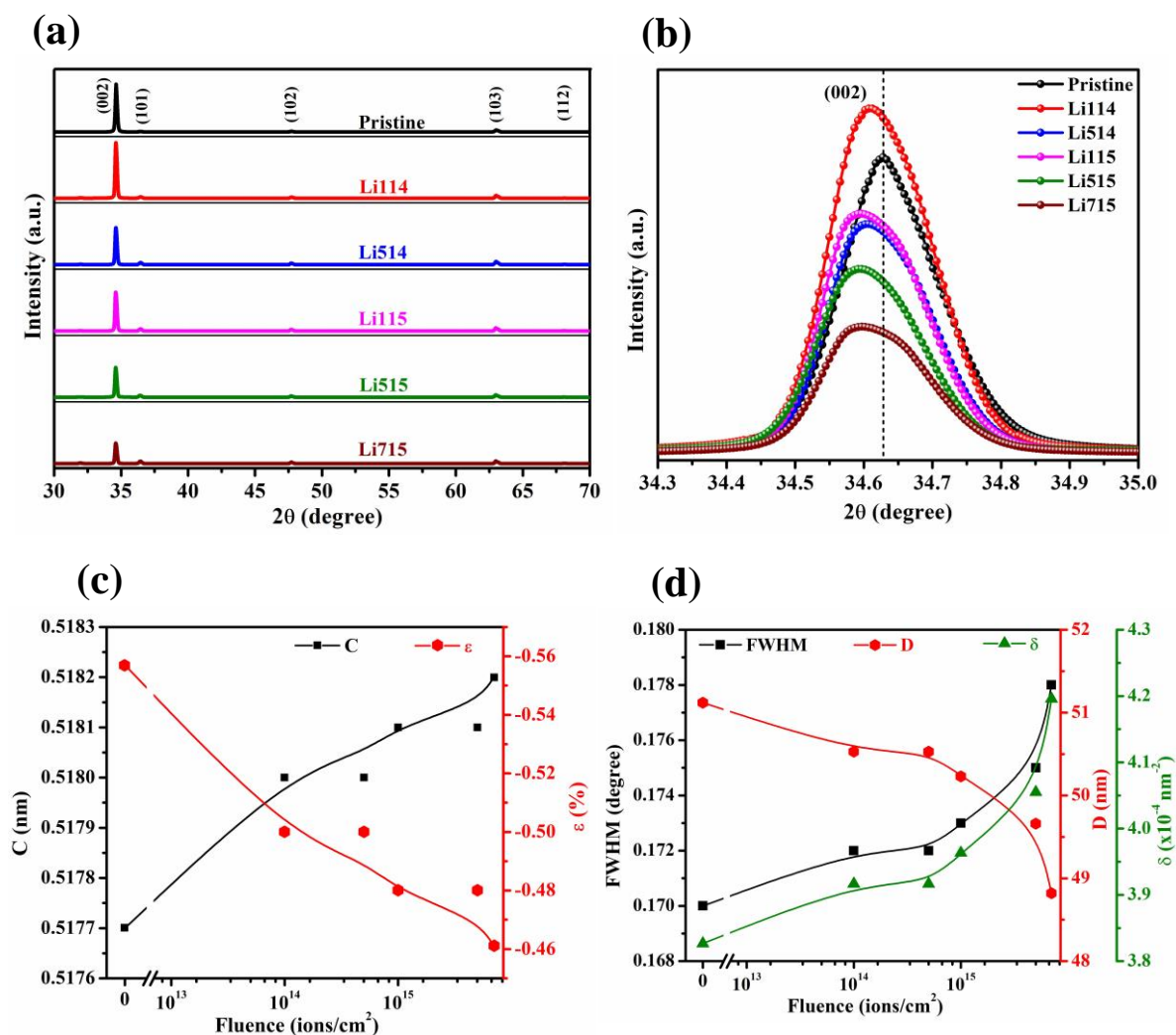
Fig. 7.2 (a) XRD patterns, (b) the enlarged view of (002) peaks, variation of (c) c-axis lattice parameter, strain, and (d) FWHM of (002) peak, crystallite size, and dislocation density with Li ion fluence.

The top view FESEM images of the pristine and a representative implanted sample Li715 in Fig. 7.3(a)-(b) shows the quasi-vertical alignment of the hexagonal ZnO NRs, which is supporting the XRD results. The diameter of the NRs has been estimated to be in the range of 100 ± 15 nm and both the top and side surfaces are smooth (Fig. 7.3(a)). The cross-sectional FESEM image of the pristine in the inset in Fig. 7.3(a) shows that the length of the NRs is ~850 nm. The rodlike morphology is retained after Li implantation (Fig. 7.3(b)) and no substantial change in the NRs' morphology is observed.

(a)

(b)
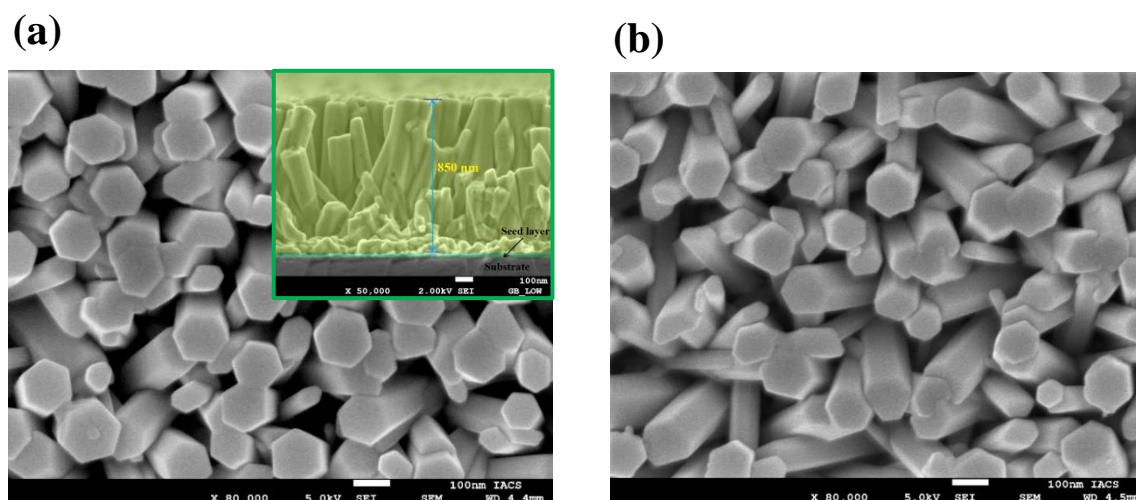
Fig. 7.3 The top view FESEM images of (a) pristine and (b) Li715. The inset in Fig. 7.3(a) is the cross-sectional FESEM image of pristine.

The XPS scans were recorded after a sputtering process for ~100 s to remove any undesired particles from the sample's surface. The C 1s binding energy level at 284.5 eV has been used as a reference energy level to eliminate the charging-dependent shift in the spectra. The full survey scans of pristine and a representative sample Li515 shown in Fig. 7.4(a) show the XPS peaks corresponding to O 1s and Zn 2p. A broad peak in the region between 53.5 and 56.5 eV due to Li 1s can be deconvoluted into two Gaussian peaks, P_1 and P_2 (Fig. 7.4(b)). The peak P_1 at 55.7 eV is related to Li^{1+} in Zn^{2+} site bonded to O [27]. The peak P_2 at 54.9 eV is usually attributed to Li-OH bonds on the surface [27]. Thus, Li_{Zn} is expected to form acceptor state in the implanted sample, although a significant amount of implanted Li makes Li-OH bonds with the surface adsorbed -OH and may limit the acceptor formation [27]. Similar to the previous chapters, the O 1s XPS peaks of the pristine and Li515 being asymmetric in nature can be deconvoluted into three Gaussian peaks as revealed in Fig. 7.4(c)-(d). According to Fig. 7.4(c)-(d), the peak area of O_b for Li515 is more than double to that of the pristine, suggesting drastic increase in the formation of V_O defects due to Li implantation. Further, the lower area of O_a in Li515 as compared to that of pristine indicates the degradation of the crystallinity. This is at par with the XRD results as discussed earlier. Considering the three main XPS peaks Zn $2p^{3/2}$, O 1s, and Li 1s and by using their peak area and relative sensitivity factor [31], the estimated atomic concentration of Li is ~ 0.12 at% for Li515.
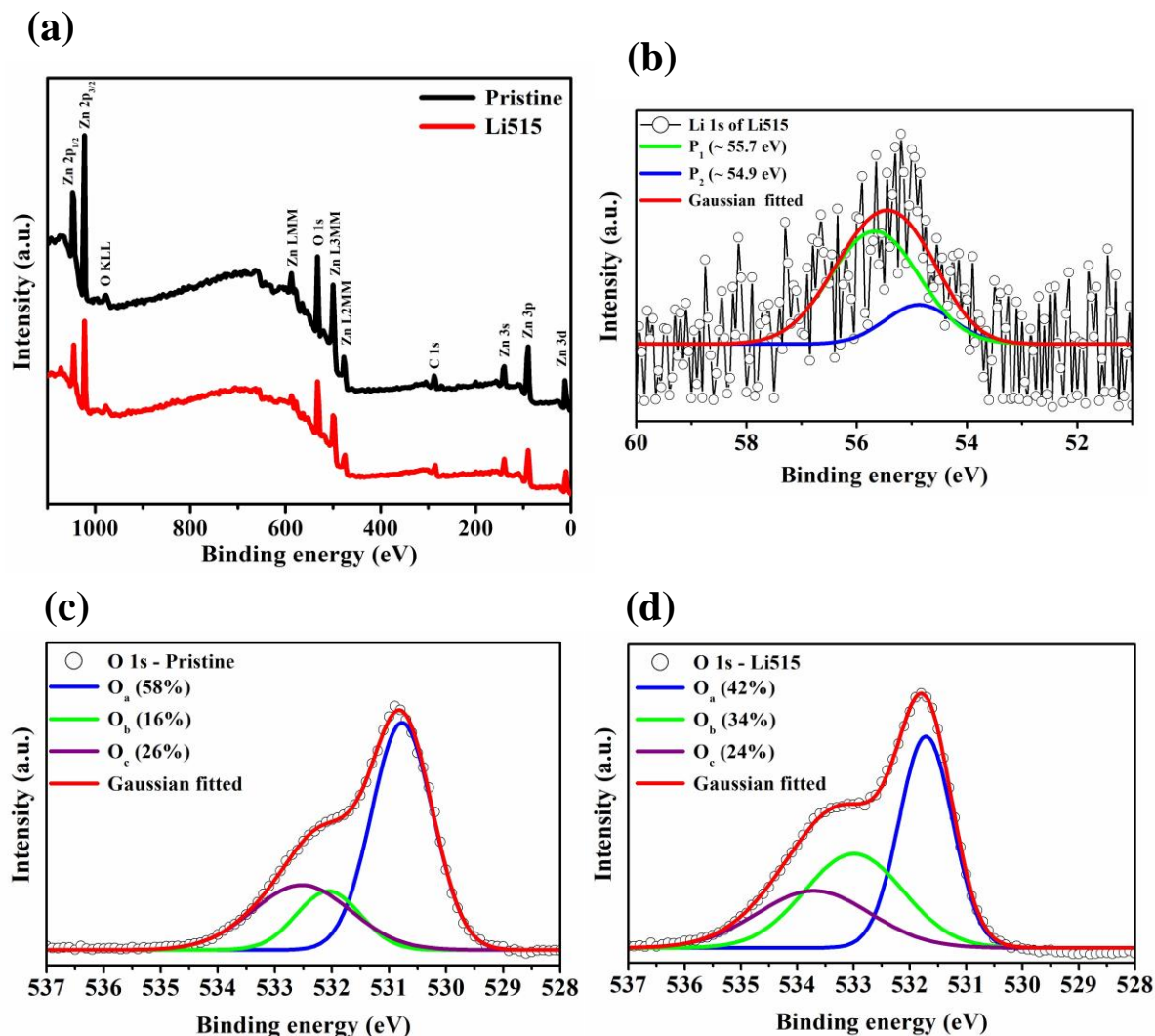
Fig. 7.4 (a) XPS survey scan of pristine and Li515 respectively, (b) Li 1s of Li515, and (c)-(d) The Gaussian fittings of O 1s XPS peaks of pristine and Li515 respectively.

The RT Raman scattering spectra (200–850 cm^{-1}) of pristine and the implanted samples are presented in Fig. 7.5(a), where the Raman modes E_2^{High} - E_2^{Low}, A_1(TO), E_1(TO), $E_2^{High,}$ and a broad band appear at 333, 380, 411, 437 ad 579 cm^{-1} respectively. E_2^{High} mode is correlated to lattice O atom and is characteristic of the high crystalline order of ZnO [32]. As observed in Fig. 7.5(a), there is an inverse correlation between the intensities of E_2^{High} and the broad band peaking at around 579 cm^{-1}. We have plotted the variation of E_2^{High} mode peak intensity with fluences in Fig. 7.5(b) by normalizing the intensity at 579 cm^{-1}. As observed in Fig. 7.5(b), the intensity of E_2^{High} mode decreases and FWHM of E_2^{High} mode increases drastically with an increase in the fluence beyond 5×10^{14} ions/cm^2, which indicates highly

increased lattice disorder in the implanted samples [33-35], and this is consistent with the XRD results also. Both the $A_1(TO)$ and $E_1(TO)$ modes though are very weak, as the Li ion fluence increases, the intensities of these two peaks decrease and from the fluence 5×10^{14} ions/cm^2, the TO modes disappear. There exists a subtle effect on the relative intensities of $A_1(TO)$ and $E_1(TO)$ modes depending on the O stoichiometry [33]. The pristine does not show any Raman mode as 511 cm^{-1}. As soon as, the NRs are implanted with Li ions, the 511 cm^{-1} mode appears and it becomes stronger as the samples are implanted with higher fluences. Though the origin of Raman mode at 511 cm^{-1} is debated, Friedrich et al. [36] have shown that the defect complex Zn_i–O_i is related to 511 cm^{-1} mode and this is very much likely in the ion implanted samples. All the samples show an evolution of a broad band Raman mode in the range ~515–645 cm^{-1} peaking at around 579 cm^{-1} (Fig. 7.5(a)), the intensity of which increases as the Li fluence increases. However, this broad band is reported to be a cumulative effect of disorder-activated four Raman modes at 540, 560, 579, and 594 cm^{-1} respectively [33, 37-39]. The 540 cm^{-1} is usually assigned to second-order Raman mode [$2B_1^{Low}$; 2LA] [38] Previous studies [40, 41] have shown that the physical origin of mode at 560 cm^{-1} can rationally be assigned to the defects related to Zn_i. The other modes at 579 and 594 cm^{-1} are assigned to $A_1(LO)$ and $E_1(LO)$ respectively. The individual contributions of these two LO modes are very much difficult to extract because of their close proximity. However, both the modes are very much sensitive to the O site disorder in ZnO lattice and thus these modes correspond to V_O type defects [33, 37, 38, 41]. The deconvoluted broad band of a representative implanted sample Li715 show three Gaussians peaks cantered at around 555, 560, and 579 cm^{-1} respectively (Fig. 7.5(c)). Here, the peak at 555 cm^{-1} is actually the shifted version of 540 cm^{-1}. We have considered a single peak at 579 cm^{-1} for 579 and 594 cm^{-1} modes at the time of deconvolution of the broad band. The specified area under 560 cm^{-1} and 579 cm^{-1} peaks for different fluences are presented in the bar diagram in Fig. 7.5(d), which shows that the peak area under both 560 cm^{-1} and 579 cm^{-1} modes increases as the fluence increases. This result indicates that the concentration of both Zn_i and V_O defects increases with an increase in the Li ion fluence, which is at par with the XRD and XPS results. Interestingly a broad hump ranging from 650-750 cm^{-1} peaking at 700 cm^{-1} has been appeared only for Li implanted NRs. In a previous report [42], two unknown Raman modes at 651 and 737 cm^{-1} have been reported for Li doped ZnO crystal. Drawing an analogy, we may assign the 700 cm^{-1} broad Raman mode to a cumulative effect of previously

reported 651 and 737 cm^{-1} Raman modes. However, the intensity of the 700 cm^{-1} Raman mode increases with an increase in the Li fluence as observed in Fig. 7.5(a). Therefore, this mode may reasonably be ascribed to the implantation-induced defects in ZnO NRs particularly in the presence of Li ions.
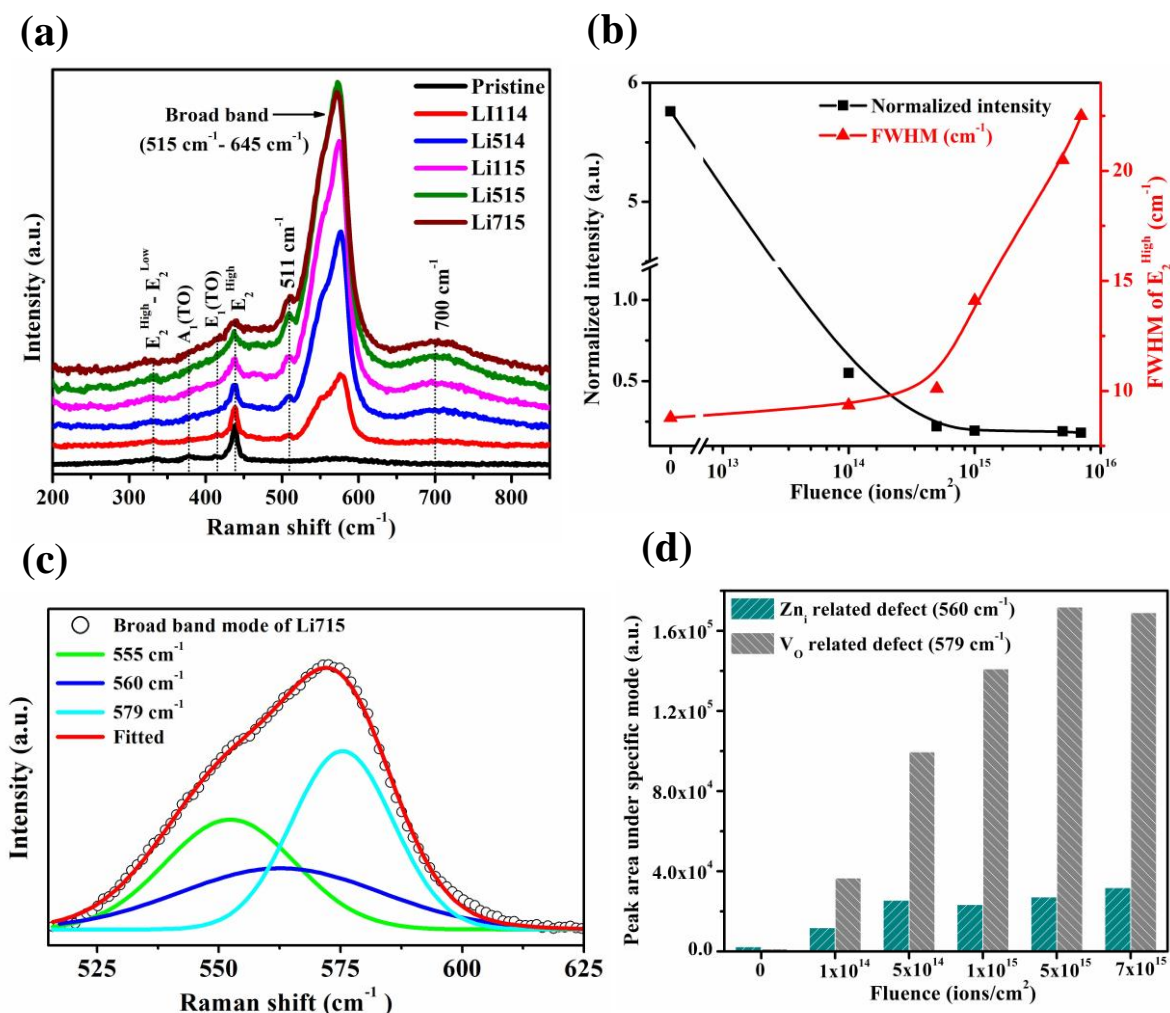
Fig. 7.5 (a) RT Raman spectra of pristine and Li implanted ZnO NRs, (b) variation of height for E_2^{High} (normalized at 579 cm^{-1}) and its FWHM with fluence, (c) fittings of the broad band Raman mode of Li715 and (d) the variation of the area under 560 and 579 cm^{-1} mode for all the samples.

The RT PL spectrum for the pristine in Fig. 7.6(a) shows a strong NBE emission at ~3.28 eV and a broad DL emission in the region 1.70 to 2.80 eV centered at ~2.2 eV [43-45]. A drastic reduction in the I_{NBE} is observed as the implantation fluence increases resulting in the

minimum intensity for the sample implanted with the highest fluence (7×10^{15} ions/cm^2) (Fig. 7.6(b)). This reduction in the I_{NBE} indicates the formation of hefty structural defects due to energetic Li ion collisions with the native Zn and O atoms, which is again in concordance with the Raman and XRD results. The NBE peak position remains fixed at 3.28 eV up to a fluence of 1×10^{15} ions/cm^2, beyond which a blue shift is observed (Fig. 7.6(b)). A ~82 meV blueshift is found for the highest fluence (7×10^{15} ions/cm^2). The blue shift in NBE emission with an increase in the Li fluence might be due to the BM effect [25, 28]. Similar to I_{NBE}, I_{DL} is maximum for the pristine and then it decreases with a large drop in the intensity for Li515 and Li715. The pristine distinctly exhibits a broad DL emission peaking at ~2.20 eV (yellow-orange), which is mainly attributed to an excess O_2/OH adsorbed on the surface of the NRs [46, 47]. Fig. 7.6(c) shows that except for Li114, the peak position of the DL emission gets shifted towards green emission at 2.40 eV for rest of the implanted samples. The transition of the yellow-orange emission to the green emission is a clear indication of a change in the defect chemistry as the implantation fluence is significant. As said in previous chapters, the commonly observed green luminescence in ZnO has many controversial defect origins [46, 48, 49]. Among these, V_{Zn} defects are mostly claimed to be responsible for the green emissions [50-52]. Formation of V_{Zn} is more likely in the ion implanted samples which gives rise to the green emission. However, a suppression in the green emission for Li515 and Li715 can be explained by the reduction of V_{Zn} (as discussed later in the theoretical simulation section). From the Fig. 7.6(d), it is observed that I_{NBE}/I_{DL} continues to decrease as the fluence increases, though it slightly increases for the higher fluences (5×10^{15} and 7×10^{15} ions/cm^2) which corroborates with the decrease in the radiative pathways for the DL emission. The ratio being always less than that of the pristine, clearly indicates formation of large number point defects in all the implanted samples, which may act as the non-radiative recombination centres. However, no defects directly related to Li have been observed in the RT PL spectrum. A Li_{Zn} acceptor state with an energy level 150 meV above the valence band maxima has been identified in the previous report [53]. Being closer to the valence band, the Li-related defects may be embedded in the defect-related band tail width in the implanted NRs.
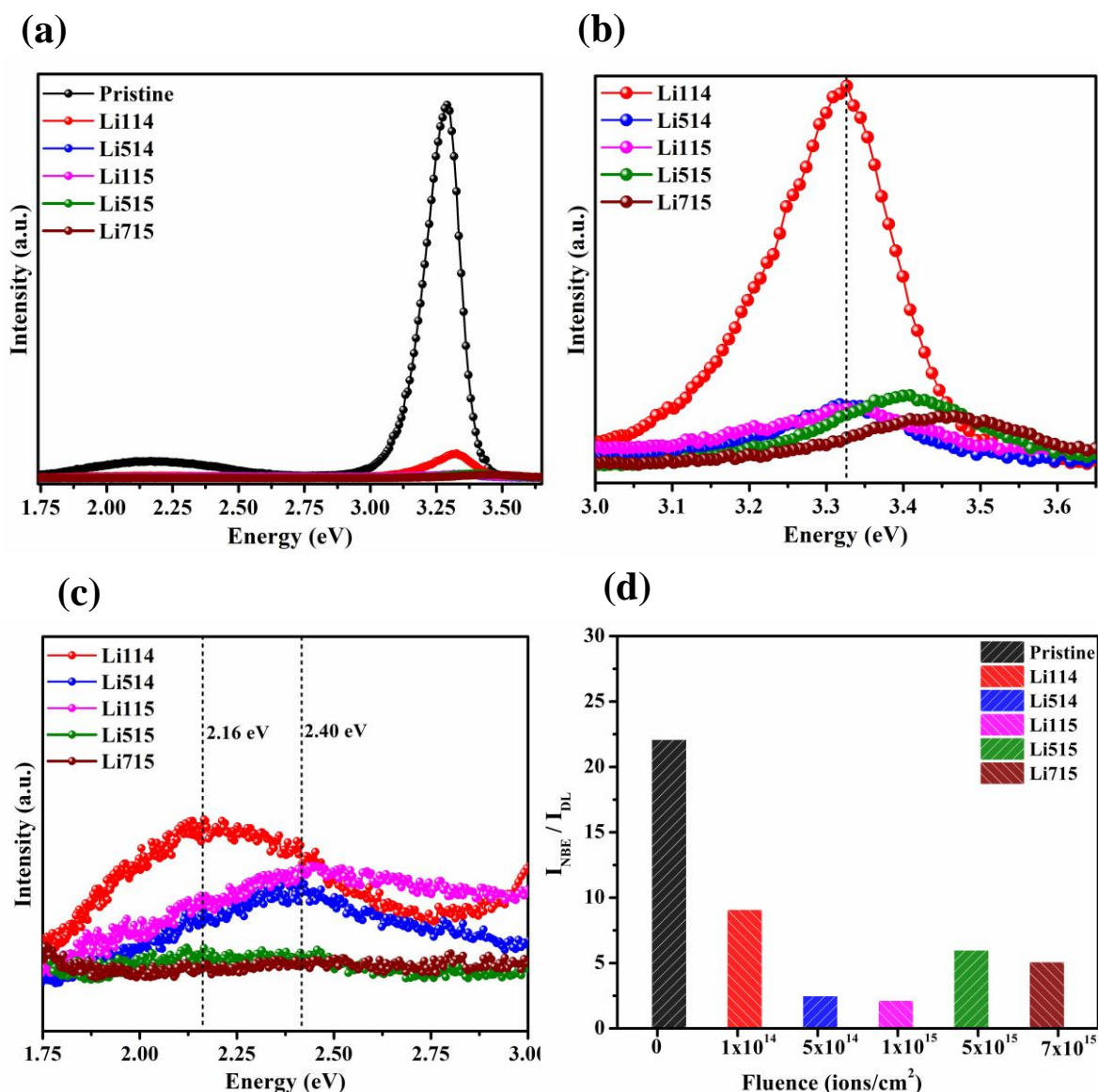
Fig. 7.6 (a) RT PL spectra of pristine and Li implanted ZnO NRs, (b) NBE and (c) DL emission of Li implanted NRs, and (d) Bar diagram representation of the ratio I_{NBE} / I_{DL} at various fluences.

To know the effect of Li implantation on the conductivity of the ZnO NRs, the electrical I-V measurement data has been analysed. The ohmic nature of the Al contacts used for I-V measurement has been confirmed from the linear I–V characteristics of pristine as well as Li implanted samples (Fig. 7.7). The value of current at a fixed bias voltage is highly lower for the implanted samples than that of the pristine one indicating an increase in the resistivity of the implanted NRs. For example, at a fixed 5 V bias voltage, the current for the pristine sample is 6.54 µA, whereas, for Li514 and Li715, the current values are 0.75 and 2.72×10^{-4} µA

respectively. In this case, the Hall measurement has not been used to measure the electrical parameters due to the measurement limitations. Though the previous study [53] has confirmed p-type conductivity in Li doped films, a very high resistivity in the samples has also been reported at high Li content and the Hall measurements provide ambiguous results in the determination of carrier type due to their low carrier concentration and Hall mobility. However, very high resistivity in our Li implanted samples probably indicates formation of both the acceptor states and various implantation-induced defects in the Li implanted NRs and this is in agreement with the XPS and PL results. Moreover, the implantation-induced defects and defect clusters probably act as carrier trapping donor centres compensating the acceptors. As a result, the resistivity of the Li implanted ZnO NRs increases.
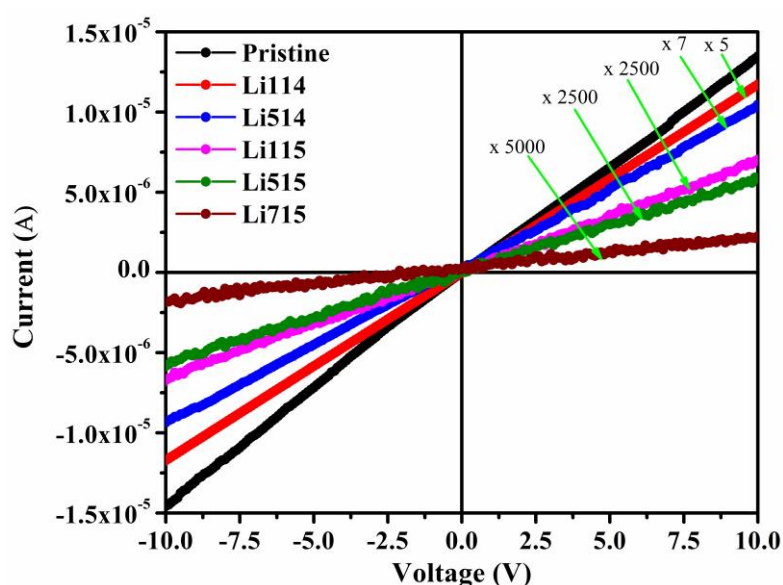
Fig. 7.7 The I-V characteristics of pristine and Li implanted ZnO NRs.

7.3.2 Theoretical simulation of Defect formation: SRIM calculation

Now, to predict the distribution of the implanted Li ions and the implantation-induced defects in the NRs, the SRIM-2008 simulation code [23] has been used considering the 'Detailed Calculation with full Damage Cascades' collision kinetics. The main parameters [33, 54, 55] used in SRIM simulation are described in the chapter 4. The Li ions implanted profile takes the well-known Gaussian distribution in the ZnO NRs as shown in the Fig. 7.8(a) along with the values of the main four statistical moments for all ions stopped within the target. The value of the average depth of the implanted Li ions from the surface (known as projected range,

R_p) is 564 nm having a standard deviation (also known as straggle) of 180 nm. The incident Li ions penetrate the vertical NRs easily with an overall range of ~900 nm, which indicates that the implanted Li ions are present along the entire length of the NRs. Skewness is a measure of the profiles tendency to lean toward or away from the surface. The negative value of the skewness in our case indicates that the distribution is shifted toward the surface, possibly due to back scattering which is a common phenomenon for lighter elements. Kurtosis measures the flatness of the Gaussian distribution. The value of the Kurtosis in our case is 2.98, which means the distribution profile is sharp near its peak. The at% of Li at R_p as calculated from the depth profile is about 0.20% for the fluence 5×10^{15} ions/cm^2, which is closely consistent with the XPS results. As described in the chapter 3, when the implanted ion enters a target material, it transfers most of its energy to the target atom by the means of inelastic collisions leading to excitation and ionization of the target atoms, which is known as electronic energy loss (S_e). As the ion moves deeper inside, the nuclear energy loss (S_n) occurs in terms of elastic collisions with the target nuclei. The energy loss through S_n produces a large concentration of atomic-scale point defects inside the target material by knocking out the target atoms from their lattice positions [55-57]. On the other hand, S_e can enhance the mobility of point defects, especially for heavy incident ions, and hence promote the formation of defect clusters [58]. Fig. 7.8(b) shows the SRIM simulated values of S_e and S_n at different incident energies of Li ions in ZnO. For 100 keV Li ion implantation in ZnO, the values of S_e and S_n are 14.86 and 1.115 eV/Å respectively with a ratio of 13.37. At the beginning of the ion track, S_e governs the stopping process and the Li ions lose a significant amount of total energy in the form of S_e. The S_n dominates the stopping process near the end of the track, where the majority of the target displacements and subsequent damages are produced. Li implantation has been carried out along the <002> direction of the NRs. The interplanar distance between (0002) planes is 2.602 Å. Therefore, the projected Li ions lose about 3 eV per lattice plane on average via S_n. However, the majority of the incident ion energy is transferred to the primary recoil atom. The recoil atoms again execute collisions with the target nuclei and thus collision cascade continues until the incident ion comes to rest [59, 60]. In this entire collision process, the implanted Li ions even at low energy (100 keV) induces both the replacement and a lot of vacancy defects (V_{Zn} and V_O) in ZnO lattice due to the target displacements. According to SRIM output file "Vacancy.txt", the total target displacements = 241/ion, whereas the total target vacancies =

236/ion and the total target replacement collisions = 5/ion. As a quantitative measure of the implantation-induced damage, a well-known parameter "atomic displacements per atom" (dpa) at each fluence (in Fig. 7.8(c)) using the SRIM results in previously reported dpa formula [61] has been calculated. The peak value of dpa at R_p increases linearly with the fluence. The minimum value of dpa is 0.007 for the fluence 1×10^{14} ions/cm^2, where a maximum of 0.52 is reached for the fluence 7×10^{15} ions/cm^2. This lower value of dpa (<1) even at the highest fluence indicates that the amorphization is not occurred in the implanted layer even though drastic structural damages appear, which is consistent with the experimental XRD results. The depth profiles of the implantation-induced vacancies (V_{Zn} and V_O) are also Gaussian type as shown in Fig. 7.8(d). The vacancy distributions are extended up to a depth of ~850 nm (Fig. 7.8(d)), which implies that the implantation-induced vacancies are present along the entire length of the NRs. Integration of the vacancy distribution curves over the entire range of the incident ion yields the total number of V_{Zn} and V_O produced per incident ion. From Fig. 7.8(d), the calculated numbers of V_{Zn} and V_O per incident Li ions are 152 and 84 respectively. Using this data, we have calculated the total number of both V_{Zn} and V_O produced per fluence and plotted them in Fig. 7.8(e), which shows that the vacancies increase linearly with an increase in the fluence. This implantation-induced defects are confined to the surrounding region of the ion track. Now, it is reasonable to assume that these simple defects are transformed into a heavily disordered and overlapping cluster as the implantation fluence increases, which is reflected in experimental XRD and Raman spectroscopy results. The high density of the disorder states may also cause a high resistivity in the Li implanted ZnO NRs, which is at par with our experimental electrical I-V measurements. Another noticeable point in Fig. 7.8(e) is that the number of V_{Zn} is always much higher than that of V_O at any fluence, which is due to the lower displacement energy of Zn than that of O [54, 55]. In fact, experimentally observed green PL emission (Fig. 7.6(a)) in the Li implanted NRs is supported by the simulated higher concentration of V_{Zn}. For the fluence $\geq 5 \times 10^{15}$ ions/cm^2, the intensity of the green emission has been seen to be suppressed contradicting the simulated higher numbers of V_{Zn}. The possible reason can be explained by considering the effect of dynamic annealing (the change of local temperature) of the target at the time of implantation [62]. The accumulated temperature of the target is small when the Li implantation fluence is low. With an increase in the fluence, a rise in the local temperature is expected. Since the migration barrier for Zn_i is very low, a small

temperature rise may cause Zn_i migration at V_{Zn}, and thus V_{Zn} decreases apparently [63, 64]. The theoretical simulation does not consider the aspect of this dynamic annealing and thus a contradiction arises. Overall, the good consistency between our various experimental and the theoretical simulation results using SRIM emphasizes our interpretations on the drastic evolution of various point defects in Li implanted ZnO NRs.
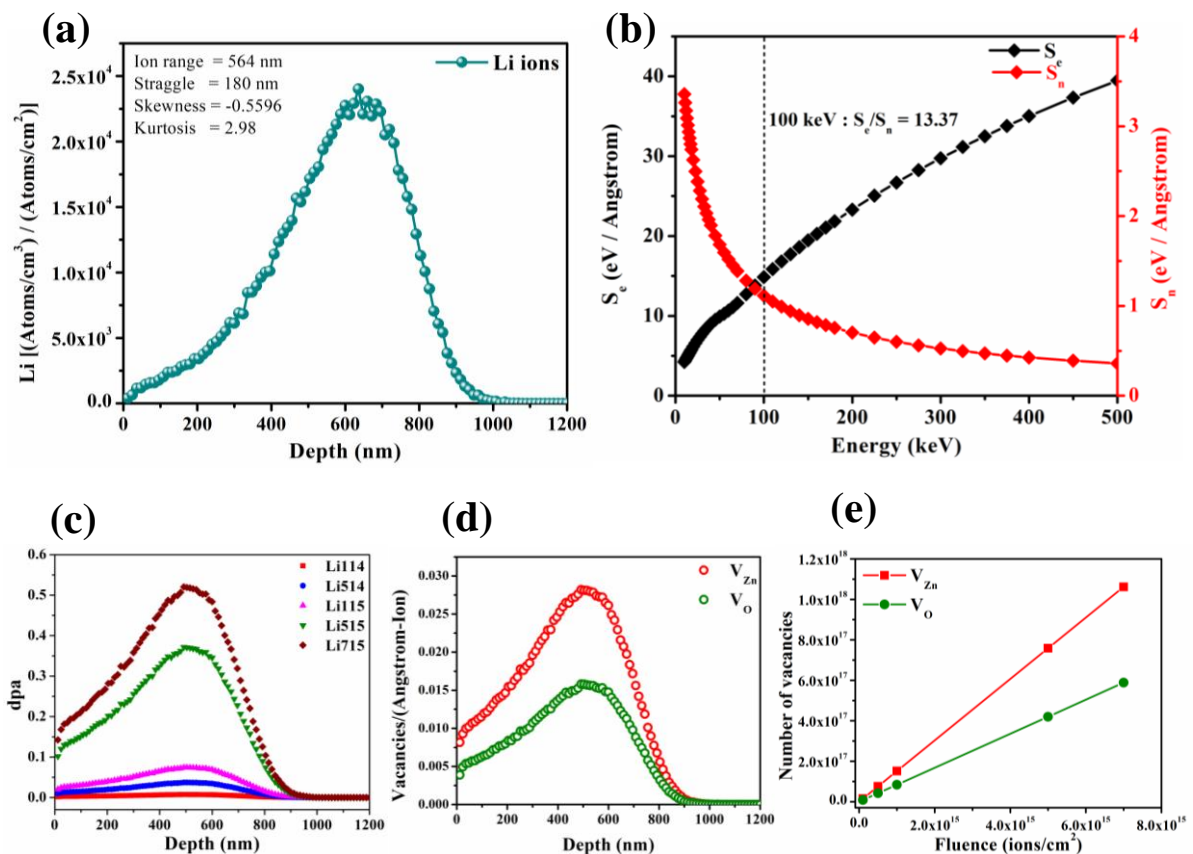
Fig. 7.8 SRIM predicted (a) depth profile of Li ions, (b) the S_e and S_n values at different ion energies, (c) distribution of dpa, (d) the defect (V_{Zn} and V_O) distribution and (e) the number of vacancies (V_{Zn} and V_O) as a function of fluence in the implanted NRs.

7.4 Conclusions

In summary, the formation and evolution of various point defects in Li implanted ZnO NRs as a function of ion fluence have been demonstrated experimentally in connection with the theoretical SRIM simulation. The ion induced structural point defects has been seen to be increased drastically with an increase in the fluence. The substitution of Li at Zn sublattice forms Li_{Zn} acceptor. The Li implanted NRs are electrically highly resistive due to both

formation of the acceptors as well as various implantation-induced defects. The transformation of the yellow-orange PL emission into a green emission in the Li implanted NRs is due to formation of large number of V_{Zn}. All the experimental results match well with the theoretical SRIM simulation results. This study can help one to understand the formation and evolution of point defects when the p-typing of ZnO NRs is performed using group I ion implantation.

7.5 References

[1] E.C. Lee, K.J. Chang, Possible p-type doping with group-I elements in ZnO, Phys. Rev. B, 70 (2004) 115210.

[2] R. Qin, J.X. Zheng, J. Lu, L. Wang, L. Lai, G.F. Luo, J. Zhou, H. Li, Z.X. Gao, G.P. Li, W.N. Mei, Origin of p-Type Doping in Zinc Oxide Nanowires Induced by Phosphorus Doping: A First Principles Study, J. Phys. Chem. C, 113 (2009) 9541-9545.

[3] F. Gallino, C. Di Valentin, G. Pacchioni, M. Chiesa, E. Giamello, Nitrogen impurity states in polycrystalline ZnO. A combined EPR and theoretical study, J. Mater. Chem., 20 (2010) 689-697.

[4] Y.T. Chuang, J.W. Liou, W.Y. Woon, Formation of p-type ZnO thin film through co-implantation, Nanotechnology, 28 (2017) 035603.

[5] Y.R. Ryu, S. Zhu, D.C. Look, J.M. Wrobel, H.M. Jeong, H.W. White, Synthesis of p-type ZnO films, J. Cryst. Growth, 216 (2000) 330-334.

[6] J. Kennedy, D.A. Carder, A. Markwitz, R.J. Reeves, Properties of nitrogen implanted and electron beam annealed bulk ZnO, J. Appl. Phys., 107 (2010) 103518.

[7] Z. Huang, H.B. Ruan, H. Zhang, D.P. Shi, W.J. Li, G.P. Qin, F. Wu, L. Fang, C.Y. Kong, Investigation on the p-type formation mechanism of nitrogen ion implanted ZnO thin films induced by rapid thermal annealing, Optical Materials Express, 9 (2019) 3098-3108.

[8] C.H. Park, S.B. Zhang, S.H. Wei, Origin of p-type doping difficulty in ZnO: The impurity perspective, Phys. Rev. B, 66 (2002) 073202.

[9] K. Tang, S.L. Gu, J.D. Ye, S.M. Zhu, R. Zhang, Y.D. Zheng, Recent progress of the native defects and p-type doping of zinc oxide, Chinese Physics B, 26 (2017) 047702.

[10] V. Avrutin, D.J. Silversmith, H. Morkoc, Doping Asymmetry Problem in ZnO: Current Status and Outlook, Proc. IEEE, 98 (2010) 1269-1280.

[11] N. Shakti, C. Devi, A.K. Patra, P.S. Gupta, S. Kumar, Lithium doping and photoluminescence properties of ZnO nanorods, AIP Adv., 8 (2018) 015306.

[12] J. Lee, S. Cha, J. Kim, H. Nam, S. Lee, W. Ko, K.L. Wang, J. Park, J. Hong, p-Type Conduction Characteristics of Lithium-Doped ZnO Nanowires, Adv. Mater., 23 (2011) 4183.

[13] H. Ahmoum, M. Boughrara, M.S. Su'ait, M. Kerouad, Effect of position and concentration of Li on ZnO physical properties: Density functional investigation, Chem. Phys. Lett., 719 (2019) 45-53.

[14] A. Das, G. Das, D. Kabiraj, D. Basak, High conductivity along with high visible light transparency in Al implanted sol-gel ZnO thin film with an elevated figure of merit value as a transparent conducting layer, J. Alloy. Compd., 835 (2020) 155221.

[15] M.J. Ying, S.D. Wang, T. Duan, B. Liao, X. Zhang, Z.X. Mei, X.L. Du, F.M. Gerriu, A.M. Fox, G.A. Gehring, The structure, optical and magnetic properties of arsenic implanted ZnO films prepared by molecular beam epitaxy, Mater. Lett., 171 (2016) 121-124.

[16] Q. Li, M.M. Yuan, M.D. Zhang, C.G. Guo, B. Liao, X. Zhang, M.J. Ying, Effects of Sm implantation on the structure and magnetic properties of polar ZnO films, J. Alloy. Compd., 894 (2022) 162402.

[17] A. Das, D. Basak, Efficacy of Ion Implantation in Zinc Oxide for Optoelectronic Applications: A Review, ACS Appl. Electron. Mater., 3 (2021) 3693-3714.

[18] W.J. Li, H. Zhang, X.Y. Zhang, G.P. Qin, H.L. Li, Y.Q. Xiong, L.J. Ye, H.B. Ruan, C.Z. Tong, C.Y. Kong, L. Fang, Non-axial N-O-V-Zn shallow acceptor complexes in nitrogen implanted p-type ZnO thin films, Appl. Surf. Sci., 529 (2020) 147168.

[19] A. Mackova, A. Jagerova, P. Malinsky, M. Cutroneo, J. Flaks, P. Nekvindova, A. Michalcova, V. Holy, T. Kosutova, Nanostructures in various Au ion-implanted ZnO facets modified using energetic O ions, Phys. Chem. Chem. Phys., 22 (2020) 23563-23573.

[20] S.K. Das, G.K. Pradhan, P.D. Bhuyan, S.K. Gupta, S. Sahoo, Influence of Li ion implantation on LO phonon broadening and bandgap opening in ZnO thin films, J. Alloy. Compd., 806 (2019) 1138-1145.

[21] S. Nagar, B. Sinha, A. Mandal, S.K. Gupta, S. Chakrabarti, Influence of Li implantation on the optical and electrical properties of ZnO film, in: Conference on Oxide-based Materials and Devices II, San Francisco, CA, 2011, pp. 239-245.

[22] C.W. Zou, M. Li, H.J. Wang, M.L. Yin, C.S. Liu, L.P. Guo, D.J. Fu, T.W. Kang, Ferroelectricity in Li-implanted ZnO thin films, Nucl. Instrum. Methods Phys. Res. Sect. B-Beam Interact. Mater. Atoms, 267 (2009) 1067-1071.

[23] J.F. Ziegler, M.D. Ziegler, J.P. Biersack, SRIM - The stopping and range of ions in matter (2010), Nucl. Instrum. Methods Phys. Res. Sect. B-Beam Interact. Mater. Atoms, 268 (2010) 1818-1823.

[24] J.P. Lv, C.D. Li, J.J. BelBruno, Defect evolution on the optical properties of H+-implanted ZnO whiskers, Crystengcomm, 15 (2013) 5620-5625.

[25] N.R. Yogamalar, A.C. Bose, Burstein-Moss shift and room temperature near-band-edge luminescence in lithium-doped zinc oxide, Appl. Phys. A-Mater. Sci. Process., 103 (2011) 33-42.

[26] S. Patrik, R. Durena, P. Onufrijevs, S. Miasojedovas, T. Malinauskas, S. Stanionyte, A. Zarkov, A. Zukuls, I. Bite, K. Smits, Morphological and optical property study of Li doped ZnO produced by microwave-assisted solvothermal synthesis, Mater. Sci. Semicond. Process, 135 (2021) 106069.

[27] S. Shawuti, A.U.R. Sherwani, M.M. Can, M.A. Gulgun, Complex Impedance Analyses of Li doped ZnO Electrolyte Materials, Sci Rep, 10 (2020) 10.

[28] R.A. Rakkesh, S. Balakumar, Structural, electrical transport and optical studies of Li ion doped ZnO nanostructures, Process. Appl. Ceram., 8 (2014) 7-13.

[29] M. Vashista, S. Paul, Correlation between full width at half maximum (FWHM) of XRD peak with residual stress on ground surfaces, Philos. Mag., 92 (2012) 4194-4204.

[30] K.R. Nandanapalli, D. Mudusu, Surface Passivated Zinc Oxide (ZnO) Nanorods by Atomic Layer Deposition of Ultrathin ZnO Layers for Energy Device Applications, ACS Appl. Nano Mater., 1 (2018) 4083-4091.

[31] J. Chastain, R.C. King Jr, Handbook of X-ray photoelectron spectroscopy, Perkin-Elmer Corporation, 40 (1992) 221.

[32] A. Kumar, S. Keshri, B. Pandey, J.B.M. Krishna, D. Das, Impact of N5+ ion implantation on optical and electrical properties of polycrystalline ZnO film, Radiat. Eff. Defects Solids, 169 (2014) 965-979.

[33] A. Mondal, S. Pal, A. Sarkar, T.S. Bhattacharya, A. Das, N. Gogurla, S.K. Ray, P. Kumar, D. Kanjilal, K.D. Devi, A. Singha, S. Chattopadhyay, D. Jana, Raman spectroscopic analysis on Li, N and (Li,N) implanted ZnO, Mater. Sci. Semicond. Process, 80 (2018) 111-117.

[34] Z. Huang, H.B. Ruan, H. Zhang, D.P. Shi, W.J. Li, G.P. Qin, F. Wu, L. Fang, C.Y. Kong, Conversion mechanism of conductivity and properties of nitrogen implanted ZnO single crystals induced by post-annealing, J. Mater. Sci.-Mater. Electron., 30 (2019) 4555-4561.

[35] Z.Q. Chen, A. Kawasuso, Y. Xu, H. Naramoto, X.L. Yuan, T. Sekiguchi, R. Suzuki, T. Ohdaira, Production and recovery of defects in phosphorus-implanted ZnO, J. Appl. Phys., 97 (2005) 013528.

[36] F. Friedrich, M.A. Gluba, N.H. Nickel, Identification of nitrogen and zinc related vibrational modes in ZnO, Appl. Phys. Lett., 95 (2009) 141903.

[37] A. Mondal, S. Pal, A. Sarkar, T.S. Bhattacharya, S. Pal, A. Singha, S.K. Ray, P. Kumar, D. Kanjilal, D. Jana, Raman investigation of N-implanted ZnO: Defects, disorder and recovery, J. Raman Spectrosc., 50 (2019) 1926-1937.

[38] M. Scepanovic, M. Grujic-Brojcin, K. Vojisavljevic, S. Bernik, T. Sreckovic, Raman study of structural disorder in ZnO nanopowders, J. Raman Spectrosc., 41 (2010) 914-921.

[39] S. Pal, N. Gogurla, A. Das, S. Singha, P. Kumar, D. Kanjilal, A. Singha, S. Chattopadhyay, D. Jana, A.J.J.o.P.D.A.P. Sarkar, Clustered vacancies in ZnO: chemical aspects and consequences on physical properties, 51 (2018) 105107.

[40] H.J. Fan, R. Scholz, F.M. Kolb, M. Zacharias, U. Gosele, F. Heyroth, C. Eisenschmidt, T. Hempel, J. Christen, On the growth mechanism and optical properties of ZnO multi-layer nanosheets, Appl. Phys. A-Mater. Sci. Process., 79 (2004) 1895-1900.

[41] J.F. Xu, G.X. Cheng, W. Yang, Y.W. Du, Raman scattering from surface phonons in fine Zn particles coated with ZnO, J. Phys. B-At. Mol. Opt. Phys., 29 (1996) 6227-6232.

[42] R. Jothilakshmi, V. Ramakrishnan, R. Thangavel, J. Kumar, A. Sarua, M. Kuball, Micro-Raman scattering spectroscopy study of Li-doped and undoped ZnO needle crystals, J. Raman Spectrosc., 40 (2009) 556-561.

[43] R. Ghosh, B. Mallik, S. Fujihara, D. Basak, Photoluminescence and photoconductance in annealed ZnO thin films, Chem. Phys. Lett., 403 (2005) 415-419.

[44] A. Das, S. Ghosh, A. Das Mahapatra, D. Kabiraj, D. Basak, Highly enhanced ultraviolet to visible room temperature photoluminescence emission ratio in Al implanted ZnO nanorods, Appl. Surf. Sci., 495 (2019) 143615.

[45] I. Parkhomenko, L. Vlasukova, F. Komarov, M. Makhavikou, O. Milchanin, E. Wendler, M. Zapf, C.J.J.o.P.D.A.P. Ronning, Luminescence of ZnO nanocrystals in silica synthesized by dual (Zn, O) implantation and thermal annealing, 54 (2021) 265104.

[46] R.B.M. Cross, M.M. De Souza, E.M.S. Narayanan, A low temperature combination method for the production of ZnO nanowires, Nanotechnology, 16 (2005) 2188-2192.

[47] J.W.P. Hsu, D.R. Tallant, R.L. Simpson, N.A. Missert, R.G. Copeland, Luminescent properties of solution-grown ZnO nanorods, Appl. Phys. Lett., 88 (2006) 252103.

[48] N. Shakti, C. Devi, A.K. Patra, P.S. Gupta, S. Kumar, Lithium doping and photoluminescence properties of ZnO nanorods, AIP Adv., 8 (2018) 5.

[49] A.B. Djurisic, Y.H. Leung, K.H. Tam, Y.F. Hsu, L. Ding, W.K. Ge, Y.C. Zhong, K.S. Wong, W.K. Chan, H.L. Tam, K.W. Cheah, W.M. Kwok, D.L. Phillips, Defect emissions in ZnO nanostructures, Nanotechnology, 18 (2007) 095702.

[50] D. Sett, S. Sarkar, D. Basak, A successive photocurrent transient study to probe the sub-band gap electron and hole traps in ZnO nanorods, RSC Adv., 4 (2014) 58553-58558.

[51] H. Chen, S.L. Gu, K. Tang, S.M. Zhu, Z.B. Zhu, J.D. Ye, R. Zhang, Y.D. Zheng, Origins of green band emission in high-temperature annealed N-doped ZnO, J. Lumines., 131 (2011) 1189-1192.

[52] F. Fabbri, M. Villani, A. Catellani, A. Calzolari, G. Cicero, D. Calestani, G. Calestani, A. Zappettini, B. Dierre, T. Sekiguchi, G. Salviati, Zn vacancy induced green luminescence on non-polar surfaces in ZnO nanostructures, Sci Rep, 4 (2014) 1-6.

[53] Y.J. Zeng, Z.Z. Ye, J.G. Lu, W.Z. Xu, L.P. Zhu, B.H. Zhao, S. Limpijumnong, Identification of acceptor states in Li-doped p-type ZnO thin films, Appl. Phys. Lett., 89 (2006) 042106.

[54] D.C. Look, G.C. Farlow, P. Reunchan, S. Limpijumnong, S.B. Zhang, K. Nordlund, Evidence for native-defect donors in n-type ZnO, Phys. Rev. Lett., 95 (2005) 225502.

[55] S. Chattopadhyay, S. Dutta, D. Jana, S. Chattopadhyay, A. Sarkar, P. Kumar, D. Kanjilal, D.K. Mishra, S.K. Ray, Interplay of defects in 1.2 MeV Ar irradiated ZnO, J. Appl. Phys., 107 (2010) 113516.

[56] W.Q. Li, X.H. Xiao, A.L. Stepanov, Z.G. Dai, W. Wu, G.X. Cai, F. Ren, C.Z. Jiang, The ion implantation-induced properties of one-dimensional nanomaterials, Nanoscale Res. Lett., 8 (2013) 1-13.

[57] K. Saravanan, G. Jayalakshmi, S. Chandra, B.K. Panigrahi, R. Krishnan, B. Sundaravel, S. Annapoorani, D.K. Shukla, P. Rajput, D. Kanjilal, The influence of carbon concentration on the electronic structure and magnetic properties of carbon implanted ZnO thin films, Phys. Chem. Chem. Phys., 19 (2017) 13316-13323.

[58] W.J. Weber, D.M. Duffy, L. Thome, Y.W. Zhang, The role of electronic energy loss in ion beam modification of materials, Current Opinion in Solid State & Materials Science, 19 (2015) 1-11.

[59] Y.W. Zhang, W.J. Weber, Ion irradiation and modification: The role of coupled electronic and nuclear energy dissipation and subsequent nonequilibrium processes in materials, Appl. Phys. Rev., 7 (2020) 041307.

[60] R.E. Stoller, M.B. Toloczko, G.S. Was, A.G. Certain, S. Dwaraknath, F.A. Garner, On the use of SRIM for computing radiation damage exposure, Nucl. Instrum. Methods Phys. Res. Sect. B-Beam Interact. Mater. Atoms, 310 (2013) 75-80.

[61] G. Velisa, E. Wendler, L.L. Wang, Y.W. Zhang, W.J. Weber, Ion mass dependence of irradiation-induced damage accumulation in KTaO3, J. Mater. Sci., 54 (2019) 149-158.

[62] Y.X. Fan, Z.W. Xu, Y. Song, T.Z. Sun, Molecular dynamics simulation of silicon vacancy defects in silicon carbide by hydrogen ion implantation and subsequent annealing, Diam. Relat. Mat., 119 (2021) 108595.

[63] P. Erhart, K. Albe, Diffusion of zinc vacancies and interstitials in zinc oxide, Appl. Phys. Lett., 88 (2006) 3.

[64] A. Janotti, C.G. Van de Walle, Native point defects in ZnO, Phys. Rev. B, 76 (2007) 22.

CHAPTER-8

Defect interaction in N-Li co-implanted ZnO nanorods

8.1 Introduction

To overcome the obstacle of creating p-type ZnO, a considerable effort has been made in research by doping with group I and V elements, such as Li, Na, N, P, As, Sb and so on [1-6]. As described in the previous chapters, the obtained p-type ZnO NRs are unstable, and even p-type conductivity disappear after a period of time. So, choosing appropriate acceptor dopant and doping method is the key problem to obtain stable p-type ZnO with excellent p-type characteristics. Among group I and V elements, Li and N are regarded as the most suitable candidates. As discussed in the earlier chapters, substitution of O by N (N_O) [7, 8] and Zn by Li (Li_{Zn}) [9-11] has been shown to form shallow acceptor levels in ZnO. In N-Li co-doped ZnO, the Li_i and N_O has been proved to form Li_i –N_O complex, which reduces the concentration of N_O acceptors as well as limits the possibility of the generation of $(N_2)_O$ donors. Though the formation of N_O acceptor is suppressed, there still exits Li_{Zn} acceptors which contributes to creating p-type ZnO in case of N-Li co-doped ZnO [12-15]. There are reports on the successful preparation of stable p-type ZnO films attributing to using Li and N as p-type dopants, which were grown by molecular beam epitaxy, pulsed laser deposition, RF-magnetron sputtering, and so on [16-19]. Low solubility of dopants is the obstacle to hinder obtaining p-type ZnO films with high hole concentration. So, in order to solve the problem, ion implantation is a useful and meaningful method to introduce a precise dopant concentration, which is established owing to its simplicity, precise depth control and compatibility with planar device technology, producing more holes [20-22]. At the same time, the lattice disorder and damage caused by ion implantation has negative effect on mobility and resistivity. It is reported that performing post-implantation annealing can reduce the types of disorder and activate p-type dopants. Therefore, it is also essential to investigate the effect of co-implantation of p-type dopant ions in ZnO NRs after post implantation annealing in order to assess the induced defects and the resultant properties achieved. In this chapter, the formation and evolution of various point defects and their interactions in vertical ZnO NRs as a function of various co-implantation fluences due to N and Li ion co-implantation resulting in the changes in structural and optical properties have been assessed extensively though various experimental techniques. SRIM has also been used to evaluate the quantitative energy loss, the distributions of the implanted N and Li ions and the point defects in the target ZnO NRs.

8.2 Experimental details

ZnO NRs were grown by the ACG method on the glass substrates as described in the chapter 3. 100 keV N ions were first implanted in the as-grown NRs at RT by varying the fluences from 1×10^{14} to 5×10^{15} ions/cm^2 according to the conditions described in the chapter 6. The N implanted NRs were then implanted with 100 keV Li under the conditions described in the previous chapter. In this case, a sample is implanted with Li ions at the same fluence with which it was implanted with N ions. After implantation, the samples were subjected to an annealing treatment at 450 °C for 1 h in Ar ambient. The nomenclatures of the samples in this study are given in Table 8.1.

Table 8.1 The nomenclature of the samples according to the corresponding co-implantation fluences.

N ion fluence (ions/cm^2)	Li ion fluence (ions/cm^2)	Sample name
0	0	Pristine
1×10^{14}	1×10^{14}	LiN114
5×10^{14}	5×10^{14}	LiN514
1×10^{15}	1×10^{15}	LiN115
5×10^{15}	5×10^{15}	LiN515

The structural, compositional and optical analyses of the samples have been carried out using XRD, Raman, XPS, and PL measurements respectively as described in chapter 3.

8.3 Results and discussion

In the SRIM simulation, the 'Detailed Calculation with full Damage Cascades' collision kinetics has been considered. The key parameters [23-25] used in the SRIM simulation have been described in chapter 4. The values of the main four statistician moments for all ions stopped within the target as estimated from SRIM simulation are shown in Table 8.2. The simulated N and Li concentration displays a well-known Gaussian profile which is shown in Fig. 8.1(a). The value of R_p for N ions is 226 nm having straggle of 84 nm, whereas the value of R_P and straggle for Li ions are 563 nm 179 nm respectively. The incident N ions penetrate the vertical NRs easily with an overall range of ~500 nm whereas Li ion can penetrate ~900 nm, which indicates that the implanted N and Li ions are present along the entire length of the

NRs. In the Fig. 8.1(a), it is seen that implanted N ions are more localized in the surface regions compared to that of Li ions. The negative value of the skewness in both ions indicates that the distribution is shifted toward the surface, possibly due to back scattering. The value of the Kurtosis in both ions is close to the value 3, which means the distribution profile is sharp near their peaks. The atomic concentration at R_p as calculated from the depth profile is about 0.20 at.% for Li and 0.39 at.% for N at the fluence 5×10^{15} ions/cm^2. Fig. 8.1(b) and Fig. 8.1(c) show the SRIM simulated values of S_e and S_n at different incident energies of N and Li ions in ZnO. For 100 keV N ion implantation in ZnO, the values of S_e and S_n are 14.86 and 1.115 eV/Å respectively with a ratio of 13.37, whereas for 100 keV Li ions, the values of S_e and S_n are 24.3 and 7.668 eV/Å respectively with a ratio of 3.17. In this entire collision process, the implanted N and Li ions even at low energy (100 keV) induces both the replacement and a lot of vacancy defects (V_{Zn} and V_O) in ZnO lattice due to the target displacements. According to SRIM output file "Vacancy.txt", the total target displacements, vacancies, and replacements collisions for both ions are presented in Table 8.3.
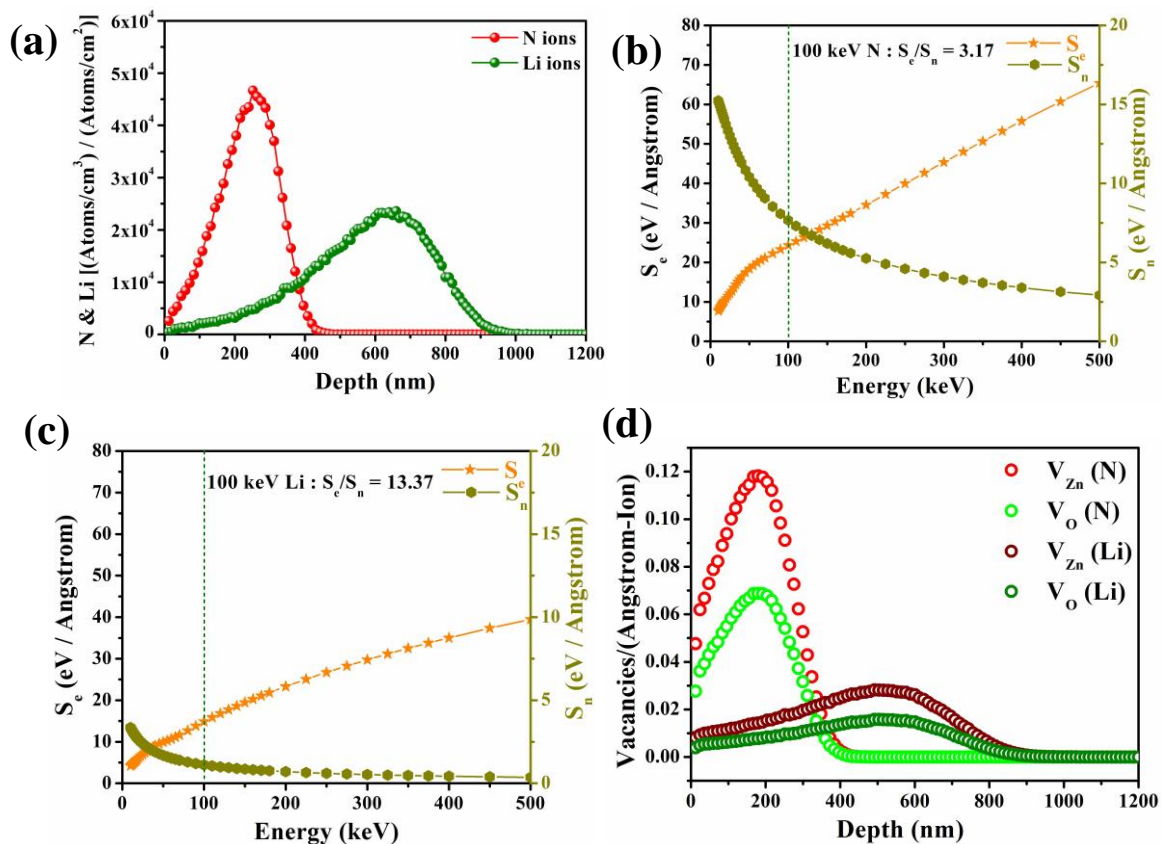

Fig. 8.1 (a) SRIM predicted (a) depth profile of Li ions, the S_e and S_n values at different ion energies for (b) N ion, (c) Li ion implantation, (d) distribution of the defects (V_{Zn} and V_O).

Table 8.2 Outcome of the statistical parameters in SRIM calculation.

Ion	N	Li
Projected Range (R_P)	226 nm	563 nm
Straggle	84 nm	179 nm
Skewness	-0.2908	-0.5643
Kurtosis	2.6125	2.9775

Table 8.3 Outcome of displacements, vacancies, and replacement collisions in SRIM calculation.

Ion	N	Li
Displacements/Ion	463	236
Vacancies/Ion	472	240
Replacements/Ion	9	4

According to the Table 8.3, the displacements, vacancies and replacements collision events are always more for N ions than the Li ions as the N ions are heavy in mass than that of Li ions. The depth profiles of the implantation-induced vacancies (V_{Zn} and V_O) are also Gaussian type as shown in Fig. 8.1(d) for both the ions. The vacancy distributions are extended up to a depth of ~400 nm for N ions and ~850 nm for Li ions, which implies that the implantation-induced vacancies are present along the entire length of the NRs and the number of V_{Zn} is always much higher than that of V_O at any fluence. Another noticeable point in Fig. 8.1(d) is that a higher fraction V_{Zn} and V_O are found near the subsurface region for N implantation compared to that for Li implantation, which indicates that N ions are more damaging for ZnO compared to Li ions of same energy.

The XRD patterns of the pristine as well as co-implanted and subsequently annealed samples are presented in Fig. 8.2(a), which indicates the presence of well distinct, sharp and narrow peaks. These peaks correspond to the diffractions from the (0002), (10$\bar{1}$1), (10$\bar{1}$2), (10$\bar{1}$3) and (11$\bar{2}$0) planes of hexagonal wurtzite ZnO (JCPDS card No. 36-1451). The diffraction peak corresponding to the (0002) plane is the strongest for all the samples, which indicates that the preferred orientation of ZnO NRs along the <002> direction remains unaffected after co-implantation and all the samples retain the same wurtzite structure. Any

extra diffraction peak due to N and Li-related impurities or any secondary phase is not observed in the XRD patterns. An enlarged view of the (002) peak of all the samples is shown in Fig. 8.2(b). The intensity of the (002) peak decreases distinctly, which indicates the formation of structural damages in NRs due to co-implantation [26]. Since the atomic radius of N atom is greater than that of O atom, but smaller than that of Zn atom, the substitution of N at O sites or the incorporation of N at interstitial sites in ZnO is likely to induce a peak shift towards lower angle [27-30]. On the other hand, Li doping in ZnO should lead to a shift in the peak position towards a higher 2θ value because of the smaller ionic radius of Li^{1+} than that of Zn^{2+} [31-33]. As seen in Fig. 8.2(b), the (002) peak shifts towards lower 2θ value up to fluence 5×10^{14} ions/cm^2 as compared to pristine and then it starts to shift in reverse (towards higher 2θ value). Therefore, it can be concluded that the effect of Li ion implantation becomes prominent at higher fluence.
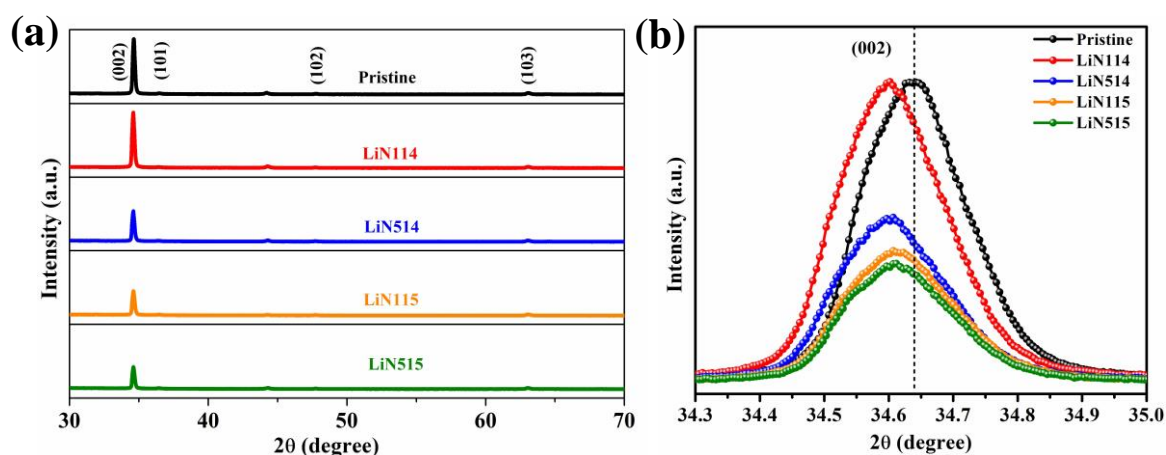

Fig. 8.2 (a) XRD patterns, (b) the enlarged view of (002) peaks of pristine and co-implanted ZnO NRs.

Due to the lower angle shift, the c-axis lattice parameter (c) increases and a tensile strain (ε) arises, which have been plotted with fluence in Fig. 8.3(a). In Fig. 8.3(b), it is seen that the value of FWHM of the (002) peak decreases up to 1×10^{15} ions/cm^2 and beyond which it increases. At higher co-implantation fluence, the creation of point defects causes strain which causes change in the FWHM values of (002) diffraction peak [34]. Considering the (002) peak, the average crystallite size (D) has been estimated using Debye-Scherrer's formula described in the chapter 3. The value of D decreases till 1×10^{15} ions/cm^2 and then it increases, which is shown Fig. 8.3(b). The values of dislocation density (δ) have also been calculated. As shown

in Fig. 8.3(b), the value of δ increases as the co-implantation ion fluence increases up to fluence 1×10^{15} ions/cm^2 and thereafter however it decreases.
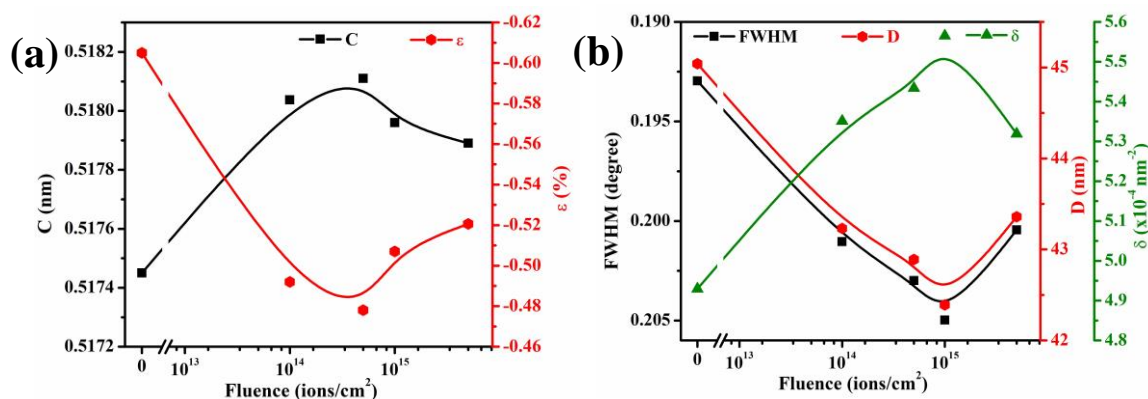

Fig. 8.3 The variation of (a) c-axis lattice parameter, strain, and (b) FWHM of (002) peak, crystallite size, and dislocation density with co-implantation fluence.

Fig. 8.4(a) shows the XPS full survey scans of pristine and a representative co-implanted sample LiN515. The XPS scans were taken by removing the undesired particles from the sample's surface using sputtering for ~100 s. The C 1s binding energy level at 284.5 eV has been used as a reference energy level. The XPS peaks corresponding to different core levels of O and Zn such as O 1s, Zn 2p are found clearly for all the samples in Fig. 8.4(a) [35]. The N 1s XPS spectrum of LiN515 as shown in Fig. 8.4(b) reveals a single peak at 399.5 eV. The origins of N 1s peak at 399.5 eV peak is generally ascribed to the N_O acceptor [27, 36, 37]. According to chapter 6, the local environment of N_O at 399.5 eV is O-rich (i.e., O-Zn-N bond). Any XPS peak corresponding $(N_2)_O$ donor has not been found. A broad peak in the region between 53.5 and 56.5 eV due to Li 1s can be deconvoluted into two Gaussian peaks, P_1 and P_2 in Fig. 8.4(c). The peak P_1 at 55.7 eV is related to Li^{1+} in Zn^{2+} site bonded to O [33]. The peak P_2 at 53.4 eV is usually attributed to Li_i [33]. Thus, Li_{Zn} is expected to form acceptor state in the co-implanted sample, although a little amount of Li_i remains left in the co-implanted NRs. As both N_O and Li_i are present in the co-implanted NRs, the N_O-Li_i complex may be formed, which decreases the concentration of Li_i as well as and limits the generation of $(N_2)_O$ donors. The absence of $(N_2)_O$ in the samples also satisfies this prediction. Similar to the previous chapters, the asymmetric O 1s XPS peaks of pristine and LiN515 are deconvoluted into three Gaussian peaks, as shown in Fig. 8.4(d-e), where it is seen that V_O defects in LiN515 is higher than that of the pristine, suggesting that excess V_O defects are produced due to co-

implantation. This is in accordance with the SRIM result. The atomic concentrations of N and Li are about 0.23 at.% and 0.12 at.%, respectively for Li515, which are close to SRIM results.
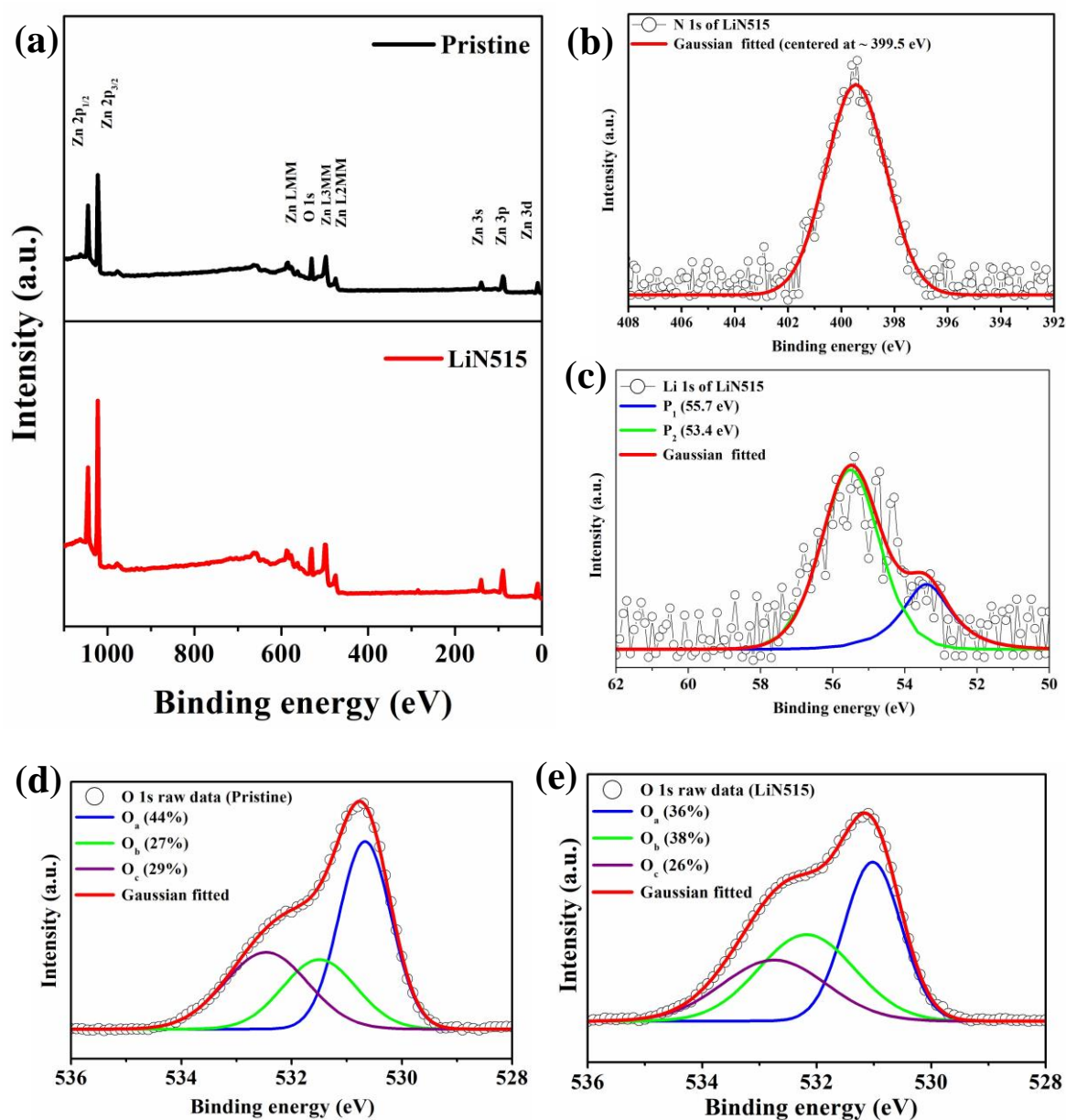
Fig. 8.4 (a) XPS survey scan of pristine and Li515 respectively, (b) N 1s of LiN515, (c) Li 1s of LiN515, and (d)-(e) The Gaussian fittings of O 1s XPS peaks of pristine and LiN515 respectively.

Fig. 8.5(a) represents the RT Raman scattering spectra (200–800 cm^{-1}) for all the samples. The assignments of the peaks have been carried out in the previous chapters. However, two main Raman modes at 437 cm^{-1} and at 579 cm^{-1} are observed in this co-implantation case. The

high intensity of E_2^{High} represents high crystalline order in ZnO [38]. The Raman mode in the range of ~510–605 cm^{-1} peaking at around 579 cm^{-1} is the cumulative effect of several disorder activated Raman modes as reported by the previous reports [25, 39]. The inverse-correlation between the intensities of 579 cm^{-1} and 437 cm^{-1} is seen in Fig. 8.5(a), which is quite obvious as the disorder increases with an increase in the co-implantation ion fluence. This confirms that the crystallinity of the implanted samples is reduced as well as more lattice disorder are introduced with an increase in co-implantation fluence. This is at par with the XRD results. In chapter 6, a Raman mode at 275 cm^{-1} has been reported for the N implanted NRs. Interestingly this mode is absent in the N-Li co-implanted samples. It was discussed that though the origin of 275 cm^{-1} Raman Mode is controversial, the Zn_i–N_O defect complex is mostly believed to be responsible for this Raman mode [40]. The absence of 275 cm^{-1} Raman mode in the present case probably indicates that the Zn_i–N_O defect complex might be decomposed into isolated N_O and Zn_i due to further Li implantation. The broad band has been deconvoluted into three Gaussians peaks entered at around 543, 560, and 579 cm^{-1} respectively for all the samples [25, 41-43]. The assignments of these modes have already been done in the previous chapters. The specified area under 560 cm^{-1} and 579 cm^{-1} peaks for different co-implantation fluences are presented in the bar diagram in Fig. 8.5(b), which shows that the peak area under both 560 cm^{-1} and 579 cm^{-1} modes increases as the fluence increases. This result indicates that the concentration of both Zn_i and V_O defects increases with an increase in the co-implantation fluence, which is at par with the XRD and XPS results.
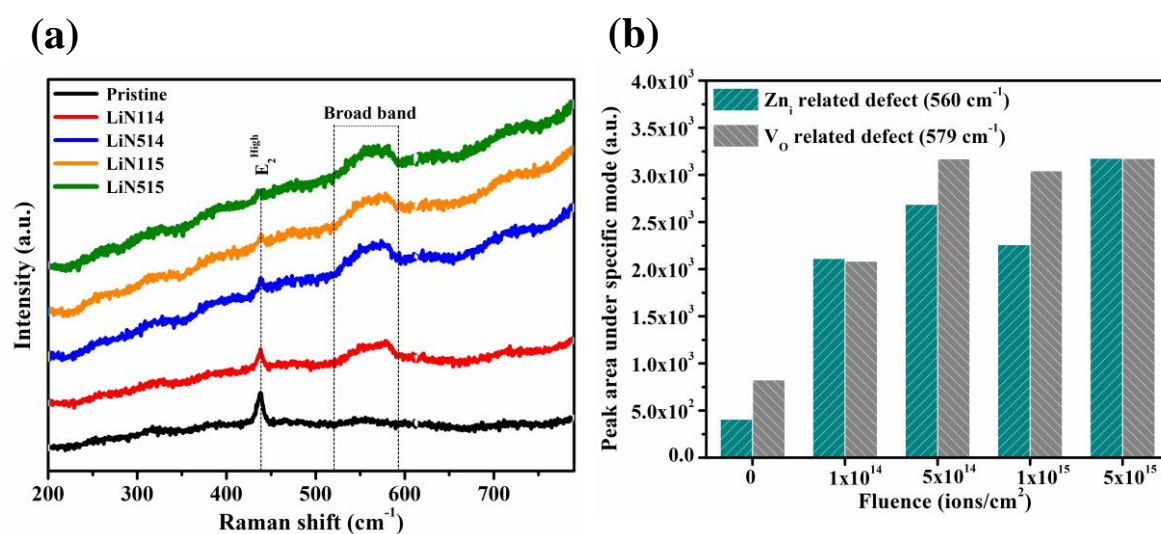

Fig. 8.5 (a) RT Raman spectra of pristine and N-Li co-implanted ZnO NRs, (b) the variation of the area under 560 and 579 cm^{-1} mode for all the samples.

The RT PL spectra of all the samples have been illustrated in Fig. 8.6 (a), wherein a strong peak at ~3.28 eV corresponds to the NBE emission and a broad emission in the visible region from 1.75 to 2.85 eV is linked to the DL emission [44, 45]. I_{NBE} is maximum for pristine. As soon as the NRs are co-implanted with N-Li ions, I_{NBE} starts to decreases from the very first fluence and it continues as the co-implantation fluence increases. The NRs implanted with the fluence 5×10^{15} ions/cm^2 (LiN515) possesses minimum I_{NBE}, indicating the presence of large number of structural defects. Similar to I_{NBE}, I_{DL} is found to decrease as compared to pristine with an increase in the co-implantation fluence. Pristine shows yellow-orange DL emission at ~2.15 eV, while the co-implanted NRs exhibit peak green emission at ~2.48 eV. The transformation of the yellow-orange emission to the green emission is again a clear indication of the changes in structural defects. As discussed in the earlier chapters, V_{Zn} defects are mostly claimed to be responsible for the green emissions [46, 47]. Formation of V_{Zn} is more likely in co-implanted NRs, which gives rise to the green emission. The ratio I_{NBE} / I_{DL} has been expressed by a bar diagram in Fig. 8.6(b). It is found in Fig. 8.6(b) that the ratio I_{NBE} / I_{DL} is maximum for pristine. The ratio continues to decrease as the co-implantation fluence increases. The concentration of point defects increases with an increase in the co-implantation fluence, which are not repaired completely even after annealing treatment. The large concentration of the point defects merges to larger open volumes defects, which act as non-radiative recombination centres and reduces the ratio I_{NBE} / I_{DL}.
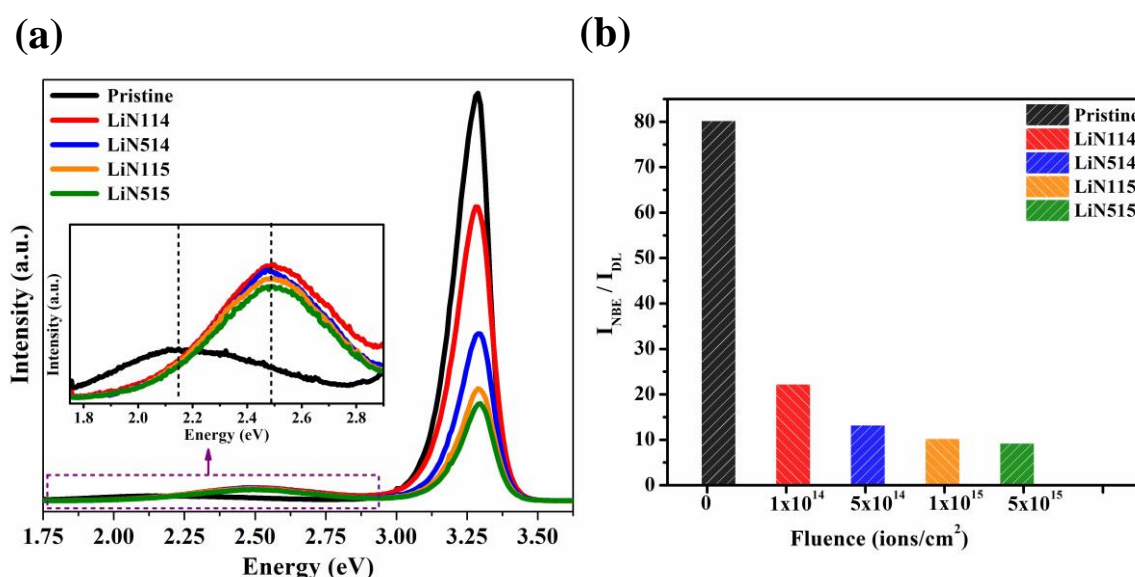

Fig. 8.6 (a) RT PL spectra of pristine and N-Li co-implanted ZnO NRs and (b) bar diagram representation of the ratio I_{NBE} / I_{DL} at various fluences.

8.4 Conclusions

In conclusion, the formation of defects and their interactions in 100 keV N-Li co-implanted ZnO NRs have discussed using various experimental techniques. SRIM has also been used to evaluate the quantitative energy loss, the distributions of the implanted N and Li ions and the point defects along the target ZnO NRs. The implantation-induced structural disorders increase with an increase in co-implantation fluence. Between N and Li ions of same energy, N ion implantation produces more damages in ZnO compared to Li ions. The implanted N ions substitute at O site forming N_O and a considerable fraction of implanted Li ions is incorporated into Zn^{2+} site forming Li_{Zn} acceptor. No $(N_2)_O$ donor is found in the co-implanted NRs. Thus, both the acceptors N_O and Li_{Zn} are produced in Li-N co-implanted ZnO NRs and the formation of N_O-Li_i complex has been predicted. The appearance of a green PL emission indicates the formation of V_{Zn} due to co-implantation. Thus, the experimental and simulation results combinedly confirms that the acceptor states are produced in ZnO NRs due to N and Li co-implantation along with the production of other structural defects.

8.5 References

[1] Y. Zeng, Z. Ye, W. Xu, D. Li, J. Lu, L. Zhu, B.J.A.P.L. Zhao, Dopant source choice for formation of p-type ZnO: Li acceptor, 88 (2006) 062107.
[2] W. Liu, F. Xiu, K. Sun, Y.-H. Xie, K.L. Wang, Y. Wang, J. Zou, Z. Yang, J.J.J.o.t.A.C.S. Liu, Na-doped p-type ZnO microwires, 132 (2010) 2498-2499.
[3] Y. Zeng, Z. Ye, W. Xu, B. Liu, Y. Che, L. Zhu, B.J.M.L. Zhao, Study on the Hall-effect and photoluminescence of N-doped p-type ZnO thin films, 61 (2007) 41-44.
[4] D.-K. Hwang, H.-S. Kim, J.-H. Lim, J.-Y. Oh, J.-H. Yang, S.-J. Park, K.-K. Kim, D.C. Look, Y.J.A.P.L. Park, Study of the photoluminescence of phosphorus-doped p-type ZnO thin films grown by radio-frequency magnetron sputtering, 86 (2005) 151917.
[5] Y. Ryu, T. Lee, H.J.A.P.L. White, Properties of arsenic-doped p-type ZnO grown by hybrid beam deposition, 83 (2003) 87-89.
[6] F. Xiu, Z. Yang, L. Mandalapu, D. Zhao, J. Liu, W.J.A.P.L. Beyermann, High-mobility Sb-doped p-type ZnO by molecular-beam epitaxy, 87 (2005) 152101.
[7] Y.J. Zeng, Z.Z. Ye, W.Z. Xu, B. Liu, Y. Che, L.P. Zhu, B.H. Zhao, Study on the Hall-effect and photoluminescence of N-doped p-type ZnO thin films, Mater. Lett., 61 (2007) 41-44.
[8] J.G. Reynolds, C.L.R. Jr., A. Mohanta, J.F. Muth, J.E. Rowe, H.O. Everitt, D.E. Aspnes, Shallow acceptor complexes in p-type ZnO, Applied Physics Letters, 102 (2013) 152114.
[9] N. Shakti, C. Devi, A.K. Patra, P.S. Gupta, S. Kumar, Lithium doping and photoluminescence properties of ZnO nanorods, AIP Adv., 8 (2018) 5.
[10] J. Lee, S. Cha, J. Kim, H. Nam, S. Lee, W. Ko, K.L. Wang, J. Park, J. Hong, p-Type Conduction Characteristics of Lithium-Doped ZnO Nanowires, Adv. Mater., 23 (2011) 4183-+.
[11] H. Ahmoum, M. Boughrara, M.S. Su'ait, M. Kerouad, Effect of position and concentration of Li on ZnO physical properties: Density functional investigation, Chem. Phys. Lett., 719 (2019) 45-53.

[12] Z. Zhang, J. Huang, S. Chen, X. Pan, L. Chen, Z.J.J.o.M.S.M.i.E. Ye, P-type single-crystalline ZnO films obtained by (Li, N) dual implantation through dynamic annealing process, 28 (2017) 16215-16219.

[13] B. Zhang, B. Yao, Y. Li, Z. Zhang, B. Li, C. Shan, D. Zhao, D.J.A.P.L. Shen, Investigation on the formation mechanism of p-type Li–N dual-doped ZnO, 97 (2010) 222101.

[14] X.-Y. Duan, R.-H. Yao, Y.-J.J.A.P.A. Zhao, The mechanism of Li, N dual-acceptor co-doped p-type ZnO, 91 (2008) 467-472.

[15] X. Tang, X. Cheng, D. Wagner, H. Lü, Q.J.J.o.A.P. Zhang, The origin of p-type conduction in Li-N codoped ZnO: An ab initio calculation study, 110 (2011) 013711.

[16] L. Liu, J.L. Xu, D.D. Wang, M.M. Jiang, S.P. Wang, B.H. Li, Z.Z. Zhang, D.X. Zhao, C.X. Shan, B. Yao, D.Z. Shen, p-Type Conductivity in N-Doped ZnO: The Role of the N-Zn-V-O Complex, Phys. Rev. Lett., 108 (2012).

[17] M.N. Amini, R. Saniz, D. Lamoen, B. Partoens, The role of the VZn–NO–H complex in the p-type conductivity in ZnO, Physical Chemistry Chemical Physics, 17 (2015) 5485-5489.

[18] Z. Huang, H. Ruan, H. Zhang, D. Shi, W. Li, G. Qin, F. Wu, L. Fang, C. Kong, Investigation on the p-type formation mechanism of nitrogen ion implanted ZnO thin films induced by rapid thermal annealing, Opt. Mater. Express, 9 (2019) 3098-3108.

[19] W.J. Li, H. Zhang, X.Y. Zhang, G.P. Qin, H.L. Li, Y.Q. Xiong, L.J. Ye, H.B. Ruan, C.Z. Tong, C.Y. Kong, L. Fang, Non-axial N-O-V-Zn shallow acceptor complexes in nitrogen implanted p-type ZnO thin films, Appl. Surf. Sci., 529 (2020).

[20] H. Ryssel, I. Ruge, Ion implantation, (1986).

[21] W.Q. Li, X.H. Xiao, A.L. Stepanov, Z.G. Dai, W. Wu, G.X. Cai, F. Ren, C.Z. Jiang, The ion implantation-induced properties of one-dimensional nanomaterials, Nanoscale research letters, 8 (2013) 1-13.

[22] J. Williams, Ion implantation of semiconductors, Materials Science Engineering: A, 253 (1998) 8-15.

[23] D.C. Look, G.C. Farlow, P. Reunchan, S. Limpijumnong, S.B. Zhang, K. Nordlund, Evidence for native-defect donors in n-type ZnO, Phys. Rev. Lett., 95 (2005) 4.

[24] S. Chattopadhyay, S. Dutta, D. Jana, S. Chattopadhyay, A. Sarkar, P. Kumar, D. Kanjilal, D.K. Mishra, S.K. Ray, Interplay of defects in 1.2 MeV Ar irradiated ZnO, J. Appl. Phys., 107 (2010) 8.

[25] A. Mondal, S. Pal, A. Sarkar, T.S. Bhattacharya, A. Das, N. Gogurla, S.K. Ray, P. Kumar, D. Kanjilal, K.D. Devi, A. Singha, S. Chattopadhyay, D. Jana, Raman spectroscopic analysis on Li, N and (Li,N) implanted ZnO, Mater. Sci. Semicond. Process, 80 (2018) 111-117.

[26] J.P. Lv, C.D. Li, J.J. BelBruno, Defect evolution on the optical properties of H+-implanted ZnO whiskers, Crystengcomm, 15 (2013) 5620-5625.

[27] M. Wang, F. Ren, J.G. Zhou, G.X. Cai, L. Cai, Y.F. Hu, D.N. Wang, Y.C. Liu, L.J.J. Guo, S.H. Shen, N Doping to ZnO Nanorods for Photoelectrochemical Water Splitting under Visible Light: Engineered Impurity Distribution and Terraced Band Structure, Sci Rep, 5 (2015).

[28] S.H. Park, Y.B. Lee, C.H. Kwak, S.Y. Seo, S.H. Kim, Y.D. Choi, S.W. Han, Structural and optical properties of nitrogen-ion-implanted ZnO nanorods, J. Korean Phys. Soc., 52 (2008) 954-959.

[29] Y.T. Chuang, J.W. Liou, W.Y. Woon, Formation of p-type ZnO thin film through co-implantation, Nanotechnology, 28 (2017).

[30] P. Kumar, H.K. Malik, A. Ghosh, R. Thangavel, K. Asokan, An insight to origin of ferromagnetism in ZnO and N implanted ZnO thin films: Experimental and DFT approach, J. Alloy. Compd., 768 (2018) 323-328.

[31] N.R. Yogamalar, A.C. Bose, Burstein-Moss shift and room temperature near-band-edge luminescence in lithium-doped zinc oxide, Appl. Phys. A-Mater. Sci. Process., 103 (2011) 33-42.

[32] S. Patrik, R. Durena, P. Onufrijevs, S. Miasojedovas, T. Malinauskas, S. Stanionyte, A. Zarkov, A. Zukuls, I. Bite, K. Smits, Morphological and optical property study of Li doped ZnO produced by microwave-assisted solvothermal synthesis, Mater. Sci. Semicond. Process, 135 (2021) 8.

[33] S. Shawuti, A.U.R. Sherwani, M.M. Can, M.A. Gulgun, Complex Impedance Analyses of Li doped ZnO Electrolyte Materials, Sci Rep, 10 (2020) 10.

[34] K.R. Nandanapalli, D. Mudusu, Surface Passivated Zinc Oxide (ZnO) Nanorods by Atomic Layer Deposition of Ultrathin ZnO Layers for Energy Device Applications, ACS Appl. Nano Mater., 1 (2018) 4083-4091.

[35] R. Al-Gaashani, S. Radiman, A.R. Daud, N. Tabet, Y. Al-Douri, XPS and optical studies of different morphologies of ZnO nanostructures prepared by microwave methods, Ceram. Int., 39 (2013) 2283-2292.

[36] X. Yang, A. Wolcott, G. Wang, A. Sobo, R.C. Fitzmorris, F. Qian, J.Z. Zhang, Y. Li, Nitrogen-Doped ZnO Nanowire Arrays for Photoelectrochemical Water Splitting, Nano Lett., 9 (2009) 2331-2336.

[37] X.H. Li, H.Y. Xu, X.T. Zhang, Y.C. Liu, J.W. Sun, Y.M. Lu, Local chemical states and thermal stabilities of nitrogen dopants in ZnO film studied by temperature-dependent x-ray photoelectron spectroscopy, Applied Physics Letters, 95 (2009).

[38] A. Kumar, S. Keshri, B. Pandey, J.B.M. Krishna, D. Das, Impact of N5+ ion implantation on optical and electrical properties of polycrystalline ZnO film, Radiat. Eff. Defects Solids, 169 (2014) 965-979.

[39] A. Mondal, S. Pal, A. Sarkar, T.S. Bhattacharya, A. Singha, S.K. Ray, P. Kumar, D. Kanjilal, D. Jana, Raman investigation of N-implanted ZnO: Defects, disorder and recovery, J. Raman Spectrosc., 50 (2019) 1926-1937.

[40] F. Friedrich, M.A. Gluba, N.H. Nickel, Identification of nitrogen and zinc related vibrational modes in ZnO, Applied Physics Letters, 95 (2009).

[41] A. Mondal, S. Pal, A. Sarkar, T.S. Bhattacharya, S. Pal, A. Singha, S.K. Ray, P. Kumar, D. Kanjilal, D. Jana, Raman investigation of N-implanted ZnO: Defects, disorder and recovery, J. Raman Spectrosc., 50 (2019) 1926-1937.

[42] M. Scepanovic, M. Grujic-Brojcin, K. Vojisavljevic, S. Bernik, T. Sreckovic, Raman study of structural disorder in ZnO nanopowders, J. Raman Spectrosc., 41 (2010) 914-921.

[43] S. Pal, N. Gogurla, A. Das, S.S. Singha, P. Kumar, D. Kanjilal, A. Singha, S. Chattopadhyay, D. Jana, A. Sarkar, Clustered vacancies in ZnO: chemical aspects and consequences on physical properties, J. Phys. D-Appl. Phys., 51 (2018) 12.

[44] R. Ghosh, B. Mallik, S. Fujihara, D. Basak, Photoluminescence and photoconductance in annealed ZnO thin films, Chem. Phys. Lett., 403 (2005) 415-419.

[45] I. Parkhomenko, L. Vlasukova, F. Komarov, M. Makhavikou, O. Milchanin, E. Wendler, M. Zapf, C. Ronning, Luminescence of ZnO nanocrystals in silica synthesized by dual (Zn, O) implantation and thermal annealing, J. Phys. D-Appl. Phys., 54 (2021) 9.

[46] H. Chen, S.L. Gu, K. Tang, S.M. Zhu, Z.B. Zhu, J.D. Ye, R. Zhang, Y.D. Zheng, Origins of green band emission in high-temperature annealed N-doped ZnO, J. Lumines., 131 (2011) 1189-1192.

[47] F. Fabbri, M. Villani, A. Catellani, A. Calzolari, G. Cicero, D. Calestani, G. Calestani, A. Zappettini, B. Dierre, T. Sekiguchi, G. Salviati, Zn vacancy induced green luminescence on non-polar surfaces in ZnO nanostructures, Sci Rep, 4 (2014) 6.

CHAPTER-9

Summary and future scope

> **Summary**

The evolution and interactions of various point defects in ZnO nanoparticle thin films and 1D NRs implanted with both donor and acceptor dopants have been presented in this thesis via the characterizations of structural, electrical and optical properties. The essence of the noteworthy outcomes of the works described in the chapters 4 to 8 is summarized below.

Al implantation in sol-gel ZnO thin films lead to the formation of structural defects causing modification in the electrical and optical transmission properties. For the highest fluence (6 $\times 10^{15}$ ions/cm^2), the sheet resistance is found to be 156 Ω/sq with an average visible transmission of 82%. The high figure of merit value of the Al implanted ZnO films indicates not only a probable use of the films as a TCO layer but also offers an opportunity to control the conductivity along with its transparency. The healing of V_{Zn} defects has been seen to enhance the conductivity of the implanted films further.

A dramatic improvement in the RT PL properties has been observed due to formation of neutral Al donor bound excitonic recombination centers for the lower fluence Al implanted ZnO NRs. For higher Al fluence, the formation of non-radiative recombination centers on the surfaces of ZnO NRs are formed causing reduced PL properties. This comprehensive study provides a significant novel route for utilizing the Al implanted ZnO NRs in solid state lighting applications.

In case of N implantation in ZnO NRs, the ion-induced structural damages are increased with an increase in N ion fluence and these structural disorders have been seen to be related to various N-related defect complexes. The implanted N ion substitutes at O sublattice and N_O acceptors are formed. Under the presence of N_O acceptors and implantation-induced V_{Zn}, the formation of N_O-V_{Zn} shallow acceptor complex has been predicted. Among various post-implantation annealing ambiences, an annealing separately in Ar and O$_2$ generates only N_O state, while an annealing in excess Zn ambient produces an unwanted $(N_2)_O$ donor state. In addition, O$_2$ and Ar play a key role to stabilize the N dopants in ZnO via suppressing V_O and/ or preserving the concentration of N-related acceptors in the ZnO NRs. These findings demonstrate a way to tailor the nontrivial compensating point defects in case of p-type doping using group V elements in ZnO.

In case of Li implantation in ZnO NRs, the implantation-induced structural point defects have also been seen to be increased drastically with an increase in the fluence. The substitution of Li at Zn sublattice forms Li$_{Zn}$ acceptor. Due to the both of formation of acceptors and various implantation-induced defects, the Li implanted NRs are electrically highly resistive. The

transformation of the yellow-orange PL emission into a green emission in the Li implanted NRs is due to formation of large number of V_{Zn}. This study can help one to understand the formation and evolution of point defects when the p-typing of ZnO NRs is performed using group I ion implantation.

In case of co-implantation in ZnO NRs with N and Li ions, it has been seen that N ions produce more structural damages as compared to Li ions of same energy. The overall structural damages are increased significantly with the increase in the fluence. Both N_O and Li_{Zn} acceptors are produced in N-Li co-implanted ZnO NRs. The N_O forms Li_i –N_O complex with the Li_i and thus the concentration of Li_i and the possibility of the generation of $(N_2)_O$ donors are reduced. Therefore, Li_{Zn} acceptor still exits and may contributes to creating p-type ZnO NRs. As a matter of fact, this N-Li co-implantation technique can be beneficial for obtaining stable and reproducible p-type ZnO NRs.

Thus, the postgrowth doping strategy by ion implantation can open up a new avenue in the quest of high-efficiency device applications of nanostructured ZnO.

➢ **Future scope**

From the summery of the thesis work, the future directions for utilizing ion implantation for achieving ZnO-based high-performance devices may be summarized as follows:

(i) The impact of ion implantation on the functionality of ZnO still requires more investigations. As a result of energetic ions irradiation, defect states, and electronic structures are modified along with possible local lattice distortions. It can be interesting to distinguish the individual radiation effects and identify the corresponding critical changes, which may lead to new properties of ZnO. The combination of advanced material characterization techniques and modeling approaches may help one to understand various radiation effects and their impact on the electrical and optical properties of ZnO.

(ii) It is still challenging to precisely tune the local properties of ZnO nanostructured thin films for practical applications. The irradiation parameters, such as ion species and their energies and fluences, intensely affect the properties of implanted ZnO nanostructures and hence influence its device performance.

(iii) Channeling effect should be reduced to obtain precise doping profiles. The most effective way to obtain doping profiles is to choose proper tilt and twist angles. This aspect needs to be exploited to reduce damage in ZnO crystals.

(iv) The in-situ characterization techniques can help us to further understand the continuous change process of atomic structures and the relationship between them and the evolution of defects in ZnO.

(v) Finally, ion implantation is undoubtedly a potential and efficient tool that can be extended to many other functional oxides to modify materials at multiple levels. It can be believed that the development of ion beam technology will attract more attention and provide more opportunities for a wide range of material research fields.